Optical Metasurfaces for Energy Conversion

Emiliano Cortés,*,# Fedja J. Wendisch,# Luca Sortino,# Andrea Mancini, Simone Ezendam, Seryio Saris, Leonardo de S. Menezes, Andreas Tittl, Haoran Ren, and Stefan A. Maier*

ACCESS | 📊 Metrics & More | 📰 Article Recommendations

ABSTRACT: Nanostructured surfaces with designed optical functionalities, such as metasurfaces, allow efficient harvesting of light at the nanoscale, enhancing light−matter interactions for a wide variety of material combinations. Exploiting light-driven matter excitations in these artificial materials opens up a new dimension in the conversion and management of energy at the nanoscale. In this review, we outline the impact, opportunities, applications, and challenges of optical metasurfaces in converting the energy of incoming photons into frequency-shifted photons, phonons, and energetic charge carriers. A myriad of opportunities await for the utilization of the converted energy. Here we cover the most pertinent aspects from a fundamental nanoscopic viewpoint all the way to applications.
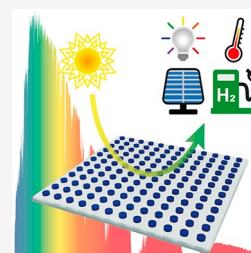
CONTENTS

1. INTRODUCTION

Materials and our ability to process and shape them have played such a major role in the development and well-being of civilizations that the history of humankind is traditionally divided into ages that reflect the dominant materials and technologies available at that time such as the bronze, the iron, or the current silicon age. Much of our understanding of the physical properties of a material comes from its interaction with electromagnetic waves: determined by their chemical (atomic) composition, each material is endowed with a unique set of electromagnetic (EM) properties such as dielectric permittivity and magnetic permeability, among others. Two decades ago, a new class of artificially structured materials started to come to the forefront of research interest in the optical sciences, where the fundamental properties governing interactions with EM radiation were not determined by their atomistic structure but by an artificial nanostructuring with a pitch size much smaller than the wavelength of radiation. These "metamaterials" (from the Greek $\mu\varepsilon\tau\acute{\alpha}$, meta, meaning beyond) derive their properties from the shape of their subwavelength and nanosized building blocks, often described as "meta-atoms", governing their resonant properties for interactions with the electric and magnetic components of electromagnetic radiation. This approach toward artificial materials has enabled fascinating progress in shaping the interaction between matter and waves (electromagnetic and acoustic) in a generalized manner and further brought disparate scientific communities together.

In this review, our goal is to outline the potential of EM metamaterials and metasurfaces, their two-dimensional counterpart, for energy conversion, that is, for the efficient harvesting and conversion of photons to photons of a different energy, of photons to phonons, and of photons to energetic charge carriers (Figure 1). A large number of excellent reviews describing the physics and history of metamaterials for shaping light—matter interactions exist in the scientific literature, with different points of focus. Here we want to mention only a few: the general physics of control over electromagnetic fields enabled via resonant meta-atoms,[1] the achievement of optical properties not found in nature via resonant metallic building blocks,[2] and the fascinating possibilities offered by dielectric resonators.[3] While

the first decade of metamaterials research was mostly dedicated to three-dimensional structures,[4] metasurfaces have recently gathered a large amount of attention as the enabler of flat optical components due to the ability to control the phase-shift of radiation at interfaces.[5,6] Moreover, a number of remarkable examples recently appearing in the literature show that metasurfaces could also strongly impact many energy conversion processes at the nanoscale, which is the focus of this review.

Briefly, metasurfaces are composed of arrays of optical antennas with subwavelength dimensions. As metamaterials, their functionalities result not from the properties of the base materials but from the designed structure. By controlling their shape, size, orientation and arrangement, a multitude of benefits not possible with conventional materials are achievable. In this review, we will focus on the utilization of such metasurfaces toward energy conversion processes. This includes the transformation of incoming photon energy into energy in the form of emitted photons, phonons, and electrons.

The list below summarizes some of the most important benefits of metasurfaces for energy conversion that make them stand out compared to current technologies and that we will cover along this review:

- Achievement of higher absorption than bulk materials but at much lower volumes.
- Absorption of light at different frequencies than their bulk counterpart and tunability of the absorption across the entire solar spectrum.
- Spatial localization of absorption, allowing photons to be absorbed where they are needed.
- Dramatic expansion of the materials toolbox by enabling the utilization of materials that are otherwise deemed to be not suitable for energy conversion.
- Dynamic tuning of optical properties.
- Scalability in the nanofabrication processes: transitioning toward applications.
- Conversion of photons into photons with different energies. This can be exploited, as an example, to harness the infrared (IR) part of the solar spectrum.
- Conversion of light into heat. This phenomenon can be exploited to obtain controlled temperature profiles at the nanomicroscale (thermal nanophotonics) for passive radiative cooling and IR camouflage.
- Enhancement of the sensitivity of chemically selective spectroscopies, where photons interact with the vibrational degrees of freedom of solids/molecules.
- Concentration of charge-carrier densities close to active reaction sites, which increases photocatalytic efficiency.
- Fine-tuning of absorption and reflection properties over a narrow spectral range enables thin-film photovoltaic (PV) devices with enhanced power conversion efficiencies.
- Realization of ultracompact, cost-effective, and integrated photodetectors with advanced functionalities such as chiral light and broadband sensing.

In the following, we will equip the reader with a basic understanding of the most important physical principles of metasurface design, allowing the efficient harvesting of photons, the "input" of energy so to speak. We will then outline fabrication approaches before reviewing in detail the possibilities of converting the harvested energy to frequency-shifted radiation, coherent phonons and heat, and to energetic charge carriers. We expect to cover the knowledge of different
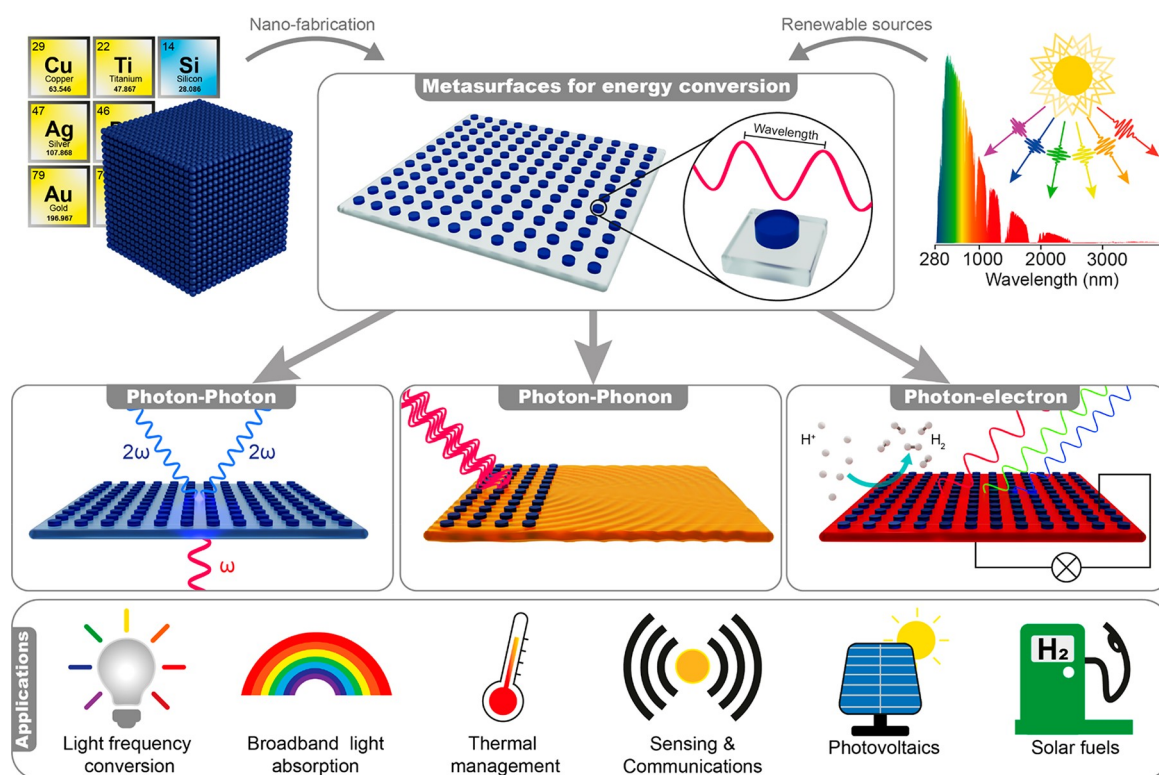
Figure 1. Metasurfaces for energy conversion. Metasurfaces are the two-dimensional form of a metamaterial, obtained by nanostructuring bulk materials into ordered 2D arrays of nanostructures, where the size of the constituent elements, that is, the meta-atoms, is comparable to or smaller than the wavelength of light. Because of their extraordinary interaction with light, they are promising candidates for the efficient conversion of photons into photons with different energies, phonons, and energetic charge carriers. These energy conversion channels can be exploited toward a variety of applications, ranging from light frequency conversion, broadband light absorption, thermal management, sensing, communication, photovoltaics and the generation of solar fuels, among others.

communities approaching this fascinating topic and, as such, we have also included didactic sections on the principles of optics, metamaterials and metasurfaces, higher harmonics generation, nanoscale energy conversion, photovoltaics and chemical reactivity, among others. We start by describing in section 2 the basic principles of light absorption and scattering in metals, semiconductors, and artificial materials.

2. FUNDAMENTALS

2.1. Light−Matter Interaction: The Basics

The efficient conversion of energy into desirable and usable resources harnesses the capability of materials for first capturing such energy from sources such as light, electrical currents and heat, and then transducing it into the other. Understanding how light−matter interactions occur at the nanoscale is a crucial step for the design of functional metamaterials with subwavelength control of light reflection, refraction, and absorption as well as for the realization of a broad range of practical applications. One clear example, holding great promises for environmental sustainability, is the production of easily stored chemical fuels and electrical energy from the efficient utilization of solar radiation. The solar spectrum delivers light frequencies from ultraviolet and visible (UV−vis) to the infrared (IR) light, with a power of roughly 10^5 TW, orders of magnitude larger than current energy requirements of humanity, predicted to be around 20−40 TW in 2050.[7,8] For efficient solar light harvesting, as in the case of photovoltaics or photocatalysis, broadband light absorption is required to fully utilize the entire electromagnetic spectrum received from the sun. Here, the key step is the

conversion of the incoming photons into electrons, and their efficient transport toward collection interfaces for the generation of photocurrents and energy storage, or at catalytic surfaces for solar fuel production. Many other applications exist that require the understanding of frequency conversion of light (photon−photon conversion) or harnessing the thermal radiation and heat (photon−phonon conversion) for low loss energy harvesting. Understanding these approaches requires the knowledge of many general concepts in physics and chemistry. In this section, we briefly review the basic quantities and parameters that are relevant to understand light−matter interactions at optical frequencies. More details can be found in many standard optics and solid state physics textbooks.[9,10]

2.1.1. Introduction to Optical Constants. Electromagnetic phenomena, such as light propagation and absorption, are described by Maxwell's equations. In vacuum, a possible solution for the electric field according to Maxwell's equations takes the form of plane waves, as

$$\overline{E}(z, t) = \hat{x}E_0 e^{i(kz - \omega t)} \tag{2.1}$$

where k is the wavenumber (the modulus of the wavevector $\overline{k}$), z the direction of propagation, and $\omega = 2\pi f$, where f is the frequency. In vacuum, the wavenumber is related to the wavelength λ_0 as $k_0 = 2\pi/\lambda_0$ and to the frequency ω as $k_0 = \omega/c$, where c is the speed of light in vacuum. The solution for the magnetic field, $\overline{B}(z, t)$, assumes the same form. The electric field $\overline{E}(z, t)$, magnetic field $\overline{B}(z, t)$, and wavevector $\overline{k}$ are all perpendicular to each other in space. The propagation of energy carried by the plane wave (per unit area and unit time) can be

described through the Poynting vector $\overline{S} = c\,\overline{E} \times \overline{B}/(4\pi)$, which points in the same direction as $\overline{k}$.

Propagation of light in a material can be described by its complex refractive index $\tilde{n} = n + i\kappa$. The real part n accounts for the reduction of the speed of light in the medium, while the imaginary part κ (also called extinction coefficient) relates to the absorption in the material. This can be readily seen by considering the time-independent form of eq 2.1 where the vacuum wavevector $k_0 = \omega/c$ is replaced by $k = \tilde{n}\omega/c$:

$$\overline{E}(z) = \hat{x}E_0 e^{ik_0 nz} e^{-k_0 \kappa z} \tag{2.2}$$

As $k_0 = 2\pi/\lambda_0$, the wavelength in the medium is reduced as $\lambda = \lambda_0/n$, while κ determines the attenuation of the field. The optical properties of a material are also often described in terms of the dielectric function $\varepsilon = \varepsilon_1 + i\varepsilon_2$, which is related to the complex refractive index by the following relations, $\varepsilon_1 = n^2 - \kappa^2$ and $\varepsilon_2 = 2n\kappa$. Another relevant quantity to describe the attenuation of light in a material is the absorption coefficient α. The light intensity after traveling a distance z in a lossy material follows an exponential decay, described by the Beer–Lambert law as

$$I(z) = I_0 e^{-\alpha z} \tag{2.3}$$

Here the intensity is defined as the modulus squared of the field, $I = |E|^2$, and from (eqs 2.2 and 2.3) the relation between the absorption coefficient α and extinction coefficient κ can be established as $\alpha = 2\kappa\omega/c$. The distance over which the field decays to $1/e$ is called the skin depth $\delta_0 = 2/\alpha$.

2.1.2. Light Absorption in Metals and Semiconductors. In the simple case of a plane wave incident on the interface of two semi-infinite materials, the EM wave is either transmitted (T) or reflected (R) back in the specular direction and, dependent on the material's absorption coefficient, absorbed (A) with the overall energy balance defined as $1 = A + T + R$. The reflection and absorption properties of a material can be described from its refractive index, or equivalently from its dielectric function $\varepsilon(\omega)$. The shape of the dielectric function $\varepsilon(\omega)$ depends on light–matter interactions in the material and has different forms for metals and semiconductors, which consequently exhibit very different optical properties. Fundamentally, metals are characterized by having half-filled electronic bands at $T = 0$ K, meaning electrons can freely move under an external applied electric field. Semiconductors, on the other hand, are characterized by having a fully filled electronic band, called the valence band (VB), which is separated in energy by a band gap E_g from the closest higher energy band, called the conduction band (CB). Semiconductors with very large band gap energies E_g are often called insulators.

The low-frequency response of metals can be well described by considering the response from a free-electron gas with density N equal to the density of electrons in the CB. Additional contributions arise at frequencies where the photon energy is sufficiently high to excite electrons from the fully filled VB to the partially filled CB. The response of a free-electron gas is well described by the Drude model, where the electrons are characterized by an effective mass m^* with an average collision time $\tau = 1/\gamma$. The corresponding dielectric function can be derived by writing the equation of motion for N electrons driven by a harmonic electric field with the collision time τ. With these assumptions, $\varepsilon(\omega)$ for a metal assumes the following form:

$$\varepsilon_1(\omega) = 1 - \frac{\omega_p^2}{\gamma^2 + \omega^2} \tag{2.4}$$

$$\varepsilon_2(\omega) = \frac{\omega_p^2 \gamma}{\omega(\gamma^2 + \omega^2)} \tag{2.5}$$

where $\omega_p = \sqrt{Ne^2/\varepsilon_0 m^*}$ is called the plasma frequency. The real part of the dielectric function $\varepsilon_1(\omega)$ is negative for metals in the frequency range below the plasma frequency ($\gamma \ll \omega_p$ in practice). Physically, $\varepsilon_1(\omega) < 0$ indicates that the electrons oscillate in phase with the incoming electric field, strongly attenuating it inside the metal and reradiating the same field as the incident one. This is why for $\omega < \omega_p$, metals are characterized by high reflectivity and small skin depths. Metals at very low frequencies (i.e., in the radiofrequency (RF) range) can be often simply approximated as perfect conductors due to the very high value of $\varepsilon_2(\omega)$ and extremely small values of δ_0. At frequencies $\omega > \omega_p$, the electrons lag behind the electric field, which then penetrates in the material. At high frequencies, the absorption coefficient in metals is low and the skin depth large. For noble metals with a high density of conduction electrons N, like gold and silver, ω_p lies in the UV range and interband transitions must be taken into account to describe their optical properties in the visible.

Beyond metals, light absorption and emission processes are likewise engineered in current optical and electronic devices based on semiconducting materials. Here, light absorption happens only if electrons can be excited from the VB to the CB by a photon of sufficient energy $\hbar\omega > E_g$, generating an electron in the CB and a positively charged hole in the VB. At $T > 0$, electrons can also be excited with the thermal energy, a process that is particularly important at room temperature for doped semiconductors. The dielectric function of a semiconductor can be described by the Lorentz model, where the equation of motion for the electrons also has an additional restoring force term compared to the Drude case. While this model does not represent the real physics of semiconductors, it adequately reproduces their optical response. The additional restoring force introduces an intrinsic oscillation frequency ω_0, which represents the energy of the interband transition. The corresponding dielectric function is

$$\varepsilon_1(\omega) = 1 + \frac{\omega_p^2(\omega_0^2 - \omega^2)}{(\omega_0^2 - \omega^2)^2 + \gamma^2 \omega^2} \tag{2.6}$$

$$\varepsilon_2(\omega) = \frac{\omega_p^2 \omega \gamma}{(\omega_0^2 - \omega^2)^2 + \gamma^2 \omega^2} \tag{2.7}$$

Different from metals, for semiconductors $\varepsilon_1(\omega)$ is positive at all frequencies and $\varepsilon_2(\omega)$ is small above and below ω_0. This means that semiconductors have very small absorption coefficients and losses at frequencies below their interband transition. Semiconductors can be further divided in two classes where the relative position of the CB minimum and VB maximum in momentum space heavily affect their light absorption mechanism. Because of the small photon momentum compared to crystal momentum in solids, optically induced electronic transitions can only happen if the initial and final electronic states have the same momentum. Direct bandgap semiconductors present a vertical electronic transition, where the electron does not change its momentum, and the CB minimum and VB maximum are located at the same position in the momentum space. On the other hand, in indirect bandgap semiconductors, the transition is not located at the same point and the additional momentum required for the transition is

given by a lattice vibration, or phonon. This additional process in the transition leads to a heavily reduced rate of absorption and emission of light, resulting in reduced efficiencies. For reference, the absorption coefficient for a direct bandgap semiconductor scales as $\alpha_{dir}(\omega) \propto 1/\omega\sqrt{\hbar\omega - E_g}$ while for an indirect bandgap semiconductor as $\alpha_{ind}(\omega) \propto (\hbar\omega - E_g \pm \hbar\omega_q)^2$ where $\hbar\omega_q$ is the energy of the phonon providing the missing momentum. For this reason, technological applications greatly benefit from the use of direct bandgap semiconductors due to their higher rate of light absorption.

Because semiconductors usually possess a large refractive index, the dielectric screening of the singular charges in the material provides the possibility of creating a bound state of the electron and hole called exciton. The exciton is a bound electron−hole pair resulting from the mutual Coulomb interaction between the particles and can be described with an analogy to the hydrogen-like problem in quantum physics. The role of excitons is of fundamental understanding for the process of light absorption, charge separation, and charge collection in many of the devices currently used for light emission, such as light emitting diodes, and PV cells for solar energy conversion.

2.1.3. Light Scattering by Small Particles. Light scattering and absorption phenomena are ubiquitous in nature and are responsible for most of the fundamental processes involving light−matter interactions, from the blue color of a clear sky to the bright color gamut of opal crystals. In this section, we introduce the basic principles of light scattering by small particles.

Different scattering processes can be described by defining a parameter $a = \frac{2\pi r}{\lambda}$, defined as the ratio between the particle size (here defined as a spherical particle of radius r) and the wavelength of light λ. For nanophotonic applications, particle sizes are on the order of tens to hundreds of nm and thus are usually comparable to or smaller than the wavelength of light.[11] In the case of a small particle compared to the wavelength of light ($a \ll 1$), Rayleigh scattering theory is utilized, with the known dependence of scattering on $1/\lambda^4$, while for particles comparable with the wavelength of light ($a \approx 1$), Mie scattering theory is used. In case of $a \gg 1$, when the particle is much larger than the wavelength of light, classical geometric optics is sufficient to describe the scattering process.

From a physical point of view, we can describe the scattering of light in terms of the attenuation (or energy loss) of the energy carried by a plane wave incident on an arbitrary particle, also called extinction (Figure 2). Electrons in the material of the particle will be accelerated by the incoming EM field and will

radiate energy in all directions. The overall energy balance can be described as[11] extinction = scattering + absorption. In case of a nonabsorbing medium, the only absorption occurring in the system is given by the material properties, specifically the imaginary part of the dielectric function. We can then define the net energy (W_a) scattered by the particle as the integral over the surface area (A) of an imaginary sphere surrounding the particle as

$$W_a = -\int_A \overline{S} \times \hat{n} \, dA \tag{2.8}$$

where $\overline{S}$ is the Poynting vector and $\hat{n}$ the normal to the surface area. The overall energy balance can be defined as $W_a = W_{incident} + W_{scattered} + W_{extinction}$, where $W_{extinction}$ is the attenuation of the incident light intensity ($W_{incident}$) as a result of the scattering and absorption processes. As $W_{incident}$ vanishes for nonabsorbing media, W_a is then the net rate at which the particle absorbs the radiation, $W_a = W_{abs}$, leading to $W_{ext} = W_{abs} + W_{scatt}$. The ratio between the energy (W) and the incident power (I_i) is the so-called cross-section $C = W/I_i$ and follows that $C_{ext} = C_a + C_{scatt}$. More importantly, we can define the scattering efficiency as C divided by area of the particle, $G = \pi r^2$, perpendicular to the incident beam as $Q_{scatt} = C_{scatt}/G$.

The scattering and extinction cross-section of a spherical particle can be derived analytically by expanding the internal and scattered field into spherical harmonics:

$$C_{scatt} = \frac{W_{scatt}}{I_i} = \frac{2\pi}{k^2} \sum_{n=1}^{\infty} (2n + 1)(|a_n|^2 + |b_n|^2) \tag{2.9}$$

$$C_{ext} = \frac{W_{ext}}{I_i} = \frac{2\pi}{k^2} \sum_{n=1}^{\infty} (2n + 1)\mathcal{R}(a_n + b_n) \tag{2.10}$$

where k is the wavevector of the incoming light and the sum terms represent the multipolar resonances ($n = 1$ dipolar, $n = 2$ quadrupolar,...) over the Mie coefficients a_n and b_n related to the electric and magnetic response, respectively.

As will be discussed in the next section, the resonant scattering of light by small metallic or dielectric particles is associated with increased near-field intensities and contributes to the modification of the far-field radiation patterns, opening up exciting pathways for enhancing light−matter interactions at the nanoscale with control over the phase and directivity of the scattered light.

2.2. Plasmonic and Dielectric Metasurfaces

Precise control of light at the nanoscale requires a specialized toolkit of nanostructured materials capable of transducing between the optical far-field and near-field regimes. Resonant nanoparticles have emerged as invaluable building blocks for nanophotonics, enabling both the spatial and spectral local-ization of EM energy. In this section, we will cover metals and high refractive index dielectrics as two of the leading nanoresonator material systems and introduce how these resonators can be arranged into metasurfaces for advanced functionalities.

2.2.1. Individual Plasmonic and Dielectric Resonators. *2.2.1.1. Plasmonic Resonators.* The discovery that coherent oscillations of the conduction electrons in metals can be driven externally using light constituted a crucial juncture in the development of nanophotonics. Dubbed plasmons, these resonant oscillations are strongly confined to a metal/dielectric interface. At first, plasmons were studied as extended surface
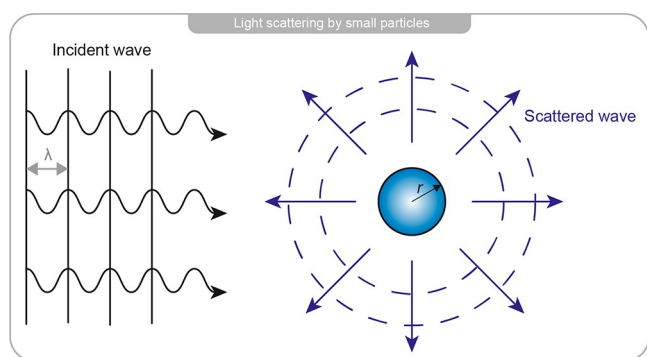
Figure 2. Schematics of the light scattering process by a small particle.
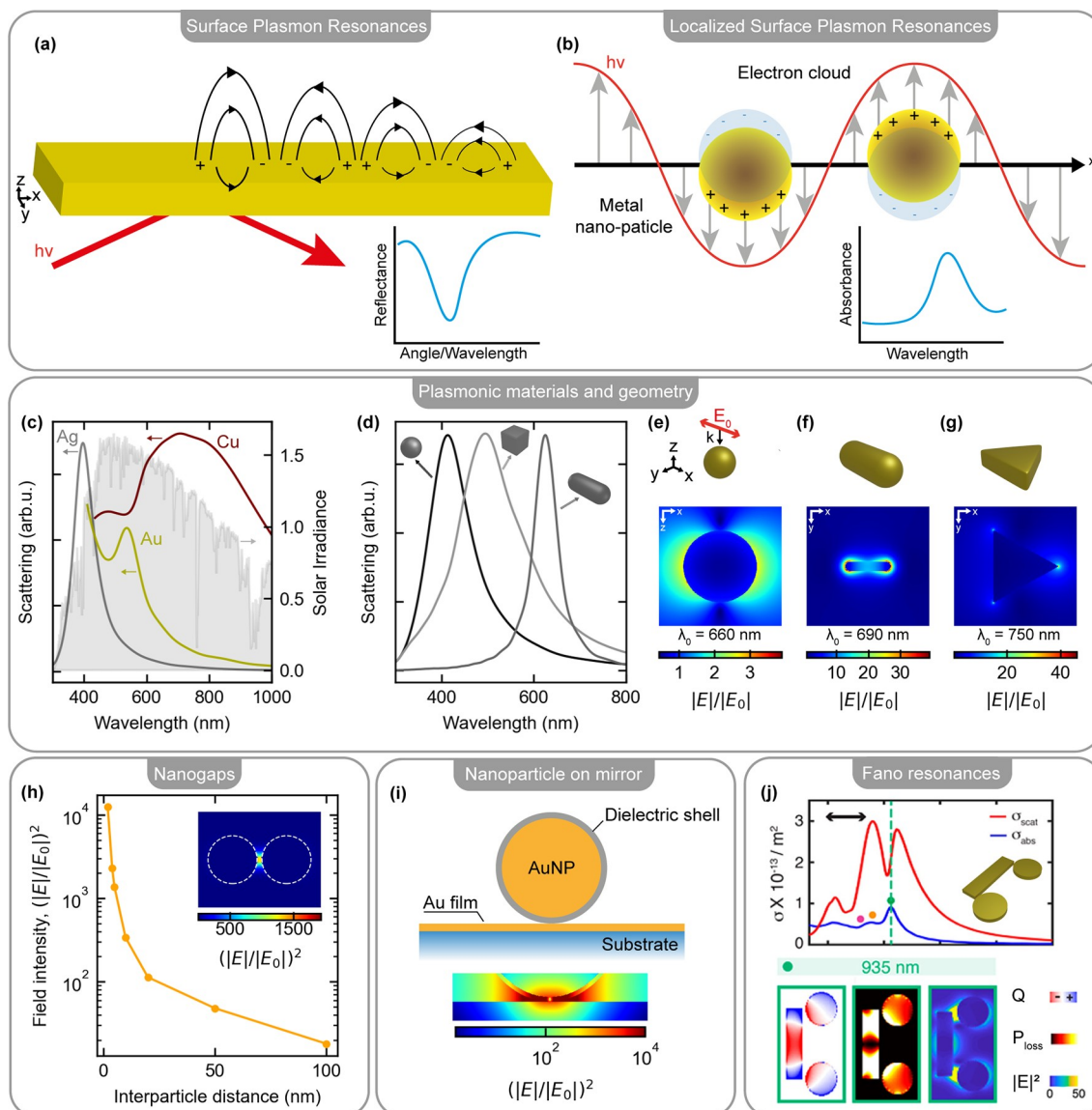
Figure 3. Plasmonic nanophotonic platforms. (a) Schematic of a surface plasmon resonance (SPR) supported on a metal/dielectric interface. Inset: Angle or wavelength-dependent reflectance of the SPR. (b) Schematic of a localized surface plasmon resonance (LSPR) supported on a subwavelength metal particle under an oscillating electric field. The cloud of conduction electrons in the particle oscillates in phase with the electric field of the incoming light. Inset: Wavelength dependent absorbance of the LSPR. (c) LSPR resonances calculated for a spherical antenna made from common metals (Ag radius 40 nm, Au radius 26 nm, Cu radius 130 nm). In gray, the solar power irradiance at sea level. (d) Size and shape dependence of plasmonic resonances in Ag nanoparticles. (e, f) Electric field distribution for gold nanoparticles with different geometries excited with linearly polarized light in free space. (e) Au sphere, radius: 90 nm. (f) Au rod, length: 76 nm radius 8 nm. (g) Au triangle, side length 105 nm. (h) The effect of gap size between a plasmonic dimer on electromagnetic field enhancement. Inset: Illustration of a hotspot of the electromagnetic field generated in the nanogap of a plasmonic dimer. (i) Top: Illustration of Angstrom sized gaps achieved by dielectric nanogap (2 nm) around a nanoparticle on a mirror. Bottom: Simulation of the electric field intensity in the nanogap. (j) Appearance of a sharp peak at 935 nm due to Fano-type interference processes in a gold rod antenna coupled to two gold nanodisks. Adapted with permission from ref 52. Copyright 2018 American Chemical Society.

waves (surface plasmon resonance, SPR, Figure 3a) traveling at the interface between a metal and air or glass. The SPR frequency, ω_{SPR}, depends on the dielectric constants of the metal and the surrounding medium, given as

$$\omega_{SPR} = \frac{\omega_p}{\sqrt{1 + \varepsilon_{diel}}} \tag{2.11}$$

Here, ω_p is the metal plasma frequency (which depends linearly on the metal free electron concentration) and ε_{diel} is the dielectric constant of the surrounding dielectric environment. However, the excitation of SPRs proved challenging, due to the

requirements of evanescent field excitation or nanostructured gratings, to overcome the momentum mismatch between light and SPRs.

A second type of plasmon resonance is present in subwavelength metal particles, named localized surface plasmon resonance (LSPR, Figure 3b). These nonpropagating modes arise from the oscillation of the conduction electrons and, more importantly, can be excited with direct light illumination. On a theoretical level, plasmonic resonances of simple nanoparticle geometries, such as spheres, can be described within the framework of Mie theory, which decomposes the internal and scattered fields of the particle into spherical harmonics.[11] For a

spherical metal nanoparticle of size a, much smaller than the wavelength of light ($a \ll 1$), a quasi-static approach can be used, where the EM oscillations are approximated to a linear perturbation, and the effect of the driving electric field is to generate a dipolar response in the sphere, equal to $\overline{p} = \alpha \varepsilon \varepsilon_0 \overline{E}_0$, where α is the polarizability of the sphere, given as

$$\alpha = 4\pi a^3 \frac{\varepsilon - \varepsilon_{diel}}{\varepsilon + 2\varepsilon_{diel}} \qquad (2.12)$$

The associated surface plasmon resonance condition is given when $\mathrm{Re}[\varepsilon(\omega)] = -2\varepsilon_{diel}$. As the resonance is directly related to the surrounding dielectric medium, LSPRs have been extensively studied for sensing applications.

When driven resonantly, large EM fields are created at the surface of the particle and consequently generate a large number of charge carriers in a nonthermalized distribution. Thus, a non-negligible part of these carriers can be found in nonequilibrium highly energetic states, also called hot electrons. The coherent motion of the plasmon oscillations is lost in the first 10 fs from the excitation light pulse and hot electrons eventually decay through two competing processes: radiative decay into scattered photons and nonradiative thermalization due to electron–electron or electron–phonon scattering processes, which occur within the first few ps. These nonradiative processes lead to an increase of the local temperatures of the metallic lattice, which radiates the excess energy back into the environment in the form of phonons, or heat, on a time scale from ps to ns. The presence of heat and hot electrons has been extensively studied in the past decade as they can drive chemical processes at the nanoscale, opening the field of plasmonic photocatalysis, further discussed in section 5.

In general, both SPR and LSPR approaches can provide strongly enhanced electromagnetic near-fields and precise control over optical resonances, enabling a multitude of applications ranging from surface-enhanced sensors[12−18] to versatile light absorbers[19−25] and devices for controlling light propagation.[26−29] In the following, our focus will be on geometries exhibiting LSPRs, because they provide great versatility for resonance engineering via the particle geometry, and generally produce a stronger spatial confinement of the electromagnetic fields ideal for boosting the efficiency of material-intrinsic processes including energy conversion, higher harmonic generation, and catalysis.

Because of the suitable high values of ω_p given by their dielectric functions, Ag, Au, and Cu are often considered among the best plasmonic materials in the visible range (Figure 3c). In addition to the choice of resonator material, the tailoring of particle geometry is another important lever for obtaining the desired optical response.[30] Figure 3d illustrates this effect by comparing the extinction spectra of three different Ag-based geometries (rods, cubes, and spheres), highlighting significant differences in resonance position and linewidth. The particle shape also critically influences the magnitude and localization of the EM near-fields (Figure 3e−g), where more complex geometries can serve as a tool to focus light even further, for instance at the sharp edges of a triangular prism (Figure 3g). Building on initial demonstrations with comparatively simple resonator shapes, more complex geometries such as nano-stars,[31,32] nanoflowers,[33] and nanodendrites have been introduced to achieve precise control over the nanophotonic enhancement.[34] Nanofabrication is at the core of all plasmonic systems, where techniques span the gamut from in-solution chemical synthesis to lithographic definition on substrates using

light, electron beams, or focused ions as described in more detail in section 2.3.

Along with the resonance position, the linewidth is another essential factor in the design and experimental realization of plasmonic systems. The linewidth is directly linked to the two main loss channels affecting resonant systems: (1) nonradiative damping associated with the intrinsic Ohmic loss in the material and (2) radiative damping associated with the decay of the resonance via coupling to the far-field.[35] To quantify the effects of these losses, the resonance quality (Q) factor is commonly chosen, which is defined as the resonance frequency divided by the full width at half-maximum (fwhm) of the resonance curve. In simple plasmonic systems affected by Ohmic damping, Q factors are often below 10 but can become much higher in structures composed of low-loss dielectrics (see section 2.2.2).

Going from individual resonators to the case of two or more nanoparticles, their arrangement in space also influences the electric field (E-field) enhancement and resonance properties. Nanoparticle dimers, formed from two nanoparticles separated by small nanoscale gaps, can show significant near-field coupling and create a plasmonic hot spot in the resulting cavity. In such hotspots, the E-field enhancement can reach very high values, with intensity enhancement factors $(|E|/|E_0|)^2$ above 10^4, where the magnitude not only depends on material and geometry but is heavily influenced by the interparticle distance (Figure 3h). Another intriguing approach for creating ultrasmall gaps leverages film-coupled systems, where a nanoparticle interacts with its mirror image in an adjacent metal film (Figure 3i).[36] Because the gap distance between the particle and the film can be precisely controlled on Angstrom length scales using, for example, tailored self-assembled monolayers of molecules,[37] such geometries can be used to probe the limits of plasmonic enhancement,[38] and to realize highly enhanced second harmonic generation via light-induced symmetry breaking.[39]

Importantly, the general Mie expansion approach mentioned above also yields higher-order multipoles (quadrupole, octu-pole, etc.) for both the electric and magnetic moments. However, magnetic modes in particular are challenging to realize in simple plasmonic particles (spheres, disks) due to the constraints introduced by boundary conditions for electric fields at the metal–dielectric interface. Nevertheless, magnetic responses could be achieved with more complex plasmonic structures[40] such as split-ring resonators,[41,42] fishnet structures,[29] or multilayer perfect absorbers.[19,20,22]

Another important mechanism for tailoring resonances in plasmonic systems is Fano interference, where resonances with large dipole moments (and associated large scattering losses) are coupled to modes with vanishing dipole moments that are not commonly accessible from the far-field.[43,44] Such Fano resonances in ensembles of near-field coupled plasmonic particles can produce narrower lineshapes and increased EM fields compared to simpler geometries, making them advantageous for biochemical sensing and enhancing catalytic processes. Established examples for Fano-resonant plasmonic systems include dolmen-type geometries,[45−47] oligomers,[48,49] and asymmetric resonators.[50,51] In a recent example, a system consisting of a rod antenna coupled to two disks was introduced,[52] where the characteristic field pattern of the Fano resonance could be imaged via the hot electron driven desorption of thiolated molecules from the gold surface (Figure 3j).

2.2.1.2. Dielectric Mie Resonators. In contrast to plasmonics, nanoparticles composed of high refractive index dielectrics can
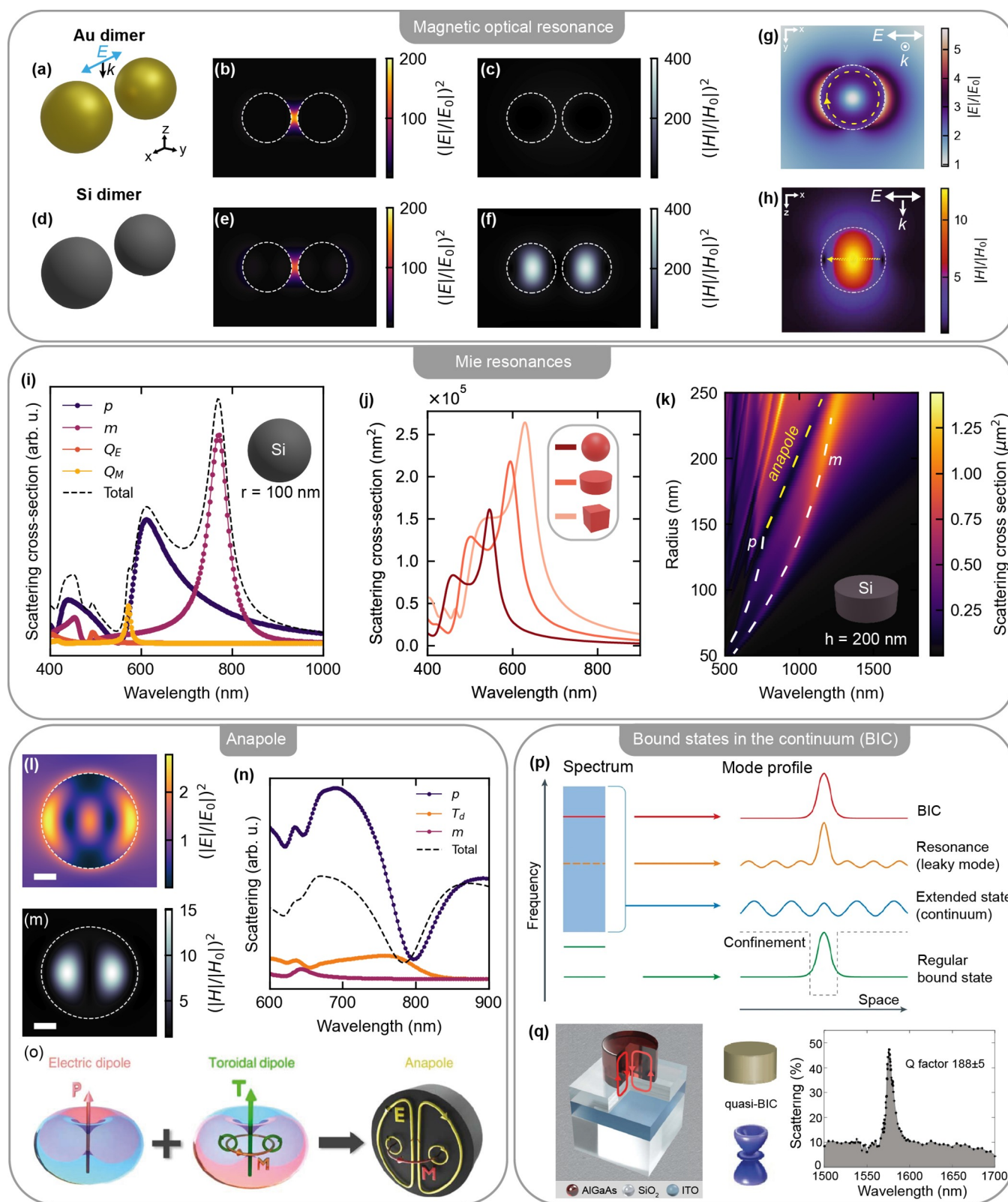
Figure 4. Dielectric nanophotonic platforms. (a−f) Comparison of the electric, $(|E|/|E_0|)^2$, and magnetic, $(|H|/|H_0|)$,[2] field intensity for two spherical particles of (a−c) gold and (d, e) silicon with a 50 nm gap separation, in free space. (g) Electric and (h) magnetic field distributions associated with the respective electric and magnetic dipole resonances of the dielectric sphere from panel i. (i) Multipole expansion of the cross-section of a silicon dielectric sphere in free space (radius 100 nm) illuminated by an electromagnetic plane wave. p, electric dipole; m, magnetic dipole; Q_E, electric quadrupole; Q_M, magnetic quadrupole. (j) Scattering cross-sections for dielectric particles shaped as a sphere, disk, and cube made of GaP and with lateral size of 150 nm. (k) Evolution of the Mie resonances for a silicon disk (height 200 nm) in free space, as a function of the disk radius. Outlined in white the evolution of the magnetic dipole (m) and electric dipole (p) resonances, in green the anapole state. (l) Electric and (m) magnetic field intensity distribution for a silicon disk (radius 430 nm, height 100 nm), on glass substrate, excited at the anapole state ($\lambda = 1500$ nm). Scale bar: 200

Figure 4. continued

nm. (n) Multipolar expansion of the scattering cross-section for the anapole state. Where p is the electric dipole, T_d the toroidal electric dipole, and m the magnetic dipole resonances. (o) Schematic of the anapole condition as the interference between an electric dipole and a toroidal dipole. (p) Physical principle of photonic bound states in the continuum in comparison with established leaky mode resonances. (q) Example of a quasi-BIC state in an AlGaAs nanodisk. Left: Schematic of the structure. Center: Spatial distribution of the scattered field at the quasi-BIC/supercavity mode in the disk. Right: Scattering from a disk with height 635 nm and diameter of 930 nm. (o) Adapted with permission from ref 66. Copyright 2015 Springer Nature. (p) Adapted with permission from ref 56. Copyright 2015 Springer Nature. (q) Adapted with permission from ref 61. Copyright 2020 AAAS.

natively support a wealth of multipolar modes predicted from Mie theory.[53] As shown in Figure 4a−c, a nanoantenna dimer composed of two gold nanospheres at a nanometer scale exhibits a strong electric field confined in the gap between the particles due to the coupling of the plasmonic resonance in each single particle. For a system with the same geometry composed of two silicon nanoparticles (Figure 4d−f), we likewise observe an electric resonance confined in the gap between the particles, but with reduced intensity compared to gold, and an additional magnetic resonance confined inside the resonators. This different behavior stems from the fact that surface plasmon resonances are only supported in the transverse magnetic (TM) polarization.[35] In dielectric particles with high enough refractive index, Mie resonances are linked to induced currents of the bound electrons in the nanoparticle, which can support both transverse electric (TE) and TM polarizations. Figure 4g and h illustrate the characteristic near-field patterns associated with the electric and magnetic dipole modes in a dielectric sphere in free space.

In the far-field scattering spectra, both modes are associated with distinct resonance positions, which can lead to the appearance of complex multipeak lineshapes. These resonances can be calculated via the relationship between the induced current density $J(r)$ and the E-field distribution $E(r)$. For a dielectric nanoparticle in free space illuminated by a plane wave, $J(r) = -i\omega\varepsilon_0(n^2 - 1)E(r)$, where ω is the angular frequency, ε_0 the permittivity of free space and n is the index of refraction of the dielectric material. From the above relation, we can derive the form of the multipolar resonances for a dielectric resonator. A rigorous derivation of the multipolar Mie modes can be found in ref 54. The accurate assignment of the modes to the resonance peaks can be carried out via multipole decomposition of the electromagnetic fields, which quantifies the contributions of individual Mie modes to the full scattering spectrum (Figure 4i). The total scattering cross-section, taking into account only the first two multipolar orders, can be then expressed as[9]

$$C_{sca} = \frac{k^4}{6\pi\varepsilon_0^2|E_0|}\left[\sum\left(|p|^2 + \left|\frac{m}{c}\right|^2\right) + \frac{1}{120} \times \right.$$
$$\left. \sum\left(|Q_e|^2 + \left|\frac{Q_m}{c}\right|^2\right) + ... \right] \quad (2.13)$$

where it is clear how the scattering cross-section is the sum of partial cross-sections due to different multipolar resonances, where p is the electric dipole, m is the magnetic dipole, Q_e is the electromagnetic quadrupole, and Q_m is the magnetic quadrupole. Intuitive mode identification is also often useful by examining the general structure of the near-fields to distinguish the characteristic patterns of the electric and magnetic dipoles.

Similar to the plasmonic case, the shape and size of the dielectric resonators greatly influence the formation, the resonance position, and linewidth of the different multipolar

Mie modes (Figure 4j). In practical realizations of all-dielectric resonant systems, one of the most widely considered geometries consists of a dielectric disk on a transparent (often glass) substrate. Here, the mode structure and resonance positions can be controlled by varying the aspect ratio of the disk, that is, the quotient of radius and height. Figure 4k shows the mode evolution in a silicon disk with a height of 200 nm and varying radius, highlighting the increasingly rich mode structure for larger resonator volumes.

This straightforward and simultaneous tuning of multiple resonant modes unlocks a great potential for controlled mode interference and mode engineering. One major target for such engineering tasks is the maximization of light concentration into the resonator material, which is highly relevant for boosting the absorption and consequently for increasing the rates of catalytic reactions in the context of energy conversion. For instance, the spectral and spatial overlap of an electric dipole and a toroidal dipole can be realized in individual dielectric nanodisks, resulting in a so-called anapole state (Figure 4l−o). This condition simultaneously combines strong enhancement of the near-fields within the resonator (Figure 4l,m) with a suppression of far-field scattering from the destructive interference of the two dipolar moments (Figure 4n). For describing the anapole state, the scattering cross-section in eq 2.13 can be rewritten with an additional term related to the toroidal dipole moment (T_d) as

$$C_{sca} = \frac{k^4}{6\pi\varepsilon_0^2|E_0|}\left[\sum\left(|p + ikT_d|^2 + \left|\frac{m}{c}\right|^2\right) \right.$$
$$\left. + \frac{1}{120} \times \sum\left(|Q_e|^2 + \left|\frac{Q_m}{c}\right|^2\right) + ... \right] \quad (2.14)$$

The anapole condition is satisfied when $p + ikT = 0$, signifying that the far-field contributions are out of phase with each other and thus interfere destructively. A schematic of this condition is shown in Figure 4o. Recently, anapole states in dielectric nanostructures have been utilized to enhance the catalytic activity in nanodisks composed of oxygen-vacancy-rich TiO_{2-x}, even when operated in an otherwise weakly absorptive spectral region of this material.[55]

Photonic bound states in the continuum[56] (BIC) have emerged as a recent approach for suppressing radiative losses in nanophotonic systems, launching a versatile new platform for realizing nanophotonic architectures with controllable resonant frequencies and high Q factors.[57] Initially discovered in quantum mechanics and since extended to a multitude of wave phenomena,[56] BICs can be considered as states situated within the radiation continuum, but with finite lifetimes and therefore Q factors approaching infinity, which strongly contrasts with the established understanding of resonances as leaky modes (Figure 4p).[58] In nanodisk resonators (Figure 4q), BICs can be realized as supercavity modes through the carefully engineered interference between Mie-type and Fabry−Perot cavity modes,
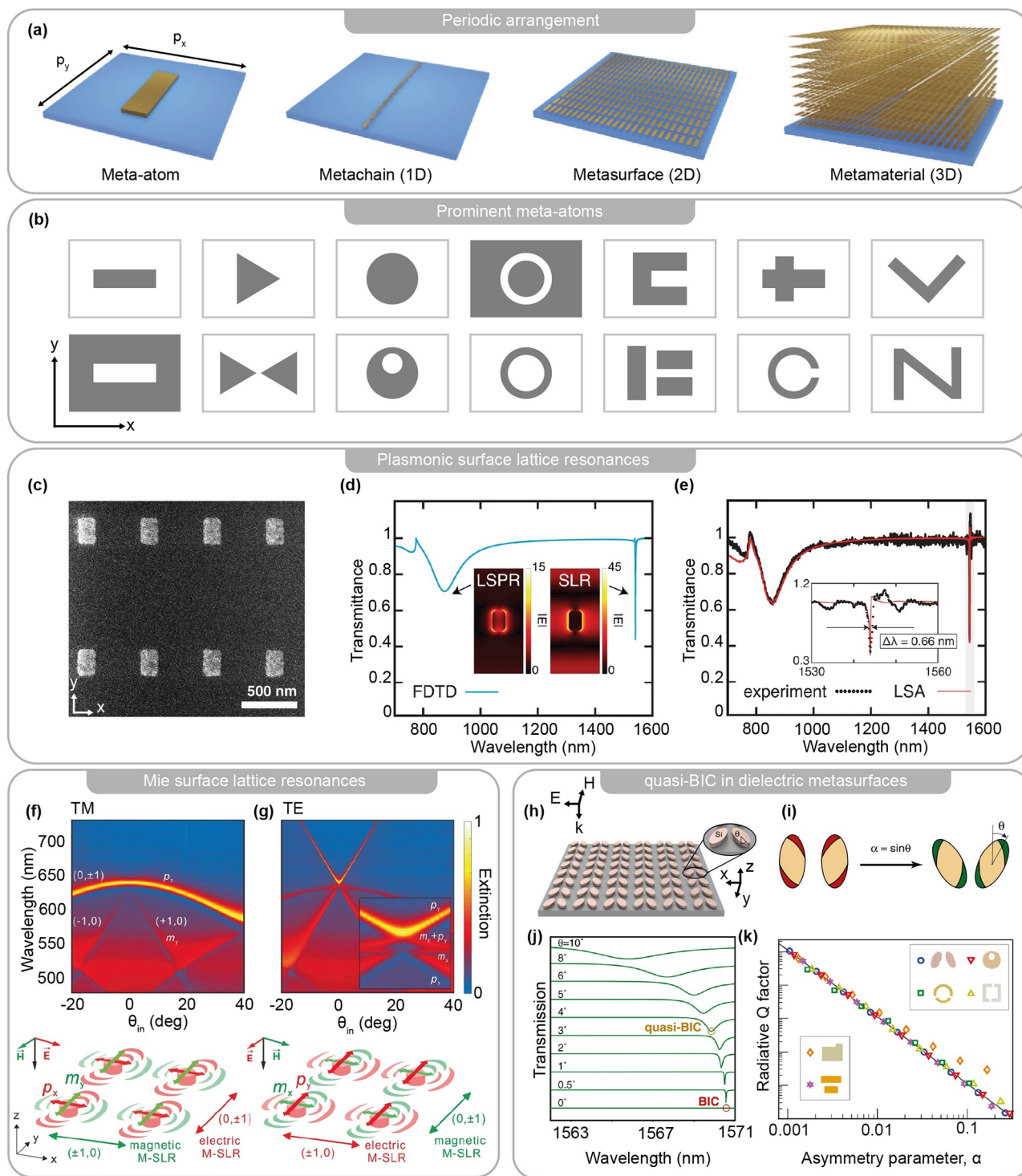
Figure 5. Periodic arrangements of plasmonic and dielectric resonators. (a) Building higher dimensional meta-arrays from single meta-atoms. (b) Top view of prominent meta-atoms examples used in the design of optical metasurfaces. (c) Electron microscopy image of a plasmonic nanoantenna array sustaining high Q factor SLRs. (d) Numerical finite-difference time domain (FDTD) calculations of the transmission spectrum of this metasurface for excitation light polarized along the x direction. Inset: numerical calculation of the electric field for a unit cell, for both LSPR and SLR resonances, in the $x-y$ plane. (e) Experimental transmission spectrum of high Q factor SLRs. (f, g) Top: Experimental dispersion of the electromagnetic lattice resonances for an array of silicon nanodisk (radius, 134 nm; height, 90 nm; array period, 430 nm) for (f) TM and (g) TE excitation. Bottom: Schematics of the induced electric and magnetic dipoles orientation in the single nanodisk, and the in-plane diffraction orders. (h) Schematics of a dielectric metasurface hosting quasi-BIC resonance. (i) Definition of the asymmetry parameter (α) for broken symmetry metasurface. (j) Theoretical transmission spectrum for (k) quadratic relationship between the asymmetry parameter and quasi-BIC resonance Q factor for different geometries of broken symmetry meta-atoms (Inset). (c−e) Adapted with permission from ref 81. Copyright 2021 Springer Nature. (f, g) Adapted with permission from ref 100. Copyright 2020 Wiley-VCH GmbH. (h−k) Adapted with permission from ref 110. Copyright 2018 American Physical Society.

enabling applications in light concentration and higher harmonic generation.[59−61] Furthermore, it has been shown that the BIC concept can act as a framework for describing and understanding diverse systems such as photonic crystals,[62] Fano-resonances,[63] and chiral arrangements.[64,65]

2.2.2. Periodic Arrangements of Plasmonic and Dielectric Resonators.

The functionalities of single plasmonic and dielectric resonators discussed in the previous section can be further extended when arranging the single nanostructures into periodic arrays. In this context, the resonators, often called meta-atoms, can be arranged into one-dimensional (1D) arrays or metachains, in two-dimensional (2D) metasurfaces, and, using more extensive fabrication processes, into three-dimensional (3D) metamaterials (Figure 5a). Because metachains provide only one direction for the in-plane coupling of the optical resonances of single meta-atoms, much of the research is focused on the realization of metasurfaces, owing to the wider parameter space to tailor resonances in the 2D array. Meta-atoms utilized for optical metasurfaces range from simple rods or disks to more complex shapes like split-ring resonators or dimers with broken symmetry. Figure 5b shows a collection of prominent meta-atom examples from literature. When the unit-cell consists of multiple structures, it is sometimes referred to as a meta-molecule instead of a meta-atom. At its core, the EM response of the array is based on the properties of the meta-atom, which can be tuned both in the material used and the subwavelength geometry and size, as discussed in the previous section. However, when engineered in periodic arrays, novel optical phenomena arise due to a collective response of the individual nanostructures, achieved by distinct modes with precise geometrical resonance conditions. In the following discussion, we will start with the description of plasmonic metasurfaces and then extend the discussion to high-refractive index dielectric metasurfaces.

2.2.2.1. Plasmonic Metasurfaces. The collective response of plasmonic meta-atoms can be grouped into two classes: near-field and far-field coupling effects. Near-field interactions occur for small distances between meta-atoms, in the order of 1−20 nm, significantly below the resonance wavelength. This effect was discussed in section 2.2.1, where plasmon hybridization of dimers was introduced. This phenomenon can be extended further from dimer structures to 1D, 2D, and 3D arrays of nanostructures. Compared to the single structure, the hybridization of plasmonic resonances leads to significant spectral shifts accompanied by higher local EM field intensities in the nm sized hotspots. However, this near-field enhancement does not typically give rise to any significant improvement in terms of the resonance linewidth.[67−71] To this end, Fano resonances of plasmonic arrays can be used[44,72] and Q factors on the order of 10^2 have been achieved.[73]

A second possible collective response is achieved when the in-plane oscillations of the field scattered by single meta-atoms are in-phase with the field scattered by the neighboring structures in the periodic array. This effect leads to the emergence of the so-called surface lattice resonance (SLR),[74,75] resulting in a significant improvement of the Q-factor. SLRs are a result of far-field (radiative) coupling of the individual scatterers by in-plane diffraction orders of the periodic array. When particles are randomly distributed, the scattered fields of the surrounding particles impinging on a given particle have no large effect. However, high Q-factor SLR resonances can emerge when the particles are arranged periodically with optical wavelength of $\lambda_{SLR} \approx n_{env}P$, where λ_{SLR} is the wavelength of the SRL resonance, n_{env} is the refractive index of either the substrate or the

surrounding medium (e.g., air) and P is the period of the array. In this condition, the scattered fields by the dipolar resonances in the single meta-atom propagate in phase with the incident light, leading to a resonance with a considerably narrower linewidth compared to the individual LSPR.[74,76−80] While the lattice configuration determines the position of a SLR, the LSPR governs its coupling efficiency to free space. The Q factors of SLRs increase with the number of particles in the array[81−83] and the number of elements necessary to reach the infinite array limit is only determined by their coupling strength.[82] Beyond engineering the individual nanostructures geometry and the period of the lattice, SLRs offer a variety of options to manipulate their optical character. SLRs can sustain both in-plane and out-of-plane character, where the balance between the two can be engineered by tuning the diameter/length and height of the meta-atom,[84] opening to the coupling of higher order SLRs modes such as "dark" quadrupole resonances.[85] Further approaches can include the introduction of periodic vacancies, by selectively removing single structures in the array,[86] employing nanogaps in dimer nanostructures,[87] or using bipartite particle systems and tuning the relative size and orientation of the single unit cell.[88]

In case of metachains and metasurfaces, record high Q factors on the order of 10^3 have been theoretically predicted[89,90] and have been realized experimentally in a recent work[81] by Bin-Alam M.S. et al. The researchers used a metasurface consisting of a square rectangular array of rectangular gold nanostructures (Figure 5c). By tuning the size and lattice parameter of the system, the SLR is found spectrally isolated from the LSPR of the single nanoantenna and provides an enhancement of approximately three-times of the electric field magnitude compared to the LSPR (Figure 5d), equivalent to approximately one order of magnitude higher near-field intensities ($I \propto |E|^2$). In fabricated samples, narrow resonances with Q factors up to 2340 were experimentally observed (Figure 5e).

2.2.2.2. All-Dielectric Metasurfaces. Similar to individual nanostructures, lattice resonances in dielectric metasurfaces[91] have gained attention because they offer lower intrinsic losses compared to their plasmonic counterparts.[92,93] Furthermore, dielectric materials offer functionalities beyond those of metallic metasurfaces for light control and wavefront shaping owing to the to the possibility of tailoring not only the electric but also the magnetic multipolar resonances.[94] Because of the orthogonality of the electric and magnetic components, the coupling of the electric resonances and that of the magnetic resonances can be tuned separately by engineering both the geometry of the single meta-atom and the periodicity of the array.[94−98] This spectral overlap can then be exploited to achieve, for example, directional scattering[94] or antireflective coatings.[99]

The nature of the electric and magnetic Mie SLRs was recently investigated experimentally in the work by Murai S. et al.[100] Figure 5f and g show the polarization dependent dispersion of the extinction spectra for a square array of silicon nanoparticles. For both polarizations, the Mie resonance of the single nanodisk is found around 520 nm and, due to the symmetry of the particles and the array, the electric and magnetic Mie SLRs, at 640 nm, are degenerate for an excitation with normal incidence ($\theta_{in} = 0$). By varying the excitation angle, this degeneracy is lifted and the character of the Mie SLRs is deduced from the relative linear or quadratic dispersion in the coupling to the diffraction orders of the array. Here, magnetic Mie SLRs are found to be generated by in-plane and out-of-plane magnetic dipole moments (m), while the electric Mie
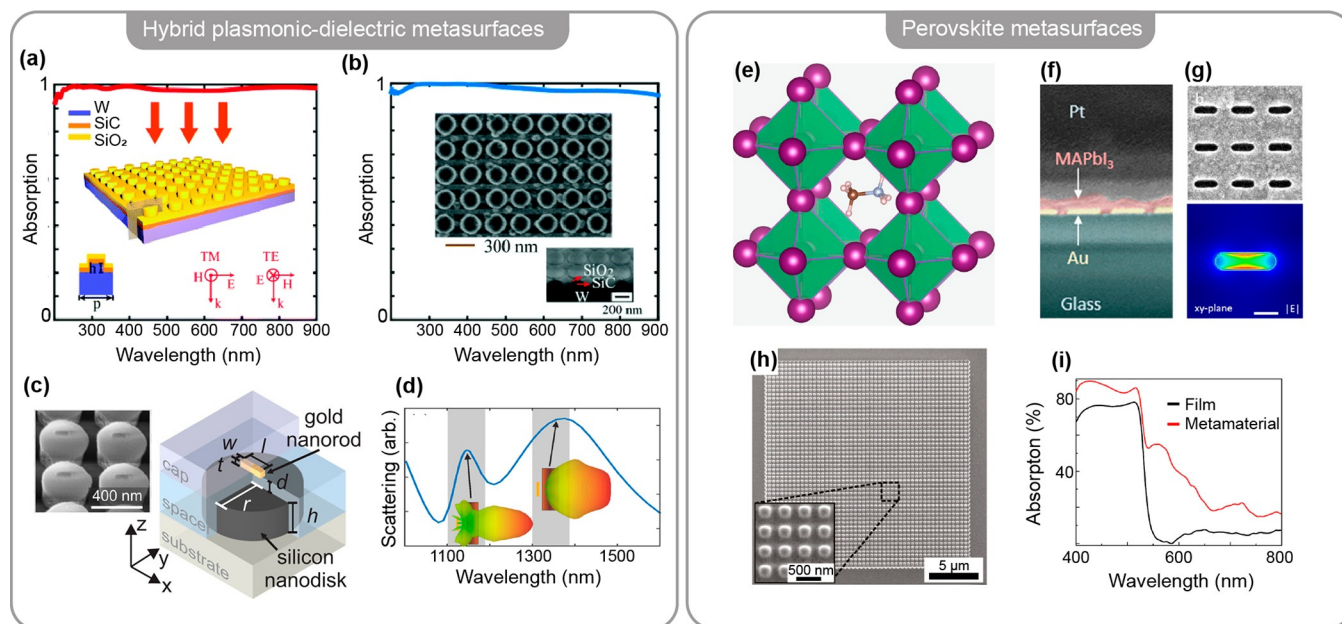
Figure 6. Hybrid plasmonic/dielectric and perovskite metasurfaces. (a) Schematic image of a multilayered hybrid W/SiC/SiO$_2$ metasurfaces and its simulated absorption. (b) Experimental broadband absorption of the fabricated multilayer metasurface. Inset: Electron microscopy images of the fabricated metasurface. (c) Left: The inset shows a magnified and SEM oblique view of the hybrid metal−dielectric metasurface. Right: schematics of the geometry of a single metal−dielectric hybrid meta-atom. (d) Scattering spectrum of the hybrid metasurface with and radiation patterns at the spectral positions marked by the arrows. (e) Schematics of the crystal structure of a hybrid organic−inorganic perovskite crystal. (f) Cross-sectional electron microscopy image of gold nanoslit metasurface covered with perovskite thin layer (MAPbI$_3$). (g) Top: SEM image of the fabricated nanoslit metasurface. Bottom: Numerical simulations of the electric field intensity for a single nanoslit. Scale bar: 50 nm. (h) Electron microscopy image of a nanostructured metasurface in a perovskite thin film. (i) Absorption spectra of the perovskite metasurface compared with the unpatterned flat perovskite film. (a, b) Adapted with permission from ref 123. Copyright 2018 The Royal Society of Chemistry. (c, d) Adapted with permission from ref 125. Copyright 2016 American Chemical Society. (e) Adapted from ref 129. Copyright 2015 Springer Nature. (f, g) Adapted with permission from ref 130. Copyright 2020 American Chemical Society. (h, i) Adapted with permission from ref 131. Copyright 2020 Walter de Gruyter Publishing Group.

SLRs are solely induced by the in-plane electric dipole resonances (p).

While metasurfaces composed of simple all-dielectric resonators can overcome nonradiative damping through the negligible losses of their constituent materials, they are nevertheless affected by radiative losses associated with their coupling to the radiation continuum. Over the years, significant research has been devoted to overcoming this radiative loss in a drive toward nanophotonic geometries with ultrahigh Q factors. Similar to plasmonic metasurfaces, all-dielectric Fano-resonant systems have been implemented for reducing the radiative linewidth including oligomers, wire pairs, and individual resonators.[101−104]

Another approach to overcome optical losses is to engineer nonradiating photonic states,[58] for instance anapole states, which have been integrated in dielectric metasurfaces with demonstrations of high Q factors and the lasing regime.[105−109] Nonradiative states can contribute to high field confinement, owing to the lack of radiative decay pathways, and further increase the available toolbox for designing of novel nanophotonic platforms. In the last years, dielectric metasurfaces with broken in-plane symmetry have been shown to sustain BIC resonances with extremely high Q factors.[110] Figure 5h shows an example of a BIC-based dielectric metasurface composed of unit cells with two elliptical resonators with a broken in-plane inversion symmetry. To describe the degree of asymmetry of the unit cell, an asymmetry parameter α is commonly introduced, defined as the tilt angle between the two elliptical resonators (Figure 5i). The continuous tuning of the structural parameter allows precise control over the optical resonance wavelength and

extinction via the asymmetry of the underlying geometry. For this reason, such BIC modes are called symmetry-protected BICs. Specifically, although a symmetric unit cell corresponds to a "true" BIC state, which cannot couple to the incident light, the introduction of a slight asymmetry opens radiative pathways, making the resulting high Q mode accessible from the far-field, usually described as a quasi-BIC resonance (Figure 5j).[58] A wide variety of symmetry broken unit cell have been demonstrated to sustain quasi-BIC resonances when arranged in planar arrays, adding to the versatility of this concept (Figure 5i, inset). Notably, for all these unit cell designs, the radiative Q factors of the quasi-BIC resonance associated with the asymmetry parameter follow a characteristic inverse square law ($Q \propto \alpha^{-2}$) (Figure 5i),[67] highlighting the fundamental nature of the symmetry-protected BIC principle. Recent demonstrations of quasi-BIC metasurfaces have been implemented for biosensing,[111,112] molecular spectroscopy,[113] and higher harmonic generation.[114−116]

2.2.3. Hybrid Metasurfaces. Beyond the fundamental building blocks and their arrangement, novel concepts and applications can be realized in hybrid metasurfaces. A hybrid device consists of different types of materials, for example, metals and semiconductors, interfaced in a single building block, to provide additional degrees of freedom in engineering exotic electrical and optical properties in metamaterials. In this section, we discuss the hybridization of optical metasurfaces with novel inorganic and organic semiconductors such as solution processed perovskites and the family of graphene and two-dimensional materials. We will also describe the development of dynamic metasurfaces (also often referred to as active or

reconfigurable), where the intrinsic properties of the meta-atom can be controlled via external stimuli like thermal excitation, voltage bias, magnetic field, optical pump, or mechanical deformations. As such, optical properties of dynamic metasurfaces can be fully controlled and tuned externally. Finally, we will briefly discuss the incorporation of metasurfaces into functional devices.

2.2.3.1. Hybrid Plasmonic–Dielectric Metasurfaces. While dielectric metasurfaces generally benefit from lower optical losses than metals, resulting in higher Q factors, the field enhancements are usually smaller than their plasmonic counterparts. This is a direct consequence of the property that, in dielectrics, light is mainly located inside the bulk material and not confined on the surface as for plasmonic resonances. An approach to improve the overall field confinement is to combine both effects in structures composed of plasmonic and dielectric subunits. These hybrid materials exhibit new optical resonances with lower losses and higher field strengths,[117−120] enabling enhanced photophysical and photochemical processes with a plethora of fabrication pathways.[121]

Here, initial studies mainly focused on the properties of individual hybrid nanostructures while simultaneously tackling fabrication challenges for combining metallic and dielectric materials in a single structure. The possible geometrical arrangements of these building blocks in periodic hybrid metasurfaces are manyfold and different configurations have been explored.[122] For instance, it is established that the use of plasmonic disk arrays on metallic substrates can achieve perfect absorption of the incoming light[19] with polarization independent and wide-angle operation. Hybrid metal−dielectric metasurfaces can be engineered to obtain nearly perfect absorption, with advantages compared to plasmonic structures, such as a higher thermal stability and broad bandwidth operation. Absorptions above 95% over a broad range of wavelengths from the UV to the near-IR have been demonstrated in multilayered W/SiC/SiO$_2$ metasurfaces (Figure 6a,b).[123] In the case of Mie resonances in silicon nanodisk metasurfaces on a gold substrate, light absorption above 99% is possible,[124] following a perfect spectral overlap between the electric and magnetic dipole resonances in the silicon disk. This idea of multipolar resonance engineering can be extended to many applications via carefully engineering the nanophotonic design of the hybrid devices. Beyond the absorption of light, controlled interference between resonances in metallic and dielectric components can be implemented for control of the directional emission and scattering from hybrid metasurfaces. For example, a hybrid metasurface concept has been introduced, where the fundamental building blocks are made of silicon nanodisks with a gold nanorod placed on the top surface (Figure 6c).[125] Here, the plasmonic particles act as a feed element and the silicon nanodisk as a director element. The device exhibits two strong windows of directional emission (Figure 6d), the first at approximately 1.2 μm is related to the superposition of the quadrupole moment in the plasmonic nanoantenna, excited by a linearly polarized light along the rod long axis, and the magnetic dipole mode of the silicon nanodisk. For the second window, above 1.3 μm, the directionality is given by the so-called Kerker condition, obtained by the superposition between the electric and magnetic dipole resonances in the single Si disk.

Interaction between resonances in hybrid nanoparticles opens up even more applications. For instance, meta-molecules consisting of silicon spheres and copper split-ring resonators placed next to each other[126] can be exploited for the generation

of optical magnetic moments and antiferromagnetic ordering, where propagation of magnetization waves is predicted. Optical properties in hybrid metasurfaces can be highly tunable, as demonstrated by Wang et al. with full color generation in a hybrid metasurface based on metal−insulator−metal sandwich nanodisks,[127] where narrow resonances (and consequently vivid colors) are tuned along the whole visible spectrum by varying the array pitch size and disk radius. Recently, hybrid CdS-coated nickel metasurfaces have been demonstrated for photoelectrochemical solar energy conversion and storage, with tunable broad resonances from 300 to 1100 nm, by exploiting different optical phenomena, which will find use for efficient sunlight harvesting.[128]

2.2.3.2. Hybridization with Perovskite Semiconductors. The combination of periodic optical nanostructures with novel semiconducting materials, such as solution processed perovskites, holds great potential for energy applications.[132] Perovskite semiconductors are hybrid organic−inorganic materials with ionic structure in the form ABX$_3$, where A is the organic cation (usually a molecule), B the inorganic cation (Pb, Sn,...), and X is a halogen atom (Cl, Br, I) in hybrid perovskites or oxygen in most all-inorganic perovskites. The A and X atoms form an octahedral structure in three dimensions, where the organic cation sits in between, giving stability to the ionic structure (Figure 6e). Perovskites present a soft lattice, tunable band gap energy via engineering the stoichiometry, and dimensionality and became one of the most studied semiconductor materials based on their exceptional performance and promise for solar energy conversion, reaching values competitive with established silicon technologies. Perovskites also exhibit optical excitonic features and can be synthesized in their low-dimensional form, either zero-dimensional nanocrystals[133] or in 2D nanosheets.[134]

One of the main advantages of perovskite materials is their compatibility with the solution processed synthesis of thin films. This opens up many options in harnessing the strongly localized fields in optical metamaterials. Adamo et al.[130] fabricated perovskite thin films on top of a gold layer patterned with periodic nanoscale slit apertures (Figure 6f,g). The combination of strong fields in the nanostructured metals and the efficient emission from the perovskite film resulted in one order of magnitude enhancement of photoluminescence due to the enhanced absorption and emission of light provided by the active perovskite material. Owing to the ease of its fabrication processes, metal and perovskite periodic gratings structures have been fabricated and shown to exhibit strongly anisotropic properties such as in hyperbolic metamaterials.[135] Besides metals, perovskites have also been integrated with dielectric nanostructures. One example is the integration with Mie-resonant silicon nanoparticles for enhanced absorption and emission of perovskite thin films and metasurfaces.[136] Furthermore, enhancement of multiphoton nonlinear optical processes (discussed in detail in section 3.1) in perovskite thin films coupled to polymeric gratings was recently demonstrated.[137]

Because perovskites materials commonly possess high refractive indexes above 3, they can also be nanostructured into Mie-resonant nanoantennas, similar to established nanophotonic dielectric materials such as Si or GaP (see section 2.1). In this direction, single perovskite nanoparticles have been shown to host optical Mie resonances[138] and lasing was demonstrated for single perovskite nanoantennas.[139] Perovskite thin films have also been nanostructured into periodic
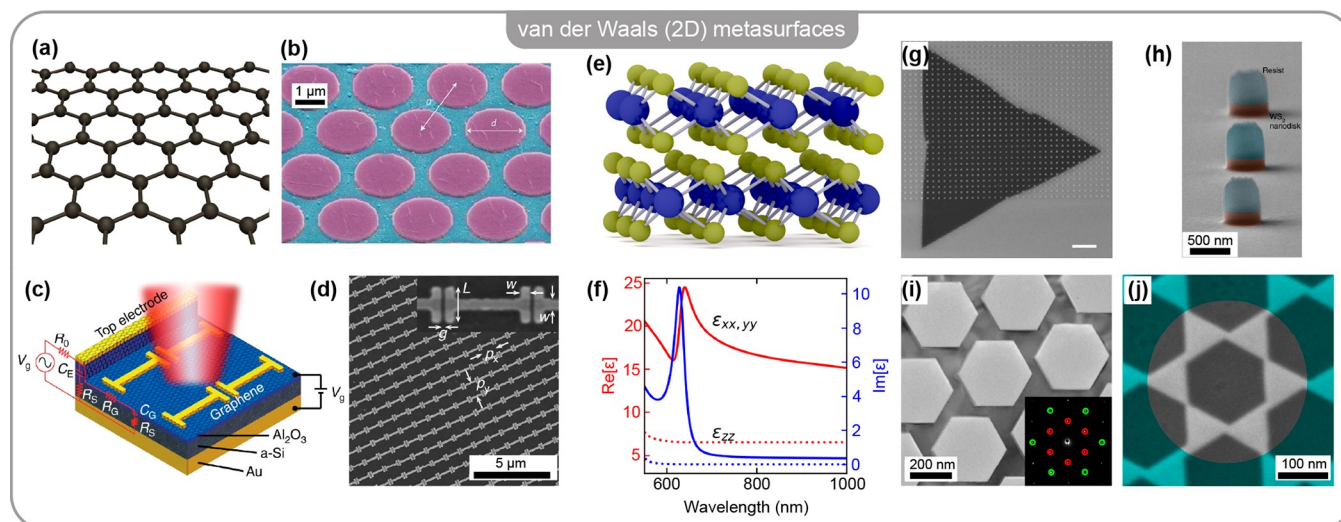
Figure 7. van der Waals materials for metasurfaces. (a) Schematic of the crystal structure of a single graphene sheet. (b) Nanopatterned graphene layers for tunable plasmonic resonances. (c) Schematics of a plasmonic-graphene hybrid metasurface (d) Electron microscope image of a fabricated plasmonic-graphene hybrid metasurface. (e) Schematics of the crystal structure of a TMD crystal. In blue the transition metal atoms, in yellow the chalcogenide atoms. (f) Real and imaginary part of the refractive index of bulk TMD WS_2. (g) Monolayer of MoS_2 transferred on top of a plasmonic nanoantenna array. Scale bar: 2 μm (h) Electron microscope image of TMDs Mie resonators. (i, j) Electron microscope image of crystalline TMD metamaterials. (b) Adapted with permission from ref 145. Copyright 2012 Springer Nature. (c, d) Adapted with permission from ref 149. Copyright 2018 Springer Nature. (f, h) Adapted from ref 166. Copyright 2019 Springer Nature. (g) Adapted with permission from ref 156. Copyright 2016 American Chemical Society. (i, j) Adapted with permission from ref 168. Copyright 2020 Springer Nature.

metasurface arrays, and the demonstration of enhancing the light absorption and photocurrent generation[131] is promising for solar energy conversion (Figure 6h,i). Moreover, metasurfaces made from solution-grown thin films have potential for photonic applications such as structural coloring[140] and antireflection coatings.[141]

2.2.3.3. Hybridization with van der Waals Materials. The rise of graphene and 2D materials in the last 15 years enabled a cascade of discoveries and potential applications in optics and electronics. Common 2D materials exhibit a crystal structure where covalently bonded single layers are held together by weak van der Waals (vdW) forces (Figure 7a). From the first isolation of an atomically thin layer of graphene in 2004, achieved by simply exfoliating the individual layers with adhesive tape, nowadays thousands of compounds have been added to the library of vdW materials, with many physical and chemical properties ranging from metals to insulators, and from semiconductors to superconductors.[142] Graphene is a promising candidate for THz and Mid-IR applications due to its electrically tunable optical properties.[143] Notably, graphene itself hosts plasmonic resonances in the mid- and far-IR regions,[144] further expanding the rich nanophotonic research on this material. Nanostructuring graphene in nanoribbons or nanoislands is a viable way to tune LSPR[145] and IR light steering[146] (Figure 7b). By combining gated graphene layers with noble metal antennas (Figure 7c,d), a complete modulation of the complex light amplitude is achievable, allowing beam steering,[147] perfect absorption,[148] and tunable resonant absorption.[149]

However, graphene is a semimetal with no bandgap, and its operational frequencies are mostly restricted to the THz and IR spectral range, limiting its use in solar cells and photodetection. In search for 2D semiconductors, the family of transition metal dichalcogenides (TMDs) holds promise to further extend the realization of hybrid photonic nanostructures. They are one of the most studied types of 2D materials beyond graphene, as they also exhibit a vdW layered structure and can be exfoliated down

to single layers (Figure 7e). TMDs in the from MX_2 (M = Mo, W; X = S, Se, Te) are semiconductors with a defined energy bandgap at visible and near IR wavelengths and with appealing optical properties such as an indirect to direct bandgap transition in their monolayer form. This direct band gap transition further increases the absorption of light, up to 10% for a single layer, and leads to the formation of tightly bound excitons, stable up to room temperature, with peculiar optical properties due to a complex band structure and spin−orbit coupling.[150] Strongly bounded excitons can diffuse along the crystal and their motion can be controlled via mechanical deformation,[151,152] or strain, producing a modulation of the bandgap energy, opening up to exciton funneling for broad-spectrum solar energy harvesting.[153]

Following the feasibility of 2D layer integration via deterministic transfer processes and the presence of luminescent excitonic emitters, TMDs have been coupled to plasmonic and dielectric optical nanostructures for the enhancement of light emission and absorption. For example, first demonstrations of weak coupling exploited either hybrid plasmonic structures[154] and Mie resonances in dielectric nanoantennas.[155] Coupling of 2D semiconductors to collective resonances in plasmonic metasurfaces has been, so far, largely devoted to the interaction with excitonic states and their fundamental optical properties. The strong light−matter coupling regime between excitons and plasmonic lattice resonances was achieved by deterministic transfer of a single TMD layer on top of plasmonic nanodisk lattices[156] or nanohole arrays[157] (Figure 7g). Hybrid plasmonic-TMD metasurfaces can also enhance nonlinear photon conversion processes (further described in section 3.2) as recently demonstrated for the generation of broadband nonlinear emission.[158] TMDs have also been integrated with dielectric nanophotonic structures, such as Mie resonant silicon metasurfaces,[159] guided mode resonance metasurfaces,[160] and Berry-phase defective photonic crystals.[161] First reports of TMDs coupled to BIC-based dielectric metasurfaces demon-

strated enhanced nonlinear optical properties[114,115] and exciton-polariton states.[162] While the above examples implemented the atomically thin materials on top of the optical nanostructures, hybrid designs where the TMD layer is placed between a metal films and photonic dielectric cavities were demonstrated for applications in the dynamic excitation control such as electrically tunable exciton−plasmon states.[163]

Beyond the unique optical properties inherent in their single layer form, vdW materials offer a wealth of nanophotonic applications following their optical properties and the large variety of layered compounds available.[164] As an example, bulk TMD crystals offer novel perspectives for nanoscale photonics. First, the presence of transition metals leads to a higher refractive index ($n > 4$) than common materials used for dielectric nanophotonics such as Si and GaP (Figure 7f) while maintaining transparency over the visible and near-IR range. The intrinsic layered nature of TMD crystals further provides record high optical anisotropy,[165] with advantages for the development of photonic components and devices. Recent reports have demonstrated that single disks of TMD crystals (Figure 7h), owing to their large refractive index, exhibit optical Mie resonances and anapole states[166] and can be fabricated with atomic precision in dimer nanoantennas[167] and optical metasurfaces (Figure 7i,j).[168] The versatility in the fabrication of TMD structures for photonic applications enables the generation of exciton plasmon polaritons in hybrid metal-TMD photonic gratings[169] or unidirectional nonlinear emission in metasurfaces[170] made entirely from bulk TMD crystals.

Overall, vdW materials hold great promise for the development of novel nanoscale optical technologies, whose full potential is only beginning to be investigated. For instance, vdW materials offer a huge library of compounds that can be arbitrarily stacked in vertical heterostructures,[171] overcoming lattice matching requirements in three-dimensional semi-conductor heterostructures and opening up the engineering of novel materials and heterostructure devices whose capabilities are only limited by current fabrication methods rather than material properties. Furthermore, twist angle engineering, a novel concept within the field of 2D heterostructures, has been applied to metasurfaces where, for example, two graphene metasurfaces are stacked in configurations with a small angle difference between the relative orientation. This concept leads to the appearance of exotic properties, and topological states with long propagation length have been demonstrated.[172] 2D materials are also promising candidates for catalytic materials owing to their intrinsic surface properties and atomically precise edges[173] and interaction with hot carriers in plasmonic particles could open to efficient photocatalytic applications.[174]

2.2.3.4. Dynamic Metasurfaces. So far, most of the discussed metasurfaces exhibit optical responses that are static and determined only by the configuration and material properties of the meta-atoms as defined during the fabrication process. Active tuning of metamaterials and metasurfaces provides a new perspective for on-demand tunability of their optical properties.[175] A crucial ingredient for these approaches is a high-speed and strong tunability of the refractive index of the constituent active materials. In this direction, thermal and optical effects with ultrashort pulsed lasers,[176,177] electrical modulation,[178] and stretchable substrates[85,179] have been demonstrated. A common approach exploiting a change in the refractive index or material absorption is achieved by integrating switchable layers with plasmonic or dielectric metasurfaces, resulting in a modification of the resonance spectrum of the metamaterial and thus the

associated operational bandwidth. Strong changes in the transmission and reflection characteristics of hybrid structures can be achieved by employing phase-change materials (PCMs) like the chalcogenide compounds GeTe, $Ge_2Sb_2Te_5$ (GST), and $Ge_2Sb_2Se_4Te$ (GSST) (Figure 8). The dielectric properties of
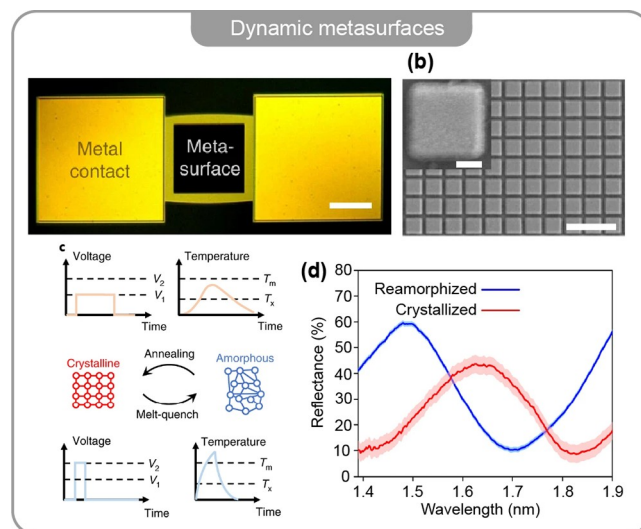
Figure 8. Active tuning of a dielectric metasurface (a) Optical image of an active metasurface device. Scale bar: 100 μm. (b) Electron microscope image of the fabricated $Ge_2Sb_2Se_4Te$ metasurface. Scale bar: 2 μm. Inset: single meta-atom. Scale bar: 200 nm. (c) Schemes of the electrical pulse and relative meta-atom temperature profiles during crystallization (top) and amorphization cycles (bottom). T_m, melting point; T_x, crystallization temperature; V_1, crystallization voltage; V_2, amorphization voltage. (d) Reflectance spectra of the metasurface under 40 sweep cycles (shaded area). (a−d) Adapted from ref 180. Copyright 2021 Springer Nature.

chalcogenide PCMs can be tuned by means of optical, electrical, or thermal switching from its amorphous state into a metastable cubic crystalline state, accompanied by a change in the refractive index and electrical resistivity.[176,180−183] Another route is to pattern the metasurface directly into the PCM layer, exploiting its own optical properties as a switchable meta-atom.[180] Another class of PCMs is correlated electron PCMs such as vanadium dioxide (VO_2) that show an insulator-to-metal phase transition. Similar to GST, the transition can be triggered optically, electrically, or thermally. However, contrary to GST (where the phases are nonvolatile), the material state in VO_2 is reset when the excitation is turned off. Active metasurfaces based on VO_2 to tune absorption, transmission, or refractive index have been explored for both metallic[184−187] and dielectric[188,189] antennas, with demonstrations of low power and fast switching performance.[185]

Besides the intrinsic properties of the materials, further methods to control and tune metamaterials have been demonstrated for microelectromechanical system actuators, which dynamically reconfigure parts of the meta-atoms,[190] metasurfaces integrated with graphene, where the optical properties can be tuned via carrier doping,[191,192] and postsyn-thesis chemical tuning of perovskites metasurfaces via anion exchange.[193]

2.2.3.5. Metasurface-Based Devices. Metasurfaces for practical applications require their incorporation into functional devices for instance when combined with electric circuits, microfluidic devices, fiber optics, or utilized in photovoltaic and
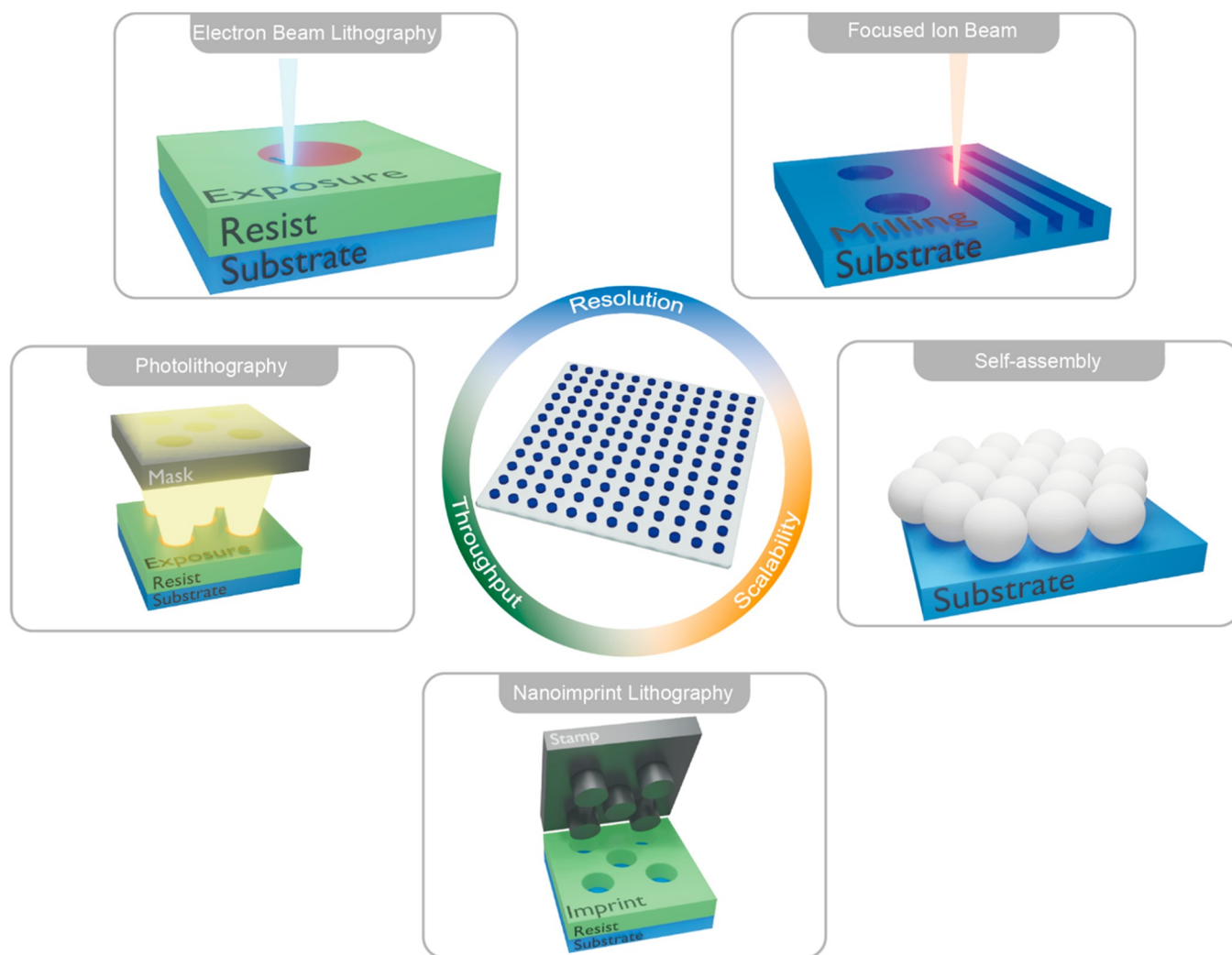
Figure 9. Frequently used fabrication techniques to generate nanoscale patterns. Available (nano) fabrication techniques differ in their resolution, throughput, and scalability. Maskless systems, such as electron-beam lithography (EBL) and focused ion beam (FIB), can enable ultrahigh resolution. Both FIB and EBL rely on the individually writing of the patterns via a focused electron or ion beam. Masked systems, such as photolithography, nanoimprint lithography, or approaches based on self-assembly, can achieve high throughputs and are scalable to large-area substrates but can have restrictions regarding their resolution.

photocatalytic cells. Besides their ability to manipulate electromagnetic radiation, metasurfaces have the advantage of being ultrathin, miniaturized building blocks that can be integrated in photonic circuits,[194,195] lab-on-a-chip technologies,[196,197] or be used for molecular barcoding,[113] detectors or other optoelectronic devices. Furthermore, metasurfaces can be incorporated into flexible materials, allowing mechanical tuning of the resonance frequencies or making devices such as photovoltaic cells more stable and mechanically robust.[198−202]

2.3. Fabrication and Design of Metasurfaces

Nowadays, a large number of fabrication techniques are available to create functional structures from simple patterns with dimensions in the nm-regime. The field is continuously pushed forward and new techniques are developed or combined with other approaches to achieve better resolution, higher throughputs, or upscaling to large-area substrates. Acknowledging all relevant techniques is barely possible and too extensive; therefore, we will focus on the principles of the most common ones.

Many considerations have to be taken into account when selecting ideal techniques for realizing nanophotonic structures.

Achieving the highest required spatial resolution is crucial for controlling and tuning resonances to desired wavelength regimes, especially for resonances in the visible, while high throughput and scalability, that is, the manufacturing of large-area substrates such as 4″ or 6″ wafers, are important for industrial applications. Material quality parameters such as crystallinity can also be critical because they can affect charge transfer, the occurrence of defect states, and the damping of phonon modes. In addition, the final metasurface might need to be decorated with additional materials, such as catalysts, or incorporated into functional devices, such as microfluidic systems, photovoltaic cells, or others, which causes further challenges. Altogether, the ideal (nano)fabrication technique(s) strongly depend on the desired purpose. Typically, there is a trade-off between achieving the highest resolutions while simultaneously enabling high-throughput and large-scale fabrication. In addition, instrument costs and the requirement for clean-room facilities might be a concern, but new techniques, for example, based on self-assembly, create new possibilities for researchers in the field and have been shown to achieve remarkable results.[203−206] Figure 9 gives an overview over
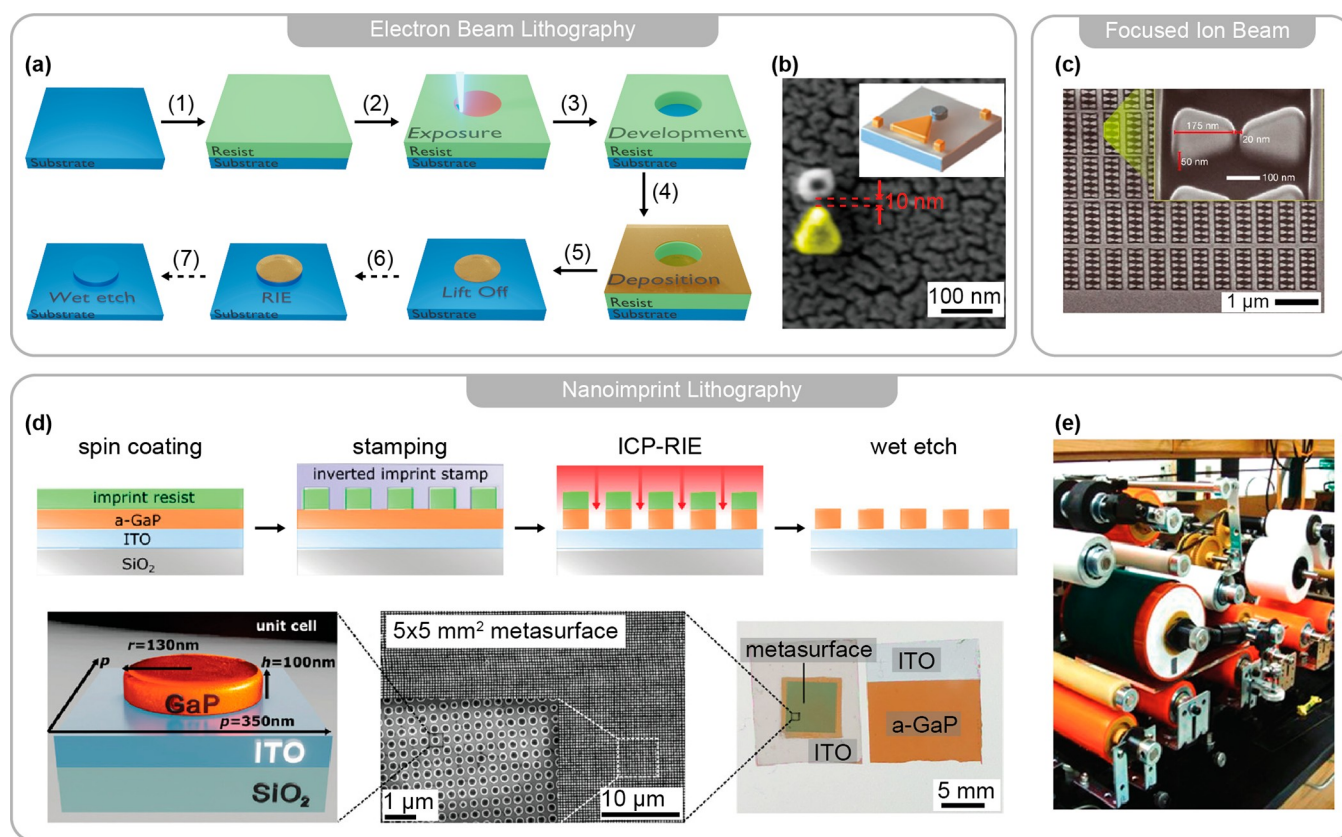
Figure 10. Lithographic approaches to produce metasurfaces with ultrahigh resolution. (a) Schematic showing the principle of EBL. (1) A thin layer of an electron sensitive resist (in green) is spin-coated onto the substrate (in blue). (2) Selective regions of the photoresist are exposed to a focused electron beam. The electron sensitive resist undergoes chemical changes (in red) upon exposure and can partially be dissolved afterward, that is, the development (3). (4) The desired material (in yellow) is deposited using thermal or electron beam evaporation covering substrate and resist. (5) The residual, undesired polymer covered with material is dissolved during lift off leading to the desired nanostructure on the substrate. (6) Optionally, the deposited material can be used as a hard mask for reactive ion etching (RIE), which removes material from the unprotected regions together with a final wet etch (7) of the hard mask. (b) Scanning electron microscope (SEM) image of palladium−gold antennae with 10 nm gap distance fabricated via two consecutive EBL steps illustrating the ultrahigh resolution of EBL. (c) Gold bow-tie elements with a 20 nm gap fabricated using FIB. The inset shows a magnified image of the fabricated nanostructure. (d, e) Nanoimprint lithography (NIL). (d) Top: Schematic showing the imprint process to transfer the pattern from the stamp into a resist. Bottom, from left to right: Scheme of the metasurface made from amorphous GaP (a-GaP) with the dimensions of the unit cell. SEM images with different magnifications. Photograph of the 5×5 mm^2 imprinted metasurface on top of an ITO-covered glass slide next to an a-GaP film. (e) Photograph of an NIL roll-to-roll apparatus for continuous large-area nanoimprinting toward industrial applications. (b) Adapted with permission from ref 210. Copyright 2011 Springer Nature. (c) Adapted with permission from ref 213. Copyright 2008 Springer Nature. (d) Adapted with permission from ref 212. Copyright 2021 Wiley-VCH GmbH. (e) Adapted with permission from ref 217. Copyright 2009 American Chemical Society.

frequently used techniques to fabricate metasurfaces and their principles will be explained in the following paragraphs.

Metasurfaces can be fabricated using lithographic techniques to create nanoscale patterns, which are then replicated into the desired material by a combination of thin film deposition, chemical and dry-etching techniques. The process is schematically illustrated in Figure 10 for electron beam lithography (EBL) but works similarly for most lithographic approaches. The principle is already centuries old[207] and was developed to write (greek: γραφία, graphy) from a carved stone (greek: λίθος, stone) to produce prints on paper. Today, lithography is the workhorse of the semiconductor and integrated circuit (IC) industry and many techniques are available, which differ in resolution, throughput and scalability and in whether the patterns are generated by masked or maskless systems (Figure 9).[208,209] Maskless systems, such as EBL and focused-ion beam (FIB), can enable ultrahigh resolution, but are limited by their throughput and scalability, since each pattern must be written individually using direct-writing techniques. Masked techniques,

such as photolithography, nano imprint lithography, and colloidal lithography, enable high-throughput production by replicating the entire mask but are often limited in resolution.

2.3.1. High-Resolution Lithographic Techniques. Beginning with the high-resolution techniques, EBL is widely used for the fabrication of metasurfaces from the single particle level up to millimeter-sized arrays. The process is illustrated schematically in Figure 10a. Glass is typically used as a substrate because it facilitates transmission measurements, but monocrystalline wafers or other materials (Si, CaF$_2$, etc.) can be used as well. At first, the substrate is covered by a thin film of an electron sensitive resist via spin coating (Figure 10a, step 1). Upon exposure with the electron beam (Figure 10a, step 2), selected regions of the resist will undergo chemical changes, which will modify their solubility or stability, and can be partially dissolved afterward, which is called the development (Figure 10a, step 3). There are two kinds of resists: for positive resists, the solubility of exposed regions increases and will be dissolved during development, whereas for negative resists, the exposed
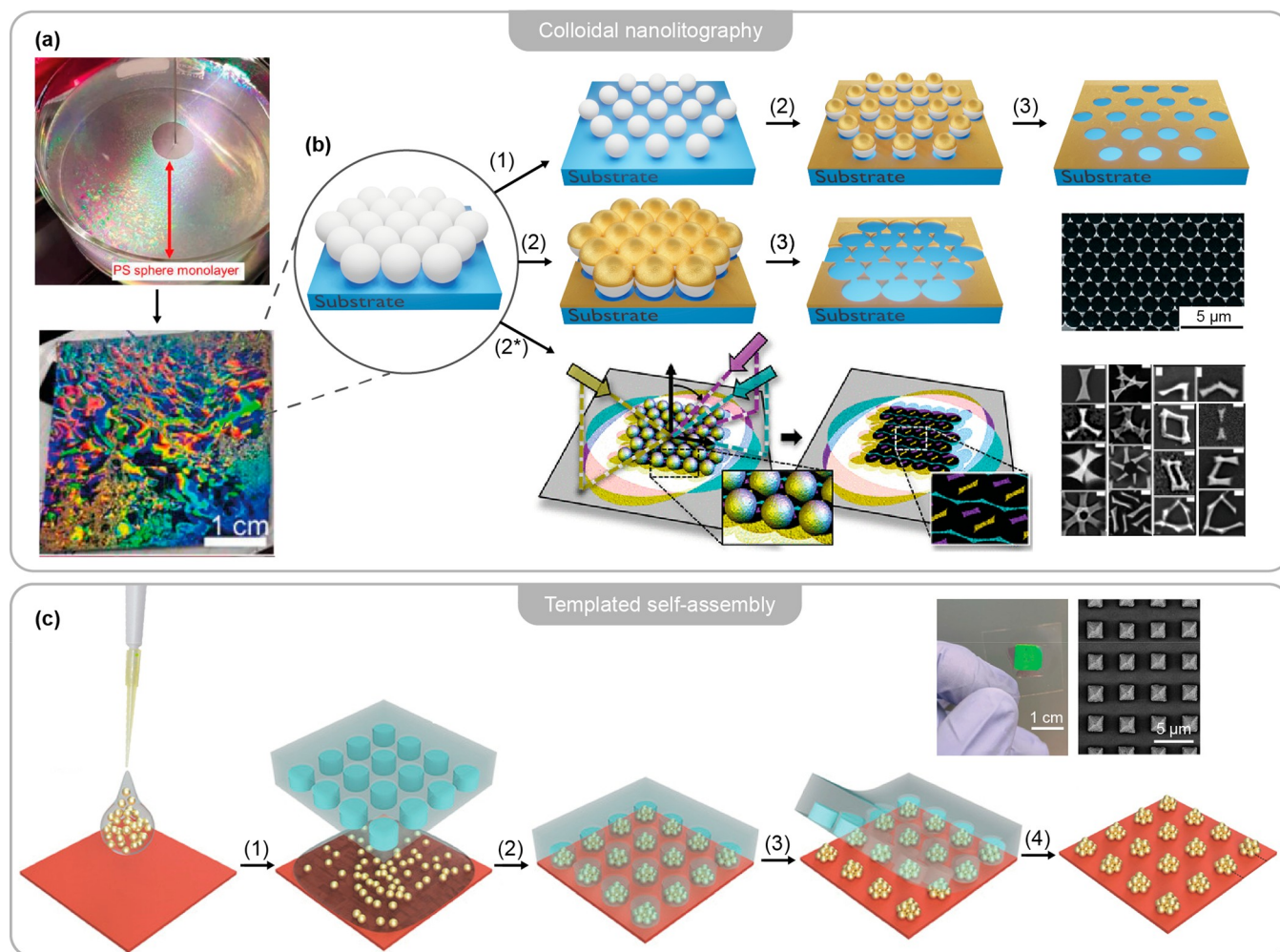
Figure 11. Nanopatterning approaches based on self-assembly. (a) Top: Photography of a polystyrene (PS) sphere monolayer self-assembled at the water−air interface. Bottom: Si wafer substrate to which the monolayer was transferred. (b) Schematic illustration of possible lithographic routes from colloidal self-assembly. Top: Size reduction (1), film deposition (2), and template removal (3) lead to large-scale nanohole arrays. Middle: Film deposition (2) and template removal (3) lead to triangular shaped metasurface. Bottom: Shadow sphere lithography. Metal depositions at oblique angles (2*) in combination with RIE can lead to all shapes of different metasurfaces. SEM images show the different possible unit cells. (c) Templated self-assembly. A colloidal sphere solution is drop-casted onto the substrate (1). A prepatterned elastomeric mold is brought in contact (2). Solvent evaporation and lift off (3) lead to well-defined arrays of self-assembled colloidal nanoparticles. Inset: Optical and SEM images showing a large-scale plasmonic pyramidal supercrystal obtained via templated self-assembly. (a) Adapted with permission from ref 225. Copyright 2020 American Chemical Society. (b) Middle: SEM image adapted with permission from ref 235. Copyright 2005 American Chemical Society. Bottom: Adapted with permission from ref 233. Copyright 2014 American Chemical Society. (c) Scheme and photograph adapted with permission from ref 236. Copyright 2021 Wiley VCH-GmbH. SEM images adapted with permission from ref 237. Copyright 2017 American Chemical Society.

regions reduce their solubility and thus will remain. The latter are typically used for inverted structures, such as holes in a film, since the required writing time will be decreased. After the development, the desired material is added onto the substrate via thin film deposition techniques such as electron beam- or thermal evaporation (Figure 10a, step 4). Next, the residual resist, which is also covered by the deposited material, is dissolved, which is called lift-off (Figure 10a, step 5). After a successful lift-off, the desired patterns are revealed. A crucial requirement is that the deposited film is not continuous over the patterned and not-patterned regions, which is established by a sufficient height difference in between the resist and deposited material. In some cases, the desired material cannot be deposited after EBL, for example, if the metasurface needs to be monocrystalline, or if thermal- or electron beam evaporation is not feasible. Subsequently, the desired material is deposited on the substrate before the process or a monocrystalline wafer is

directly used. EBL is performed in the same way as mentioned before using a positive or negative photoresist. After development, a hard mask is deposited on the material, often made from chrome or silica (SiO_2), and lift-off is performed (Figure 10a, step 5). Subsequently, dry etching with reactive gases, known as reactive ion etching (RIE), is utilized to etch into the material (Figure 10a, step 6), which is not protected by the hard mask and the metasurface is revealed after subsequent dissolution of the hard mask (Figure 10a, step 7). Figure 10b shows a scanning electron microscope (SEM) image of palladium−gold nano-antennas separated with a 10 nm gap distance.[210] The different materials were fabricated with two consecutive EBL steps and require precise alignment of the instrument, illustrating the ultrahigh resolution that can be achieved using EBL. The high lateral resolution of EBL relies on the use of the electron beam for exposure, which can be focused down to a few nanometers and is limited by the beam column rather than the wavelength of

electrons.[211] Despite that, each pattern must be written individually; thus, the fabrication of large-scale substrates is time-consuming and, as an example, can take 50−60 h for a 5 × 5 mm² substrate.[212]

Similarly to EBL, FIB is a direct writing technique where a focused ion beam is scanned over the surface, removing material through ion bombardment (Figure 9). FIB can be used to directly create nanostructures on the substrate and is therefore not a classical lithographic technique but allows ultrahigh resolution with features in the 5−20 nm regime.[209,213] An array of bowtie antennas with 20 nm gap width fabricated via FIB is shown in Figure 10c.[213]

Besides EBL and FIB, optical nanoprinting can be utilized to position colloidal particles into metasurfaces at the single-particle level with high precision.[214−216] Optical nanoprinting relies on optical forces, that is, optical tweezers, to trap particles inside the focal spot of a laser, which can be combined with additional electric fields or temperature gradients, known as optoelectronic or opto-thermophoretic printing, respectively.[214] During exposure, the particle is pushed toward the substrate and the repulsive forces between particles and substrate are overcome, which results in the binding of the particle due to attractive van der Waals forces.[215] This allows the positioning of nanoparticles one by one allowing to have single colloidal structures as meta-atoms of metasurfaces. Moreover, combination of particles of different materials for hybrid metasurfaces can be easily implemented compared to lithographic techniques.

2.3.2. Scalable and High-Throughput Lithographic Techniques.
EBL and FIB can create all types of two-dimensional structures with ultrahigh resolution. However, they have restrictions regarding their throughput and scalability for large-area arrays. Photolithography is considerably faster by illuminating selected regions on the substrate simultaneously via a patterned mask (Figure 9). Otherwise, photolithography follows the same experimental procedure as EBL, only a light-sensitive photoresist is utilized during exposure, whereas development, lift-off, and RIE are identical (Figure 10). The masks must be fabricated once via EBL or purchased commercially, but afterward high-throughput fabrication is possible. However, since light is utilized, a drawback is that the lateral resolution is diffraction-limited and depends on the utilized wavelength, with $R_{x,y} = \lambda/(2\ NA)$, where NA is the numerical aperture. Consequently, the highest resolution depends on the available light source of the instrument. Nevertheless, photolithography is the working horse of the semiconductor and IC industry, continuously decreasing the utilized wavelength, even down to 13.5 nm in extreme-UV lithography.[209,218] However, the costs of such instruments are not bearable for research facilities or small industries even at larger wavelengths.

Nanoimprint lithography (NIL) has emerged as a promising candidate to fabricate metasurfaces with both ultrahigh resolution and high-throughputs, while still being affordable and scalable.[208,219,220] In NIL, a nanostructured stamp, that is, master, is pressed into a resist, which transfers the desired pattern (Figure 9). Depending on the desired structure, the master must be inverted or can be used directly. The imprinting can be achieved via hot embossing,[220] UV-nanoimprint, or soft lithography.[219,221,222] In hot embossing, the resist is heated to its glass transition temperature to allow continuous material flow while the stamp is imprinted. In UV-nanoimprint, a transparent stamp is imprinted into a UV curable polymer, which is then illuminated. After imprint, the master is removed and

metasurfaces can be fabricated via the conventional lithographic fabrication route (Figure 10a). In soft lithography, the nanoimprint of the stamp transfers molecules such as self-assembled monolayers (SAMs) to the surface. Such SAMs are too thin to be used as etch resists for RIE but can be processed in similar ways to create metasurfaces.[222] In another approach, soft lithography was used to pattern perovskite films into metasurfaces.[221] In general, NIL allows an excellent reproduction of the stamps geometrical features and photonic resonances with ultrahigh resolution (Figure 10d).[212] While the master must be fabricated once via direct writing-techniques, such as EBL, it can be reused multiple times with high throughput.[208,220] The technique is scalable and large-area roll-to-roll or roll-to-plate techniques are already available enabling continuous and high-throughput production toward industrial applications (Figure 10e).[217]

2.3.3. Self-Assembly.
While NIL can duplicate large-scale patterns with high throughput, the patterns have to be produced once via EBL in the first place. This is a restriction with regards to flexibility for cases where, for example, multiple large-area surfaces with varying architectures are required. Techniques based on self-assembly have emerged and can completely circumvent the need for clean-room facilities and expensive equipment (Figure 11). Colloidal lithography is based on the self-assembly of a spherical monolayer, often made from polymers such as polystyrene. When assembled on the water−air interface or using a Langmuir−Blodgett trough, large-scale and almost defect-free hexagonal close-packed (hcp) mono-layers are formed, which can be used as template for nanofabrication.[223−225] The technique is affordable and offers a high flexibility in terms of possible structures (Figure 11a,b). Besides hexagonal arrangements, chain and square arrangements can be achieved by assembling microgels.[226] After self-assembly, the monolayers can be transferred to nonclose packed architectures by size reduction[224] or using core−shell particles.[227] In combination with thin-film deposition techniques and reactive ion etching, a wide range of metasurface can be fabricated, such as triangles,[205,228] nanohole architectures,[229−231] chiral crescents,[232] and much more complex structures.[205,233,234] Conveniently, all important geometrical parameters can be controlled with the initial and reduced size of the polymeric spheres.

Besides using polymeric spheres as lithographic template, colloidal self-assembly can also be directly performed from metal nanoparticles, resulting in close-packed architectures of nanoparticles with different shapes (Figure 11c).[238−240] Interparticle spacing and packing density can be controlled by polymer chains on the nanoparticle surface and particle concentration, respectively.[228,241] In addition, capillary-assisted particle assembly (CAPA)[242] or templated self-assembly[236,237,243,244] can also be used to fabricate ordered nanoparticle arrays from colloidal solutions. The colloidal solution is drop-casted and then confined in between the target substrate and a template, usually made from polydimethylsiloxane (PDMS), since it can be conveniently replicated from a master. During solvent-evaporation, the nanoparticles self-assemble and form super-structures replicating the size and shape of the template cavities.

2.3.4. Three-Dimensional Techniques.
Metasurfaces are typically planar nanostructures. Controlling nanoscale architectures in the third dimension poses an additional challenge for the nanophotonics community.[4] Using techniques such as deep-reactive ion etching (D-RIE),[245−247] chemical wet etching,[248−250] or chemical vapor deposition (CVD),[251,252] high-
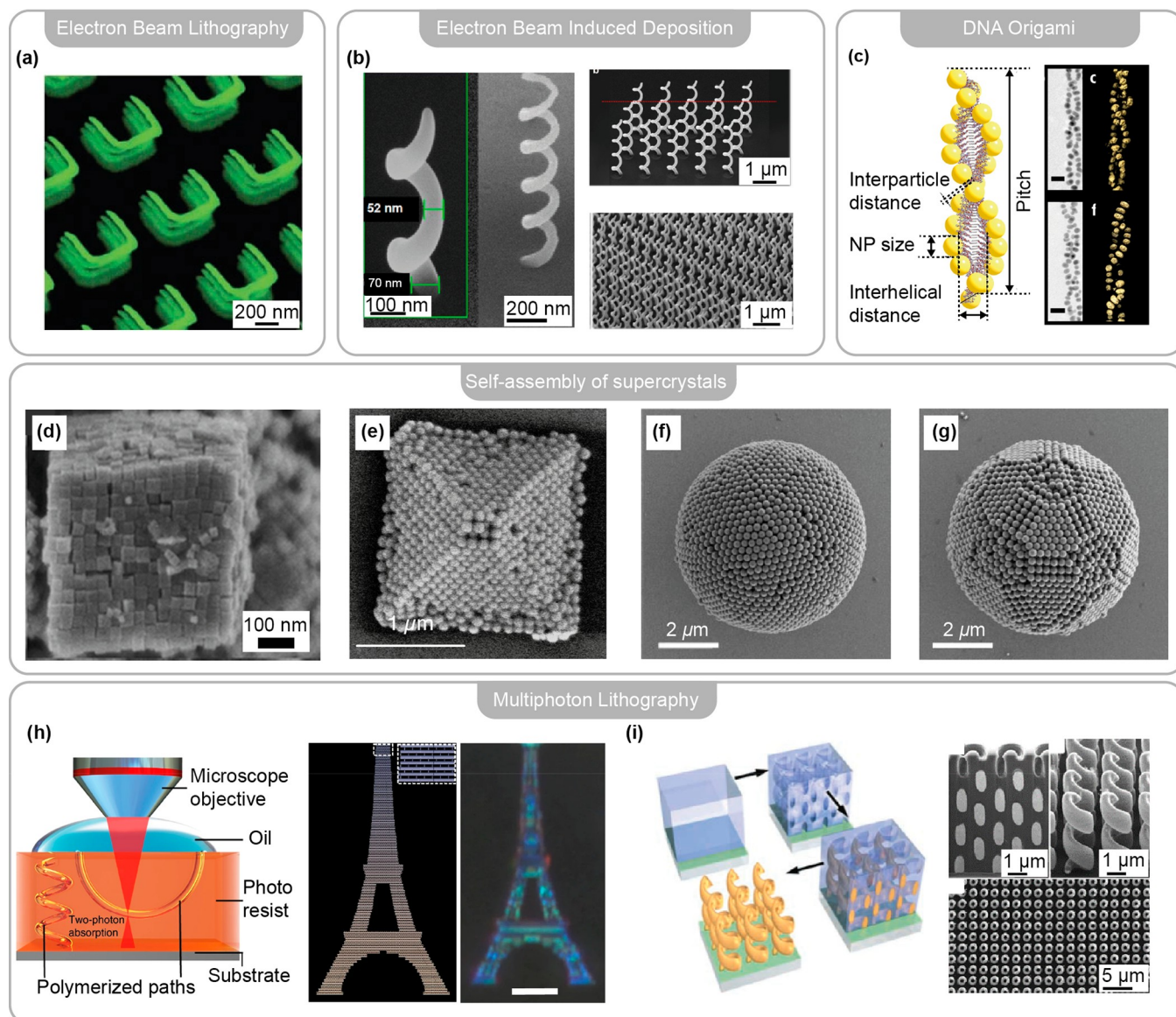
Figure 12. Nanopatterning in three dimensions. (a) Layered 2D metasurfaces fabricated via EBL. The first metasurface is embedded in a spacer layer and a second EBL process is aligned on top. (b) Ultrahigh-resolution 3D metasurfaces via focused-electron-beam or focused-ion-beam induced deposition. (c) Accurate self-assembly of gold nanoparticles in DNA Origami. Scale bars: 20 nm. (d−g) Self-Assembly of colloidal particles into 3D metamaterials, that is, supercrystals, of various shapes. (d) Cube. (e) Pyramid. (f-g) spheres. (h) Left: Schematic of the technique in which a photoresist polymerizes upon two-photon absorption in the focal point of the laser. Right: 3D printed Eiffel Tower. Scale bar: 10 μm. (i) Multiphoton lithography to produce 3D metallic metasurfaces. Left: Schematic. A 3D polymeric template is built up via multiphoton lithography and the pores are filled up with electrochemical deposition. Right: SEM images of the fabricated metal helices. (a) Adapted with permission from ref 253. Copyright 2008 Springer Nature. (b) Adapted with permission from ref 257. Copyright 2015 American Chemical Society. (c) Adapted with permission from ref 204. Copyright 2013 American Chemical Society. (d) Adapted with permission from ref 278. Copyright 2009 The Royal Society of Chemistry. (e) Adapted with permission from ref 237. Copyright 2017 American Chemical Society. (f,g) Adapted with permission from ref 203. Copyright 2018 Springer Nature. (h) Left: Adapted with permission from ref 269. Copyright 2020 Springer Nature. Right: Adapted with permission from ref 268. Copyright 2019 Springer Nature. (i) Adapted with permission from ref 271. Copyright 2009 AAAS.

aspect ratio architectures like pillars, sheets, or nanowire arrays can be fabricated from planar metasurfaces. In the microelectronic and IC industry, multiple lithographic steps are aligned toward each other to fabricate complex, functional devices. Similarly, layered structures from two-dimensional metasurfaces have also been fabricated by embedding the first metasurface inside a spacer layer and aligning a second EBL process on top (Figure 12a).[253−256] Using specialized equipment, such as focused ion beam induced deposition or focused electron beam induced deposition, complex 3D nanosystems

can directly be written with ultrahigh resolution in all three dimensions (Figure 12b)[257] but face restrictions regarding their fabrication speed, scalability, and instrumental cost.

Self-assembly can be utilized to create 3D hierarchically organized metamaterials, that is, supercrystals (Figure 12d−g).[258] In these cases, the meta-atoms are the nanoparticles themselves. There are several possible approaches to achieve this, for example, by applying geometric confinement via assembling inside emulsion droplets to create colloidal supercrystals[203,259] or inside a template (Figure 11c),[237,260] or by

increasing short-range attraction.[261] Moreover, this idea has been extended to 3D films of self-assembled nanoparticles (sometimes named in the literature as plasmonic superlattices). Striking optical properties can be achieved by using these nanoparticle-based metamaterials such as strong light−matter coupling, standing waves inside the material, or even dark plasmon modes.[262−264]

Multiphoton lithography has emerged as a promising technique to perform high-resolution 3D lithography.[265,266] The technique utilizes a femtosecond laser which is focused into a curable photoresist. The polymerization of the resist depends on a two-photon absorption process, which only happens at the focal point, where the light intensity is the highest. By building up the structure layer-by-layer similar to a 3D printer, complex structures such as photonic crystals can be fabricated (Figure 12h).[267−269] However, drawbacks are that nanoscale resolution is hard to achieve due to the dependence on the diffraction-limited spot size and that only electrical insulators can be printed such as polymers, hydrogels, siloxanes and organic/inorganic hybrids.[265] To reach nanoscale resolution, structures printed via multiphoton lithography can be size decreased by annealing or plasma treatments,[268,270] while metallic structures can be obtained by printing a 3D template and subsequent metallization via electrochemical deposition (Figure 12i).[271] Another promising research field toward two and three-dimensional, photonic nanostructures is DNA Origami.[272,273] DNA origami can already be utilized to self-assemble gold nanoparticles in 3D with ultrahigh resolution (Figure 12c).[204] While this approach is mostly utilized in solution or for randomly distributed assemblies on surfaces, examples combining DNA Origami with lithographic approaches to create ordered arrays are already available[274−277] and offer new exciting synthetic routes for metasurfaces with exquisite three-dimensional positional control.

For many applications, it is necessary to decorate or combine metasurfaces with additional materials that can bring new functional properties to the existing architecture. Metasurfaces can be utilized to control the luminescence of emitters such as semiconductor quantum dots,[279,280] dye molecules[281,282] or perovskite nanocrystals.[130,283,284] In photocatalysis, light absorbing metasurfaces are decorated with catalytic materials to increase photocurrents and onset potentials,[212,285] while the incorporation of plasmonic particles to existing semiconductor architectures can enhance light absorption for photovoltaic and photocatalytic applications (see section 5).[198,286−288] In addition, metasurfaces are combined with 2D materials, such as graphene, as they offer the possibility to be transferred on top of the nanostructures with deterministic transfer processes, or sandwiched between different materials to increase the fabrication options and their integration with optical meta-materials.[289] Such material combinations can bring additional challenges for the synthesis and the processes must be adapted slightly, for example, to account for different material stabilities during wet or dry etching. In the simplest case, additional molecules or colloidal particles can easily be drop-casted or spin-coated, thin films can be deposited,[290,291] 2D monolayers can be transferred on top of the metasurface,[160] or the metasurface can be fabricated on top of other materials.[156] In more sophisticated approaches, chemical synthesis or self-assembly on function-alized surfaces can be utilized to incorporate colloidal particles or other molecules to the existing architecture.[292,293] Never-theless, controlling hybrid metasurface structures in three-dimensions, where the individual metaatoms are decorated hierarchically with additional nanostructures, remains a challenge.

Electrochemical techniques have emerged as promising platforms to allow such precise 3D control where the patterning of specific locations is accomplished by passivation,[294] by controlling the deposition via illumination,[55,295−297] or by templated electrochemical synthesis, providing three-dimensional spatial resolution of up to 5 nm.[298,299] In a comparable approach, plasmonic hot electrons can be utilized to perform nanolocalized surface chemical reaction, which can guide the assembly of other nanomaterials in these hot spots.[300] Such approaches open new avenues for the design of complex, hierarchically organized three-dimensional metasurfaces with improved functionalities and performance.

2.3.5. Rational Design of Metasurfaces: Inverse Design and Artificial Intelligence.
Beyond the techniques for nanoscale fabrication, a milestone for enabling the advantages of metasurfaces in practical devices is the development of rules for the rational design of the meta-atoms geometry and arrangement to achieve tailored optical properties and opera-tional bandwidth. In this section, we will briefly review the techniques and approaches commonly used to design optical metasurfaces.

A reliable EM model connecting the geometry and materials in a metasurface to its corresponding optical resonances is not a trivial problem. Meta-atoms made either from metals or semiconductors exhibit optical resonances generated by to the presence of light-induced currents in the nanostructure. Thus, a fundamental approach behind the design of optical metasurfaces relies on solving the Maxwell's equations for a selected geometry and evaluating the EM response. In the majority of optical metasurfaces studied in literature, the designs are selected with an approach based on a direct design of the nanostructure. The direct design process relies on selecting the meta-atom parameters via an intuition based trial-and-error process while using full EM simulations for finding the correct geometry. This is done by varying many parameters, for instance, the shape, material, and size of the meta-atoms, the array pitch dimensions, the materials combination and substrates. At first, the material, size, and shape of the meta-atom are selected following the rules governing optical resonances in a single nanostructure, known from previous empirical and theoretical knowledge as discussed in Section 2.2. Then the array parameters are computed through long EM simulations, for example, with finite element methods (FEM) and finite difference time domain (FDTD) methods, by solving Maxwell's equations for a given geometry design by feeding the geometry to the numerical software. This process is repeated until satisfactory parameters of the array are found, as a compromise between the desired optical resonance and the retrieved output from the numerical solver. Direct design methods have many drawbacks, as this trial and error basis is dispersive and relies heavily on the experience of the designer. Moreover, it leverages only simple geometries, such as bars or cylinders and their combinations, seeking a precise balance between the meta-atom geometry and array parameters via a long, repetitive, and heavy computational effort. The knowledge acquired through this effort is usually lost when reiterating the same combination or geometry for different materials and wavelengths, and optical limitations of the constituent materials and the use of simple geometries further reduces the efficiency of this approach. Nevertheless, the direct design of metasurfaces still constitutes the most effective approach for designing simple device geometries. Compared to new computational methods,

direct design approaches lack the possibility to provide insights on the connection between the optical properties and the geometry of the metadevices and can compute only one solution between the many available in a larger space of parameters.

Because of the many constraints of the direct design method, in recent years the inverse design of metasurfaces has rapidly gained interest in nanophotonic design. The fundamental concept behind inverse design methods is that of feeding the algorithm the desired optical properties as an input and retrieving one, or many, of all the design solutions as the output of the computational process. With the advent of large computational systems and improved artificial intelligence (AI) algorithms, the concepts of machine learning and artificial neural networks started to permeate a vast range of disciplines across physics and chemistry. In recent years, these concepts have been applied by the nanophotonics community, to calculate, for example, the resonances of plasmonic[301] and dielectric metasurfaces,[302] structural coloration with plasmonic particles,[303] near field and far field patterns of nanoantennas,[304] and optimization of thermal emitters.[305] We will not review here in depth the different types of machine learning algorithms applied to photonic design, due to the vast and rapidly developing field, but we will introduce the concepts related to this new frontier in computer science applied to metasurface design. For more in-depth discussions, we refer the reviewer to recent reviews on the topic.[306−308]

The first approaches of inverse design in nanophotonics were based on gradient optimization algorithms.[309] After defining a figure of merit, or cost function, describing the desired optical characteristics, the optimization algorithm is set to find a minimum in a parameter distribution. The parameter distribution is usually defined as the permittivity and position of the materials in the unit cell of a metasurface by discretization of the space in pixels, with sizes achievable by nanofabrication techniques. The algorithm thus seeks to minimize the cost function by producing at every iteration a new design of the meta-atom, until the whole process converges to a minimum of the cost function. During the process, however, no real information is stored or extracted at the end of the computation, and the whole process needs to be repeated after applying any change in the design. Moreover, optimization approaches find only one solution, as the local minimum in the parameter space, leaving out the possibility of finding similar, or even better, geometries, which would still be a solution to the same optical input set by the user.

In recent years, AI methods, such as machine learning and deep neural networks, have reshaped the computational approaches used in metasurface design due to their extraordinary capability in finding solutions from a large data set or parameter space. They offer new ways to find both the best design solution and a rational one-to-one correspondence between the optical properties and metasurface design, contrary to optimization methods, which tend to find many designs for the same output. A common classification divides machine learning into supervised, unsupervised, and reinforcement learning schemes, although nowadays the differences between these schemes are blurred. A fundamental aspect of neural networks is the presence of numerous layers of computation that are iteratively connected to provide the desired output. A drawback of neural network algorithms, beyond their intrinsic complexity and low control of the computational layers, is that all of them have prediction abilities that require vast training data sets to begin with. Hence, in recent years, hybrid methods have

been applied to nanophotonic design where the prediction abilities of neural networks are merged with optimization techniques to compute faster and more reliable optimal solutions to the desired input properties. The neural networks are assisted by optimization algorithms in order to increase the reliability of the solutions found by the evolutionary algorithms using gradient minimization algorithms to steer the prediction force of AI methods toward concrete geometries.

Nanophotonic inverse design represents a new and evolving research field with yet to be discovered functionalities for nanoscale optical devices. Compared to direct design or optimization methods, deep learning possesses transfer learning features, expected to have a decisive role in future inverse design.[307] Moreover, inverse design methods offer a way to gain deeper insights into the relationship between geometry and optical properties of metasurfaces. Finally, due to the complexity of the AI models and the instability of neural networks, AI generated structures must include the constrains set by the resolution of nanoscale fabrication methods and the robustness against imperfections during fabrication steps[310] to be fully compatible with a future large scale production.

3. PHOTON−PHOTON ENERGY CONVERSION

In this section, we summarize recent research that involves energy conversion between photons and photons. The fundamentals of different photon−photon energy conversion processes, including nonlinear optical processes that allow the generation of coherent photons at new frequencies as well as upconversion and quantum cutting processes that involve incoherent populations of electronic (and vibronic) states, will be introduced. Because of the fact that the intrinsic nonlinear and upconversion processes are very weak in naturally occurring materials, it has attracted considerable research efforts to enhance the efficiency of these processes. Recent advances in ultrathin metasurfaces have opened an unprecedented opportunity to boost the photon−photon conversion efficiency. As such, followed by the fundamental overview of different photon−photon interactions, we will focus on reviewing recent progress in metasurface-mediated photon−photon energy processes.

3.1. Fundamentals of Nonlinear Optical Responses

Nonlinear photonics, a key aspect of modern photonic science and technology, allows the generation of light at new frequencies and the control of photon−photon interactions via nonlinear optical materials (NOMs). Although nonlinear optical responses are naturally weak, different NOMs have been developed for strong photon energy conversion and nonlinear light manipulation. As such, NOMs have been applied for widespread photonic applications including ultrashort pulsed lasers,[311] optical modulators,[312] ultrafast all-optical switches,[312,313] nonlinear holography,[314] ultrafast nonlinear imaging,[315,316] and on-chip nonlinear optical sources.[317]

From a fundamental point of view, when light impinges upon NOMs, the collective displacement of electrons generates a scattered field oscillating synchronously and interfering with the impinging light.[318] For small electric field amplitudes, the scattered field is linearly proportional to the impinging one and creates linear optical responses, such as reflection, refraction, and absorption. For sufficiently large amplitudes, electronic bindings in the NOMs become asymmetric and bound electron orbits get distorted, causing higher-order nonlinear optical responses. Figure 13a illustrates the scenario in which the
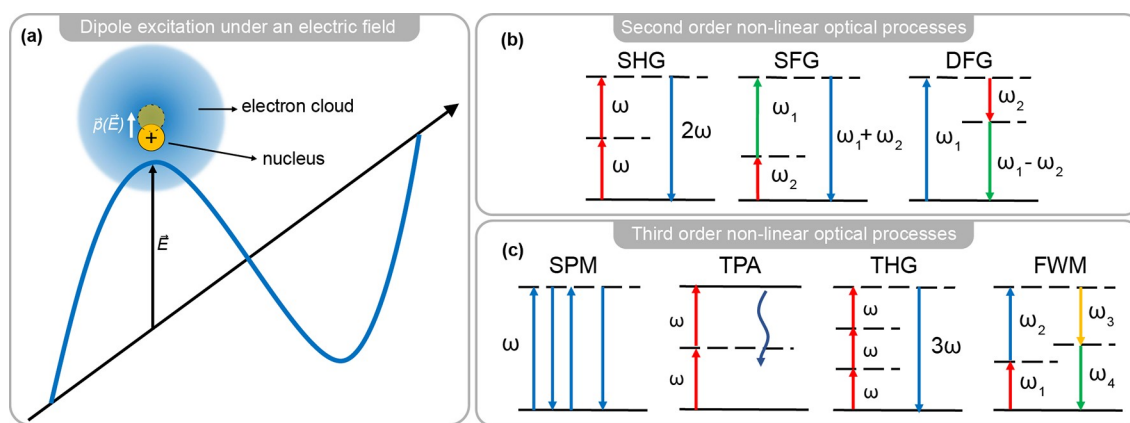
Figure 13. Dipole excitation and energy level diagrams based on second- and third-order nonlinear dipole transitions. (a) Electric field component of an electromagnetic wave interacts with an atom and induces a dipole oscillation, $\overline{p}\,(\overline{E})$. (b) Energy level diagrams presenting possible second-order nonlinear optical processes: second harmonic generation (SHG), sum-frequency generation (SFG), and difference-frequency generation (DFG). (c) Energy level diagrams presenting some of the possible third-order nonlinear optical processes: self-phase modulation (SPM), two-photon absorption (TPA), third-harmonic generation (THG), and nondegenerate four-wave mixing (FWM). Solid (dashed) horizontal lines represent real (virtual) electronic energy levels.

electric field of impinging light resonates with the electrons in the outer shells of the atoms and produces an induced polarization, related to the displacement of an electron orbital with respect to the nucleus.

The instantaneous dielectric response in NOMs to an applied optical field can be expressed by expanding the polarization $\overline{P}(t)$, as a power series in terms of the optical field amplitude $\overline{E}(t)$, as follows:

$$\overline{P}(t) = \varepsilon_0(\chi^{(1)}\overline{E}(t) + \chi^{(2)}\overline{E}^2(t) + \chi^{(3)}\overline{E}^3(t) + ...) \quad (3.1)$$

where ε_0 is the vacuum permittivity and $\chi^{(i)}$ is the ith-order optical susceptibility tensor. The first term $\chi^{(1)}$ describes the linear optical effect associated with a complex refractive index and is related to the dielectric function by the simple expression $\varepsilon = (1 + \chi^{(1)})$. However, if the impinging field is intense enough or the higher-order susceptibilities are large, the higher-order ($i \geq 2$) terms become significant and lead to radiation at new frequencies different from the incident light frequency. Here, we discuss the nonlinear effects associated with second- ($\chi^{(2)}$) and third-order ($\chi^{(3)}$) susceptibility coefficients.

3.1.1. $\chi^{(2)}$ Processes. Unlike the first-order susceptibility term $\chi^{(1)}$ concerning dipole excitations with bound and free electrons induced by a single photon, here we discuss the excitations that involve two different frequency components ω_1 and ω_2:

$$\overline{E}(t) = \overline{E}_1 e^{-i\omega_1 t} + \overline{E}_2 e^{-i\omega_2 t} + c.\,c. \quad (3.2)$$

where *c.c.* stands for complex conjugate. The nonlinear polarization related to second order is

$$\overline{P}^2(t) = \varepsilon_0 \chi^{(2)} \overline{E}^2(t) \quad (3.3)$$

Therefore, the second-order nonlinear polarization is expressed as

$$\overline{P}^2(t) = \varepsilon_0\chi^{(2)}[(\overline{E}_1{}^2 e^{-i2\omega_1 t} + c.c.) + (\overline{E}_2{}^2 e^{-i2\omega_2 t} + c.c.)$$
$$+ (2\overline{E}_1\overline{E}_2 e^{-i(\omega_1+\omega_2)t} + c.c.)$$
$$+ (2\overline{E}_1\overline{E}_2{}^* e^{-i(\omega_1-\omega_2)t} + c.\,c.\,)]$$
$$+ 2\varepsilon_0\chi^{(2)}[\overline{E}_1\overline{E}_1{}^* + \overline{E}_2\overline{E}_2{}^*] \quad (3.4)$$

In the above equation, several complex-amplitude frequency components of the second-order nonlinear polarization appear. The first two terms are referred to as second harmonic generation (SHG) and the third and fourth terms are known as sum-frequency generation (SFG) and difference frequency generation (DFG), respectively. The fifth term addresses a static electric polarization in the nonlinear medium and does not contribute to the radiation. These second-order wave mixing processes are principally illustrated in Figure 13b. It should be mentioned that the second-order susceptibility term $\chi^{(2)}$ is absent in centrosymmetric crystals such as silicon. This property stems from the fact that if the field $-\overline{E}(t)$ is applied to a centrosymmetric crystal or structure, due to the spatial inversion symmetry, the nonlinear polarization vector satisfies $-\overline{P}^2(t) = \varepsilon_0 \chi^{(2)}(-\overline{E})^2(t)$ according to eq 3.3, leading to $-\overline{P}^2(t) = -\overline{P}^2(t)$, implying that $\chi^{(2)}$ must be zero. This result is of fundamental importance because it explicitly forbids bulk crystals with centrosymmetric lattices to exhibit second-order nonlinear responses, regardless of the intensity of the applied field. In this case, the third-order nonlinearity is the main origin of nonlinear processes in such materials. The same symmetry constraints apply to artificially made metasurfaces for the second-order nonlinear processes.

3.1.2. $\chi^{(3)}$ Processes. Now we discuss third-order nonlinear polarization, given by

$$\overline{P}^3(t) = \varepsilon_0 \chi^{(3)} \overline{E}^3(t) \quad (3.5)$$

which is induced by an impinging electric field with three frequency components

$$\overline{E}(t) = \overline{E}_1 e^{-i\omega_1 t} + \overline{E}_2 e^{-i\omega_2 t} + \overline{E}_3 e^{-i\omega_3 t} + c.\,c. \quad (3.6)$$

By substituting eq 3.6 into eq 3.5 and expanding the frequency components of the third-order nonlinear term $\chi^{(3)}$, we obtain a
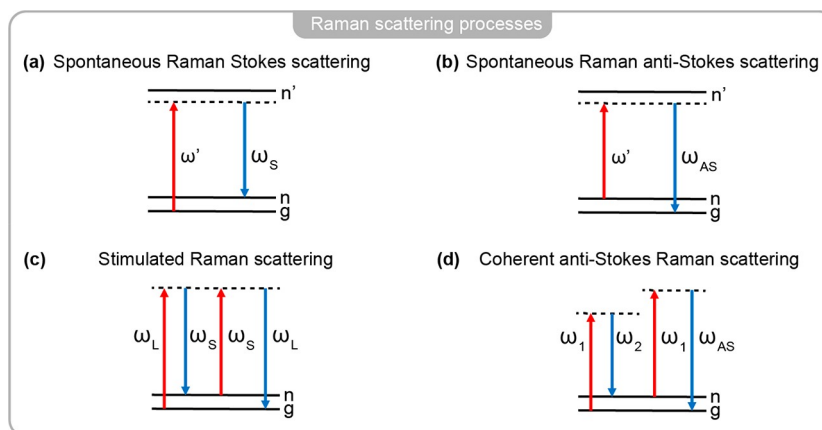
Figure 14. Energy level diagrams of different Raman scattering processes. (a) Spontaneous Raman Stokes scattering. (b) Spontaneous Raman anti-Stokes scattering. (c) Stimulated Raman scattering. (d) Coherent anti-Stokes Raman scattering. Solid (dashed) horizontal lines represent real (virtual) electronic energy levels.

multitude of terms at new frequencies for the third-order polarization $\bar{P}^3(t)$:

$$
\begin{aligned}
\bar{P}^3(t) = {} & 3\varepsilon_0\chi^{(3)}[(|\bar{E}_1|^2\bar{E}_1 e^{-i\omega_1 t} + c.c.) + \therefore\,] \\
& + 6\varepsilon_0\chi^{(3)}\left\{\left(\left|\bar{E}_2\right|^2 + \left|\bar{E}_3\right|^2\right)E_1 e^{-i\omega_1 t} + c.c.\right) \right. \\
& \left. + \therefore\,\right\} + \varepsilon_0\chi^{(3)}\left[\bar{E}_1{}^3 e^{-i3\omega_1 t} + c.c.\right) + \therefore\,\right] \\
& + 3\varepsilon_0\chi^{(3)}\left[\left(\bar{E}_1{}^2\bar{E}_2 e^{-i(2\omega_1 + \omega_2)t} + c.c.\right) + \therefore\,\right] \\
& + 3\varepsilon_0\chi^{(3)}\left[\bar{E}_1{}^2\bar{E}_2 e^{-i(2\omega_1 - \omega_2)t} + c.c.\right) + \therefore\,\right] \\
& + 6\varepsilon_0\chi^{(3)}\left[\bar{E}_1\bar{E}_2\bar{E}_3{}^* e^{-i(\omega_1 + \omega_2 - \omega_3)t} + c.c.\right) + \therefore\,\right] \\
& + 6\varepsilon_0\chi^{(3)}\left[\bar{E}_1\bar{E}_2\bar{E}_3 e^{-i(\omega_1 + \omega_2 + \omega_3)t} + c.c.\right) + \therefore\,\right]
\end{aligned}
$$

$$(3.7)$$

Where the symbol $\therefore$ stands for all possible permutations of frequencies. Each of the terms on the right-hand side of eq 3.7 corresponds to a nonlinear optical excitation, of which a few important ones are illustrated in Figure 13c. The first term in eq 3.7 corresponds to a phenomenon called self-phase modulation (SPM), which results from dipole excitations induced by three photons. SPM leads to an intensity-dependent refractive index change, which in turn modifies the spectral composition of the same optical pulse that has generated it. SPM could therefore broaden the pulse spectrum. The photons that generate SPM can also excite an energetically higher state, as depicted in the two-photon absorption (TPA) diagram of Figure 13c. TPA excitations are absorbing because they energetically excite electrons in the valence band to the conduction band, which lead to an intensity-dependent linear absorption coefficient. The intensity-dependent refractive index and absorption changes related to the SPM and TPA processes affect the complex refractive index n by the relation

$$
n = n_0 + n_2 I - i\frac{\lambda}{4\pi}(\alpha_0 + \alpha_2 I) \tag{3.8}
$$

where I is the intensity, and n_0 and α_0 are the linear refractive index and absorption coefficient, respectively. n_2 (the Kerr coefficient) and α_2 are interrelated with the real and imaginary parts of the third-order susceptibility as

$$
n_2 = \frac{3}{4}\frac{1}{c^2 n_0{}^2 \varepsilon_0}Re(\chi^{(3)}) \tag{3.9}
$$

$$
\alpha_2 = \frac{3}{2}\frac{-\omega}{c^2 n_0{}^2 \varepsilon_0}Im(\chi^{(3)}) \tag{3.10}
$$

where c is the speed of light in vacuum. To achieve ultrafast optical modulation in nonlinear optics, it is important to find naturally occurring NOMs or artificially designed NOMs that have both a large Kerr nonlinear coefficient and a small TPA coefficient.

The second term on the right-hand side of eq 3.7 represents cross-phase modulation, in which a first signal at ω_1 influences a second signal at ω_2. The third term in eq 3.7 describes the third harmonic generation (THG) process. THG allows a new signal oscillating at $\omega_{THG} = 3\omega_1$ to be produced from a signal at ω_1. The remaining terms in eq 3.7 describe the generation of new waves through four-wave mixing (FWM), in which three incident photons generate a fourth photon at an idler frequency ω_i. The incident photons are allowed to be degenerate, with one possible energy diagram shown in Figure 13c. FWM is an ultrafast process that has a wide range of applications, for instance in wavelength conversion, parametric amplification, and sampling. We should mention that the third-order nonlinear responses, such as the SPM, THG, and FWM, are not bound by the symmetry constraints that apply to the second-order nonlinear processes.

After discussing the specific nonlinear optical processes above, we will now review how these nonlinear processes can be significantly enhanced from the use of ultrathin metasurfaces ranging from plasmonic and dielectric nanoantennas to 2D materials.

3.1.3. Raman Scattering. The Raman effect based on inelastic light scattering (the scattered light contains frequencies different from those of the excitation) has offered a powerful platform for sensing, optical amplification, and supercontinuum lasing. Raman scattering of light by molecules was first predicted using classical quantum theory by Smekal in 1923[319] and experimentally observed by Raman and Krishnan in 1928.[320] Raman spectroscopy measures the inelastic scattering of photons due to vibrations in molecules or phonon modes in crystalline materials, which has become a prominent analysis technique particularly when analytes have strong light absorption.[321,322] Frequency components shifted to lower
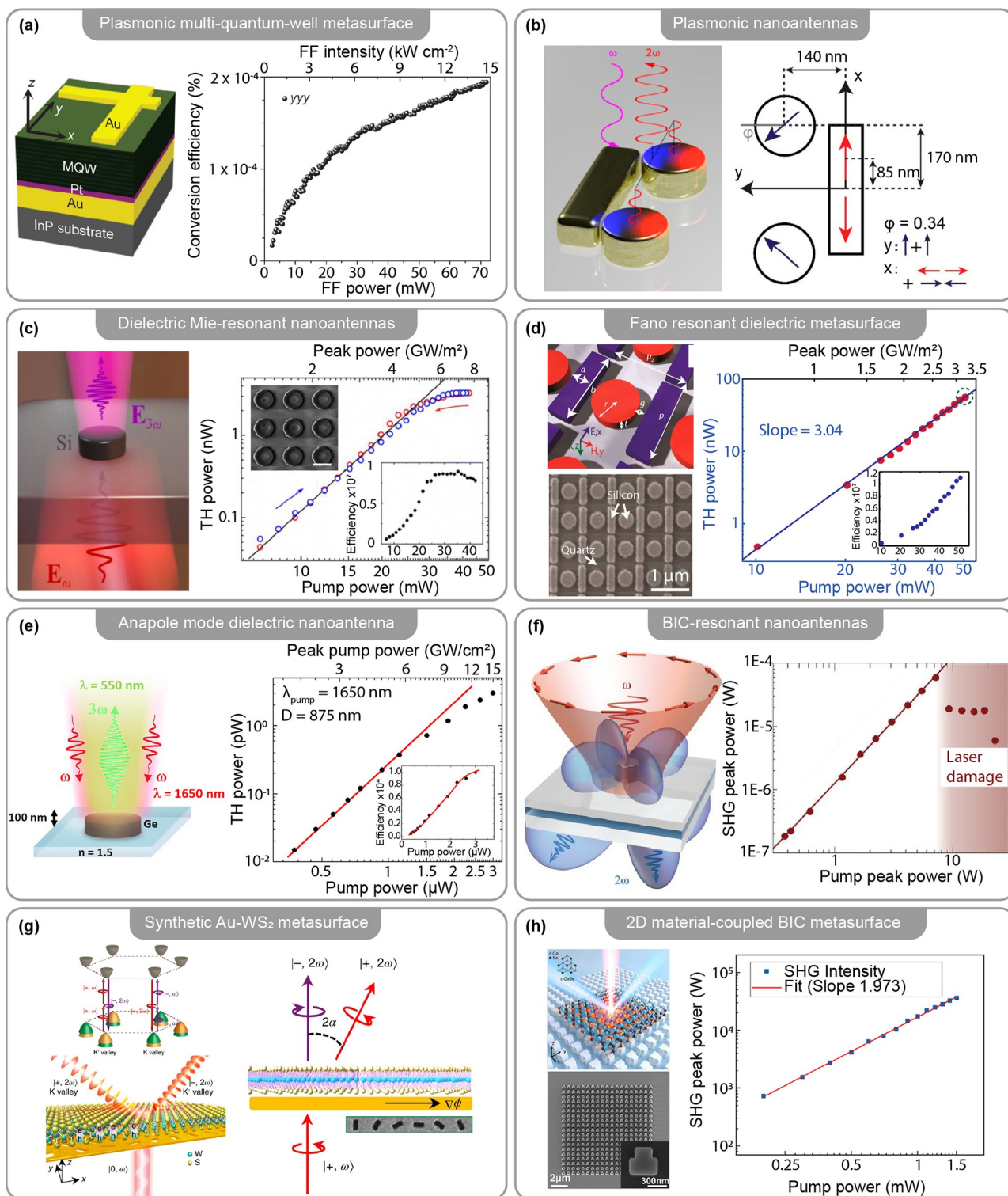
Figure 15. Enhanced nonlinear optical properties through different resonant nanoantennas and metasurfaces. (a) SHG from a plasmonic multiquantum-well (MQW: $In_{0.53}Ga_{0.47}As/Al_{0.48}In_{0.52}As$) metasurface with broken inversion symmetry. SHG power conversion efficiency as a function of fundamental frequency peak power (bottom axis) or peak intensity (top axis) at a fundamental frequency wavenumber of $1240 \, cm^{-1}$ for the yyy polarization combination. (b) SHG from plasmonic nanoantennas breaking inversion symmetry. (c) THG from all-dielectric Mie-resonant nanoantennas. (d) THG from Fano-resonant dielectric metasurface. (e) Enhanced THG from a Ge nanoantenna excited at the nonradiative anapole state resonance. (f) THG from dielectric nanoantennas excited at the BIC resonance. (g) Nonlinear chiral valley photons with a synthetic Au−WS₂ metasurface. (h) Enhanced SHG from a few-layer GaSe coupled to a BIC metasurface. (a) Adapted with permission from ref 328. Copyright 2014 Springer Nature. (b) Adapted with permission from ref 335. Copyright 2016 American Chemical Society. (c) Adapted with permission from ref 337. Copyright 2014 American Chemical Society. (d) Adapted with permission from ref 102. Copyright 2015 American Chemical Society. (e) Adapted with permission from ref 338. Copyright 2016 American Chemical Society. (f) Adapted with permission from ref 61. Copyright 2020 AAAS. (g) Adapted with permission from ref 340. Copyright 2019 Springer Nature. (h) Adapted with permission from ref 114. Copyright 2021 American Chemical Society.

frequencies are called Stokes components (ω_S), and those shifted to higher frequencies are called anti-Stokes components (ω_{AS}).[323] Here we discuss a few popular Raman scattering processes, considering both spontaneous and stimulated Raman scattering (SRS) and coherent anti-Stokes Raman scattering (CARS). Their energy level diagrams are shown in Figure 14.

Spontaneous Raman Stokes scattering can be represented as a transition from the ground state g to the final state n by means of a virtual intermediate level associated with the excited state n' (Figure 14a). This implies photon energy transfer to the vibrational mode in molecules. Consequently, spontaneous Raman anti-Stokes scattering is a transition from level n to level g with n' serving as the intermediate level (Figure 14b). In general, the spontaneous Raman scattering process is extremely weak, the scattering cross-section per unit volume for the Raman Stokes scattering is only $\sim 10^{-6}$ cm^{-1}, indicating that only approximately 1 part in one million of the incident radiation will be scattered into the Stokes frequency after propagating 1 cm distance in the scattering medium.[323]

However, under excitation by an intense laser beam, highly efficient Raman scattering can occur because of a stimulated scattering process. SRS and CARS have become prominent four-wave mixing techniques that are manifested by a third-order nonlinear susceptibility $\chi^{(3)}$. The origins of SRS and CARS can be understood from the energy level diagrams in Figure 14c and d, respectively. For the SRS process, owing to the excitation of a molecule or lattice (a phonon mode) vibration, the refractive index of the scattering medium can be temporarily modulated and induce frequency sidebands (shifted from the laser frequency by $-\omega_V$) onto the laser field. The Stokes field at frequency $\omega_S = \omega_L - \omega_V$ can beat with the laser field (at the frequency of ω_L) to produce a dynamic modulation of the total intensity. This modulated intensity coherently excites the molecule or lattice vibration ω_V at frequency $\omega_V = \omega_L - \omega_S$. These two processes reinforce one another and lead to a stronger molecule or lattice vibration and thereby stronger Stokes fields. The SRS is described by a nonlinear susceptibility of the form $\chi^{(3)}(\omega_S = \omega_S + \omega_L - \omega_L)$ (Figure 14c). For the CARS process, two laser beams at frequencies ω_1 and $\omega_2 < \omega_1$ are applied to the Raman medium, and a beam at a new frequency $\omega_{AS} = 2\omega_1 - \omega_2$ is generated as a consequence of the susceptibility $\chi^{(3)}(\omega_{AS} = \omega_1 - \omega_2 + \omega_1)$. Note that the nonlinear response experiences a resonance when the input frequencies ω_1 and ω_2 are selected so that $\omega_1 - \omega_2$ is equal to a vibrational frequency ω_V of the molecule or lattice system. Therefore, CARS has offered a very useful diagnostic tool for determining the presence of chemical species by means of their Raman vibrational modes.

3.2. Nonlinear Interactions with Metasurfaces

The intrinsic nonlinearities in natural materials are extremely weak (e.g., $\chi^{(2)} \approx 10^{-12}$ m/V, and higher-order terms are even smaller), which is intrinsically due to the phase mismatch between propagating waves in bulk NOM.[311] For efficient nonlinear frequency conversion, phase matching is therefore required in bulk NOMs. The development of efficient phase-matching techniques has attracted much attention in nonlinear photonics. Some of the popular techniques include birefringent phase matching,[324] quasi-phase matching in periodic media,[325] and modal phase matching in nonlinear optical waveguides.[326] However, because of strict phase-matching requirements, the subwavelength control of nonlinear optical fields in bulk NOMs is not possible.

Ultrathin metasurfaces with subwavelength thickness open an alternative way to achieve efficient nonlinear optical interactions without suffering the phase matching requirement. Furthermore, strong field enhancement in subwavelength meta-atoms allows shaping the nonlinear tensor and boosting the efficiency of different nonlinear processes by orders of magnitude. Strikingly, subwavelength meta-atoms additionally offer tailored control of local nonlinear emission through engineering of their morphology, resulting in different amplitude, phase, and polarization responses.[327] In the following part, we will highlight different physics of developed nonlinear nanoantennas and metasurfaces, with constituent materials ranging from artificial semiconductor media, plasmonic and dielectric materials, to 2D materials.

A new class of artificial semiconductor media, the so-called multiquantum-wells (MQWs), has been developed to exhibit strong bulk nonlinearities.[328] MQWs are composed of stacks of different III−V semiconductor layers serving as a set of potential wells and barriers for charge carriers moving in the transverse direction. Electrons and holes confined in these wells occupy discrete energy levels that can be precisely engineered by controlling the layer thickness using modern semiconductor growth technology. MQWs enable the use of smaller volumes for the nonlinear processes, significantly relaxing phase-matching requirements. However, a limiting factor of using MQWs for the nonlinear light control is that the transitions are polarized in the direction perpendicular to the layers, and therefore they are not accessible by plane waves at normal incidence. To facilitate the coupling of normally impinging light into longitudinal electric fields within MQWs, the use of plasmonic nanoantennas and metasurfaces on top of MQWs has been proposed. As an example, asymmetric gold cross nanoantennas on top of a MQW heterostructure enable efficient light coupling to intersubband transitions in MQWs with SHG efficiency of almost 2×10^{-6} using a pump intensity of only 15 kW cm^{-2}, exhibiting orders of magnitude enhanced SHG efficiency (Figure 15a).[328]

Instead of stacking multiple layers in MQWs, another promising and rapidly growing field targeting efficient nonlinear generation is the use of ultrathin metasurfaces. Unlike 3D bulk NOMs, nonlinear metasurfaces can exhibit strong nonlinear optical responses at ultrathin thicknesses (much smaller than the operating wavelengths), removing the phase-matching requirement. Surface plasmons supported at metal−dielectric interfaces offer an efficient approach for enhancing nonlinear light−matter interactions due to the strong light confinement. The shape of plasmonic structures can be tailored to resonantly enhance light−matter interactions at different frequencies, boosting the efficiency of nonlinear generation.[329] Like the case of bulk NOMs, second-order nonlinear effects in metasurfaces, such as SHG, are subject to the same symmetry constraints.

The effective nonlinear response of the metasurface is proportional to the spatial overlap integral among fields excited in the structure at pump and harmonic frequencies with specific polarization combinations, weighed by the local nonlinear susceptibility tensor and averaged over the meta-atom (unit cell of a metasurface) volume V:[330,331]

$$\chi_{lmn}^{(2)} = \frac{1}{V} \sum_{ijk} \int_V \chi_{ijk}^{(2)}(r) \frac{E_{i(l)}^{2\omega}(r) E_{j(m)}^{\omega}(r) E_{k(n)}^{\omega}(r)}{E_{inc,l}^{2\omega} E_{inc,m}^{\omega} E_{inc,n}^{\omega}} \, \mathrm{d}^3 r$$

$$(3.11)$$

where $E_{j(m)}{}^{\omega}$ is the j-polarized component of the field excited in a metasurface by a m-polarized incident beam $E_{inc}{}^{\omega}$. It is evident from eq 3.11 that, to maximize the SHG response, the structure must provide strong field enhancement at both fundamental (ω) and harmonic (2ω) frequencies. Similar expressions can be derived for other nonlinear processes. Therefore, to achieve efficient nonlinear mode conversion, it is necessary to ensure good field overlap between the generated nonlinear local field and the fundamental mode. When two or more plasmonic nanoantennas are in proximity, it is possible to harness the mode coupling and overlap for strong nonlinear interactions. In this context, various plasmonic nanostructures, such as split-ring resonators,[332] L-shaped,[333] and G-shaped nanoantennas,[334] have been used to achieve strong nonlinear responses. As an example, Figure 15b shows a plasmonic structure that consists of multiple coupled resonators.[335] When the disk dipoles (blue arrows in Figure 15b) are positioned in a noncentrosymmetric arrangement, constructive interference between them allows an enhanced SHG emission, which can be turned into a dark mode when the structure is in a centrosymmetric configuration. However, plasmonic nanoantennas have several disadvantages limiting their applications for nonlinear photonics, including high dissipative losses and inevitable thermal heating that could result in low optical damage thresholds.

To circumvent the constraints in plasmonic structures, nonlinear metasurfaces made of pure dielectric materials have been explored. The use of all-dielectric metasurfaces supporting Mie-type resonances, with much higher pump field intensities, provides a promising route to obtain higher nonlinear conversion efficiencies.[336] Silicon metasurfaces have been developed to generate highly efficient THG signals (with a conversion efficiency of 0.9×10^{-7}) through exploiting both the electric and the magnetic Mie resonances in silicon meta-atoms (Figure 15c).[337] Unlike plasmonic nanostructures, the electric field confined in dielectric resonators is not limited to the surface. Even though the electric field enhancement inside dielectric resonators is typically smaller than in plasmonic structures, an overall enhancement factor could be larger, due to the fact that the nonlinear susceptibility tensor in eq 3.11 is a volume-based integration.

Apart from Mie resonances, Fano resonances provide an alternative approach to enhancing light−matter interactions and nonlinearities. At the Fano resonance frequency, the near field of the resonant nanostructure is enhanced via the destructive interference of resonant and nonresonant modes, leading to a typical nonsymmetrical dip in the scattering spectrum. A Fano-resonant silicon metasurface was recently developed to show strong field enhancement within the volume of the silicon resonator while minimizing TPA. Figure 15d shows a Fano-resonant metasurface consisting of resonant silicon nanodisks that provide highly resonant dark modes, and silicon nanoslits supporting a bright mode.[102] This Fano-resonant metasurface realized strong THG with measured conversion efficiency of 1.2 $\times 10^{-6}$ and an average pump power of 50 mW at a peak pump intensity of 3.2 GW/cm^2.[330]

High-index dielectric nanostructures can support other unusual electromagnetic scattering modes. For instance, anapole modes have been produced based on the excitation of both electric and toroidal dipole moments, supported by different dielectric nanostructures. The term anapole means "without poles" in Greek, and it is characterized by a specific state that supports zero net dipolar radiation. The dramatically reduced scattering in excited anapole modes could significantly enhance

the local field confinement and boost the nonlinearities. Figure 15e presents an example of a germanium anapole nanodisk exhibiting strong THG signals, with a measured THG conversion efficiency of around 10^{-4} for 1 μW (15 GW/cm^2) pump power.[338]

Enhanced SHG was also observed in a single AlGaAs cylindrical resonator that supports high-Q factor BICs on a silica/indium tin oxide (ITO)/silica substrate (Figure 15f).[61] In this structure, ITO features an epsilon-near-zero condition at around 1.2 μm, acting as a conductor (insulator) above (below) this wavelength. A quasi-BIC resonance was obtained at 1.57 μm through the interference between magnetic dipolar modes in the strong coupling regime. At the SHG wavelength, ITO behaves like glass, enabling collection of the radiated light both in the forward and backward directions. To maximize the coupling of the pump beam to the quasi-BIC, azimuthally polarized incident light was used to better match the field profile of the excited quasi-BIC mode. The SHG process produced a conversion efficiency of 1×10^{-4} at a peak pump intensity of 0.07 GW/cm^2.[61]

Another emerging class of nonlinear media are 2D materials, for instance single- or multilayer graphene, TMDs, MoS$_2$, MoSe$_2$, hexagonal boron nitride, and black phosphorus.[339] These atomically thin structures can have large nonlinear coefficients, potentially being able to replace conventional NOMs in integrated photonic systems. Recently, hybridizing metasurfaces with 2D materials have been demonstrated to exhibit advanced light−matter interactions and enhanced nonlinearities (see section 2.2.3). In this context, TMDs have been integrated with metasurfaces for enhanced optical nonlinearities, in which TMDs feature a direct bandgap in the visible frequency range and a large excitonic binding energy. The broken time reversal symmetry of the atomic structures in TMDs induces the opposite Berry curvatures and pseudospins in the electronic band structures, lifting the valley degeneracy and resulting in a valley-contrast absorption and emission of spin-polarized photons.[150] This inversion symmetry breaking allows the strong photonic spin-dependent SHG coupling to the interband transition in different valleys. A hybrid metasurface integrated with 2D TMDs was recently developed to address the valley excitons in the SHG emission.[340] Figure 15g presents the hybrid metasurface design, capable of coherent addressing the valleys and producing valley-contrast SHG emissions. The plasmonic metasurface underneath the TMDs layer carries the geometric phase that is spin-dependent and boosts the light−matter interaction due to its strong field confinement. This hybrid metasurface could access and pump the valleys coherently and result in SHG photons with a spin-valley-dependent geometric phase. As a result, the SHG emissions from the opposite valleys could be controllably separated and steered to different directions.[340] As another example of hybrid metasurfaces, giant SHG enhancement was observed by coupling 2D GaSe flakes to silicon metasurfaces supporting quasi-BIC mode under continuous-wave operation (Figure 15h).[114] Taking advantage of both high-Q factors and large mode areas of quasi-BICs, SHG from a GaSe flake is uniformly enhanced by nearly four orders of magnitude, offering a promising way to realize high-power coherent nonlinear light sources.[114] Various nanostructures have been developed to enhance the Raman effect. Plasmonic nanostructures were considered as the best candidates through the generation of surface plasmons,[341] but these metallic compounds suffer from strong dissipative losses reducing their Raman scattering. Recent

Table 1. SHG Performance of Different Plasmonic and Dielectric Metasurfaces[a]

material	physical mechanism	pump wavelength (nm)	pump intensity (kW/cm²)	conversion efficiency	ref
$In_{0.53}Ga_{0.47}As/Al_{0.48}In_{0.52}As$	MQWs	8064.52	15	2×10^{-6}	328
$In_{0.53}Ga_{0.47}As/Al_{0.48}In_{0.52}As$	MQWs	~10 000	15	7.5×10^{-4}	354
$In_{0.53}Ga_{0.47}As/Al_{0.52}In_{0.48}As$	MQWs	7800	11	1.5×10^{-4}	355
$Al_{0.18}Ga_{0.82}As$	Mie resonance	1550	1600	10^{-5}	356
AlGaAs-on-AlOx	Mie resonance	1554	1600	7×10^{-5}	357
GaAs	Mie resonance	1020	3400	2×10^{-5}	358
$LiNbO_3$	Mie resonance	1550	4300	10^{-6}	359
alternating Au and ZnO layers	hyperbolic metamaterials	800−1300		1.13×10^{-6}	360
AlGaAs	quasi-BIC resonance	1570	70	10^{-4}	61
ε-GaSe flake	quasi-BIC resonance	1331.8			114

[a]Conversion efficiency is defined as $\eta_{SHG} = P_{SHG}/P_{pump}$, where P_{SHG} and P_{pump} denote the power of the SHG signal and the input power, respectively.

advances in subwavelength dielectric resonators pave the way toward low-loss Raman scattering via all-dielectric nanostructures.[61] Different-shaped high-index dielectric nanostructures, such as spheres,[342] disks,[343] octahedral,[344] and even irregular shapes,[345] have been used to excite the Raman scattering through their Mie resonances. For instance, an experimental 140-fold enhancement of the Raman intensity has been observed in silicon nanoparticles, due to the excitation of the magnetic dipole resonance.[346] In addition to the Mie resonance, the anapole state of thin silicon nanodisks has been demonstrated to achieve an 80-fold enhancement of the Raman scattering, in which the toroidal and electric dipole moments interfere destructively in the far-field, leading to the generation of an optically dark anapole state.[343] For those interested in more dielectric structures used for enhancing the Raman scattering, comprehensive reviews have been written.[347,348]

Particularly relevant for the field of quantum optics is the second-order process known as spontaneous parametric down-conversion (SPDC), which is in the present days the most versatile method of generating twin photons over a broad spectral range. Twin photons (TPs) can be used as a heralded source of single photons[349] as well as to create entangled photons states in a variety of degrees of freedom, in discrete[350] and continuous variables.[351] The implementation of SPDC normally relies on the use of nonlinear crystals like β-barium borate (β-BBO), exploiting the second-order nonlinearity of such material.[352] Depending on the specific application of the TPs generated by SPDC, β-BBO crystals with thicknesses ranging from some millimeters down to a few hundreds of micrometers are used. In any case, the fact that the generation of the TPs is a random process that can happen at any place along the crystal, there is an uncertainty in the moment when the TPs are created, which can lead to experimental difficulties. In this framework, the use of ultrathin metasurfaces may allow the generation of TPs at ultrashort time scales. Moreover, the ultrathin characteristic of these metasurfaces mitigates one problem of the canonical SPDC approach using thick crystals, which is the phase matching: in such ultrathin materials phase matching is automatically satisfied, leading to the observation of SPDC across an order of magnitude larger spectral range as compared with those obtained using the traditional SPDC implementation method. A delightful perspective paper discusses the use of metasurfaces for enhancing the performance of important elements for quantum optics technology, like sources of quantum light, single photon manipulation, and nonclassical photon state excitation and detection with quantum

light.[353] To provide a more direct comparison of previous metasurfaces developed for enhancing the SHG and THG nonlinear processes, with respect to the used materials, physical mechanisms, pump wavelengths and intensities, and nonlinear conversion efficiencies, here we summarize their metasurface performance in Tables 1 and 2, respectively.

Table 2. THG Performance of Different Plasmonic Dielectric Metasurfaces[a]

material	physical mechanism	pump wavelength (nm)	pump intensity (kW/cm²)	conversion efficiency	ref
Si	Mie resonance	1260	5000	9×10^{-8}	337
Si	Fano resonance	1280 and 1340	5000	10^{-6}	361
Si	Fano resonance	1350	3200	1.2×10^{-6}	102
Ge	anapole excitation	1650	15 000	$\sim10^{-4}$	338
Si	quasi-BIC resonance	1400 to 1460		10^{-6}	362
Si	quasi-BIC resonance	1550		10^{-7}	363
ZnO on Au	quasi-BIC resonance	1060	11 950	0.11	364

[a]Conversion efficiency is defined as $\eta_{SHG} = P_{SHG}/P_{pump}$, where P_{SHG} and P_{pump} denote the power of the SHG signal and the input power, respectively.

Having discussed the basics of metasurface-assisted photon−photon nonlinear energy conversion processes, in what follows we now focus on a technologically relevant application of such nonlinear processes.

3.3. Metasurfaces for Enhancing Upconversion and Quantum Cutting

From the point of view of applications and extending the discussion introduced in the previous section, two very relevant photon−photon energy conversion processes are the frequency (or energy) upconversion (UC) and quantum cutting (QC). These processes normally involve changes in the populations of electronic (and vibronic) states, thus being incoherent, which differs them from the processes discussed in the previous two sections. In what follows, we introduce the physical origins and mechanisms leading to UC and QC and discuss how metasurfaces can enhance the efficiency of such incoherent nonlinear photon−photon conversion processes.
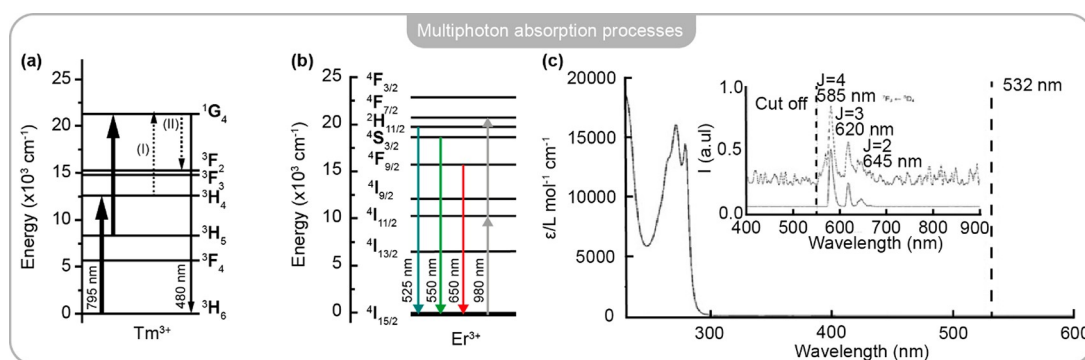
Figure 16. Examples of multiphoton absorption processes. (a) Sequential two photon absorption in Tm^{3+} ions pumped at 795 nm in a tellurite glass. (b) Resonant two-photon absorption in Er^{3+} ions when pumped at 980 nm in hafnium oxide nanocrystals. (c) Absorption spectrum of Tb^{3+} ions in a crystallized protein excited at 532 nm, where the sample does not present any absorption feature from 300 nm on. Inset: luminescence spectrum due to two-photon absorption in an aqueous solution of the protein hosting the Tb^{3+} ions. (a) Adapted with permission from ref 373. Copyright 2002 AIP Publishing. (b) Adapted with permission from ref 374. Copyright 2010 AIP Publishing. (c) Adapted with permission from ref 375. Copyright 2007 Wiley-VCH GmbH.

3.3.1. Upconversion. In an UC process, photons are emitted by the sample (e.g., nanoparticles of a given material or a metasurface) having energies larger than the energy of the excitation photons. This emission of higher energetic photons can be the consequence of various kinds of physical mechanisms, like anti-Stokes Raman Scattering, which is a phonon-assisted photon absorption process, and multiphoton absorption.[365] UC processes can be particularly useful in photovoltaics/solar cells and biological imaging applications. In the first case, since a significant amount of energy in the solar spectrum is found in the IR spectral range and the materials used to fabricate such devices present highest efficiencies in the visible, one way of increasing the efficiency of such devices is converting the "wasted" infrared photons into visible photons. In biological imaging, the use of UC processes is very interesting because using IR for illumination allows a deeper penetration in biological tissues, while the detection of light in the visible range allows the use of high efficiency photodetectors upon a virtually zero background. As a nonlinear optical process, its efficiency strongly depends on the excitation power, which is particularly critical when using continuous wave light, like the one coming from the sun. Thus, UC enhancement mechanisms can be decisive in enabling technologies based on photon−photon conversion through UC.

Applications of phonon-assisted UC processes can be found, among others, in solid state optical thermometry in bulk[366] and in nanoscale[367,368] deep tissue superresolution (sub 50 nm) imaging,[369] and optical refrigeration.[370] In the first case, ions in a host matrix can be promoted from the ground state to an excited electronic state *via* linear optical absorption. This is then followed by the absorption of lattice phonons, which can then bridge the gap to a higher lying, thermally coupled energy level from which fluorescence can be emitted. It is found that the fluorescence intensity is temperature dependent. This can be understood by remembering that the phonon population in the host matrix increases as the sample temperature increases and that the phonon absorption probability depends on the phononic population density. By weakly exciting the system, in a perturbative manner, it is then possible to use the phonon-assisted UC fluorescence intensity as a thermometric quantity. The situation changes however when the excitation rates are made sufficiently high. If the population of ions in the excited state is large enough, which can for example be achieved under strong pumping conditions, the phonon annihilation rates due

to the promotion of the ions to the thermally coupled state can be so large that the host matrix temperature decreases: thermal energy is converted then in optical energy, which is dissipated in the form of fluorescence. This is the basic idea of optical refrigeration. UC in nanoscale finds many other applications, including investigations of *in vitro* and *in vivo* biological systems[371] and cancer treatment, can be found in ref 372.

Multiphoton UC processes are intrinsically nonlinear and as such in principle occur less probably than linear optical processes. Therefore, the usefulness of structures that can enhance such processes, like metasurfaces, becomes evident. The lowest number of absorbed excitation photons in a multiphoton UC process is two, in which two photons of an excitation beam get converted into one higher energetic photon. The results can be either the emission of fluorescence (when one has changes in the populations of the involved energy levels, like the TPA process), which is incoherent, schematized in Figure 13c, or the emission of parametrically generated radiation (when there are no population changes, like in second harmonic generation and sum frequency generation, see Figure 13b, which is a coherent process).

Let us consider three processes involving changes in the electronic states' populations. In the first one, the so-called sequential two-photon absorption, which is schematized in Figure 16a, the electrons are first promoted from the ground state to an excited electronic state by absorbing a photon from the excitation beam. Then the electrons can nonradiatively relax to a close lower-lying excited state, from which they can absorb another photon of the excitation beam, ending up in a high energetic state, and then UC fluorescence can be emitted from it. The energy difference between the ground state and the higher lying intermediate state and between the lower lying intermediate state and the highly energetic state from which the UC radiation is emitted is in the ideal case the same, and close to the excitation photons' energy. Such a process can always happen when using continuous wave (CW) lasers as excitation sources, like the one investigated in ref 373. However, in experiments using pulsed lasers, the process will be possible only if the nonradiative transition between the two intermediate states is fast, in the sense that the inverse of the nonradiative relaxation rate must be smaller than the pulse duration. In time-resolved experiments, the rise time of the UC signal is influenced by the nonradiative transition characteristic time. The second
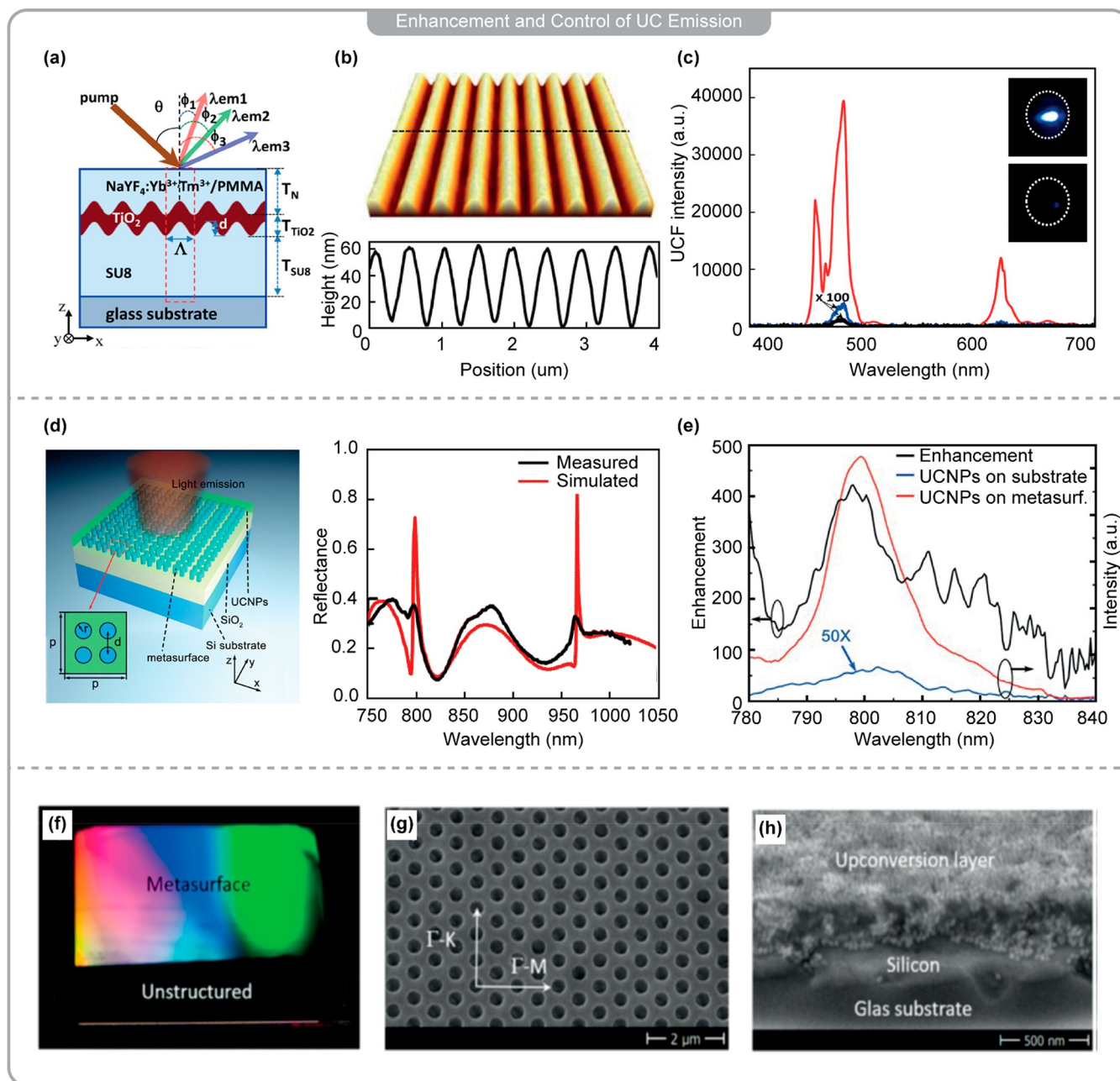
Figure 17. Using metasurfaces for enhancing UC processes. (a) Scheme of a 1D rare-earth-doped polymer resonant waveguide grating. (b) AFM image of the TiO_2 resonant waveguide grating used as a substrate for supporting the doped polymer film. The spatial period and the groove depth of the grating are 466 and 60 ± 5 nm, respectively (bottom). (c) UC spectra of the rare-earth-doped polymer under different excitation conditions: on-resonance with the grating (red line), off-resonance (blue line), and from a nonpatterned area (black line). Insets are optical images of UC fluorescence emitted by the sample when illuminating the excitation beam under on-resonance (upper inset) and off-resonance (lower inset) conditions, respectively. (d) Left: Scheme of a dual resonance metasurface with unit cells based on metamolecules composed of four silicon cylinders (period $p =$ 520 nm, each cylinder 270 nm high, radius 68 nm, and centers 200 nm apart from each other). The metamolecules are etched on a 2 mm thick SiO_2 layer (gray color), which in turn is deposited on a silicon substrate (cobalt blue color). The UC nanoparticles are dispersed on the metasurface (greenish color). Right: the metasurface simulated (red) and measured (black) reflectance spectra, showing peaks which coincide with the excitation and emission wavelengths used in the experiment. (e) Measured UC fluorescence from the nanoparticles on the metasurface (red) and on the substrate (blue). The calculated fluorescence enhancement (black) is also shown. Compare with the reflectance spectra shown in the right panel of part e). (f) Photo of a Si metasurface on 5 cm × 5 cm glass substrate (shiny part) with the unstructured reference region (edges). (g) SEM image of the metasurface with indicated high-symmetry directions. (h) SEM image of the metasurface coated with a PMMA film containing UC nanoparticles. (a–c) Adapted with permission from ref 377. Copyright 2015 American Chemical Society. (d, e) Adapted with permission from ref 383. Copyright 2019 The Royal Society of Chemistry. (f–h) Adapted with permission from ref 384. Copyright 2020 American Chemical Society.

process, called resonant two-photon absorption, is sketched in Figure 16b and differs from the first one due to the absence of one of the intermediate states. In this case, the absorption of an

excitation photon promotes the electron from the ground state to the single intermediate excited state and from there a second excitation photon is immediately absorbed taking the electron to

the highest energetic state, from which the UC fluorescence is emitted.[374] The energy gap between the ground state and the intermediate excited state and between this state and the highest energetic state is in the ideal case the same and again close the excitation photons' energy. In time-resolved measurements, the rise time of such an UC signal is shorter than for the process previously described. Besides this, due to the absence of any intermediate steps when promoting the electrons between the two intermediate excited states, this process is less dependent on the use of continuous wave or pulsed lasers to occur. The third process is the two-photon absorption, which is characterized by the absence of intermediate states in the electronic transition from the ground state to the higher energetic, emitter state,[375] see Figure 16c. The energy gap between these states is close to twice the energy of the pump photons. Since this is a nonresonant transition, it can only happen within a very short period of time, as allowed by the Heisenberg uncertainty principle and thus can only be observed with the use of ultrashort, high intensity laser pulses as excitation source. In the solid-state phase, these kinds of nonlinear optical processes are very easy to observe in systems doped with rare-earth trivalent ions since they present atomic-like optical transitions giving origin to relatively narrow band light emission.

Higher-order UC processes are less common to find, and their complexity involves the occurrence of resonant, nonresonant, phonon-assisted and energy transfer processes along the excitation path, as exemplified in ref 376 for a three-photon excitation scheme. Metasurfaces made from high permittivity dielectric materials, not suffering from Joule losses[280,377−379] (Figure 17a−c) and presenting electric and magnetic multipolar resonances can be used to design hybrid systems originating strong localized fields,[380−382] which then lead to dramatic enhancement of UC efficiencies due to the nonlinear nature of such a process.

They also allow for applications demanding large active areas. In ref 383, a metasurface based on silicon cylinders that are distributed on a lattice of silicon cylinder clusters and which support electric and magnetic dipole Mie resonances is investigated. For specific distances between the silicon cylinders and the clusters, lattice resonances can lead to the enhancement of both kinds of resonances simultaneously, like schematized in Figure 17d and e. Sodium−yttrium fluoride (NaYF$_4$) nanocrystals (average diameter: 70 nm) codoped with Yb^{3+} and Tm^{3+} ions were chosen for probing effects of the metasurface on the UC emission of the nanoparticles. In such system, due to the fact that Yb^{3+} has a very large absorption cross-section at 965 nm, it is used as sensitizer for absorbing pump photons at 970−980 nm and transfer energy to the Tm^{3+} ions, from which UC fluorescence bands around different wavelengths can be observed, with a very strong one at 800 nm.[385] Numerical simulations were performed to tune the resonances to the excitation wavelength at 965 nm (the pump wavelength resonant to the Yb^{3+} ions absorption band) and the UC emission band peak at 800 nm from Tm^{3+} ions, resulting in near-field enhancement at these wavelengths. The corresponding metasurface was fabricated and microphotoluminescence ensemble experiments performed with a control system, the nanocrystals on a substrate, and with the nanocrystals on the metasurface, ensuring similar coverage rates. It was then found that the overall UC emission enhancement was about 400 when using the metasurface, which also played a role in changing the spatial emission pattern, increasing the system's collection efficiency.

In another work, Wuerth et al. used nanoimprinting methods to fabricate a metasurface consisting of a silicon layer with holes (325 nm in diameter) arranged in a hexagonal pattern (lattice constant 600 nm).[384] UC experiments were performed exciting at 975 nm ensembles of ∼25 nm in diameter NaYF$_4$ nanocrystals codoped with Yb^{3+} and Er^{3+}, within the strong absorption band of the sensitizer Yb^{3+} ions (Figure 17f−h).

This is a classical host-dopant combination used to investigate UC processes for many applications, like solar cells[386] and microthermometry.[387] In such systems, the role played by the Yb^{3+} ions, like in the previous case, is to efficiently absorb pump photons around 975 nm and transfer the energy to the Er^{3+} ions. These present strong UC emission bands in the green region, around 525 and 550 nm, besides a very strong band in the red, at 660 nm. White light transmission measurements were used to locate the resonances provided by the metasurface. Along determined directions of the lattice in k-space, field enhancements around 30 have been observed for the excitation wavelength with TM polarization. A capping layer of the nanocrystals in polymethylmethacrylate (PMMA) could be deposited with different thicknesses on the metasurface. A total enhancement of 10^3 of UC emission integrated over the three bands has been observed for nanocrystals capping layers thinner than 100 nm, evidencing the near-field enhancement generated by the metasurface. Moreover, this work shows that the distribution of enhanced electric fields is inhomogeneous within the capping layers and that the green and red UC emissions can be used as a field sensor to locally measure local field energies.

As for the majority of rare-earth ions, the absorption cross-sections of Er^{3+} transitions are small as compared to, for example, those of organic dye molecules. As mentioned previously, codoping the matrix with similar ions, like Yb^{3+}, can be a good strategy for increasing the excitation rates in such systems. However, the wavelength range in which this is advantageous is restricted to the bandwidth of the Yb^{3+} ions absorption profile. At some technologically relevant wavelengths, as ∼1550 nm, important for telecom and excitation of biological tissues in the third biological window, this codoping strategy is not effective and the Er^{3+} ions need to be directly excited. A metasurface similar to the one described previously was used in ref 388 for enhancing the UC emission of NaYF$_4$ nanocrystals, this time doped only with Er^{3+} ions. Its design followed the holes (diameter: 400 nm) hexagonal array (lattice constant: 1000 nm) on a silicon layer (thickness: 53 nm), resulting in the appearance of resonances at 1551 nm, coincident with the excitation wavelength. An integrated UC enhancement by a factor of 2400 has been observed in relation to the experiment performed under the same condition, but on a nonstructured substrate. In attempting to boost the local field enhancement, aiming at even stronger UC emissions, the same group designed another kind of metasurface, a double layer stack formed by a hexagonal lattice photonic crystal slab integrated with a structure very similar to the metasurface used in the previous case.[389] Following the same approach, the stack metasurface was coated with a PDMS film containing Yb^{3+}/Er^{3+} codoped NaYF$_4$ nanocrystals. Performing transmission spectroscopy with the coated and uncoated metasurfaces, intense spectra were recorded. A fraction of the observed resonances was associated with the Rayleigh-Wood anomaly provided by the metastructure, absent in the single layer metasurface investigated in the previous work, which presented the strongest field enhancement according to numerical simulations. Upon similar excitation conditions as in ref 388, UC emission
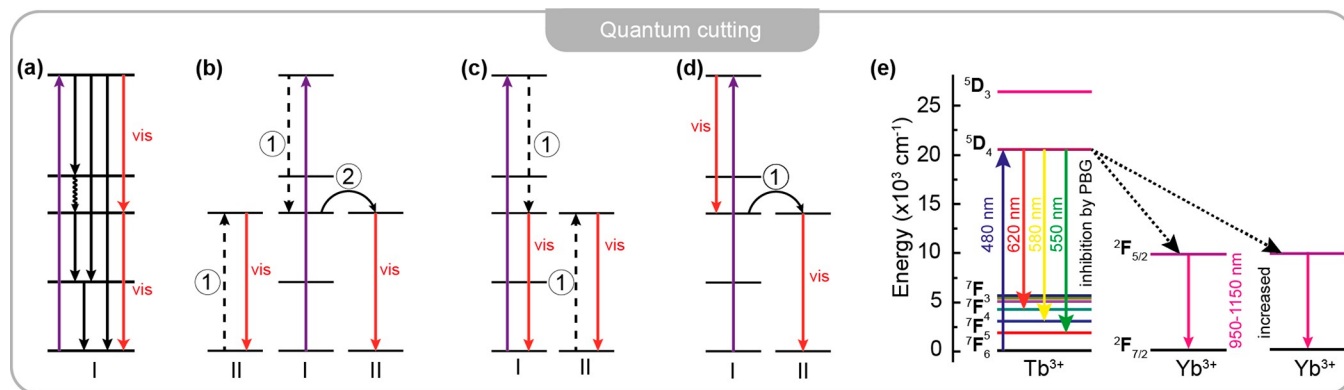
Figure 18. Energy level diagrams for two types of lanthanide ions for illustrating the phenomenon of QC. Type I is an ion for which emission from a high energy level can occur, while type II is an ion to which energy transfer takes place. (a) QC on the single ion I by the sequential emission of two visible photons. (b) QC by a two-step energy transfer. (c, d) Two QC possibilities that involve only one energy transfer step from ion I to ion II. (e) Simplified energy level scheme of the cooperative QC process in a Tb^{3+}/Yb^{3+} doped system. (a–d) Adapted with permission from ref 391. Copyright 1999 AAAS. (e) Adapted with permission from ref 394. Copyright 2016 Science Direct.

intensities enhanced by a factor of 2.7 as compared to the single layer metasurface have been recorded, this being attributed to the synergetic effects of the enhanced local fields and light trapping by the resonant modes.

3.3.2. Quantum Cutting. In lighting and display systems, the energy of a vacuum UV photon is more than twice that of a visible photon, and thus, it is possible to achieve the emission of two photons in the visible range from the absorption of a vacuum UV photon.[390] QC is an energy downconversion process, in which a high energetic photon is converted by a nonlinear material into two photons of lower energies.[391] A typical QC process happens when a high-energy photon gets absorbed by a sensitizer fluorophore, which undergoes an electronic transition from the ground to the excited state. Then, *via* dipole–dipole interaction, this sensitizer transfers its energy to two acceptor fluorophores A and B, ending up again in the ground state. As a result of the energy transfer process, the acceptors A and B then get excited from their ground states to their excited states, from which these acceptors can emit less energetic photons. A scheme with subtle variations of this main concept is depicted in Figure 18a–d. The final result is that one incident photon is converted into two emitted photons with energies lying within the sensitizer transparency window, virtually eliminating reabsorption losses. The process is efficient when the energy of the incident photon is equal to the sum of the energies of the excited states from the acceptor fluorophores A and B. The QC process happens on a picosecond time scale or less, as determined by transient absorption studies.[393]

Metal-halide perovskite nanocrystals, with structure $CsPbX_3$ (X = Cl, Br, I), have been extensively studied in the past decade due to their broad absorption spectra, spectrally narrow photoluminescence presenting high quantum yields and wide bandgap tunability, achieved by exploiting quantum confinement effects *via* nanocrystal size control and composition.[395,396] These characteristics have made these crystals a very promising material for photon–photon energy conversion.

Besides this, lanthanide ions have been intensively explored as optically active dopants in inorganic crystal hosts for decades. Doping such ions into traditional semiconductor nanocrystals, such as CdSe, is a challenging task because of the tetrahedral coordination in these materials. Fortunately, $CsPbX_3$ (X = Cl, Br, I) perovskite nanocrystals present the octahedral coordination suitable for hosting lanthanide ions. Because of the

extremely simple energy level structure of its optically active electrons, the ground state $^2F_{5/2}$ and the single excited state $^2F_{7/2}$, and the energy difference between these levels which matches well with the band gap of 1.12 eV of silicon, Yb^{3+} ions were chosen as the most proper luminescent center to achieve QC to the near-infrared. For energy losses reduction in silicon photon converting cells, a suitable Yb^{3+} doped QC layer overlying the device could efficiently absorb the photon with a wavelength of shorter than 550 nm (twice energy gap) and achieve two near-infrared photon emission with exactly the energy of the band gap. Colloidal Yb^{3+}-doped $CsPbCl_3$ halide perovskite nanocrystals have demonstrated very high photoluminescence quantum yields in the near-infrared, approaching the theoretical limit of 200%, attributed to a picosecond quantum-cutting process in which one photon absorbed by the nanocrystal generates two photons emitted by the Yb^{3+} dopants.[397] The quantum yield of the perovskite excitonic for undoped samples is ~20% and decreases sharply to <1% upon increasing the Yb^{3+} concentration to ~0.7%, indicating an efficient energy transfer process from the excitons to the Yb^{3+} ions and confirming the QC mechanism.

There are several reports in the literature on QC in undoped and doped perovskites nanocrystals. However, studies on microstructure- or metasurface-assisted QC are much rarer, which represents an opportunity for improving the efficiency of such devices using this approach. In ref 394, an inverse opal photonic crystals structure was fabricated using $Yb^{3+}:Tb^{3+}$ codoped YPO_4, prepared by sol–gel technique with self-assemble method (Figure 19). The energy difference between the $Yb^{3+} {}^2F_{5/2}$ and $^2F_{7/2}$ levels is approximately half of the energy difference between the $Tb^{3+} {}^5D_4$ and $^7F_6$ levels, and the electronic transitions in Yb^{3+} do not find any resonances among the possible electronic transition in Tb^{3+} ions. The fluorescence quenching in Tb^{3+} ions when the matrix was doped with Yb^{3+} led to an enhancement of the fluorescence emitted by the last ones, indicating an efficient energy transfer mechanism, resulting in a QC process as schematized in Figure 18e. With the influence of the photonic band gap presented by the inverse opal structure, the QC phenomenon was investigated in spectrally and time-resolved experiments. The results show that, when the spontaneous emission of the sensitizer Tb^{3+} ions is inhibited by the photonic band gap, the QC quantum efficiency could be enhanced.
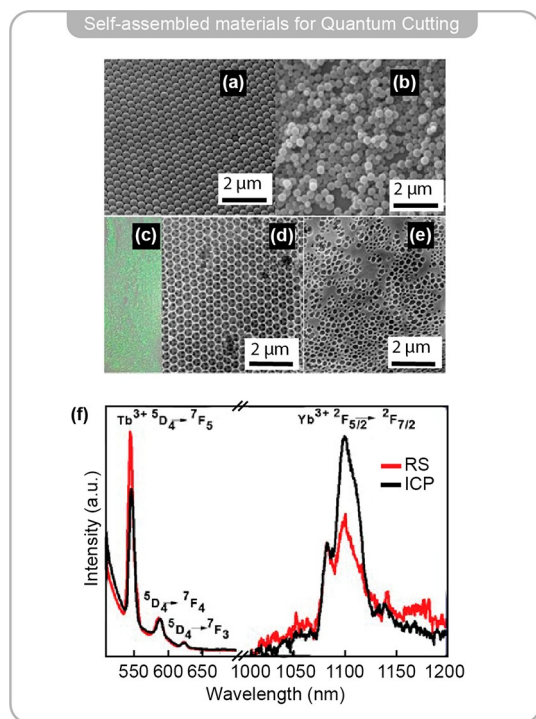
Figure 19. Use of a self-assembled metamaterial, an inverse opal, for enhancing a QC process. (a, b) SEM images of (a) unitary opal templates constructed with polystyrene microspheres 410 nm in diameter and (b) binary templates constructed with polystyrene microspheres 220 and 410 nm in diameter. (c) Optical micrograph of the fabricated inverse opal photonic crystal. (d, e) SEM images of the inverted opal crystal and a disordered structure sample. (f) Emission spectra of the opal photonic crystal (IPC) and the disordered structure samples (RS) under excitation at 480 nm. Adapted with permission from ref 394. Copyright 2016 Science Direct.

We finish by highlighting a technologically very important application of metasurface-enhanced UC and QC processes. In the context of solar cells and photovoltaics, the usefulness of such higher-order processes is very promising. In the case of UC, these processes allow to convert photons with energies in the NIR region and beyond, in which a large fraction of the solar spectrum is located, to the visible range. This is important because NIR photons have low energies and thus many kinds of photodetectors and photon absorbing systems are transparent for them. As a result, without the use of efficient UC processes, the photons in the NIR coming from the sun are often wasted. On the other hand, QC does not only provide the possibility of bringing UV and deep UV light from solar radiation to the visible spectral region, where photodetectors are more efficient, but also represents a way of enhancing the quantum yield of photoluminescent systems to values beyond 100%. Moreover, the common fluorophores presently used in these devices, such as organic dyes and colloidal quantum dots, often suffer from reabsorption loss of photoluminescence photons along the waveguiding path, lowering the internal quantum efficiency of the device.[392] In the literature, concrete applications of metasurface-enhanced UC or QC processes in solar cells and photovoltaics are still not reported; however, they represent a promising research niche in a world more and more concerned about the generation of green energy.

3.4. Section Summary

To summarize, this section has reviewed different physical processes that involve photon−photon energy conversion.

1. The fundamentals of coherent nonlinear optical processes that involve second- and third-order susceptibilities have been discussed.

2. The second-order nonlinear effects including SHG, SFG, and DFG are principally illustrated. The intensity-dependent refractive index and absorption changes related to the SPM and TPA processes are illustrated.
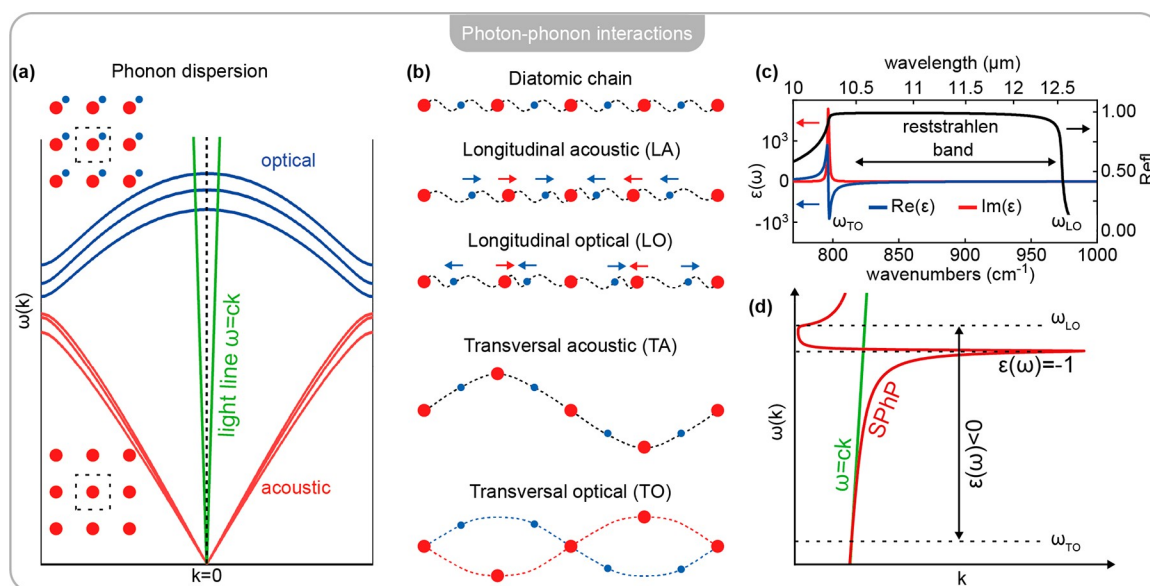
Figure 20. Basics of photon−phonon interactions. (a) Sketch of the dispersion relations for phonons in a 3D lattice, consisting of three acoustic branches (red) and three optical branches (blue). Optical branches are present only for lattices with more than one atom in the unit cell. The light line intersects optical phonons close to the $k = 0$ point. (b) Sketch of the four phonon modes existing for a diatomic 1D chain free to move in a 2D space. (c) Real (blue) and Imaginary (red) parts of the dielectric function for SiC, a polar dielectric. In the Reststrahlen band, $\varepsilon_1 < 0$ and the reflectivity approaches unity. (d) Dispersion diagram for SPhPs in a semi-infinite SiC slab together with the light line.

3. The third-order nonlinear effects including SPM, THG, and FWM that are not bound by the symmetry constraints are principally illustrated.

4. Enhanced nonlinear optical properties have been experimentally achieved from different nanoantennas and metasurfaces including plasmonic MQW metasurfaces, plasmonic nanoantennas, all-dielectric Mie-resonance nanoantennas, Fano-resonant dielectric metasurfaces, anapole-mode metasurfaces, BIC dielectric metasurfaces, a synthetic Au−WS$_2$ metasurface, and a 2D material-coupled BIC metasurface.

5. Some applications of UC and QC in solar cells and photovoltaics have been shown, in which the efficiency of these processes is boosted by the use of metasurfaces and metamaterials.

4. PHOTON−PHONON ENERGY CONVERSION

In this section, we summarize recent research involving energy transfer between photons and phonons (i.e., the lattice excitation states in a crystal) mediated by the presence of a metasurface. Photon−phonon energy conversion is of technological relevance, for example, because thermal energy in a solid is primarily stored in phonons, and as such engineering the optical properties of a material can modify its radiative thermal emission properties, leading to applications such as daytime radiative cooling.[398] Moreover, chemically selective spectroscopic techniques, such as Raman scattering and infrared absorption, involve energy exchange between photons and phonons. Engineering the optical properties of substrates employed for enhanced spectroscopies can push their sensitivities to very low amounts of molecules. We start this section by reviewing the basic properties of phonons and the role they play in determining the specific heat of a solid. We describe mixed light-phonon states analogous to surface plasmon polaritons (SPPs), in which light strongly couples to optical phonons forming surface phonon polaritons (SPhPs). We then review applications involving thermal effects before moving to other photon−phonon interactions such as nanoantenna-assisted excitation of surface acoustic waves in solids and light−matter coupling involving the excitation of SPhPs.

Phonons are quasi-particles representing the quantum mechanical description of the collective motion of atoms in the periodic lattice of a crystal.[399] In general, two different types of phonons can be excited in a periodic arrangement of atoms, which are named acoustic and optical phonons. For a three-dimensional lattice with p atoms in the primitive cell, there are $3p$ phonon modes, out of which three are acoustic and $3(p\text{-}1)$ are optical, as shown in Figure 20a for a crystal with $p = 2$. Acoustic phonons are characterized by having a linear $\omega(k)$ dispersion around the zero-momentum point, where the slope of the linear dispersion determines the speed of sound in the material, hence the name acoustic. In lattices with more than one atom in the primitive cell, optical phonons also exist. Optical phonons are characterized by having nonzero energy at the zero-momentum point and mostly flat dispersions. Because of the linear dispersion of photons, the light line $\omega = ck$ intersects the dispersion of optical phonons, but not the acoustic phonons, as it is shown schematically in Figure 20a. Therefore, only optical phonons can directly couple to photons. Because of the small photon momentum compared to the phonon momentum, excitation of optical phonons can only occur close to the $k = 0$ point. The energy of phonons can vary from few to hundreds of

meV, lying in the mid to far-IR region of the electromagnetic spectrum.

Albeit with smaller probability, interaction between photons and phonons can also happen through inelastic scattering in which the photon can either absorb (Anti-Stokes process) or lose (Stokes process) energy to a phonon. Inelastic scattering with acoustic phonons is named "Brillouin scattering",[400,401] while inelastic scattering involving optical phonons is known as "Raman scattering".[402,403]

For a diatomic 1D chain allowed to vibrate in a 2D space, four phonon modes exist. In Figure 20b, these different modes are schematically sketched. The linear chain can support both longitudinal modes (abbreviated as LA and LO for acoustic and optical, respectively), where the displacement of the ions is in the same direction of the phonon k vector, and transverse modes (abbreviated in TA and TO for acoustic and optical respectively), where the displacement is orthogonal to the k vector direction. In a 3D lattice, for each phononic branch, there is one longitudinal and two transverse modes. Depending on the structure of the crystal, many of the $3p$ phononic branches can be energetically degenerate along lattice directions characterized by high symmetry.

In part of this photon−phonon section, we discuss thermal effects in which either a photon is emitted due to blackbody radiation or the absorption of a photon induces a temperature increase. Metasurfaces can be used to tailor both the absorption of optical energy and the emission of photons through blackbody radiation. The connection between temperature and phonon processes is justified by the fact that the specific heat of a solid at room temperature (i.e., the energy needed to increase the temperature of 1 kg of the solid by 1 K) is almost entirely determined by its phonon structure. A contribution to the specific heat due to electrons can be appreciable only in metals at very low temperatures. The turning point in which the electronic specific heat becomes smaller than the lattice specific heat is on the order of just a few Kelvins.[399] For some solids, the specific heat at room temperature is well approximated by the Dulong-Petit law, according to which each ion contributes $3k_B$ to the lattice specific heat, where k_B is the Boltzmann constant. The Dulong-Petit approximation works well when the thermal energy $k_B T$ is much larger than all the phononic energies so that all states are highly excited and the detailed phononic dispersion can be ignored. This is analogous to the high temperature limit of the quantum mechanical Bose−Einstein and Fermi distributions, where both tend to the classical Maxwell−Boltzmann behavior. The temperature above which all phononic states are highly excited is called the Debye temperature Θ_D, from the homonymous model of the lattice specific heat. For solids with no optical phonons (i.e., lead or gold, with FCC crystal structure and 1 atom per primitive cell), Θ_D is low and the Dulong-Petit law constitutes a good approximation even below room temperature.[399,404,405] Conversely, materials supporting highly energetic optical phonons (i.e., diamond or silicon, diamond crystal structure with 2 atoms in the primitive cell) are characterized by high Θ_D, which can be even greater than the melting temperature of the crystal.[399,406,407]

An interesting form of photon−phonon energy conversion is the excitation of mixed light−matter states called SPhP[408,409] analogous to SPPs at frequencies below ω_p where $\varepsilon_1(\omega) < 0$. Polar dielectrics are a class of insulators and semiconductors with strong optical phonons. Some examples are silica (SiO$_2$),[410] silicon carbide (SiC),[411] and hexagonal boron nitride (hBN)[412] for which the highly dispersive form of $\varepsilon_1(\omega)$ at the frequency of

a TO phonon leads to an $\varepsilon_1(\omega) < 0$ region, where the material behaves similarly to a metal. In Figure 20c, the dielectric function of the polar material SiC is shown together with its reflection spectra. Around the TO point, the dielectric function of an isotropic polar dielectric is well described by a single Lorentz oscillator:

$$\varepsilon(\omega) = \varepsilon_\infty\left(1 + \frac{\omega_{LO}{}^2 - \omega_{TO}{}^2}{\omega_{TO}{}^2 - \omega^2 - i\gamma\omega}\right) \tag{4.1}$$

where ω_{TO} and ω_{LO} are the frequencies of the TO and LO phonons, γ is the damping constant associated with the phonon oscillation, and ε_∞ is the high frequency permittivity. The dielectric function in Figure 20c is obtained from eq 4.1 using the following parameters: $\varepsilon_\infty = 6.6$, $\omega_{TO} = 797$ cm^{-1}, $\omega_{LO} = 973$ cm^{-1}, $\gamma = 973$ cm^{-1}.[413] The $\varepsilon_1(\omega) < 0$ region is called the Reststrahlen band and is bounded below by a TO phonon and above by a LO phonon. In the Reststrahlen band, the reflectivity of the material abruptly increases to unity, as one would expect from a metal at $\omega < \omega_p$. The Q factor at the Fröhlich condition $\varepsilon_1(\omega) = -2\varepsilon_m$ for localized phonon polaritons (LPhPs) in the mid-IR is higher than what can be achieved in the visible range by noble metals. This is because the lifetime of SPhPs is longer than for SPPs (order of ps vs order of tens of fs) due to the smaller phonon–phonon scattering rate compared to the electron–electron scattering rate governing SPP decay. In Figure 20d, the dispersion of a SPhP in a semi-infinite slab in air environment is reported. SPhPs can propagate between $\omega = \omega_{TO}$ and the frequency where $\varepsilon_1(\omega) = -1$. The $\varepsilon_1(\omega) = -1$ point is analogous to the $\omega = \omega_p/\sqrt{2}$ frequency for SPPs in vacuum, where the in-plane k vector tends to infinity if losses in the material are neglected. As shown in Figure 20d, the light line intersects the SPhP dispersion only at the ω_{TO} frequency and in the back bending region above $\varepsilon_1(\omega) = -1$ where SPhPs cannot propagate. Therefore, similar to the energy-momentum mismatch for SPPs, direct coupling to SPhPs can only be achieved in patterned surfaces[414,415] or by near-field sources with high momentum, as evanescent waves in total internal reflection[416−418] or atomic force microscopy (AFM) tips used in scanning near-field microscopes.[412,419−424] Whereas the dielectric function in metals is isotropic, polar dielectrics can exhibit different values along the three axes ε_{xx}, ε_{yy}, ε_{zz} if the crystal is anisotropic. When the dielectric function is not negative along all the three axes, only certain directions are allowed for SPhPs propagation.[425,426] This leads, for example, to hyperbolic out-of-plane SPhPs propagation in hBN,[427−430] in plane hyperbolic propagation in α-MoO$_3$,[428,431−433] and ghost phonon-polaritons in CaCO$_3$.[434]

In the following, we divide the section into two main subsections. First, we describe applications involving thermal effects, where energy is stored into phonons with many different energies. Next, we review photon–phonon coupling phenomena where phonons at specific energies are involved in the energy conversion process.

4.1. Photon-to-Heat and Heat-to-Photon Energy Conversion

4.1.1. Thermal Nanophotonics.
When a photon is absorbed by a solid, part of its energy decays in a nonradiative way into low energy acoustic phonons, increasing the temperature of the solid. The heat power density generated as a result of absorption in an antenna can be expressed as[435]

$$q(r) = \frac{\omega}{2}\varepsilon_2(\omega)\varepsilon_0\left|\overline{E}(r)\right|^2 \tag{4.2}$$

where $\varepsilon_2(\omega)$ is the imaginary part of the dielectric function of the material and $\overline{E}(r)$ the electric field distribution inside the antenna. The overall heat produced is calculated as $Q = \int_V q(r)\,dr$, where V runs over the antenna volume. A very common example of this effect is the dissipation of energy due to electron–electron scattering when an induced current is generated in a metal. This effect is known as Joule heating, and it happens whenever light interacts with a metallic antenna. At longer wavelengths in the radiofrequency range, metals behave as perfect conductors. This means that even if $\varepsilon_2(\omega)$ is large, the field does not penetrate into the material, leading to a low value for $q(r)$. Instead, Joule heating is strong at optical frequencies for plasmonic antennas as the ratio between the skin depth and the free-space wavelength δ/λ_0 strongly increases[408] and the field penetrates into the metal. Dielectric resonators are often made from high index materials with extremely small values of $\varepsilon_2(\omega)$ to obtain high Q resonances,[53,436,437] and as such the heat dissipation is practically negligible in this case. However, efficient heat generation can be achieved in critically coupled (i.e., when radiative and nonradiative losses are equal) dielectric nanoantennas.[438]

The dissipation of localized surface plasmon polaritons (LSPPs) at visible frequencies is detrimental for applications requiring small losses,[439−441] but it can be leveraged to create localized nanosources of heat. The field of research investigating heating effect from plasmonic antennas is known as "Thermoplasmonics".[435] While plasmonic nanoantennas can confine EM fields to deeply subwavelength scales and produce very localized heat sources, dielectric antennas supporting Mie resonances can be even more efficient for the light to heat energy conversion process.[442] This is because the heat generation is the integral of eq 4.2 over the antenna volume, which can be rewritten as $Q \approx \sigma\langle|E(r)|^2\rangle V_{eff}$ where $\sigma(\omega)$ is the material conductivity, $\langle|E(r)|^2\rangle$ is the average square modulus of the electric field inside the antennas, and V_{eff} the resonance mode volume. As such, dielectric particles with high mode volumes can outperform plasmonic antennas for which the conductivity $\sigma(\omega)$ is higher, but the mode volume is smaller due to the small skin depth of metals.[438,442] In this context, metasurfaces can be used to tailor the absorption properties of metals and dielectrics over large scales and control the overall temperature increase by carefully choosing the geometrical arrangement of the individual antennas. Baffou et al. showed both theoretically and experimentally that the temperature profile obtained from an illuminated square array of gold nanoparticles can transition from a localized regime to a delocalized one.[443] Depending on a single dimensionless parameter ξ_2 related to the geometrical properties of the array, the temperature profile can be either delocalized over the whole array, as shown in the left panels of Figure 21a, or localized around the single heat sources as in the right panels. ξ_2 quantifies the ratio between the temperature increase due to heating of a single nanoparticle and the temperature increase due to all the other particles in the array. $\xi_2 \propto \Delta T_0^s/\Delta T_0^{ext} = p^2/3LR$ where the subscript 0 indicates the particle at the center of the array, p is the pitch of the array, L the size of the illuminated area, and R the nanoparticles radius. In this model, Baffou et al. assumed the elements of the array to be optically uncoupled, which is usually not the case for metasurfaces, so care should be taken when applying this model to dense particle arrangements. In the same work, it was
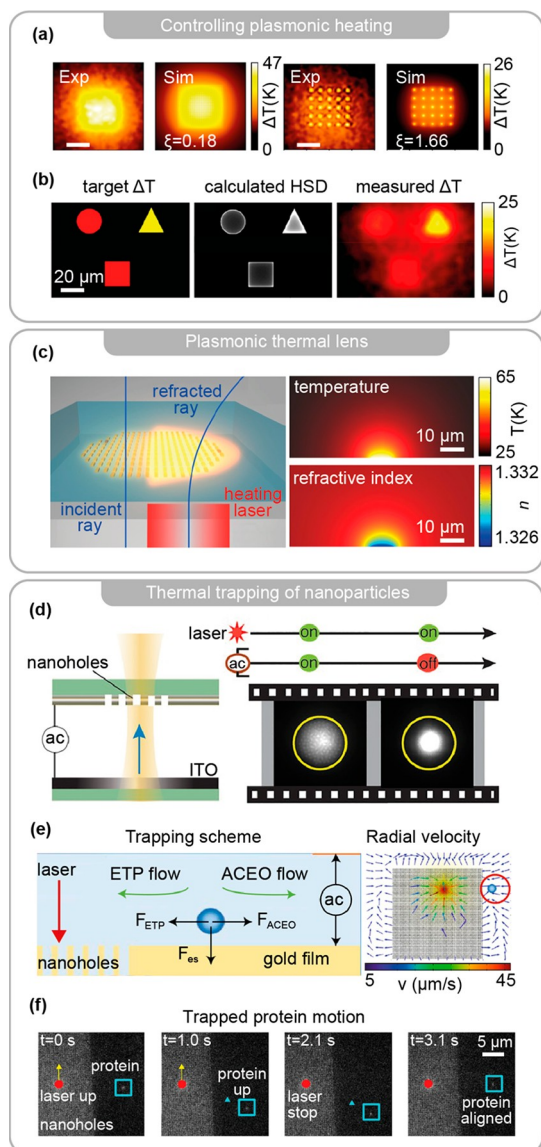
Figure 21. Metasurface-assisted thermoplasmonics. (a) Experimental (left) and simulated (right) temperature maps for a square array of gold nanoparticles under 532 nm laser illumination for two different geometries, showing that temperature profiles can be shaped with metasurfaces. (b) Engineered temperature profiles over a homogeneous array of nanoparticles. The target temperature distribution is obtained by calculating the required HDS, which is then realized by shaping the excitation wavefront with a SLM. (c) Sketch of the mechanism of the thermal lens, where light is focused due to thermoplasmonic temperature increase in the surrounding medium, together with the simulated temperature and refractive index maps around the metasurface. (d) Sketch of the device used for ETP trapping of nanoparticles. The frequency of the AC voltage can be used to tune the nanoparticles concentration as shown in the right panel. (e) Scheme of the forces involved in trapping of nanoparticles far away from the laser spot by combining ETP and ACEO effects together with a plot of the simulated radial velocity profile. Red circle indicates the position of trapping. (f) Trapping and manipulation of a protein with the nanohole array sketched in (d). (a) Adapted with permission from ref 443. Copyright 2013 American Chemical Society. (b) Adapted with permission from ref 446. Copyright 2019 American Chemical Society. (c) Adapted with permission from ref 449. Copyright 2015 American Chemical Society. (d) Adapted with permission from ref 472. Copyright 2014 American Chemical Society. (e, f) Adapted with permission from ref 473. Copyright 2020 Springer Nature.

also shown that pulsed illumination can create much more localized steady-state temperature profiles compared to a CW source with the same power density. Careful engineering of the particle arrangement can be leveraged to obtain on demand temperature profiles at the nanoscale.[444,445] The desired temperature profile can be achieved by solving the inverse problem, resulting in the determination of the corresponding heat source density map, which can be realized by lithographic patterning of a matching nanoparticle array. Reconfigurable temperature distributions can be obtained by combining an array of metallic nanoparticles with a spatially varying illuminating beam obtained with a spatial light modulator (SLM).[446] In this case, the nanoparticle array is homogeneous and the target temperature profile is obtained by shaping the illumination wavefront. In Figure 21b, an example of this strategy is shown, where an arbitrary temperature profile over a hexagonal array of 28 nm nanoparticles with an average spacing of 72 nm is achieved experimentally through the calculation of the heat source density (HSD) map, which is realized by wavefront shaping of a 532 nm laser using a SLM.

The refractive index n of a material is generally a function of temperature $n(T)$. This phenomenon is referred to as the of thermo-optic effect[447] and can be used as an additional tool to control light propagation. For example, the thermo-optic effect is leveraged to optically measure the plasmon-induced temperature distribution shown in Figure 21a and b by recording the optical path difference of a transmitted beam generated by the spatially dependent refractive index.[443,448] A metasurface composed of gold nanorods was demonstrated to act as an adaptive thermal lens based on the thermo-optic effect induced in the surrounding environment.[449] A sketch of the device and the correspondent temperature and refractive index distributions above the metasurface are shown in Figure 21c. Tunable focal length was achieved by changing the input power and utilizing the subsequent temperature increase, opening the way to reconfigurable flat optical elements. One of the advantages of local heating using absorbing nanoantennas compared to global heating is the reduced thermal inertia, allowing rapid temperature changes. For example, the same tunability offered by the adaptive thermal lens can be achieved by using a dielectric metasurface in conjunction with electrically driven heating of the substrate to shape the local refractive index profile.[450] However, due to the larger thermal inertia of the bulky substrate, this device showed much slower response compared to the thermal metalens. Faster response times can be obtained by reducing the size of the heat-generating metallic circuit.[451] Recently, optimization of the thermal properties of a multilayer stack allowed the realization of a SLM based on the thermo-optic effect with a rise time of only 70 μs,[452] two orders of magnitude faster than conventional SLMs. While in this implementation, the temperature increase was provided by randomly assembled gold nanorods, one can envision to improve the thermal SLM design by leveraging the control over the heating profile that can be obtained with a carefully designed plasmonic metasurface. The thermo-optic effect has also been used to engineer heat-tunable all-dielectric metasurfaces, since common high index materials (i.e., Si and Ge) also feature high thermo-optic coefficients.[453−456] The temperature increase can be provided by either an external source for low loss metasurfaces,[455,457,458] or can be a consequence of light-induced heating in lossy structures.[459,460] Using the thermo-optic effect, reconfigurable directionality[458] and beam steering[459] have been demonstrated in all-dielectric metasurfaces. Light-induced heating can also be

used as a fabrication tool, where the size of individual unit cells of a metasurface can be modified by an incident laser.[461] The local temperature increase can be monitored by Raman thermometry and has been used as a feedback parameter for the fabrication process.[462]

The presence of strong temperature gradients produced by plasmonic nanoantennas in solution can be used to manipulate the motion of nanoscopic objects.[463] There are many temperature-related physical−chemical processes that can influence the trajectory of nanoparticles[463] such as thermophoresis,[464] thermoelectricity,[465] photophoresis,[466] and natural convection.[467] For example, a near-infrared (NIR) broadband Moiré plasmonic metasurface was used to capture and immobilize *E. coli* bacteria dispersed in solution through a laser-induced photothermal effect.[468] Micro bubbles were generated under 1300 nm laser illumination due to plasmon-enhanced heating. *E. coli* bacteria were trapped in the bubbles by a combination of Marangoni convection, surface tension, and gas pressure effects. By switching off the illuminating laser, Wu et al. were able to release the microbubble and obtain deposition of the trapped *E. coli*. A combination of plasmon-induced heating and applied alternating current (AC) electric fields can be used to produce an electro-thermoplasmonic (ETP) flow in solution.[469] In the ETP effect, the temperature gradient induces a gradient in the permittivity and conductivity of the host fluid. The applied external AC field then drags particles toward the plasmonic hotspot through the electric body force of the fluid. The ETP effect can be leveraged to trap particles around nanostructures to increase the performance of plasmonic biosensors by overcoming the diffusion rate governed by Brownian motion.[470,471] Trapping large ensembles of nanoparticles in an inverted geometry (i.e., against gravity) was achieved by leveraging ETP flow.[472] A sketch of the device used for nanoparticle trapping is shown in Figure 21d. A laser beam passes through the substrate and the solution before illuminating the metallic nanohole array used to generate thermoplasmonic heat. The bottom substrate is coated with ITO so that an AC voltage can be applied in the microfluidic channel, enabling the activation of an ETP flow and trapping of the nanoparticles. Because of dipole−dipole repulsion, applying an external AC field can control the interparticle distance of the trapped particles, as shown in Figure 21d. It was found that the particle spacing was inversely proportional to the frequency of the applied AC field. Interestingly, large-ensemble trapping was not achievable when using a single nanohole and was obtained only when leveraging the extended metasurface. The radial velocity of the trapped particles was also found to be enhanced by the presence of the metasurface. By leveraging ETP flow in conjunction with AC electro-osmotic (ACEO) flow, trapping of sub-10 nm particles far away from the heating spot was achieved on an array of gold nanoholes.[473] When an AC out-of-plane field is applied, the balancing between ETP and electro-osmotic forces generates a region with zero net flow velocity, which is in a different spot from where the illuminating laser is placed, as schematically shown in the left panel of Figure 21e. When the laser is placed on the nanohole array, the ETP effect induces a force in the direction of the laser, while the ACEO effect produces an outward flow. In the right panel of Figure 21e, the simulated radial velocity field is reported, showing a region where the velocity goes to zero due to balancing of the opposite flows, where particles are trapped. Localization of the particle in the out-of-plane direction is achieved through particle−surface attraction resulting from the interaction between the surface

charges on the particle and its image charge in the conducting plane. The trapping distance from the nanohole array can be tuned by changing the frequency of the applied AC field. This achievement is relevant for trapping of tiny biological objects that can degrade in the presence of high temperature or high optical fields when using optical tweezers.[474] In Figure 21f, trapping and laser-induced transport of a protein using the nanohole array are shown. At $t = 0$, the protein is trapped outside of the array and the laser is displaced in the upward direction. The protein then follows along the laser displacement and aligns with the final position of the laser once it stops, showing dynamical trapping of small biological particles.

Additional control over the generated temperature profile in microfluidic applications can be obtained by employing chiral metasurfaces in which the absorption is strikingly different when using either left- or right-circularly polarized light (LCP and RCP, respectively) for illumination.[475] It was theoretically shown that a chiral antenna would produce an asymmetric temperature profile under LCP/RCP illumination, leading to a chiral velocity field in the vicinity of the antenna due to natural convection.[475]

While thermoplasmonic effects are not as efficient in the mid-IR due to the smaller skin depth of metals, coupling to molecular vibrations can be used to gain additional control over the achievable temperature increase. Chemically selective heating can be obtained by coupling plasmonic metasurfaces resonating in the mid-IR to the molecular vibrations of target molecules. One can then have a different degree of heating depending on the type of molecules placed in the hotspot of the antennas.[476−478]

Recently, emerging applications of metasurfaces for water desalination,[479] antifogging,[480] ice adhesion control,[481] and more[482] have leveraged light to heat conversion to achieve the desired functionality. Even though these structures do not strictly match the definition of optical metasurfaces we use in this review, we mention them here for their potential technological impact.

While silver and gold have been the materials of choice for most plasmonic applications, due to their low damping rates, they have relatively low melting points, making them unsuitable for high temperature applications. Moreover, reshaping of metallic nanoantennas generally happens at temperatures below the melting point of their constituent bulk material due to surface melting effects.[483−485] Consequently, alternative plasmonic materials more suitable for thermoplasmonics have been researched in recent years.[486] Titanium nitride (TiN) and zirconium nitride (ZrN) have been shown to be promising candidates to replace noble metals thanks to their high melting point and good plasmonic responses in the NIR and visible regions.[486−492] TiN metasurfaces have been shown to perform better than comparable gold structures for thermoplasmonic applications[490] and for broadband absorption under high illumination conditions.[493] Since broadband absorption can cause high temperature increases under high intensity illumination, the employment of high melting point materials is crucial to achieve device stability. A metal−insulator−metal (MIM) metasurface composed of TiN-SiO₂−TiN was demonstrated to achieve broadband visible absorption.[493] To test the robustness of the metasurface under high temperature, the structure was measured before and after annealing at 800 °C. In Figure 22a, the spectra of the MIM metasurface showed almost no alteration after annealing, confirming its thermal robustness. For reference, an identical structure was fabricated with TiN
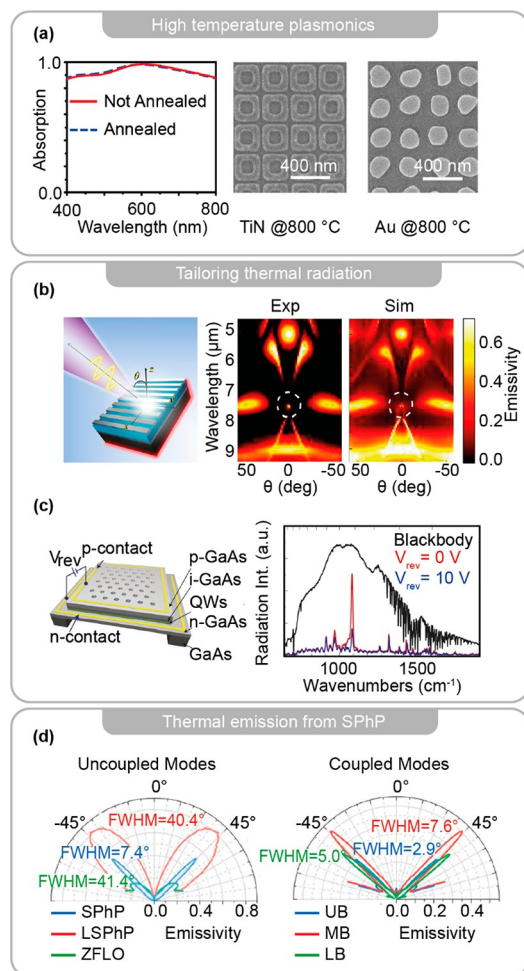
Figure 22. Controlling thermal emission with metasurfaces. (a) Spectra of a broadband TiN absorber metasurface before and after annealing at 800 °C (Left). SEM images of the TiN (middle) and equivalent gold metasurface (right) before and after annealing. (b) Al/SiN/Al metasurface with experimental and simulated angle-resolved emissivity spectra. The modes of the metasurface were engineered to have emission in the normal direction at 7.1 μm, as highlighted by the dashed white circle. (c) Electrically tunable thermal emission from a stack of quantum wells. Tunability is achieved by modulating the number of carriers populating the intersubband transition. (d) Angle-resolved thermal emission from a metasurface of SiC pillars. Narrowing of the angular emission can be achieved by reaching strong coupling between the different modes (left panel). (a) Adapted with permission from ref 493. Copyright 2014 Wiley-VCH GmbH. (b) Adapted with permission from ref 517. Copyright 2019 American Chemical Society. (c) Adapted with permission from ref 524. Copyright 2014 Springer Nature. (d) Adapted with permission from ref 537. Copyright 2021 American Chemical Society.

replaced by Au. While the TiN structure was intact after annealing, heavy reshaping of the antennas in the Au sample could be observed under SEM, as shown in the right panels of Figure 22a. The same experiment was also carried out for a high intensity laser illumination with a power density of 6.67 W/cm^2 at 550 nm similarly showing substantial damage for the Au structure but not for the TiN one. Conventional high melting point metals like tungsten (W) can also be used for high temperature applications when employed in an antenna-reactor arrangement where light-absorption is achieved through a noble-metal antenna while the W reactor absorption is increased by the enhanced near-fields.[494] According to eq 4.2, the heat

power density generated in a nanoantenna is proportional to the imaginary part of the dielectric function ε_2. One could then wonder if materials with high losses would be better suited for thermoplasmonic applications. However, to have high losses, high field inside the antennas are required, meaning that a strong plasmonic response is still required for efficient heat production, favoring materials with low values of ε_2.[486]

The heat produced by absorbing metalling antennas can also be used to speed up the rate of chemical reactions. In photocatalysis, energy from the sun is absorbed by a material which acts as a catalyst for a given chemical reaction. Since the speed of a chemical reaction depends on temperature through the Arrhenius equation, metasurfaces can be employed to change the rate of the process through the thermoplasmonic effect.[495] However, chemical reaction rates depend on a number of effects that are difficult to disentangle from the pure temperature contribution, as carrier-injection and field-enhancement.[496,497] As such, metasurfaces for photocatalysis will be discussed in the following section 5 (photon−electron energy conversion).

4.1.2. Metasurface-Controlled Far-Field Thermal Emission. Any object at nonzero temperature emits thermal radiation following Planck's law. The so-called blackbody radiation is nearly isotropic, broadband, incoherent, and unpolarized.[498] These characteristics of blackbody radiation are a consequence of Planck's law, which is derived from ray optics and assumes that the all the dimensions involved in the phenomena are much smaller than the wavelength of peak thermal radiation λ_{th}.[499−501] For objects at room temperature $\lambda_{th} \approx 10$ μm, meaning that nanostructuring of the surface material can completely modify its thermal emission properties. Because mid-IR sources are either inefficient thermal sources[502] or expensive quantum cascade lasers (QCLs),[503] achieving highly directional and narrow bandwidth thermal emission would be beneficial for many sensing applications.[504] Metasurfaces have been extensively employed to tailor far-field thermal emission, achieving narrowband,[181,505−513] polarized,[101,511,514] and directional emission.[501,515−520] Leveraging more complex types of structures is predicted to enable higher control over the thermal emission profile, allowing the realization of thermal self-focusing and holography[521] and higher emission efficiencies.[305] Engineering of the radiative heat transfer properties of a material can be achieved with many different nanophotonic designs. Zhang et al. designed the resonances of a MIM (Al/SiN/Al) metasurface to obtain directional emission in the normal direction.[517] In Figure 22b, the design of the metasurface is shown, along with the angle-resolved emissivity maps obtained experimentally and theoretically by normalizing to a blackbody emitter. By strong coupling of the SLR and magnetic resonance of the structure, the authors demonstrated unidirectional thermal emission in the surface-normal direction for a wavelength of 7.1 μm. The unidirectional emission spot is highlighted by a dashed circle in Figure 22b and is a result of the Fano line shape obtained by engineering the modes of the metasurface.

A challenge in designing thermal IR sources is the realization of high emission modulation speeds due to the slow time scale related to thermal dynamics of bulk systems. Reduction of thermal inertia can be achieved by reducing the overall mass of the heated object, as for example by reducing the device thickness. By using this approach, modulation speeds beyond 10 MHz using a platinum metasurface were recently achieved.[522] For reference, conventional globar or membrane-based thermal

IR sources can be modulated only up to some Hz.[523] In Figure 22c, an example of a narrow-band IR thermal emitter built from an array of micrometer holes in a p-doped gallium arsenide (GaAs) film fabricated on top of a stack of quantum wells (QW) made of GaAs/n-AlGaAs is shown.[524] The QW stack was designed to have an intersubband transition at 1090 cm^{-1} and the hole array geometry was optimized to achieve high absorption and emission at this frequency. The authors also demonstrated tuning of the thermal emission strength by applying a voltage through the QW stack. Tuning is achieved by carrier injection/extraction from the QWs, which modifies the strength of the intersubband transition and the absorption/emission properties of the device. The emissivity achieved with 0 and 10 V applied bias when heating up the device to 200 °C is shown in Figure 22c together with the blackbody emission at the same temperature. High tuning speeds of 600 kHz were achieved thanks to the rapid nature of bias-induced carrier injection in QWs. Dynamically reconfigurable thermal emission was also demonstrated by employing a metallic metasurface separated with a dielectric layer from the substrate constituted by a heavily doped semiconductor acting as a plasmonic material at IR wavelengths.[525] Applying a voltage between the doped insulator and the metallic layer allowed for tuning of the gap plasmonic resonance and thermal emission properties of the device.

A particularly interesting platform to control thermal radiation consists of metasurfaces made of polar materials supporting SPhPs. In particular, SiC has been the material of choice for many thermal applications thanks to its high melting point (above 3000 K)[526] and Reststrahlen band wavelengths (approximately 10 to 12.5 μm) matching the peak thermal wavelength λ_{th} for room-temperature emission.[409] While the far-field emissivity for an unpatterned SiC surface in the Reststrahlen band is very small due to the high reflectivity, structuring the surface can produce strong thermal emission at specific wavelengths. In a pioneering work, highly coherent and directional emission from a SiC grating was demonstrated.[527] These striking thermal emission properties were attributed to the excitation of SPhPs and directly related to their dispersion $\omega(k)$. The role of SPhPs was also confirmed by a polarization dependent measurement: while p-polarized data showed high directionality, s-polarized experiments showed angle-independent emissivity. Carefully designed SiC gratings were recently theoretically demonstrated to achieve focusing[528] and asymmetric spatial profiles[529,530] of thermal radiation, and various SiC metasurface geometries have been realized for thermal emission engineering.[531,532] Spin-splitting thermal emission has been observed in inversion-asymmetric lattices.[533−535] The spin-splitting phenomena are related to the symmetry of the lattice which imposes constraints on the coupling of SPhPs to far-field propagating modes. Because the emission is proportional to the absorption, this effect is manifested in structures characterized by a linear or circular dichroism response that can be probed by standard reflection/transmission measurements. Narrowing of the angular emission of thermal radiation was shown in a metasurface achieving strong coupling between localized and propagating modes together with zone-folded longitudinal optical (ZFLO) phonons. ZFLO phonons exist in crystal lattices with elongated unit cells, where the additional Bragg plane causes back-folding the phonon dispersion. In the case of 4H-SiC, the ZFLO phonon falls within the Reststrahlen band, appearing as a dip in reflectivity spectra.[536] When strong coupling is achieved, the three distinct modes assume a mixed

character and are indicated as upper (UB), middle (MB), and lower (LB) bands. Varying the pitch of the array allowed the authors to move from coupled to uncoupled modes and compare their different angular emission properties, as shown in Figure 22d.[537] The same group also demonstrated that narrowband mid-IR emission with powers up to 10 mW can be reached by heat-waste recycling from a standard operating CPU by covering it with a SiC metasurface.[538]

4.1.3. Metasurfaces for Radiative Cooling and IR Camouflage. Manipulation of the absorption and emission properties of a surface can lead to striking effects such as daytime radiative cooling under sunlight illumination.[501] The rate of energy transfer through thermal emission between two objects at temperatures T_1 and T_2 is proportional to the difference of their fourth powers $dQ/dt \propto \left(T_1{}^4 - T_2{}^4\right)$, where T_1 and T_2 must be expressed in Kelvin. This means that to cool something through radiative transfer we need a second object with lower temperature to absorb the energy without re-emitting it. Luckily, the universe constitutes the perfect heat sink with its low temperature of 3K and practically infinite thermal capacity. However, to make use of the coldness of the universe, thermal radiation must be transmitted through the much hotter earth atmosphere. Fortunately, the atmosphere is mostly transparent in the 8−12 μm wavelength region, where blackbody radiation peaks for objects around room temperature. Radiative daytime cooling can then be achieved for an object reflecting the entire solar spectrum, while having at the same time strong emission in the mid-IR transparency window of the atmosphere. A metasurface composed of truncated cones made out of alternating layers of germanium and aluminum was optimized to achieve near-unity broadband emission in the 8−13 μm range.[539] The cooling power was theoretically estimated, predicting a device temperature about 9 °C lower than ambient temperature under sunlight illumination when coupled to solar reflectors. A hybrid metasurface composed of doped silicon and a silver film deposited on top was also proposed for daytime radiative cooling, with a temperature reduction of 8 °C under sunlight.[540] An adaptive metasurface was theoretically proposed by leveraging a MIM geometry.[541] The dielectric layer material was chosen to have a larger expansion coefficient, resulting in a dynamical on/off tuning of the cooling properties under temperature variations. In this way, the authors obtained a cooling device under high ambient temperatures and a heating device at low ambient temperature. A similar adaptive effect can be obtained by leveraging the temperature-induced metal-insulator transition of VO$_2$.[542] Conductive oxides, which are transparent in the visible and have metallic properties in the IR, can be used to design metasurfaces for high IR emissivity while naturally providing low absorption in the visible due to their transparent nature.[541] While optimal radiative cooling requires no absorption of solar radiation, solar cells require strong absorption of sunlight. However, the increase of their operational temperature can decrease their efficiency. Radiative cooling on solar absorbers can then be used to maintain high efficiency for solar cells even under continuous exposure to sunlight. Zuh et al. demonstrated such a device by using a metasurface composed of silica placed on top of a doped Si layer acting as a visible absorber.[543] SiO$_2$ was chosen due to its transparency in the visible range. However, the presence of SPhP in the mid-IR results in a low emissivity region matching the IR atmospheric window. Patterning of the SiO$_2$ surface allowed for increased mid-IR emissivity in the Reststrahlen band thanks to the presence of localized SPhP modes, which lowered the

reflectivity. In Figure 23a, the optical properties of the bare visible absorber (black) with the addition of the SiO$_2$ layer (blue) and SiO$_2$ metasurface (red) are shown. The absorption of light in the visible is almost unchanged by adding the SiO$_2$ surface and is high at the frequencies where the solar spectrum is more intense, as shown by the orange curve. While the emissivity
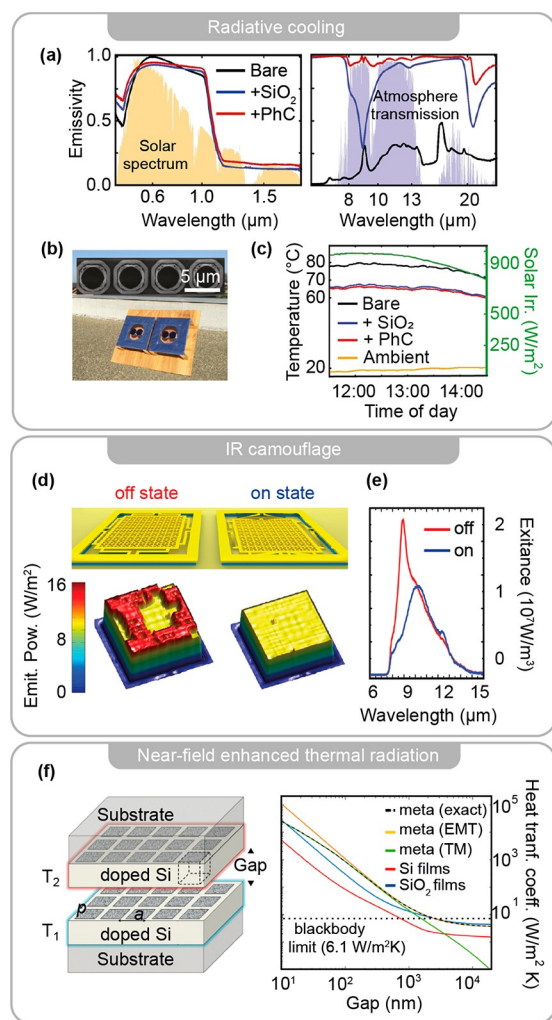
Figure 23. Metasurfaces for thermal radiation energy management (a) Radiative cooling of a solar cell by addition of a SiO$_2$ metasurface. Absorptivity/emissivity in the visible (left) and mid-IR (right) from the bare device (black), the device plus a SiO$_2$ layer (blue) and plus the metasurface (red). (b) Picture of the setup used for the experimental evaluation of the device and SEM image of four unit cells of the metasurface. (c) Measured temperature increase of the device with and without the metasurface under sunlight exposure during the day, together with solar irradiance at the same time. (d) Sketch of a device for reconfigurable IR camouflage, achieved by mechanical deformation of a suspended metasurface. An on state can be obtained by collapsing the metasurface on the bottom surface. Images obtained with an IR camera show the different emissivity for the two states (bottom panels). (e) Measured spectral exitance for the metasurface in the on and off states. (f) Enhanced NFRHT between two metasurfaces made of holes drilled in highly doped silicon slabs separated by a gap. The calculated HTC as a function of the gap distance is reported for the metasurface and compared to parallel surfaces of doped silicon and SiO$_2$. (a–c) Adapted with permission from ref 543. Copyright 2015 National Academy of Sciences. (d, e) Adapted with permission from ref 190. Copyright 2017 Optica Publishing. (f) Adapted with permission from ref 560. Copyright 2017 American Physical Society.

of the bare device in the mid-IR is poor, almost unity emissivity is achieved with the SiO$_2$ metasurface due to the presence of localized SPhP modes, as reported in the bottom panel of Figure 23a. The light blue curve represents the atmospheric transmission, highlighting the high emissivity of the metasurface over the whole atmospheric window. In Figure 23b, a photo of the setup used to experimentally prove the radiative cooling effect is shown. Few unit cells of the metasurfaces imaged with a SEM are presented in the inset. Graphs of the temperature of the different devices with and without the SiO$_2$ layer are shown in Figure 23c along with the measured ambient temperature and solar irradiance during the day, confirming that patterning of the SiO$_2$ surface results in the lowest overall temperature while slightly increasing light absorption in the visible.

The same strategy used for daytime radiative cooling can be also applied for IR camouflage. IR detection based on thermal emission is often used for night vision, where visible light is scarce, as it is sensitive to anything having a temperature higher than the environment.[544] Consequently, lowering the temperature of an object through radiative cooling can be effectively used as a way to circumvent thermal radiation detection. A mechanically flexible metasurface with low IR emissivity was experimentally demonstrated by combining an ITO structure with a deformable dielectric.[545] On top of the low thermal emissivity and mechanical properties, the large-scale fabricated metasurface was transparent in the visible range and was designed to achieve high absorption at GHz frequencies, making it invisible to radar detection. A tunable metasurface composed of a MIM structure, where the top metal surface is patterned to achieve high emissivity in the mid-IR and the dielectric layer is composed of a liquid crystal, was theoretically investigated for dynamic thermal camouflage.[546] Reconfigurable thermal emissivity has been experimentally demonstrated for a MIM metasurface based on physical deformation of the structure when applying a voltage between the top and bottom metallic layers.[190] An "on" state could be achieved when sufficient voltage was applied to make the top patterned surface touch the bottom metallic layer, changing the emissivity properties of the structure. A sketch of the device in both states is shown in Figure 23d together with the corresponding maps of emitted power obtained with an IR camera, showing highly reduced emissivity in the on state. The spectral radiant exitance in the off state shows a strong peak around 8 μm, where the atmosphere is transparent, which is strongly damped in the on state as shown in Figure 23e. The authors also demonstrated efficient modulation of the emitted power in the on/off states up to 100 kHz. Modulation of thermal radiation for IR camouflage has also been demonstrated by injection of free-carriers due to above-bandgap UV illumination in a dielectric ZnO spacer layer placed below a metasurface of gold disks.[547]

4.1.4. Near-Field Radiative Energy Transfer. Radiative heat transfer between objects separated by a distance smaller than the thermal radiation peak wavelength λ_{th} can be highly modified by the contribution of evanescent surface waves (as SPPs in metals or SPhPs in polar dielectrics) that can tunnel through the gap.[499,548,549] For example, the thermal radiation from an unpatterned SiC surface at a distance of 100 nm is strikingly different from its far-field thermal emission.[550,551] While far-field thermal radiation drops sharply in the Reststrahlen band due to high reflectivity, the near-field shows a sharp peak at a specific frequency. Near-field thermal emission can be monochromatic and exhibit high spatial coherence, while at the same time the net energy flux of thermal energy can be

much higher than in the far-field.[552,553] This is because SiC supports SPhPs, which are evanescent in the direction perpendicular to the surface. The peak in the near-field thermal emission corresponds to the frequency at which SPhPs have a high density of electromagnetic states at $\varepsilon_1(\omega) = -1$.[424,550,554] Experimental verification of the predicted near-field radiative heat transfer (NFRHT) enhancement is not easy due to the necessity of reaching small gaps in the tens of nanometers range. Initial efforts have been concentrated on a sphere-surface geometry that is easier to achieve experimentally but shows relatively low NFRHT.[549,554−557] Only recently NFRHT has been experimentally probed for two flat surfaces separated by a gap of only 30 nm, reporting an enhanced energy transfer on the order of 10^3 with respect to the far-field value.[558,559] Many theoretical works have studied the possibility of employing metasurfaces to control NFRHT. In Figure 23f, one of these examples is reported, where two metasurfaces composed of squared air holes drilled in doped silicon films at two different temperatures are separated by a narrow gap.[560] The doped silicon films support SPPs, of which the dispersion can be engineered through the metasurface geometry to enhance the NFRHT. In the graph of Figure 23f, the calculated heat transfer coefficient (HTC) for the metasurface (dashed black), parallel planar films of doped Si (red, supporting SPPs), and SiO_2 (blue, supporting SPhPs) are shown for different spacing distances. The metasurface has the highest HTC, well above the blackbody limit, confirming the usefulness of nanostructuring to enhance NFRHT. The HTC of the metasurface was evaluated both with an exact calculation (dashed black line) and by using effective medium theory. The green line indicates the contribution to the HTC of the metasurface coming from evanescent transverse magnetic (TM) polarized waves. Because of the high difficulty of NFRHT experiments, confirmation of metasurface-based enhanced NFRHT has yet to be demonstrated in a lab.

4.2. Photon−Acoustic Phonon Energy Conversion

Miniaturization and speed of electronic and optical components represent essential steps toward the achievement of high performance, low environmental impact, and lightweight devices. Various fundamental building blocks based on diverse technologies are already fully available for applications. Perhaps the most evident example is photonics: the exploitation of the generation and control of photons is found in a myriad of devices and structures, like light modulators and waveguides, which are routinely used to transport and manipulate photons.[561] Recently, new approaches to this subject aiming at more compact and fast devices, exploiting the lattice strain created in a solid described by its fundamental excitations (that is, the quasiparticles called phonons), are gaining attention in the fast-growing field of phononics.[562] Phonons are particularly interesting due to the possibility of interacting with virtually any excitations observable in the solid-state phase, going from the most common ones, like excitons and polarons, to rarely discussed ones, like magnons. Acoustic phonons present inspiring analogies with photons. For example, both sound in a solid and light in a transparent medium present linear dispersion relations and are weakly attenuated. There is, nevertheless, an important difference in the behavior of these elementary excitations: the propagation velocity for phonons in a transparent solid is in the range of a few km/s, which is $\sim 10^5$ times smaller than the speed of light in the same medium. Phononics-based devices take direct advantage of this: in the RF domain (hundreds of MHz to tens of GHz), extremely relevant

for the realization of microwave devices and for telecommunications, photon-based devices are bulky due to the fact that the wavelength of light lies in the range of meters to centimeters. Meanwhile, phononics-based devices operating in the same frequency range can be reduced in size by a factor of 10^5, to the range between 10 μm to 100 nm, fitting into small, micrometer-sized chips. It also enables electronic signal processing in the tens of GHz range, a frequency region already in the limit of expensive and bulky electronics-based microwave generators. A promising way for achieving this is using surface acoustic waves (SAWs) produced by nanoscale mechanical oscillators coupled to a substrate. The generation of acoustic waves can be done usually in millimeter- to micrometer scales using (i) mechanical oscillators, like tuning forks (waves with frequencies up to hundreds of MHz), (ii) interdigital transducers (IDTs) (frequencies from hundreds of MHz to tens of GHz), which demands the use of piezoelectric substrates, and (iii) picosecond laser pulses incident on metallic thin films (frequencies from tens to hundreds of GHz).[563] Techniques using the approaches (i) an (ii) are too bulky for nanophotonic applications. For techniques following the strategy (iii) in the best cases, a picosecond laser pulse focused down to 20 μm on a metallic thin film transducer produces a bulk acoustic wave that quickly spreads over the whole substrate. An excellent paper describes in detail the whole mechanism governing this phenomenon.[564]

In some structures, the absorption of photons may trigger a cascade of events that can result in the coherent production of acoustic phonons. In one of the first experiments with nanometer-sized metal (Au) nanoparticles (NPs), employing spectrally resolved transient absorption spectroscopy with ultrashort laser pulses, it was verified that the excitation pulses "bleached" the plasmon resonance and the time-resolved results showed a signal time evolution presenting different decay times, each associated to different electronic relaxation processes, the fastest one being related to hot electrons thermalization, and the slowest one related to the lattice (phononic) relaxation.[30] As a result of this series of relaxation/thermalization processes, the NPs start oscillating in their mechanical normal modes of vibration, with frequencies depending on the NPs shape and size. Because of the coupling to the substrate, SAWs may be produced there, being detectable at least a few micrometers away from the oscillating source NP.[565] The approach of producing SAWs with single nanoparticles was further exploited to produce plane SAWs by using metallic nanowires, which can be seen as nanorods with very high aspect ratios.[566] On the other hand, the use of oscillating single NPs coupled to a substrate represents the smallest realization of a SAW source, leading to the possibility of designing ultracompact devices with frequencies in the few-GHz range. Some decades ago, it was observed using a transient absorption technique that by exciting a colloid with 15 nm Au NPs with ultrafast laser pulses a transient bleaching of the metal plasmon resonance occurred. After the excitation of a plasmonic NP with pulsed light at the appropriate wavelength (usually its dipolar plasmon resonance, or an interband transition), an excited electronic population is produced in the metal, followed by thermalization and lattice heating. The relaxation of the created hot electron gas happens through a cascade of processes, each having different characteristic decay times.[567] These ranged from an unresolved (<450 fs) electron/electron scattering, 2.5 ps for electron/phonon scattering and >50 ps for the phonon/phonon scattering (lattice relaxation). In addition to mere heat, this relaxation/energy transfer cascade leads to the excitation of
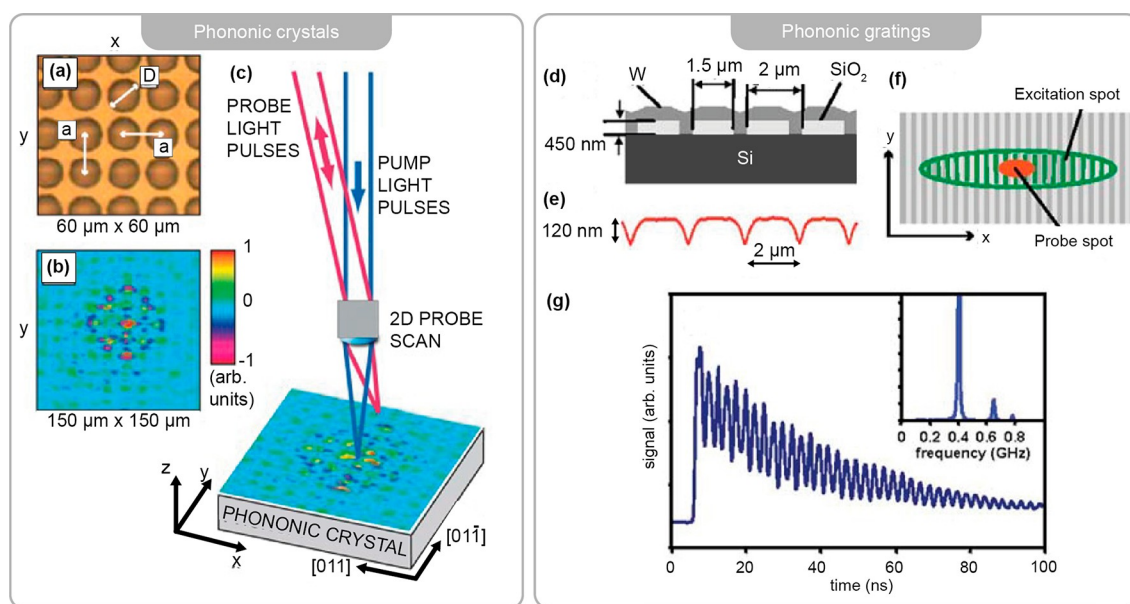
Figure 24. Metasurfaces for generating directional phononic modes. (a) Optical microscope image of the silicon phononic crystal coated with a 40 nm gold layer. The hole diameter is $D = 12\ \mu$m with lattice constant $a = 15\ \mu$m. (b) SAW image at delay time $t = 7.4$ ns. (c) Outline of experimental setup with SAW image at $t = 10.3$ ns. (d) Sample schematic cross-section. (e) AFM profile of the sample surface. (f) Laser spot configuration on the sample. (g) Typical signal waveform measured at the wavenumber of 0.9 mm^{-1} (acoustic wavelength of 7 mm). Inset: frequency spectrum of the acoustic oscillations. (a−c) Adapted with permission from ref 573. Copyright 2009 American Physical Society. (d−g) Adapted with permission from ref 574. Copyright 2009 AIP Publishing.

normal modes of mechanical oscillation (acoustic phonons) compatible with a symmetric strain profile of the plasmonic nanostructure. The induced coherent acoustic phonons field, in turn, modulates the optical properties of the NP such as its reflectivity or transmissivity. This dynamic change is interrogated by a second probe pulse, for which there will be maximum sensitivity at wavelengths near the localized dipolar surface plasmonic resonance of the NP. In fact, this behavior was observed in single Ag nanorods embedded in a glass matrix.[568] The internal pressure exerted by the hot electron gas generated by the excitation pump pulses drove the Ag NPs to anisotropic mechanical vibrations, with different oscillation frequencies along the long and short nanorod axes. The physics behind this hot electron relaxation dynamics observed with pump-and-probe experiments and the corresponding effects on the optical properties of metal NPs ensembles were studied in detail in refs 569 and 570 for the case of single metal NPs, in a much more challenging experimental situation. The idea of using the mechanical oscillations of single metal NPs to generate SAWs was demonstrated in ref 571.

The natural step at this point is to be able to manipulate and to use SAWs generated by a triggering optical process, for example, by creating directional emission, which was achieved in ref 572. In this work, directionality of SAWs has been achieved first by the use of single V-shaped Au nanoantennas, and then a collection of nanoparticles made from different metals configured in a nanoscopic version of a Yagi-Uda antenna, which we can consider as being a metamolecule, was studied and numerical simulations showed the potential of such an array to generate directional SAWs. Contrary to what is done in the previous work, in which the properties of a single meta-atom are exploited, metasurfaces have been designed to generate and control SAWs, making use of the collective behavior of the constituent meta-atoms or metamolecules. A phononic crystal has been realized by using a metasurface fabricated with a silicon

slab, on which air holes ($\sim$12 μm diameter, $\sim$10 μm depth) were etched in a square lattice ($\sim$15 μm lattice constant) and subsequently coated with a 40 nm thick Au film.[573] Using a dynamic imaging technique based on a pump-and-probe configuration but without varying the delay line and scanning the transversal position of the probe beam, ultrafast laser pump pulses are focused between four air holes to generate the SAWs, like schematized in Figure 24a−c. The probe beam interrogates the amplitude of the generated SAWs at diverse positions around the point where the SAWs emanate, leading to direct probing of the phononic crystal eigenmodes as well as determining the dispersion relation and a directional stop band. The finding of this directional stop band possibly motivated the same group to design a metasurface for the study of well-known phenomena in crystalline semiconductors and in photonic crystals, like the behavior of the matter and light waves close the edge of the Brillouin zone, but in the phononic regime.

For instance, 1D metasurfaces made from bars of amorphous silica (1.5 μm wide, 0.45 μm thick) on a silicon wafer have been demonstrated.[574] The period of the structure was 2 μm and it was coated with a 0.45 μm-thick tungsten film (see Figure 24d−g). A variation of the pump-and-probe technique was used to pump the tungsten film with a dynamic grating. This could be done by splitting the pump beam in two and recombining them on the metasurface, forming an angle. This produced an elongated interference pattern with variable period (determined by the angle between the two pump beams) on the sample, which was associated to a grating wave vector lying on the metasurface plane. The probe beam was focused at the center of the interference pattern of the pump beam. For a given angle between the two pump beams (that is, for a given periodicity of the interference pattern created), the absorption of the pump light by the tungsten film could generate a SAW pattern with a wavevector close to the microstructure Brillouin zone boundary.
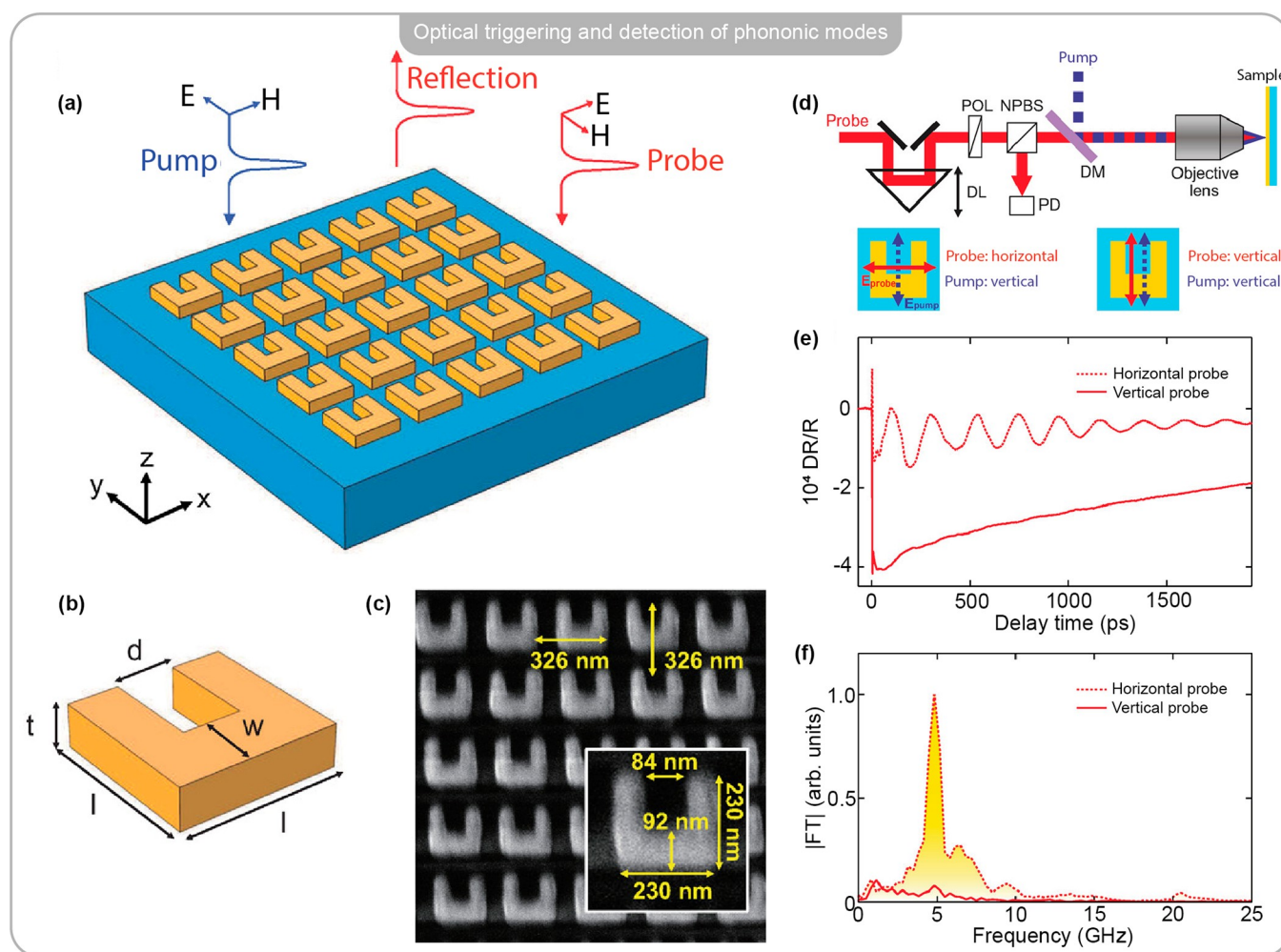
Figure 25. Optical triggering and detection of phononic modes. (a) Scheme of the sample configuration for horizontal probe polarization. (b) Definitions of the dimensions of the SRR. (c) SEM of the gold SRRs (thickness t = 60 nm) fabricated on a BK7 glass substrate. (d) Scheme of the experimental setup based on an optical pump−probe technique. Directions of linear polarization for the pump (dashed blue arrows) and probe (solid red arrows) beams are also shown. (e) Experimental pump-induced reflectivity changes of the sample versus delay time for horizontal (dotted red curves) and vertical (solid red curves) probe-beam polarizations, using a vertically polarized pump beam. (f) Corresponding moduli of the temporal Fourier transforms as a function of the frequency on a normalized scale. (a−f) Adapted with permission from ref 577. Copyright 2017 American Chemical Society.

With this, by varying the delay between pump and probe pulses, very long-lived states could be detected, corresponding to phononic stationary states, that is, surface vibrational modes with zero group velocity.

An elegant extension of this technique was used to map the band structure of a 1D surface phononic crystal composed of copper lines (width 2 μm) embedded in a 0.8 μm thick silica film deposited on a silicon substrate, forming a 1D structure with a 4 μm period.[575] By using the same experimental approach of the previously described work and simply rotating the elongated pump beam interference pattern on the metasurface plane, the dispersion surfaces for the lowest three acoustic modes of the 1D periodic structure could be obtained. A similar 1D metasurface (a grating made of aluminum rods 190 nm wide, 40 nm high and periodically spaced by 380 nm, deposited on a 1.0 mm silica substrate and with a total area of 100×100 mm^2) was used for generating longitudinal and shear coherent acoustic waves after the absorption of ultrafast laser pulses, in a pump-and-probe like configuration for exciting and detecting the acoustic waves.[576] This time-resolved Brillouin scattering experimental scheme

allowed researchers to generate and detect both kinds of acoustic waves diffracted along different orders by the grating.

In a notable work,[577] Imade et al. reported on the optically triggered acoustic vibrations of a metasurface consisting of coherently oscillating gold U-shaped split-ring resonators (SRRs) on BK7 glass, an archetypical metamaterial system intensively explored for its optical properties as left handed materials, negative refractive index systems, and others[578] (see Figure 25). Under the chosen optical excitation conditions, also in a pump-and-probe like configuration, tens of SRRs, here behaving as nanoscopic tuning forks, were excited and the resulting stress field−the SAWs could induce coherent oscillation of a few hundreds of SRRs, at frequencies corresponding to the acoustic wave vectors in the metasurface, which acted as a phononic crystal. The influence of the opening/closing of the SRRs gap was shown to be the main mechanism dominating the collective acousto-plasmonic interactions on the metasurface.

The famous experiment leading to the observation of extraordinary optical transmission through an array of nano-holes showed light concentration far beyond the diffraction limit
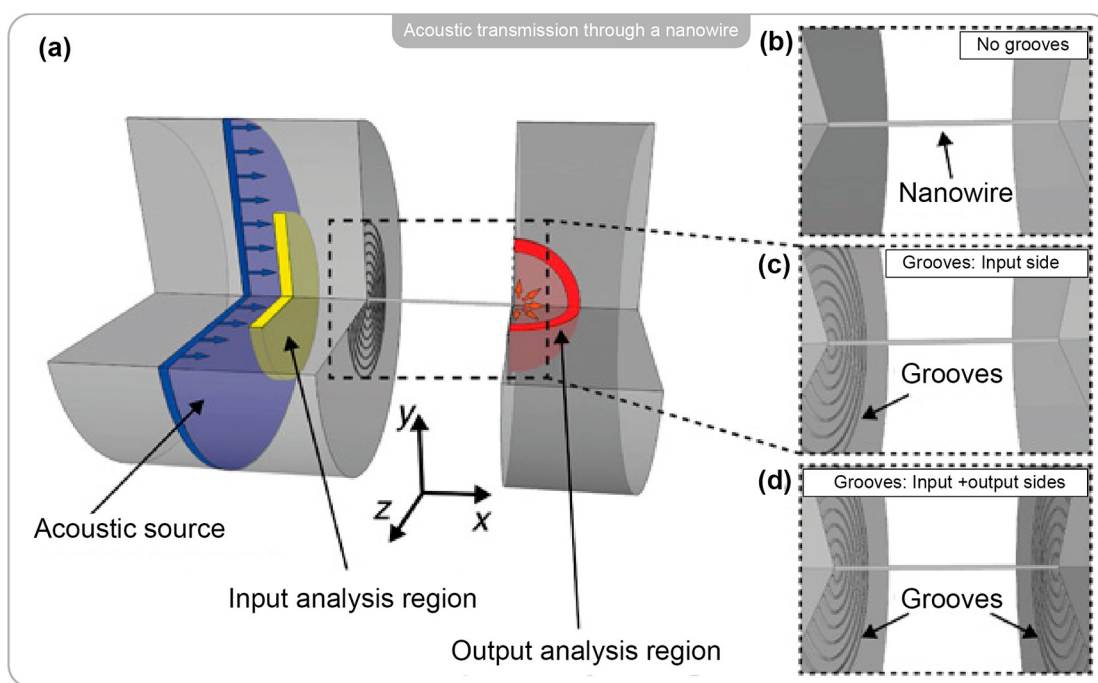
Figure 26. Extraordinary acoustic transmission architectures employing a nanowire with or without additional concentric grooves. (a) Scheme of the extraordinary acoustic transmission geometry, showing a section through a subwavelength-diameter W nanowire connecting two W bulky structures. Three different cases are studied: (b) case of no grooves, (c) case of grooves on the input side, and (d) case of grooves on both input and output sides. Adapted with permission from ref 580. Copyright 2020 Springer Nature.

and represented a milestone for high resolution imaging.[579] This work was a motivation for investigating whether a similar phenomenon could be observed in the phononic regime. In ref 580, the authors investigate the use of a metasurface for squeezing a longitudinal acoustic wave incident from a cylindrical tungsten block (110 nm in diameter) through a 5 nm tungsten nanowire, which is ~20-times smaller than the acoustic wavelength, as schematized by Figure 26. The feasibility of huge transmission efficiencies has been demonstrated, to which a four orders of magnitude enhancement of acoustic energy density is associated. This has been achieved by fabricating concentric grooves with optimized sizes and positions at the end of the input tungsten block (roughly speaking, in a kind of Fresnel lens for acoustic waves) and thus by fabricating a phononic metasurface there. It has also been shown that by engraving such grooves at the entrance of the output tungsten block one could manage to control the directionality of the output acoustic beam.

4.3. Photon−Optical Phonon Energy Conversion

4.3.1. Metasurfaces for Surface Phonon Polariton Engineering.
Mixed light-photon states can exist in the Reststrahlen band of polar dielectrics, where $\varepsilon_1(\omega) < 0$. As for SPPs, surface patterning can be used to engineer the dispersion of SPhPs, allowing intersection with the light line and coupling with far-field sources, which is otherwise forbidden due to energy-momentum mismatch as shown in Figure 20d. Metasurfaces composed of SiC antennas have been extensively studied both from the far-field[415,532,581,582] and the near-field,[413,532] enabling the realization of very high Q resonances with simple arrays of cylindrical pillars. As the existence of long-lived SPhPs relies on the high crystallinity of the constituent material, resonators supporting LSPhPs need to be realized by etching in a wafer protected by a hard mask rather than relying on evaporation as is most common for plasmonic structures. As a

consequence, metasurfaces made from polar dielectrics are often placed on a surface made from the same material, which also supports SPhPs. In this type of structure, LSPhPs and SPhPs can exist at the same time and can achieve strong coupling between themselves for certain geometrical parameters of the metasurface.[583,584] Hybridization of LSPhPs supported by a metasurface with ZFLO phonons has also been achieved, giving a longitudinal character to otherwise purely transverse LSPhPs.[536] As electrical currents mainly produce LO phonons, this effect has been proposed as a way to electrically excite LSPhP. SHG in the mid-IR has also been explored with the same SiC structure, showing stronger emission when spectrally overlapping the modes of the metasurface with the ZFLO phonon of anisotropic 6H-SiC polytype.[585,586] One of the drawbacks of SPhPs-based nanophotonics is the limited spectral range of the Reststrahlen band, which is material dependent and with limited and challenging tunability. Above-bandgap illumination has been shown as a method to tune the Reststrahlen band frequency through injection of carriers, adding a Drude contribution to the dielectric function of the material.[587] Carrier photoinjection from both CW and pulsed illumination has been shown as a method to tune the optical properties of SPhPs metasurfaces.[588] In Figure 27a, the transient reflectivity of an array of SiC pillars recorded 5 ps after above bandgap illumination at 266 nm is shown. The spectra are normalized to the response of the SiC substrate, showing two dips corresponding to the resonances of the array. The spectra are reported for different pump powers, showing a blueshift of the resonances upon stronger illumination, until the high carrier injection causes a softening of the Reststrahlen band, leading to a bulk-like response modified by the free-carrier contribution. The time-resolved response at the dipolar resonance (936 cm^{-1}) is shown in Figure 27b. The black curve represents the response of the bare substrate, which is consistent with Reststrahlen band softening

Figure 27. continued

due to carrier injection. On the arrays, higher reflectivity right after pump arrival is due to detuning of the resonance from its original frequency. In the right panel of Figure 27b, a sketch of the dipolar LSPhP with and without carrier injection is shown. The recovery of the response after above bandgap pumping happens due to relaxation of the excited carriers through three different pathways corresponding to (1) relaxation within the pillar, (2) surface recombination, and (3) diffusion and relaxation within the bulk.

Anisotropic crystals can have different signs of $\varepsilon(\omega)$ along the three principal axes, leading to peculiar SPhP propagation in these materials. A well-known crystal exhibiting this property is hBN, which is characterized by opposite signs of the dielectric function in the in-plane direction $\varepsilon_t(\omega)$ and in the one perpendicular to it $\varepsilon_z(\omega)$.[414] In Figure 27c, the real part of the hBN dielectric function in the two perpendicular directions is shown. Two Reststrahlen bands are present in the mid-IR, one in which $\varepsilon_z(\omega) < 0$ and $\varepsilon_t(\omega) > 0$ (lower band), and one in which the signs are reversed (upper band). The momentum isofrequency surfaces are hyperboloids of either Type 1 (lower band) or Type 2 (upper band), as shown in the inset of Figure 27c. As a consequence, surface waves excited in this material are called hyperbolic phonon polaritons (HPhPs), which can only propagate in a specific direction with respect to the optical axis, determined as $\theta(\omega) = \arctan\left(\sqrt{\frac{\varepsilon_z(\omega)}{i\varepsilon_t(\omega)}}\right)$.[414] Arrays of hBN cones supporting localized HPhPs have been investigated in the far-field[414] and near-field.[589−591] HPhPs are internally reflected at specific angles in the cones, as it can be seen from electromagnetic simulations and near-field measurement performed with scattering−scanning near-field optical microscopy (sSNOM)[589] as shown in Figure 27d for the UTM_{13} resonance of the structure (U stands for the upper band, TM indicates the transverse magnetic nature of the mode, $l = 1$ and $m = 3$ indicate the z-axis angular momentum and orbital index, respectively). Similar near and far-field studies have been carried out with different hBN metasurface geometries.[592−594] An extremely high Q factor of up to 500 was obtained with image HPhPs, where the hBN layer is separated from a metal mirror by a nanometric gap. Coupling with far-field radiation was obtained by patterning the underlying metallic mirror in a metasurface geometry.[595] While hBN naturally supports out-of-plane HPhPs, in-plane hyperbolicity can be obtained by patterning of the surface. A metasurface composed of grooves in a hBN slab was demonstrated to support in-plane anisotropic HPhPs, which were directly measured with sSNOM.[596,597] In Figure 27e, a sketch of the effect of the metasurface on HPhP propagation is shown. A dipole placed close to a hBN slab produces out-of-plane HPhPs that are isotropic in the plane as can be seen from the simulated $Re(E_z)$. If the dipole is placed close to the metasurface, the HPhPs acquire also an in-plane hyperbolicity, as can be seen from Figure 27e. To confirm the in-plane anisotropy, a gold antenna was fabricated on the metasurface,

Figure 27. Phonon polariton metasurfaces. (a) Tuning of LSPhPs in a SiC pillar array by carrier injection through above-bandgap pumping at 266 nm. Reflectivity spectra are taken at different pump powers and normalized by the SiC substrate. (b) Time resolved change in the reflectivity at 936 cm^{-1} following carrier injection and scheme of the different recombination mechanisms. (c) Real part of the in-plane (green) and out-of-plane (purple) components of dielectric function of hBN. Inset: momentum isofrequency surfaces for the two Reststrahlen bands. (d) Simulated tangential E-field and sSNOM measured near field profiles in a hBN truncated cone. (e) Real part of E_z from a dipole source emitting close to a hBN slab (top) and metasurface (bottom). (f) Launching of in-plane anisotropic HPhPs on the hBN metasurface: topography (left) and sSNOM image (right). (g) Boundary between a topologically trivial and nontrivial Si triangular holes metasurface. A hBN flake (green region) is deposited on the metasurface, achieving strong coupling. (h) Launching of topologically protected HPhPs edge states, which are directionally locked to the photon spin. f_{TO} indicates

Figure 28. Metasurfaces for SEIRA. (a) SEM images (top) of NPG vertical nanoantenna array and EM simulation (bottom) at 8 μm for bulk gold and at 9 μm for NPG. (b) Reflectance spectra (left) for NPG vertical antenna arrays for different pitches with a 3 nm SiO$_2$ coating (phonon in the light blue area) and evaluation of SEIRA coupling (right) for gold and NPG structures by Fano fit. (c) Transmittance spectra for a hBN ribbon metasurface covered with a layer of CBP for various thicknesses. (d) Same metasurface covered with a 30 nm-thick CBP layer with varying ribbon width. (e) SEM (top) and EM simulation at resonance for a Si metasurface supporting BIC states. (f) Reflectivity spectra of the pixelated metasurface composed of arrays with different scale factors, shifting the BIC resonance. In the top panel, images of the full pixelated metasurface at different frequencies are shown. (g) Modulation of the pixelated metasurface upon physisorption of A/G protein of the surface. (a,b) Adapted with permission from ref 616. Copyright 2017 The Royal Society of Chemistry. (c, d) Adapted with permission from ref 628. Copyright 2018 Springer Nature. (e−g) Adapted with permission from ref 113. Copyright 2018 AAAS.

acting as a source of HPhPs, which were measured with sSNOM. In Figure 27f, the result of the sSNOM measurement is shown, confirming the in-plane anisotropy and hyperbolic nature of the HPhPs launched from the gold rod.

Recently, the possibility of creating topological edge states with SPhPs has been explored.[598,599] Topological edge states have attracted considerable interest as they enable unidirectional propagation free from back scattering.[600] These edge states arise at the boundary between two structures characterized by different topological phases (i.e., one structure can be obtained from the other by a topological phase transition). For SPhPs, edge states can be created by direct patterning of a suitable material[599] or by achieving strong coupling between a polar material and an underlying topological metasurface.[598] In Figure 27g, an example of this latter method is shown, where a few-layer hBN flake is deposited on a Si metasurface with nontrivial topology. Reaching the strong coupling regime is necessary to impart to the HPhPs of hBN the topological properties of the underlying metasurface. The employed structure made of triangular holes is known to support a topological transition when the unit cell is modified from shrunken to expanded.[601,602] The shrunken structure with nontrivial topological phase is characterized by having the triangles in the unit cell closer to each other than the triangles of the adjacent unit cell, while the opposite happens in the expanded structure. The edge states are achieved at the zigzag boundary between the two topological phases, on top of which the hBN is deposited, as shown in Figure

27g. The results obtained by exciting edge HPhPs at different locations with different polarizations are reported in Figure 27h. In the top panel, the excitation position on the boundary and the polarization used are reported. By tuning the wavelength and in-plane momentum of the excitation, the ratio of phononic to photonic character f_{TO} of the mode can be tuned ($f_{TO} = 1$ corresponds to a purely phononic mode, $f_{TO} = 0$ to a purely photonic one). The measurements show that when the mode has both phononic and photonic character ($f_{TO} = 0.48$), HPhPs are unidirectional and locked to the spin of the incident light, which are typical characteristics of edge states. When the mode is instead mainly phononic ($f_{TO} = 0.88$), these properties are lost. As the thermal conductivity of thin films depends on the presence and characteristics of SPhPs,[603,604] topological edge states are promising for achieving unidirectional heat sinks at the microscale.[598]

While we concentrated on metasurfaces made of either SiC or hBN, other polar dielectrics have been recently explored for LSPhPs such as GaN,[605] InP,[588] and calcite.[606] Reconfigurable devices have been demonstrated by combining hBN with a phase change material, which influences the propagation of HPhPs and allows the realization of 2D metalenses.[420]

4.3.2. Metasurfaces for Surface Enhanced Infrared Absorption and Surface Enhanced Raman Spectroscopy. Spectroscopic investigation of the vibrational properties of molecules or solids allows their unambiguous chemical identification because the vibrational fingerprint is different for

every molecular composition. The most common vibrational optical characterization techniques are IR spectroscopy[607] and Raman spectroscopy.[608] These processes involve the energy transfer between an incident photon and the lattice excitations of a solid or vibrational levels of a molecule. Molecular vibrations are IR active if their excitation causes a change in their dipole moment,[607] while they are Raman active if they are associated with a change in polarizability.[608] Unfortunately, IR vibrational cross-sections are quite commonly due to the size mismatch between typical molecules (on the order of nm) and IR wavelengths (on the order of μm),[609] while Raman intensities are inherently weak because they originate from a scattering phenomenon.[610] To achieve the highest possible sensitivity, optical antennas can be used to enhance local EM fields in nanoscale hotspots and increase the energy transfer between photons and molecular vibrations or phonons in crystals. Here, we review some examples of the many different metasurfaces that have been devised in the past years for surface enhanced IR absorption[14] (SEIRA) and surface enhanced raman scattering (SERS).[610]

In SEIRA, the direct IR absorption of target molecules is enhanced by concentrating the local near-fields around the surface of optical antennas resonating in the mid-IR.[14,609] Metasurfaces have been extensively explored for SEIRA to obtain enhancement over large areas. The first SEIRA experiments have employed the near-field enhancement provided by resonant plasmonic antennas and metasurfaces.[16,17,51,148,611−617] The ratio between the field amplitude with and without the antenna can reach values of 10−100 in the hotspots, depending on the detailed geometry. The vibrational signal is enhanced by a factor of $|E/E_0|^2$,[618] providing SEIRA enhancements exceeding 10^4 in best case scenarios.[619] Most metals behave similarly in the mid-IR, much below the plasma frequency and interband transition, where they are characterized by large negative values of the real part of the dielectric function and low penetration depths. In Figure 28a and b, an example of SEIRA with 3D plasmonic vertical antennas[620,621] is shown.[616] To increase the overlap between the target molecules, nanoporous gold (NPG) was used to fabricate the antennas, as shown in the SEM image in Figure 28a. NPG can be modeled with effective medium theories,[616] and the electromagnetic simulations demonstrate that in this configuration the field penetrates much more inside the antennas compared to an identical structure made of bulk gold. The antennas were then covered with 3 nm of SiO_2 and their reflectivity spectra were measured for different pitches P of the array. The results are shown in Figure 28b, where the antenna resonance blueshifts with decreasing pitch, finally overlapping with the SiO_2 phonon at 1240 cm^{-1} (indicated by the light blue area) for the smaller pitches. When the two dips from the antenna resonance and from the molecular vibration overlap, the depth of the dip is reduced. This is a general phenomenon arising due to interference between the dipole induced in the antenna and the dipole induced in the molecule and can be described as a Fano resonance.[14,622] The reflectivity lineshapes were fitted with a Fano model, which allowed the estimation of the energy transfer between plasmonic antenna and the SiO_2 phonon. The coupling term is plotted in the right panel of Figure 28b, showing higher energy transfer for the NPG antennas (red curve) compared to an identical gold structure (blue curve).

In the mid-IR, plasmons can be sustained not only by metals but also by highly doped semiconductors, in which the plasma frequency is pushed to high frequencies by the high density of

carriers.[623,624] Doped semiconductors are particularly interesting for mid-IR plasmonics as they are similar to metals in the visible, being characterized by small negative values of ε_1 and possibly providing better confinement. Moreover, they can be integrated more easily in state-of-the-art silicon foundries, as they are complementary metal−oxide−semiconductor (CMOS) compatible, while most metals are not. SEIRA has been investigated in doped semiconductor antennas, showing remarkable enhancement of vibrational absorption.[624−626] Since, to obtain high SEIRA enhancements, frequency matching between the plasmonic structure and the molecular vibrations is needed, it would be ideal to employ a tunable metasurface so that different molecular vibrations can be investigated. This was achieved by leveraging the tunability achieved through electric gating of a nanoribbon graphene metasurface.[627]

Metasurfaces supporting LSPhPs have also been investigated for applications in SEIRA.[627,629,630] While LSPhPs can provide better enhancement than plasmonic materials due to lower losses, they exist in a small, material-dependent frequency range, limiting their usage as sensors to few selected molecular vibrations. In Figure 28c and d, an example of SEIRA with hBN nanoribbons supporting localized HPhPs is reported.[628] The ribbons are fabricated on an IR-transparent CaF_2 substrate and covered by thin layers of 4,4′-bis(N-carbazolyl)-1,1′-biphenyl (CBP), which has a vibrational absorption (vertical gray dashed line) in the Reststrahlen band of hBN, as can be seen from the top spectra of Figure 28c. Twenty nanometers of CBP in the absence of any SEIRA effect produced a signal below the noise threshold. The transmission spectra of the bare nanoribbon metasurface are shown in Figure 28c, characterized by a dip corresponding to the resonance frequency of the antennas. The resonance redshifts with increasing thickness of the CBP layer covering the antennas due to change in the refractive index of the surrounding. When the resonance of the antenna matches the frequency of the vibrational absorption of CBP, a Fano line shape appears as a result of the coupling between the antenna and the vibrational resonances. For each CBP thickness, the spectra of the bare metasurface are shown as a guide to the eye, with a shift in the frequency to match the refractive index induced redshift. In Figure 28d, a similar experiment is reported, where the CBP thickness is constant and the antenna resonance is shifted across the vibrational absorption by changing the ribbon thickness. The typical Fano line shape is observed in this case, too, with an anticrossing behavior attributable to strong-coupling between the antenna resonance and the molecular vibration.[628] The Q factor of the antenna resonances and the corresponding SEIRA efficiency has been recently shown to be increased when using monoisotopic ^{10}B hBN (the subscript 10 indicates here the atomic mass number of Boron) instead of naturally abundant hBN (composed by 80.1% of ^{11}B and 19.9% of ^{10}B)[427] due to the reduced phonon scattering rate associated with having a single isotope in the material.[631]

With the recent development of BIC-based dielectric metasurfaces, IR fingerprint sensing with these extremely narrow resonances has been developed in the past few years.[113,631−633] BIC resonance frequencies can be finely tuned by changing the scale factor S of the unit cell of the metasurface. By implementing small increments of the scale factor, pixelated metasurfaces made of arrays with different resonant wavelengths covering a broad frequency range can be fabricated.[113] Pixelated metasurfaces can be used in conjunction with a tunable QCL emitting in the IR and an IR camera to perform on-resonance SEIRA for many different frequencies, resulting in the retrieval

of the full vibrational spectrum under investigation with enhanced sensitivity in a single measurement run. In Figure 28e−g, the results obtained for a pixelated metasurface made of tilted elliptical silicon antennas are reported. For the array with S = 1, a representative SEM image and simulation of the near-field electric field intensity for the unit cell are shown in Figure 28e. By changing the scale factor from 1.00 to 1.34, the resonant frequency of the metasurface is shifted from approximately 1300 cm^{-1} to 1800 cm^{-1} in 100 steps without significant change in the line shape profile. The normalized reflectivity spectra for 21 of the 100 pixels are shown in Figure 28f together with four reflectivity images of the full pixelated metasurface at four selected frequencies. An image of the full pixelated metasurface highlighting the resonant peak wavelength for each pixel is also reported in Figure 28f. When adding a thin layer of protein A/G on top of the metasurface, the reflectivity for each pixel is modulated following the vibrational spectrum of the adsorbed molecules. For each pixel, the reflectivity is strongly suppressed at frequencies matching the vibrational fingerprint of the molecules, as shown in Figure 28g. Spectral integration of each pixel can be used to produce a 2D absorption map, which represents the molecular barcode of the protein.[113]

While in IR absorption spectroscopy, the illuminating wavelength must match the frequency of the target vibrational level, Raman scattering involves excitation to a virtual level and in principle can occur for any pumping wavelength.[608,610,634] In practice, the Raman scattering cross-section scales with the pumping frequency as $\sigma \propto \omega^4$ and so shorter wavelengths in the optical regime are preferred.[322] The Raman scattering cross-section has other frequency-dependent properties, related to the electronic levels of the investigated molecule. In particular, close to a real electronic transition, Raman cross-sections can be orders of magnitude larger, leading to the so-called resonant Raman effect.[635] While in SEIRA the signal enhancement due to the presence of an antenna scales as $|E/E_0|^2$, in SERS the scaling goes as $|E/E_0|^4$ enabling the realization of much higher enhancement factors.[610] The reason of the $|E/E_0|^4$ dependence can be intuitively understood as follows: the absorption of the molecule is enhanced by the intensity of the electric field at the illumination frequency $|E(\omega_L)|^2$, while the emission of the induced dipole is also enhanced by the local field at the emission frequency, by a factor that can be approximated by $|E(\omega_L \pm \omega_{vib})|^2$, where ω_{vib} corresponds to the frequency of the vibrational level with which energy was exchanged.[610,636] The $\pm$ signs indicate the possibility of having both Stokes ($\omega_{scatt} = \omega_L - \omega_{vib}$) and anti-Stokes ($\omega_{scatt} = \omega_L + \omega_{vib}$) processes. As the Raman shift is generally small compared to the illuminating frequency, often the product of the SERS enhancement is approximated by the field at the pumping frequency $|E(\omega_L)|^2 \times |E(\omega_L \pm \omega_{vib})|^2 \approx |E(\omega_L)|^4$. In the absence of very narrow resonances, this is a good approximation for the enhancement of Raman signals in the vicinity of an antenna.

Because metasurfaces can be used to confine EM fields over large areas, they have been explored for SERS. In particular, SERS active plasmonic metasurfaces have been investigated in flexible electronics devices for ultralow detection of biomolecules.[636−638] Supercluster metamaterial nanoparticles[259] and plasmonic supercrystals[262,639,640] were explored for SERS due to their high density of hot-spots and confined optical modes inside the structures. To obtain optimal enhancement, plasmonic metasurfaces can be designed to precisely enhance both excitation and emission processes in SERS by supporting resonances at both frequencies.[641] Fabrication efforts have been

directed toward the realization of controlled large scale methods to achieve mm and cm sized plasmonic substrates[642−644] with nanometric gaps for high SERS enhancement and low fabrication costs.[642,645−647] In Figure 29a, an example of a
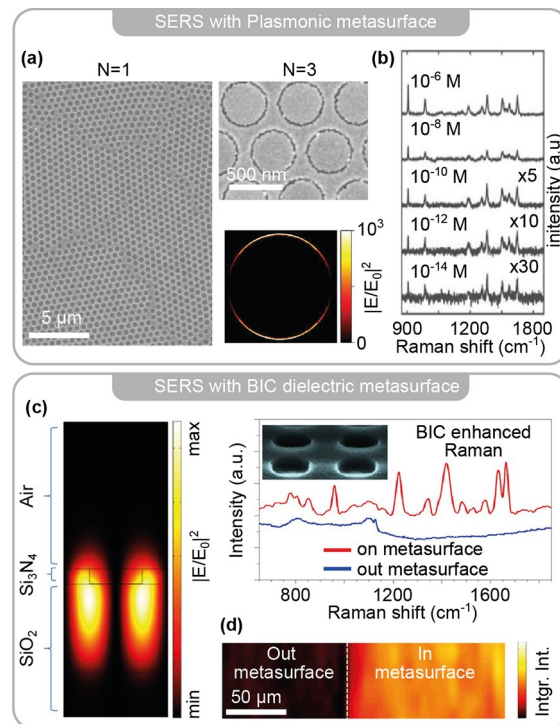
Figure 29. Metasurfaces for SERS. (a) SEM image (left) of large area surface NRG array with 3 nm gap (N = 1 SAM monolayer). SEM image (right, top) of a close up portion of a NRG array with 10 nm gap and F.E. intensity simulation for a NRG in the array for N = 1. (b) SERS signal for the NRG array with 3 nm gap for different concentrations of R6G. (c) F.E. intensity simulation (left) for a unit cell of the BIC metasurface and SERS signal in and out of the structure from crystal violet dye. (d) Integrated Raman intensity in and out of the metasurface decorated with gold NPs. (a, b) Adapted with permission from ref 648. Copyright 2021 Wiley-VCH GmbH. (c, d) Adapted with permission from ref 653. Copyright 2018 American Chemical Society.

large area nanoring array (NRG) structure obtained by a combination of nanosphere lithography, physical peeling, and SAM is reported.[648] The gap size of the NRG is controlled by changing the number of SAM molecules attached to the gold surface. The resulting gap size is approximately a multiple integer N of the SAM length, which is around 3 nm. The NRG arrays were investigated for SERS under 633 nm laser illumination, achieving a detection limit of 10^{-14} M for rhodamine 6G, as reported in Figure 29b. A special feature and benefit that has been investigated with metasurfaces for SERS is the broadband design, which makes the platforms more reproducible over a large spectral range and widely applicable to many different target molecules, a key aspect in SERS.[635] To this end, broadband response has been obtained by specifically engineering both ordered[649] and disordered[650,651] metasurfaces.

Besides plasmonic structures, it has been recently shown that dielectric nanoantennas can also enhance the Raman signal of molecules.[292,652,347] Even though dielectric metasurfaces generally present lower field enhancements compared to plasmonic analogues, the absence of temperature increase related to ohmic losses makes them promising in biological
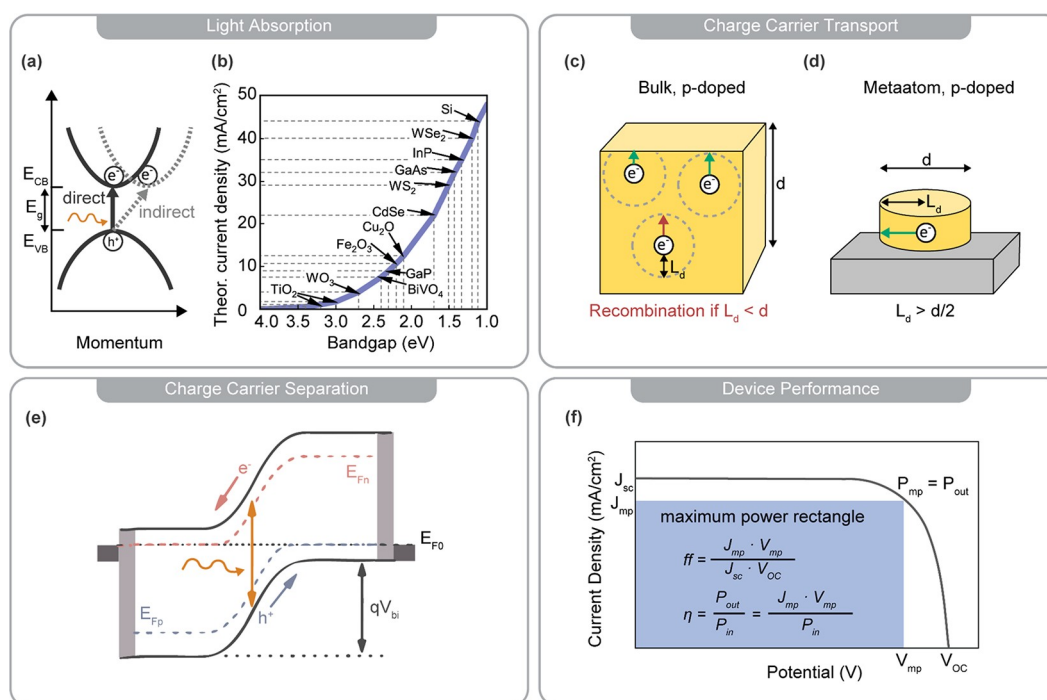
Figure 30. General requirements for photon-electron energy conversion. (a) Schematic illustration of light absorption inside a direct or indirect semiconductor. (b) Theoretical maximum photocurrent density in dependence of the band gap for semiconductors under one-sun illumination. (c, d) Charge carrier transport in (c) bulk material and in a (d) meta-atom. L_d is the minority charge carrier diffusion length. Recombination occurs if the thickness d is larger than L_d. However, the thickness d needs to be large enough which is necessary for many semiconductor materials to allow sufficient light absorption. Because of their small size, metasurfaces allow to utilize materials with small L_d, which could not have been utilized as bulk material. (e) Band diagram of a $p-n$ junction utilized for charge carrier separation. Illumination generates electron (e^-)–hole (h^+) pairs, which are separated by moving in opposite directions using the built-in potential V_{bi}. E_{F0} is the aligned Fermi level of the n-doped and p-doped semiconductor after equilibrium. E_{Fn} and E_{Fp} are the quasi-Fermi levels during illumination. (f) Exemplary current density–potential plot to evaluate device performance of photovoltaic and photocatalytic devices. (b) Adapted with permission from ref 659. Copyright 2014 American Chemical Society. (e) Adapted with permission from ref 660. Copyright 2019 Wiley-VCH GmbH. (f) Adapted with permission from ref 661. Copyright 2011 Academic Press.

applications with delicate samples. As such, all-dielectric metasurfaces have been tested for enhancing the Raman signal of small molecules[653] or even viruses.[654] A BIC-based metasurface made of holes in a 50 nm Si_3N_4 layer on glass was demonstrated to achieve an enhancement of 10^3 for SERS detection for the reference dye crystal violet.[653] Tuning to the BIC resonance allowed a clear enhancement compared to the unpatterned surface, as shown in Figure 29c. Coupling of the BIC resonance to LSPR was also explored by covering the whole surface with randomly dispersed 40 nm gold NPs. A 13-fold enhancement of the metasurface compared with the unpatterned area was achieved in this way. An integrated SERS map covering the boundary of the metasurface is shown in Figure 29d, allowing direct visualization of the enhancement provided by the metasurface when the sample is covered by plasmonic NPs.

4.4. Section Summary

To summarize, metasurfaces can contribute to photon-phonon energy conversion in the following ways:

1. Ohmic losses from plasmonic metasurfaces (thermoplasmonic effect) can be used to control temperature profiles at the nanoscale.

2. Coupling of light to nanostructured polar dielectrics leads to the excitation of mixed photon-phonon states in the mid-IR called surface phonon polaritons, analogous to SPP in metals, but with lower losses.

3. Patterning the surface of a material at dimensions below the thermal radiation wavelength λ_{th} can lead to modification of standard blackbody radiation achieving polarized, frequency selective and unidirectional thermal emission.

4. Metasurface-controlled thermal radiation can be engineered to achieve applications such as IR camouflage and passive daytime radiative cooling.

5. Near-field radiative energy transfer can be manipulated with metasurfaces, but its experimental realization has not been demonstrated thus far.

6. Incidence of light on metasurfaces allows generation of tailored SAWs and their manipulation, making them directional and creating phononic band gaps.

7. Metasurfaces have been employed for enhanced spectroscopies such as SEIRA and SERS.

5. PHOTON−ELECTRON ENERGY CONVERSION

The efficient conversion of photon energy into electricity holds great promises for environmental sustainability. Up to now, the primary global energy sources are still coal, oil, and gas, which cause release of greenhouse gases. The amount of solar power delivered, roughly 10^5 TW, is significantly larger than human requirements, predicted to be around 20−40 TW in 2050.[7,8,655] Hence, it should be sufficient to cover 1% of the land on earth by photoelectrochemical (PEC) cells with 10% efficiency to satisfy our energy demand, as pointed out by Jiang et al.[655,656] Clearly, efficient photon-electron energy conversion would allow human

society to meet the energy needs from a carbon free, renewable source. Currently, photovoltaic cells are utilized to convert the energy of the sun into electricity and more than 90% of all solar cells are made from silicon.[657] From a material perspective, silicon has great properties to be used for solar cells. Its small band gap of about 1.14 eV allows the absorption of even near-IR photons, while the material is nontoxic and abundant. Since silicon is extensively used in the microelectronic and IC industry, silicon wafers can be mass-produced at large scales. However, silicon is an indirect gap semiconductor and requires a sufficient thickness to absorb large portions of the incoming light (see section 2.1) and in addition, a high purity is necessary, since impurities will cause recombination of charge carriers.[658] Therefore, researchers are trying to develop new materials for photon−electron energy conversion with enhanced functionality, performance, and decreased material costs to accelerate their worldwide implementation.[286] In this section, we summarize recent research involving metasurfaces for photovoltaics and photocatalysis as well as other applications benefiting from improved photon−electron energy conversion such as photodetectors.

5.1. General Requirements for Photon−Electron Energy Conversion

There are several aspects to consider when designing the ideal material for photon−electron energy conversion. In general, light absorption and energy transport are important for both photovoltaics and photocatalysis, while photocatalytic cells have additional thermodynamic and kinetic requirements to drive the desired chemical reactions (section 5.4.1). We will begin by summarizing the shared requirements for both fields together with important characteristics to evaluate their performance, which are schematically illustrated in Figure 30.

5.1.1. Light Absorption. Illumination of a semiconducting material above its bandgap energy will lead to the formation of charge carriers, that is, electrons and holes in the conduction and valence band, respectively (Figure 30a). The physical principles of light absorption and formation of excitons were already treated in more detail in section 2.1. It is possible to define two types of excitons based on the relative length of the radius between the particles, a_B, also called Bohr radius, and the lattice constant of the material, $a_{lattice}$. For the case that $a_B \approx a_{lattice}$, the exciton is confined inside a unit cell of the crystal. These are so-called Frenkel excitons and are usually found in organic or polar materials. However, in most semiconductor materials, we find the case where a_B is larger than $a_{lattice}$ and the exciton extends over multiple unit cells of the crystal. These are the so-called Wannier-Mott excitons, which provide the possibility for a generated electron−hole pair to diffuse throughout the materials. In this way, excitons can reach an interface where they can dissociate into free charges, giving rise to an effective current flow, or recombine in a radiative process where the annihilation of the electron−hole pair results in the emission of a photon, with energy corresponding to the exciton binding energy, smaller than that of the material's energy gap.

To achieve broadband light absorption and the highest possible photocurrent density, the semiconductor band gap E_g should be as small as possible. Figure 30b shows the theoretical maximal photocurrent densities of different (bulk) semiconductors under one-sun illumination assuming that all incident photons above the band gap contribute to the photocurrent.[659] Traditionally, solar cells made from mono- or polycrystalline silicon are utilized, having a small indirect band

gap, which requires a sufficient thickness of material for light absorption. In general, the thickness of the photoactive material should be large enough to generate a high density of charge carriers and an important parameter is the light penetration depth (LPD, also named as skin depth), which is defined as the depth at which the electric field amplitude falls to $1/e$ ($\sim 37\%$). The LPD depends on the absorption coefficient of the material and therefore varies for different wavelengths. For example, in silicon, blue light (400 nm) is absorbed within 0.1 μm while NIR light (900 nm) already requires a thickness of several hundreds of micrometers.[286,662] To account for this thickness-dependence of the optical absorption, a photovoltaic band gap E_g^{PV} can be defined. Contrary to the optical bandgap E_g, the E_g^{PV} is not an intrinsic material property.[663] In general, most semiconductors, even direct ones, require at least a couple hundreds of nanometers to absorb sufficient amount of light.[286]

While the absorption coefficient is an inherent material property, metasurfaces and nanostructuration can enhance light absorption by engineering the local density of photonic states and also by employing alternative light trapping techniques. This allows reduction of the required amount of material, decreasing fabrication costs and allowing consideration of new materials for photovoltaic and photocatalytic devices.[286,664−668] For example, excitation of localized surface plasmon resonances in metals can highly increase the absorption cross-section in metal nanoparticles,[669] giving rise to energetic (hot) charge carriers that can be used in photovoltaics, photodetection, and photocatalysis.[287,670−672] In the same direction, dye-sensitized solar cells take advantage of the high surface area of nanostructured substrates to maximize the loading of dye molecules that assist in light absorption.[673,674] Light trapping techniques, such as guided modes, Fabry-Pérot resonances, refractive index gradients, and diffraction, can also enhance charge carrier generation in poor absorbing materials such as thin films or large band gap semiconductors.[249,286,675−677] In addition, nanostructured surfaces might also be utilized on top of bulk material to avoid the necessity of antireflective coatings.[678,679]

In this section, we focus on photonically engineered resonances in metasurfaces, which can be tuned to the desired wavelength regime by controlling the size and arrangement of individual building blocks and that allow precise control of light absorption and photocurrent enhancements. Metasurfaces can be utilized to improve photon−electron energy conversion for all types of materials from silicon to other semiconductors such as perovskites.[131,286,677,680]

5.1.2. Charge Carrier Transport and Separation. Once charge carriers are generated in the material, they must be efficiently separated and transported to the surface to be collected. For photovoltaic cells and photodetectors, the charge carriers should be harnessed directly at some electrical contacts, while for photocatalytic cells a chemical reaction should occur at the surface. However, even before charge carriers reach the surface, charge transport needs to be considered since charge carriers can recombine (Figure 30c,d) and consequently lose their energy as heat.

A critical parameter to consider is the minority charge carrier diffusion length L_d, that is, the length charge carriers can travel before recombination. L_d is defined via the diffusion coefficient D and the charge carrier lifetime τ with $L_d = \sqrt{D\tau}$. The diffusion coefficient D depends on the temperature T and the carrier mobility μ with $D = \mu \frac{kT}{q}$.[681] For bulk materials, L_d should be larger than the thickness d of the semiconductor

and recombination occurs when $L_d < d$ (Figure 30c), while d should be larger than the LPD to achieve sufficient light absorption. In general, L_d in semiconductors can vary from a few nm up to several mm but is significantly shorter for polycrystalline or amorphous materials, which are generally more affordable than single crystalline materials.[681−685] In (bulk) solar cells or photodetectors, recombination is mitigated by creating a $p−n$ or $p−i−n$ (i = intrinsic) junction that separate the charge carriers by transporting them in opposite directions (Figure 30e), where they are collected at metal conductors at the front and back of the cell.[660,686−688] A $p−n$ junction is established by bringing a n-doped and p-doped semiconductor into contact. Once in contact, the Fermi levels of both semiconductors align (E_{F0} in Figure 30e), which results in a built-in potential V_{bi} in the depletion region, which is the driving force of the separation. Contrary to electron diffusion, the movement of electrons caused by V_{bi} or in general, due to an electric field, is known as drift mobility. Upon illumination, the Fermi level splits into the quasi-Fermi levels E_{Fn} and E_{Fp} and their energetic difference is the open-circuit potential V_{oc}.[655] A more extensive explanation on the details of the physics of $p−n$ junctions can be found in refs 660 and 686−688. For photocatalytic devices, $p−n$ junctions are utilized for large microstructures to enhance charge separation,[689] while doping in general will cause band bending at the semiconductor−liquid interface, which is discussed in more detail in section 5.4.1.

Because of the small size of the individual building blocks, metasurfaces reduce recombination losses since charge carriers only have to travel small distances to reach the surface or interface of materials (Figure 30d). This is especially true for long-aspect ratio nanostructures, such as nanowires, where charge carrier transport can occur in the radial direction, orthogonal to the axial direction of light absorption, efficiently decoupling light absorption from charge separation.[7,249] In general, metasurfaces or nanostructures avoid the necessity of having semiconductor thicknesses comparable to the LPD, since light absorption is enhanced by photonic states and light trapping techniques. This allows the utilization of materials with small charge carrier diffusion lengths, such as polycrystalline or amorphous semiconductors, which are much more affordable than their monocrystalline counterparts or materials with promising photocatalytic properties, such as Fe_2O_3 or $BiVO_4$, which could not be utilized as bulk materials.[682,683,690,691] Furthermore, since metasurfaces or nanostructured surfaces are ultrathin, they can be embedded inside organic hole-transporting polymers, such as poly(3,4-ethylene dioxythiophene):poly(styrenesulfonate) (PEDOT:PSS), allowing a simplified and more affordable manufacturing process and the production of flexible PV or sensor devices, which are lightweight and mechanically more robust.[198,200,692,693]

5.1.3. Evaluation of Device Performance.
The standard characterization technique for photovoltaic and photocatalytic devices is current density J versus potential plots V (Figure 30f). The measured photocurrent I is normalized to the geometric surface area of the cell and plotted against the applied external potential V. Illumination should be performed by using a solar simulator matching the spectrum of natural sunlight, generally known as AM 1.5 G (air mass coefficient 1.5 global) to have realistic operating conditions and allow a comparison of different literature results. Important parameters, characterizing the performance of the cell, can be directly determined from the $J−V$ plots such as the short-circuit current density J_{sc} and open-circuit potential V_{oc} and the current density and voltage at the

maximum power point, J_{mp} and V_{mp}, respectively (Figure 30f). The filling factor ff is then defined via $ff = \frac{J_{mp} \times V_{mp}}{J_{sc} \times V_{OC}}$ and compares the maximum power under operating conditions ($P_{mp} = J_{mp} \times V_{mp}$, illustrated by the maximum power rectangle in Figure 30f) with the theoretical maximum power under open-circuit and short-cut conditions ($P_{max, theor.} = J_{sc} \times V_{oc}$). The filling factor is related to surface and bulk recombination[694,695] as well as solution resistances (for photocatalytic cells)[694] or contact resistances (for PV cells).[695,696] The overall efficiency η is then defined by the ratio of the maximum power under operating conditions $P_{mp} = P_{out}$ and the incoming illumination power P_{in}:

$$\eta = \frac{P_{out}}{P_{in}} = \frac{J_{mp} \times V_{mp}}{P_{in}} = \frac{J_{sc} \times V_{oc} \times ff}{P_{in}} \tag{5.1}$$

For a more detailed analysis of the cell performance, the external and internal quantum efficiencies should be determined, EQE and IQE, respectively. These efficiencies can reveal fundamental properties of the photovoltaic or photocatalytic cell and characterize whether light absorption, charge transport, or charge transfer limit the performance. Quantum efficiencies are also important in evaluating the performance of photodetectors. For photocatalytic cells, which often require external voltage to operate, EQE and IQE values are more frequently reported than efficiencies. The EQE is often called the incident-photon conversion efficiency (IPCE). IPCE or EQE measures the ratio between the collected electrons by the cell against the number of incident photons,[212,697] and is defined, as

$$EQE(\lambda) \ [\%] = IPCE(\lambda) \ [\%]$$
$$= \frac{electrons \ [cm^{-2} \ s^{-1}]}{incident \ photons \ [cm^{-2} s^{-1}]} \times 100$$
$$= \frac{c \times h \times J_{ph}(\lambda)}{\lambda \times P_{Light}(\lambda)} \times 100 \tag{5.2}$$

with c being the speed of light, h being the Planck constant in eVs, $J_{ph}(\lambda)$ the photocurrent density at the wavelength λ, and $P_{Light}(\lambda)$ the irradiance of photons at the wavelength λ. The IPCE should be measured using a monochromatic lamp or band-pass filters with narrow bandwidths. For photocatalytic cells, which often require an additional external potential, measurements should be performed in the dark and under illumination (or chopped) to obtain the photocurrent density $J_{ph}(\lambda)$ by subtraction. In addition, the applied external potential should be reported. High IPCE values indicate perfect conversion of the incident photons. The IQE can then be calculated from the IPCE curve by dividing the IPCE by the measured absorbance A ($A = 1 − R − T$). The IQE is defined as the absorbed photon-to-current conversion efficiency (APCE):[697]

$$IQE(\lambda) \ [\%] = APCE(\lambda) \ [\%] = \frac{IPCE(\lambda)}{absorbance(\lambda)} \tag{5.3}$$

The APCE decouples the IPCE from the absorbance of the device. Therefore, the APCE is dependent on the charge-transport ($\eta_{separation}$) and charge-transfer efficiency ($\eta_{transfer}$), with APCE $\approx \eta_{separation} \times \eta_{transfer}$, while IPCE is additionally dependent on the charge generation efficiency with IPCE $\approx \eta_{optical} \times \eta_{separation} \times \eta_{transfer}$.[7,697]
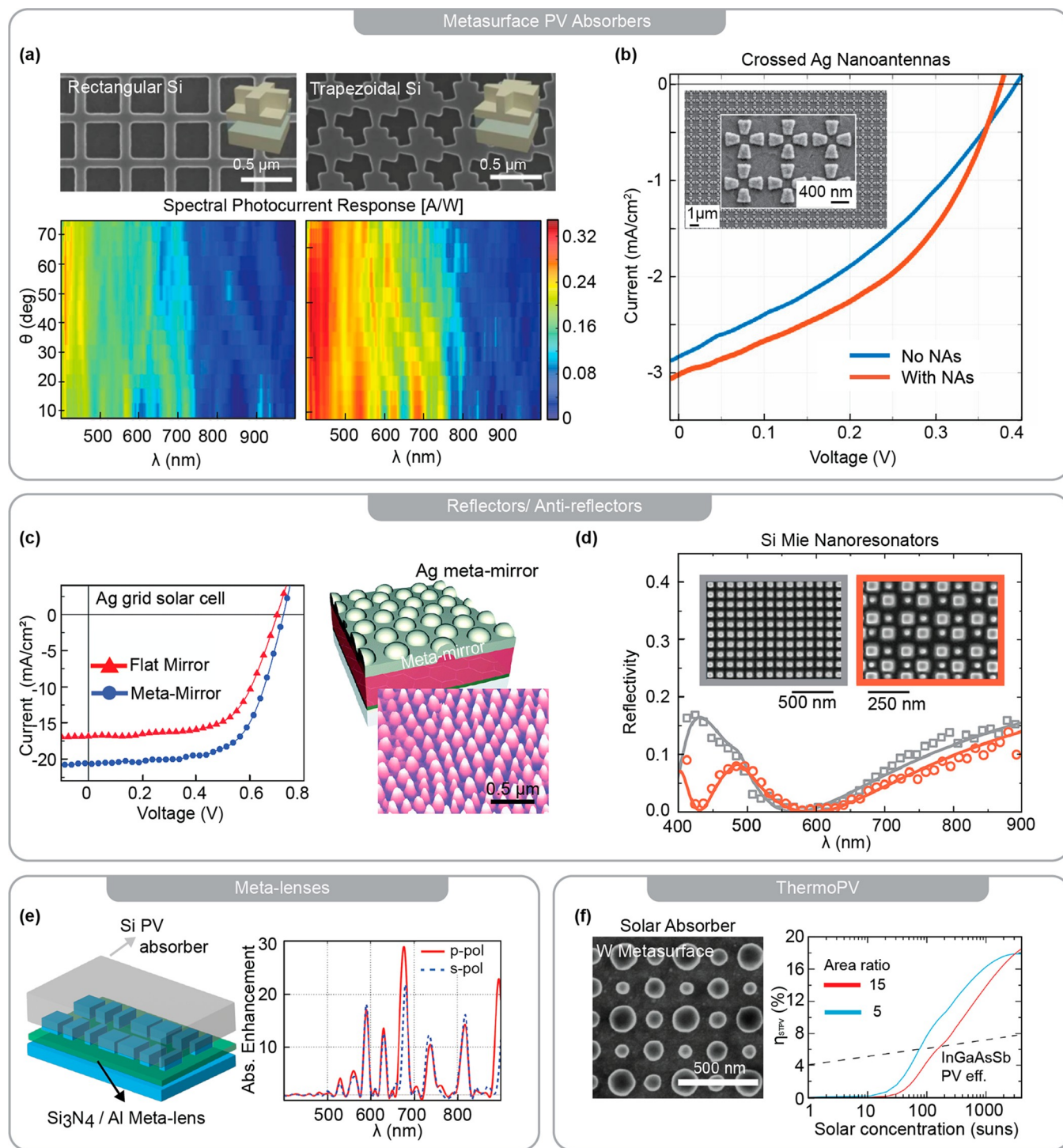
Figure 31. Metasurfaces for photovoltaic devices. (a) Rectangular and trapezoidal Si Mie resonators with omnidirectional and broadband spectral response. (b) Ag nanostripped metasurface sustaining collective leaky-domino modes in an organic PV device resulting in enhanced power conversion efficiency. (c) Plasmonic Ag meta-mirror as a back-reflector in an organic PV device. (d) Si Mie resonator antireflective metasurfaces with tunable reflectivity. (e) Silicon nitride/aluminum meta-lenses showing absorption enhancement in a thin-film Si PV device. (f) Refractory tungsten metasurfaces solar absorbers for thermophotovoltaics showing calculated STPV efficiencies of metasurfaces with different emitter to absorber ratios (red and blue) compared to a single InGaAsSb PV device (black dotted line). (a) Adapted with permission from ref 709. Copyright 2016 Springer Nature. (b) Adapted with permission from ref 721. Copyright 2018 American Chemical Society. (c) Adapted with permission from ref 722. Copyright 2016 The Royal Society of Chemistry. (d) Adapted with permission from ref 725. Copyright 2018 American Chemical Society. (e) Adapted with permission from ref 726. Copyright 2018 Optica Publishing Group. (f) Adapted with permission from ref 727. Copyright 2018 American Chemical Society.

5.2. Metasurfaces for Photovoltaics

Many important aspects considering the basic operation principle of photovoltaic cells were already discussed in the previous sections, such as light absorption in semiconductors (section 2.1), the theoretical maximum photocurrent density and light penetration depth (section 5.1.1), charge carrier transport (section 5.1.2), and important characteristics to evaluate cell performance (section 5.1.3). The upper limit for the conversion of photons into electricity for a single $p-n$ junction-solar cell is given by the Shockley-Queisser (SQ) model, which is based on thermodynamic considerations.[663,698] The SQ limit takes into account the solar spectrum, the theoretical maximum optical absorption given by the materials bandgap and the operating temperature. The main losses are due to the transparency of the solar cells to photon energies below the band gap (~25% losses for $E_g \approx 1.3$ eV) and thermalization losses of photons with energies above the band gap (~30%).[699] Smaller losses account for the power conversion efficiency of a Carnot engine (heat engine), radiative recombination, and the angular inequality of incident and emitted radiation.[699] Usually, real devices will not reach these values due to several assumptions done in the model. For example, the bandgap is treated as a step function with a sharp absorption onset having a quantum efficiency of 100%,[700] and defects leading to nonradiative recombination are not considered.[663,701] Nevertheless, deviations from the optimum performance can be evaluated to improve device performance.[696] Because of their ability in concentrating light, nanostructured devices are promising candidates for exceeding the SQ limit,[699,702−704] For a rigorous discussion of the SQ limit and state-of-the-art (bulk) photovoltaic technologies, we refer the readers to refs 663, 696, 699, and 700.

PV systems can effectively absorb solar energy and convert it into clean electrical power, ultimately providing one of the most outstanding strategies to supply for the increasing global energy demand. The PV market has been largely dominated by bulk crystalline Si solar cells, with absorber thicknesses around 150–300 μm, which require stringent fabrication conditions in terms of material purity and crystallinity. Hence, a lot of recent research effort has been concentrated on developing thin-film PV technologies to reduce production cost and facilitate large scale implementation (e.g., a-Si, GaAs, CdTe, CIGS, organic semiconductors, quantum dots, perovskites). However, since ultrathin layers absorb only a limited fraction of the incident solar light, their power-conversion efficiency has been suffering compared to traditional thick-wafer silicon PV systems. Some of the methods to improve thin-film solar cell efficiencies were focused on material development, engineering of interfaces, and modifying charge carrier dynamics.[705−707] An alternative and highly promising strategy is to utilize light-management strategies to focus and trap light within the absorbing thin-film, alleviating the problem of limited absorption. In this regard, nanostructured plasmonic and dielectric metasurfaces constitute perfect platforms for thin-film PV devices that can be used as antireflective coatings, light-scattering and focusing layers, and broadband superabsorbing films themselves. Additionally, metasurface structures can also play an important part in thermophotovoltaic applications, paving the way to exceed the SQ limit for single $p-n$ junction devices. In this section, we will review some of the main light-management schemes and other novel ideas of using metasurface designs in PV systems.

There are two main requirements for enhancing light absorption in thin film PV devices: (1) to increase the local density of optical states across the solar spectrum and within the light-absorbing material and (2) to have efficient broadband light-coupling from the resonance modes of the photonic structure into the light-absorbing layer. Improvements in these two respects are expected to produce lower recombination currents, higher open circuit voltages, and higher conversion efficiencies in solar cells. Hence, designing metasurfaces that can sustain multiple strong resonances becomes highly important to satisfy these two requirements. To address this challenge, efforts so far have been primarily focused on incorporating dielectric and plasmonic nanostructures arrays in PV devices.

Dielectric Mie resonators, particularly based on silicon, have been investigated as broadband absorbers directly incorporated into the photoactive medium in solar cells.[708] In one highly interesting example, Pala et al. have incorporated lithographically patterned 2D arrays of silicon nanoresonators onto thin film crystalline silicon absorbing layers.[709] They have investigated both rectangular and trapezoidal metasurfaces designs for their absorption properties and spectral photocurrent response (Figure 31a). Silicon nanoresonators exhibit Mie resonances that serve to enhance the short-circuit current densities by at least 2.5-fold compared to flat thin films made from the same material. Furthermore, engineering the metasurfaces into the trapezoidal structures serves to broaden the spectral response of the absorber layer relative to the rectangular design, particularly in the red region of the visible spectrum (Figure 31a). The increased absorption arises from the high-index ridges of the trapezoid not only due to the emerging localized fields in individual ridge regions but also due to the delocalized waveguide modes coming from the interaction of the entire periodic ridge array. Naturally, the frequencies of the emerging resonant modes can be tuned by the size of the trapezoids or the periodic patterns, which outlines the importance of detailed metasurface nanostructuring for achieving higher efficiencies in thin film PV devices. Absorption in dielectric metasurfaces can also be enhanced *via* further nanostructuring of the Si resonators into nanopillars. Länk et al. have fabricated such large area Si metasurfaces by hole-mask colloidal lithography and have demonstrated polarization-independent near-perfect absorption as high as 97%.[710] This value corresponds to an impressive ~50-fold absorption enhancement compared to polycrystalline Si at equal surface average volume density, which can be utilized in solar-harvesting applications such as PV devices.

Compared to the more recent investigations on dielectric Mie resonator absorbers, using plasmonic architectures constitutes a more traditional route in enhancing light-absorption in thin film PV devices.[711−714] Many examples in this regard use regular arrays of plasmonic nanoantennas of various shapes (or metasurfaces) that can effectively transform the EM field of the incoming waves into the near-field, creating hot-spots of concentrated energy. A crucial point to consider when using nanoantennas for light-management schemes in PV applications is the location of these created hot-spots. Ideally, hot-spots formed exclusively on the photoactive medium would result in significant increases in solar light absorption and device efficiency. In one intriguing example, Aydin et al. managed to achieve broadband and polarization-independent superabsorption with Ag trapezoidal ridged metasurfaces in the entire visible range, an architecture similar to the one discussed in Figure 31a in the previous paragraph.[715] While such nanosystems open up paths to realize ultrathin black absorbers in thermal emission applications, from the standpoint of hot-spot locations they can

be undesirable as light-management schemes in PV devices. In this particular example, and more broadly in dipolar plasmonic structures, the EM hot-spots are primarily located within or close to the surface of the metallic nanoantenna resulting in the "harmful" dissipation of solar energy as heat, which is one of the main drawback of using plasmonic metasurfaces for solar cells. Therefore, creating hot-spots beyond the nanoantenna volume would immensely benefit light-absorption within the photoactive medium.

Designing multipolar nanoantenna scatterer arrays and utilizing their collective modes has been the main approach in extending the EM hot-spots further into the near field while keeping broadband absorption in the visible range.[716−718] A number of theoretical and experimental reports in this respect have demonstrated that arrays of tapered Ag nanostrips formed into cross-like structures can sustain multiple collective resonances known as leaky-domino modes. These guided resonances were first demonstrated to emerge in 1D metallic arrays of finite-length parallel strips resembling a chain of domino pieces.[719] The distinctiveness of the domino mode is the very weak penetration of the electric field inside the metallic component. This results in spread-out EM hot-spots rather than concentrating the incoming light to near-surface regions or within the metallic nanoantenna (Figure 31b).[718−720] Particularly in the presence of a nearby absorbing film, the hot-spots can branch into the film and enhance absorption.[720] Accordingly, to investigate the effect of these leaky-domino modes on the efficiency of thin-film PV devices, Voroshilov et al. incorporated such Ag metasurfaces as light-trapping structures into organic photoactive layers (Figure 31b).[721] They observed significant enhancements in all of the main PV parameters including improved short-circuit currents, fill factors, and an 18% increase in the power conversion efficiency of the device (Figure 31b). The leaky-domino modes sustained by the metasurface split the incoming solar light into the hot-spot regions within the organic photoactive layer, decreasing the loss of the light-management scheme and increasing the overall broadband absorption of the device.

Other than being directly implemented into the photoactive absorber layer, metasurfaces can also be utilized in PV applications for their reflection and scattering properties, as back reflecting meta-mirrors (Figure 31c) or as antireflection coatings on the front side of the photoactive layer (Figure 31d). Beginning with the former, conventional metallic mirrors are widely employed in a number of optoelectronic applications as back-reflectors to avoid transmission losses of the incident radiation and trap it within the photoactive absorbing layer.[722,723] However, one of the main drawbacks of these mirrors occurs when they are in direct contact with a semiconducting absorber such as in the architecture of a solar cell. When light is reflected from the mirror surface, the electric field strength is significantly lowered on the near-surface region within one-quarter wavelength of the incident wave.[724] This effect becomes particularly problematic when the absorbing layer is a thin-film with a subwavelength thickness, as it significantly reduces the potential absorption from the reflected light. This problem can be sidestepped and the electric field magnitude at the reflector surface can be increased by using mirrors made out of metasurfaces and metamaterials (i.e., meta-mirrors). By incorporating subwavelength structures onto a conventional metal mirror and modulating their size and shape, one can engineer the reflection properties of the mirror such as its reflection phase and surface impedance.[724] Using these

concepts, a working thin-film organic PV device with a plasmonic Ag meta-mirror as the back-reflector has been demonstrated by Ou and co-workers (Figure 31c).[722] Comparing the meta-mirror device with a reference flat mirror solar-cell has yielded enhancement in the broadband light-absorption and an increase in power conversion efficiency of ∼10%. The broadband enhancement has been largely attributed to the quasi-randomly distributed arrays of nanostructures in the meta-mirror (Figure 31c).

While meta-mirrors can be employed at the back-contact of a solar cell to avoid transmission losses, the front-face of the device can be covered with metasurface antireflective coatings (ARC) to avoid reflection losses (Figure 31d).[677,728,729] In a PV device, a strong reflection arises when the incident solar light hits the surface of the photoactive semiconductor that exhibits a large refractive index. In conventional Si solar cells, 35% of the incoming light in the visible and IR range will be reflected, a remarkable loss for the most important part of the solar spectrum.[730] To circumvent this issue, ARCs have been employed with a common approach of using single or multilayer thin films, such as silicon oxide or silicon nitride,[731] to avoid reflection through the destructive interference principle. Although an ideal ARC is required to exhibit broadband and omnidirectional reflection, these simple thin-film ARCs have narrow wavelength and low angle of incidence ranges.[728] Inspired by the compound eyes of insects and moths, an alternative approach is to use nanostructured arrays to achieve gradient refractive index ARCs, with a wide variety of shapes and sizes, some of which include nanorods, nanocones, and nanopyramids.[732−735] These gradient-index ARCs provide broadband and omnidirectional reflection; however, this is at the expense of fabrication ease and costs.

Novel strategies have been based on using high-index dielectric metasurfaces based on Mie-resonators.[725,736−738] In a pioneering work, Spinelli et al. have shown that a Si nanodisc metasurface with individual discs of 250 nm in diameter yields broadband almost zero total reflectance at a broad range of incidence angles up to 60 degrees.[737] Further design principles of dielectric metasurfaces for ARCs have been explored by Pecora et al.[725] At sufficiently low nanodisc density, metasurface ARCs have been shown to behave significantly different than conventional nanostructured ARCs, with their antireflection primarily dominated by Mie resonances rather than effective optical properties such as the complex refractive index of the film. At this low-density regime, the antireflection properties of the metasurface were argued to rely on the forward scattering of the incident waves toward the underlying photoactive substrate when Mie resonances were excited. Hence, these resonators can enable antireflection in areas larger than their geometric size. Importantly, using dielectric metasurfaces opens the possibility of manipulating the reflectivity of the ARCs by changing the position of the Mie resonance through tuning the shape and size of individual components. For example, by introducing nanodiscs of different sizes in a metasurface, the authors have achieved broader band reflectivity compared to a control metasurface where all the components have a single size (Figure 31d). Other types of resonances can also be incorporated into these metasurfaces, such as the Fabry-Pérot resonance, to improve the spectral energy range of the ARC.[738]

The high control over the spectral and angular range of reflection that can be achieved with dielectric metasurfaces can also pave the way for more focused applications in the PV industry such as the development of integrated solar panels with

various colors. Novel solar cell architectures are necessary for the large-scale implementation of PVs into urban regions such as residential areas and contemporary city buildings. From an aesthetic point of view, the blue/black color of commercial Si devices does not always match with the urban design. Hence, it is increasingly important to develop modules that can have various colors but without sacrificing their power conversion efficiencies. With this aim in mind, tuning the Mie-resonance of dielectric metasurfaces not only enables control over the spectral energy range of reflectivity, by suppressing certain modes and enhancing others, but also can be used to incorporate directionality into the reflected light.[739,740] Among the few examples of metasurface coatings incorporated for colored-PV applications, Uleman et al. have demonstrated a rooftop module where off-resonant blue, green, and near-IR light is transmitted through, while on-resonant red light is selectively scattered between 30 and 75 degrees.[741−743] This gives a red panel appearance to the observers near the building, while light from remaining angles is transmitted to avoid significant losses in power conversion efficiency of the device.

There are a few important points worth mentioning regarding material choice, stability, and fabrication of dielectric metasurfaces for reflective applications. The long-term stability for ARCs can be a point of concern; however, the above-mentioned photonic effects retain even in the presence of a thin surface passivation layer.[725] Compared to conventional nanostructured ARCs and other type of reflectors, these highly ordered metasurfaces can be fabricated with cost-effective methods such as substrate-conformal imprint lithography, nanoimprint lithography, and rolling-mask lithography[736,738] making their implementation into real-life devices much more straightforward. Overall, with such control over the tunability of their reflectivity properties, dielectric metasurfaces hold great promise of outcompeting traditional ARC and reflector systems, with lower fabrication costs and choice of potential materials that can be utilized.

A noteworthy approach in using metasurfaces within a solar cell module is to incorporate them at the back-contact as nanoscale flat lenses (i.e., meta-lenses).[726,744] Focusing incoming light into a photoactive absorbing layer has been previously investigated in the PV community using large and inconvenient 3D lenses installed at the top of the panels.[745] However, nanoscale flat meta-lenses can be fabricated from both plasmonic[746] and dielectric materials[747] based on the concept of optical phase discontinuities, the details of which can be found with an interesting historical perspective elsewhere.[748,749] In a recent work, a reflective Si_3N_4/Al meta-lens was integrated into a thin-film Si solar cell where the focal point was designed to lie within the photoactive absorber layer (Figure 31e).[726] This architecture averted the considerable escape of incident solar light back into the air, enhancing the absorption of the device (Figure 31e) and resulting in a ~1.4-fold increase in the short-circuit photocurrent for both TE and TM polarizations.

Metasurface can also enhance light absorption in solution-processable solar cells based on organic polymers, perovskites, or colloidal quantum dots. These devices often suffer from small diffusion lengths due to associated defects and impurities inherited from their fabrication and require a compromise between efficient charge extraction and efficient light absorption.[750] While plasmonic nanoparticles can be embedded in or between active layers, these systems often suffer from parasitic light absorption, where the excited photocarriers in metal particles decay nonradiatively into heat potentially

degrading the system.[750] In this regard, metasurfaces offer a high flexibility in terms of tuneability to control the enhancement, particularly in the long-wavelength regime, where the optical absorption of these device is low. He et al. designed a plasmonic metasurface at the bottom of a perovskite $MAPbI_3$ layer, which extends the optical absorption around 670−750 nm over a wide angular range, where the absorption of the 100 nm-thick perovskite layer is low.[680] Similarly, metal oxide-based nonresonant metasurface can be utilized as light trapping structures on top of perovskite films.[751] Furthermore, using FIB milling, solution-processed perovskite films could be structured into metasurfaces, such as nanogratings, nanoslits,[140] nanocubes[131] or nanohole arrays,[752] allowing to directly engineer optical Mie resonances in the active layer without the need of additional materials.

As discussed thus far, both plasmonic and dielectric metasurfaces can be integrated into solar cells as components of the photoactive absorber layer, reflectors and antireflectors at the back and front contact, and as nanoscale flat lenses, all of which serve the purpose to improve the power conversion efficiency of traditional PV modules. However, metasurfaces can also pave the way for transitioning into alternative PV concepts, one of which include solar thermophotovoltaics (STPV). The single-junction solar cell efficiency is limited by the predicted SQ limit of 41% with maximum solar concentration due to the energy losses coming from below-band gap photons and hot-carrier thermalization, consequences of the broadband nature of the solar spectrum ranging from 200−2500 nm.[698,704,753] STPV is one of the promising strategies to overcome the SQ limit for solar energy harvesting, with impressive theoretical efficiencies reaching up to 85% under concentrated solar irradiation.[753] In this concept, an intermediate absorber/emitter structure absorbs the incident light, heats-up, and undergoes thermal emission, which is picked up by a PV cell for power conversion. Therefore, an ideal absorber/emitter structure must absorb the whole solar spectrum, withstand high temperatures (>1000 °C), and have a narrowband thermal emission that corresponds to the energy range above the band gap of the accompanying PV device.[753] While a number of material systems have been demonstrated for STPV devices such as photonic crystals, metal/dielectric layers, and doped semiconductors,[754−756] the efficiencies still remain low due to thermal stability issues and poor spectral selectivity.

In this respect, metasurfaces provide a novel platform to investigate absorption/emitter structures in STPV technologies due to their highly tunable optical properties.[493,509,727,757−759] A crucial theoretical and experimental work by Chang et al. has demonstrated this possibility by using refractory W metasurface solar absorbers/emitters coupled to InGaAsSb solar cells that have a bandgap of ~0.55 eV (Figure 31f).[727] The refractory metasurface has been shown to exhibit good thermal stability upon cycling at 1200 °C, which is one of the important shortcomings of other material systems. Using W nanodiscs of different size helped to achieve broadband absorption in the visible to near-IR range (Figure 31f) while modulating the size of the nanodiscs allowed control the thermal emission band. Balance calculations have revealed that a fully integrated W metasurface−InGaAsSb PV system can yield STPV efficiencies of up to 18%, a significant improvement compared to single InGaAsSb device (Figure 31f). Additionally, increasing the emitter-to-absorber area ratio can also be used to increase the efficiencies in the device in a certain solar concentration window (Figure 31f). Even though this work shows great potential for

Table 3. Metasurfaces for Photovoltaic Devices[a]

year	PV material	metasurface design	J_{SC} (mA/cm²)	V_{oc} (V)	FF (%)	PCE (%)	metasurface enhancement on PCE	ref
2021	amorphous Si−H thin film	dielectric nanoarray, GaP on PV layer	12.0					708
2012	amorphous Si thin film	plasmonic nanoarray	19.7 (theo.)			~15 (theo.)		717
		Ag on PV layer nanoarray						
2016	Si thin film	patterned Si PV layer						709
		- rectangular	7.8					
		- trapezoidal	12.0					
2017	Si heterojuction colored PV	dielectric nanoarray, Si coating	33.2	0.7		13.7		742
2018	organic PV phtalocyanine-C60	plasmonic nanorray, Ag on PV layer	3	0.38	43.4	0.49	1.2	721
2016	organic PV PTB7:PCBM	plasmonic nanoarray, Ag Meta-mirror	20.4	0.7	64.2	9.30	1.3	722
2018	thermoPV InGaAsSb	refractory metal, W absorber/emitter				18 (STPV, theo.)		727

[a]Summary over the most important parameters of various metasurface designs for photovoltaic applications. J_{sc}: photocurrent density. V_{oc}: open-circuit potential. FF: fill-factor. PCE: photo-conversion efficiency. Metasurface enhancement on PCE is the ratio by comparison to a reference film.

metasurfaces in STPV applications, the efficiencies are substantially below the theoretical possibilities for STPV technologies, and also lower than commercial single-junction Si solar cells. This is due to the fact that the thermal emission is still quite broad in these structures with its significant proportion either being lower in energy than the InGaAsSb band gap or much higher, being prone to losses due to carrier thermalization in PV devices. Further investigations and optimization on the different material choices, area ratios, sizes, and shapes of metasurfaces is expected to take STPV technologies a step closer to their promising capacity.

As demonstrated, metasurfaces in PV technologies have been investigated to a great extent in the past decade with diverse functionalities and for various concepts. The most important parameters of various metasurface designs for photovoltaic applications are summarized in Table 3. A significant remaining challenge is to optimize all the design parameters related to the metasurface architecture for an appropriate function. To this end, recent reports have utilized machine learning and genetic algorithms to predict the optical properties of previously unknown metasurface designs.[760−762] Further research in this direction holds the potential of discovering novel metasurfaces and functionalities that can be beneficial for PV as well as other energy conversion applications.

5.3. Metasurfaces for Photodetectors

5.3.1. Requirements for Photodetection.
Principally, photodetectors work quite similarly to PV cells. They absorb EM waves generating electron−hole pairs (section 5.1.1), which are separated and collected (section 5.1.2) and by this the incoming EM wave is converted into an electronic signal. Hence, photodetectors are optoelectronic systems that operate as optical-to-electrical transducers. Depending on the desired purpose, photodetectors might require narrow or broadband light absorption in different wavelength regions (from ultraviolet to terahertz). Besides light absorption and charge carrier separation, photodetectors require a high sensitivity, spectral selectivity, signal-to-noise ratio, speed, and stability ("5S - requirements").[763]

The most important characteristics to evaluate the performance of photodetectors are the quantum efficiencies (EQE and IQE, section 5.1.3), responsivity R, detectivity D^*, noise current i_n or noise equivalent power (NEP), and response time.[764−767] Ideally, every photon from the desired wavelength range

impinging the detector is converted into an electron−hole pair and collected without recombination, corresponding to a high sensitivity and a theoretical EQE and IQE of 100%, respectively. The responsivity $R = I_{ph}/P_{in}$ is the ratio between the electrical output, that is, photocurrent I_{ph} and the incident power given in AW^{-1}.[765,768] In general, there will always be undesired signal fluctuations by uncorrelated arrival of electrons or thermal excitation, that is, shot noise or Johnson noise, respectively.[768,769] These undesired fluctuations give rise to the signal-to-noise ratio, characterized by the noise current i_n or NEP $= i_n/R$. The photodetector detectivity D^* can then be determined with $D^* = (A\Delta f)^{1/2} \times R/i_n = (A\Delta f)^{1/2}/NEP$ and is measured in units of Jones (cm $Hz^{1/2}$ W^{1-}) with A being the effective photodetector area in cm² and Δf the electrical bandwidth in Hz.[764,765] The detectivity can be interpreted as the signal-to-noise ratio of the photodetector under normalized conditions, that is, active area of $A = 1$ cm² at incident power of $P_{in} = 1$ W when the electrical bandwidth is $\Delta f = 1$ Hz.[768] However, to get realistic values for D^*, the noise spectrum should be analyzed with great care, and ref 768 gives a detailed discussion and equations for an accurate determination of i_n. Finally, the response time is the duration the photodetector requires to respond to changes from the input signal and is typically characterized by its −3 dB bandwidth (visit ref 765 for more details).

Applications of photodetectors span from optical communication, medical analysis, photography to astronomy, environmental sensing, safety, and many more.[677,763,770] Metasurfaces are in many senses perfect as photodetectors. Metasurfaces are ultrathin optical building blocks that can easily be incorporated into devices and fabricated via lithographic approaches, which are standard for the microelectronic and IC industry. Their optical response can be precisely tuned to the desired wavelength range and purpose by adjusting the architecture. Contrary, tuning the wavelength regime of bulk material can be rather complex and is achieved by material selection, precise band gap engineering via doping,[771−774] alloying,[775−777] or morphology modification,[778,779] and by the engineering of defect states,[780,781] heterojunctions,[782−784] or incorporation of tunable nanocrystals or quantum dots.[765,785,786] Furthermore, metasurfaces can bring advanced functionalities such as improved response time emerging from their reduced dimensions, and enhanced photoresponse and sensitivity due
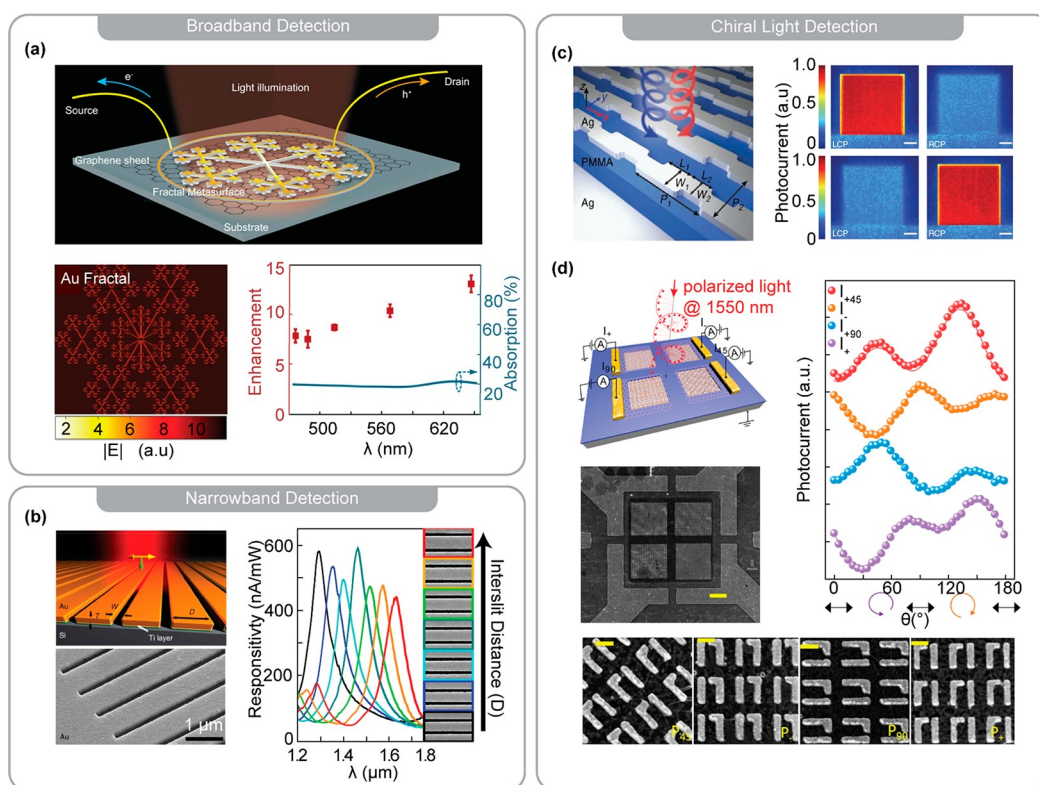
Figure 32. Metasurfaces for photodetectors. (a) Graphene and fractal Au metasurface photodetectors with broadband photoresponse in the entire visible spectrum. (b) Plasmon-induced narrowband photocurrent response in Au grating metasurfaces showing high tunability in the near-IR spectral range. (c) Hot-electron based circularly polarized light photodetector with Ag chiral metasurface design. (d) Full-Stokes near-IR polarimeter based on Au chiral plasmonic metasurfaces characterizing the state of polarization of incident light (a) Adapted with permission from ref 807. Copyright 2017 American Chemical Society. (b) Adapted with permission from ref 809. Copyright 2013 Springer Nature. (c) Adapted with permission from ref 790. Copyright 2015 Springer Nature. (d) Adapted with permission from ref 810. Copyright 2020 American Chemical Society.

to longer charge carrier lifetimes originating from their large surface-to-volume ratios.[677,770] In addition, metasurfaces offer an interesting bridge between photodetection and photothermal effects offering an alternative photodetection mechanism independent of semiconductor bandgaps.[787−789] Thermoelectric devices, where the absorbed electromagnetic radiation is converted to heat raising the temperature of the device resulting in an electron flow, can be utilized as photodetectors when combined with light-absorbing layers. Metasurfaces allow the design of ultrathin absorbers that can be utilized as coatings on commercially available thermoelectric devices.[787] Finally, metasurfaces might even bring novel properties such as the detection of chiral light.[790]

5.3.2. Metasurfaces for Photodetection. In this section, we summarize and describe a selection of various concepts in using metasurfaces in photodetection applications and their benefits for the development of integrated, ultracompact, and efficient devices with novel functionalities. We focus our discussion on photodetectors that are active in the visible and IR spectral range, which is where most photonic applications lie. We refer the reader to the following reviews for sensing in the microwave and THz regime[791] as well as a more extended discussion on light-trapping and absorbing schemes for photodetectors.[763,770,792−794]

The development of high-performance broadband photodetectors is extremely beneficial for cost-effective, small, and lightweight devices that exhibit low-power consumption.[795,796] They can be conveniently implemented in a plethora of applications that require high-response multispectral sensing.

For example, various optical communication technologies require photodetectors in the wavelength range between 600 nm and 1.5 μm from access networks to long-distance applications.[797] To date, to realize such a feat, multiple narrowband photodetectors are integrated to achieve broadband sensing, increasing the complexity and volume of optoelectronic systems, resulting in excessive production costs. Additionally, conventional photodetector materials can be environmentally harmful and toxic (e.g., HgCdTe for mid-IR), while their further miniaturization can be difficult considering Moore's law.[795,796]

Novel broadband absorbing materials have been investigated in the past years for their photodetection capability, and 2D materials, with graphene in particular, have been demonstrated as highly appealing and became the main research focus for this application.[796,798] The gapless electronic structure of graphene enables charge carrier generation by light absorption over an unprecedented large spectral range from UV to terahertz regime.[796,798] Additionally, it exhibits high charge carrier mobility at room temperature, mechanical flexibility, and dynamic tunability of optical and electronic properties, all promising characteristics for efficient conversion of photons into electricity for broadband photodetection.[796,798] Hence, graphene has been widely investigated in various photodetection schemes, where metal−graphene−metal (MGM) photodetectors were demonstrated to be the most promising candidates.[799−801] While MGM detectors display broadband operation, uniform wavelength sensitivity, fast response time, and zero power consumption, they have been notably low in

their responsivity. This is due to graphene being an atomically thin material and absorbing only 2.3% of incident light.[798] Hence, integration of absorption enhancement schemes with metasurfaces into MGM photodetectors can provide the final push for these devices for commercial applications.

Naturally, plasmonic nanostructures were primarily employed to enhance optical absorption in MGM photodetectors. Some of the photonic structures include but are not limited to metal gratings, single and dimer nanoantenna metasurfaces, and nanorod arrays.[802−804] Even though these hybrid plasmonic−graphene structures show better responsivity as photodetectors, the improvement is narrowband due to the limitations related to the sharp resonant nature of the plasmonic elements. As a potential solution, fractal plasmonic metasurfaces were then proposed to expand the responsivity enhancement to a wider spectral range. Fractal metasurfaces can sustain multiple resonances due to the branching and self-similarity of the architecture.[805,806] In one prominent example, Fang et al. have suspended a graphene layer on a Au fractal tree that mimics a snowflake geometry (Figure 32a).[807] By optimizing the angle between each branch and their width and thickness, they can modulate the optical properties to fit the requirements for broadband absorption. Integrating the fractal metasurface into an MGM photodetector demonstrates absorption enhancement factors of 8−13 over the whole visible spectral range with increased photovoltages (Figure 32a). Further building on the concept, De Nicola et al. have changed the geometry of the fractal metasurface from a snowflake to a Sierpinski carpet pattern.[808] Because of the strong EM enhancements within the interantenna gaps, the absorption in the graphene is enhanced by an unprecedented factor of ∼105 in the visible to mid-IR spectral range, with a ∼100-fold increase in the responsivity of the MGM photodetector. Few other advantages of fractal metasurfaces should also be mentioned. First, the photoresponse enhancement is polarization-independent, an important consideration for broadband photodetection schemes. Second, due to the continuous nature of the Au and graphene junction, both the absorption intensity and bandwidth can be dynamically tuned through a gate voltage. Lastly, the use of fractal metasurfaces can also be extended to other materials for photodetectors based on photothermoelectric and photovoltage principles. Overall, optimized designs of fractal metasurfaces in broadband photodetectors can pave the way to a new generation of multiband sensing applications.

Plasmonic metasurfaces were also used to a great extent in hot-electron based photodetectors. The nonradiative decay of SPRs results in the formation of energetic hot-electrons, which can then be collected for a number of light-harvesting applications. For photodetectors, this implies putting a metal in contact with a semiconductor, creating a Schottky barrier. If the plasmon-induced hot-electrons can transport into the Schottky junction before thermalization, then they can overcome this energetic barrier and get transported to the conduction band of the semiconductor, resulting in an electrical signal.[671] Hot-electron photodetectors that are based on plasmonic structures have been investigated in the past years out of nanorods, nanowires, and waveguides.[811−814] The tunability of the nanoantenna properties through geometric changes makes this type of detectors highly versatile in terms of controlling the spectral range and polarization dependence. However, the photoresponsivities of these hot-electron detectors have been suffering, being in the order of tens of μA/W. Such low values are most likely a consequence of the

inefficient injection of hot-electron through the Schottky barrier.[815]

In one of the seminal examples, Sobhani et al. have fabricated an extended Au metal grating on a Si substrate.[809] These gratings can sustain propagating SPPs along the upper surfaces as well as within the slits (Figure 32b). The resulting hot-electron photodetectors exhibit tunable narrowband responsivity in the near-IR range, reflecting the resonance of the propagating modes (Figure 32b) and reaching values of up to 600 μA/W. This substantial increase compared to previous reports has been ascribed to the extended nanostructuring of the metal layer and the creation of hot-spots (and subsequent hot-carrier generation) near the Schottky junction. However, due to the asymmetric grating structure, the response will be highly dependent on the incident light angle. By patterning the top metal film into arrays of rectangular nanoantennas, Li et al. created a near-perfect absorber layer and demonstrated omnidirectional and polarization insensitive response.[815] Similarly, these metasurfaces exhibit LSPRs and Fabry−Perot cavity modes, with further enhancement in photoresponsivity to 1.8 mA/W. Recent theoretical efforts have suggested there is still room for improvement in the performance of these devices if one utilizes plasmonic metasurfaces with quasi-BICs resonances in a near-perfection absorption design (see section 2.2 for BIC resonances).[816] The sharp and strong resonances can potentially produce highly narrowband detection in comparison to what have been demonstrated by Li et al. and at least an order of magnitude higher photoresponsivities. Furthermore, engineering the metal−semiconductor interface for a lower Schottky barrier can facilitate the injection of hot-carriers to the semiconductor conduction band, and the near-IR spectral response can be shifted to visible range if the semiconductor is changed from Si to a wider-band gap material such as TiO_2.[815]

Metasurface designs can also be employed to add extra functionalities to photodetectors and expand their range of potential applications. For example, circularly polarized light (CPL) is used in a wide range of applications such as quantum computation, magnetic recording, and spin-based optical communication.[817−819] Hence, a useful functionality for a photodetector is distinguishing between LCP light and RCP light. It is challenging for traditional photodetectors to do this feat as most conventional semiconductors lack intrinsic chirality. Implementing polarization sensitivity to such photodetectors requires the integration of several optical elements like quarter wave plates, polarizers, and beam splitters, complicating the process of miniaturization required for the outlined applications above.[790] A natural solution for developing integrated CPL detectors is to employ chiral photoactive media. One strategy in this direction is exploring novel semiconductors with intrinsic chirality such as organic−inorganic hybrid perovskites.[820,821] Alternatively, nanostructuring the photoactive layer into chiral geometries would also aid with polarization sensitivity. Indeed, chiral plasmonic metamaterials (e.g., helices, spirals, twisted structures) have been shown to exhibit strong chiroptical properties, orders of magnitude larger than chiral molecules.[271,822,823] Accordingly, chiral metasurfaces were investigated for their potential in integrated CPL photodetectors.[790,810,822,824,825]

In an influential work, Li et al. proposed using a Z-shaped Ag metasurface on top of a polymer spacer and an optically thick Ag back-reflector.[790] A Schottky junction is then formed by placing an n-type Si film on the Ag chiral metasurface (Figure 32c). The fabricated device exhibits a size-tunable plasmonic resonance in

Table 4. Metasurfaces for Photodetectors[a]

year	design	spectral range	enhancement	QE [%]	responsivity R	response time	ref
Graphene							
2011	graphene + plasmonic Au NPs	530, 550, 575, 633 nm	15	EQE: 1.5%	6.1 mA/W		802
2014	graphene + plasmonic Au rods	4450 nm			0.2 mA/W	30 ns	804
2015	graphene + hexagonal boron nitride (hBN)	1550 nm		IQE: 72−87%	0.36 A/W	3 ps	800
2016	graphene + dielectric Si + plasmonic Au	1550 nm	10	IQE: 7%	0.37 A/W		811
2017	graphene + plasmonic Au fractals	476, 488, 514, 530, 568, 647 nm	8−13				807
2020	graphene + plasmonic Au fractals	VIS-MIR	100	IQE: up to 100%	∼0.3 A/W		808
Schottky Barrier							
2013	dielectric Si + plasmonic Au rods	1200−1800 nm	25		65 nA/mW		813
2013	dielectric Si + plasmonic Au grating	1300, 1350, 1400, 1475, 1525, 1575, 1650 nm		IQE: 0.2%	0.6 mA/W		809
2014	plasmonic nanostripe antennas	400−700 nm			250 nA/W		814
2014	dielectric Si + plasmonic Au metamaterial	1200−1500 nm			∼3 mA/W		815
2021	plasmonic Ag BIC + guided modes	800−1050 nm			9.12 mA/W		816
CPL Detection							
2015	dielectric Si + plasmonic chiral Ag	1250, 1350, 1450, 1550, 1650 nm		IQE: 0.2%	2.2 mA/W		790
2020	graphene + dielectric Si + plasmonic chiral Au	1550 nm			Stokes Parameter	10 μs	810

[a]Summary of the most important parameters of various metasurface designs for photodetectors applications. The table is separated in different sections to highlight the progress of graphene and Schottky barrier detectors as well as the progress for circularly polarized light (CPL) detection.

the near-IR range (1200−1700 nm) and circular dichroism (CD) ($CD_{LCP (RCP)} = A_{LCP (RCP)} − A_{RCP (LCP)}$) values of 0.9. This implies that a left-handed metasurface reflects 90% of the RCP light and vice versa, showing great selectivity between the two polarizations. The photoresponsivity of the device is ∼2.2 mA/W, which corresponds to quantum efficiencies higher than chiral organic transistors. The large CD values correspond to large distinctions between LCP and RCP light as evident by the photocurrent maps for both left- and right-handed metasurfaces (Figure 32c). With this approach, multiple functionalities can also be added to a single compact device, where you can incorporate left- and right-handed metasurfaces for CPL selectivity, or Z-structures of different dimensions for wavelength selectivity.

A further advancement with photodetectors from chiral metasurfaces is to build integrated polarimeters in which the state of polarization of the incident light can be fully characterized. For example, knowing about the phase properties of light can be crucial in applications for remote sensing, astronomy, and medicine.[826−828] To this end, Li et al. have recently demonstrated an integrated full-Stokes near-IR polarimeter from a set of chiral plasmonic metasurfaces (Figure 32d).[810] The state of polarized light is generally described by four Stokes parameters (S_1, S_2, S_3, and S_0) containing intensity information about the linear and circular polarization components as well as the total power of incident light. Hence, to measure all these four parameters simultaneously, they have implemented four sets of chiral Au metasurfaces, with different orientations and chiralities, on a single chip (Figure 32d). Impressively, this quadrant Schottky photodetector was shown to resolve circular and linear polarizations and obtain the state of the arbitrarily polarized incident near-IR light with information regarding its intensity, orientation, and ellipticity (Figure 32d). It is possible to make these polarimeters ultracompact and scale them down to ∼2 μm, which can be fundamental parts of lab-on-a-chip devices.

Although plasmonic metasurfaces have been researched more widely, investigations on photodetectors with dielectric resonators have been mostly theoretical based.[131,829−831] A simulation study has shown that patterning high-refractive index semiconductors, such as GaAs, into interconnected nanoantenna arrays can create perfect absorption due to emerging Mie resonances, at the same time enabling electrical conductivity within the metasurface for photodetection applications.[830] While interconnected GaAs metasurfaces have narrowband resonances in the near-IR range (700−850 nm), further theoretical work has demonstrated that mid-IR detectors with dual-band spectral sensitivity can be realized by using Si gratings on metallic films.[829] The two sharp resonances (6.1 and 7.8 μm) arise from the dielectric guiding modes on the surface and within the Si grating. Furthermore, chiral Si metasurfaces were demonstrated to be potential polarimeters that can perform full Stokes characterization.[831] Even though experimental work on dielectric metasurface photodetectors has been largely lacking, they hold great promise both for narrowband sensors, due to the sustained strong and sharp resonances, as well as for broadband detectors due to the possibility of multipole and multimode engineering.[690,832] Additionally, compared to plasmonic metals, they are low loss and they open up a large set of potential materials with high refractive-index, which can then be patterned to obtain Mie resonances. Particularly, anapole modes (see section 2.2.1) confined within the dielectric material are expected to increase charge carrier generation and be highly beneficial for photodetection applications. For example, recently demonstrated organic−inorganic perovskite metasurfaces are promising candidates,[131] and following theoretical work outlined they can be fabricated into interconnected structures and investigated for their use in photodetection schemes. Overall, the coming years in photodetector research is also expected to focus on realizing devices with dielectric metasurfaces being at the core of the designs. Table 4 summarizes the most important parameters, such as spectral range, enhancement, responsivity, and response time for
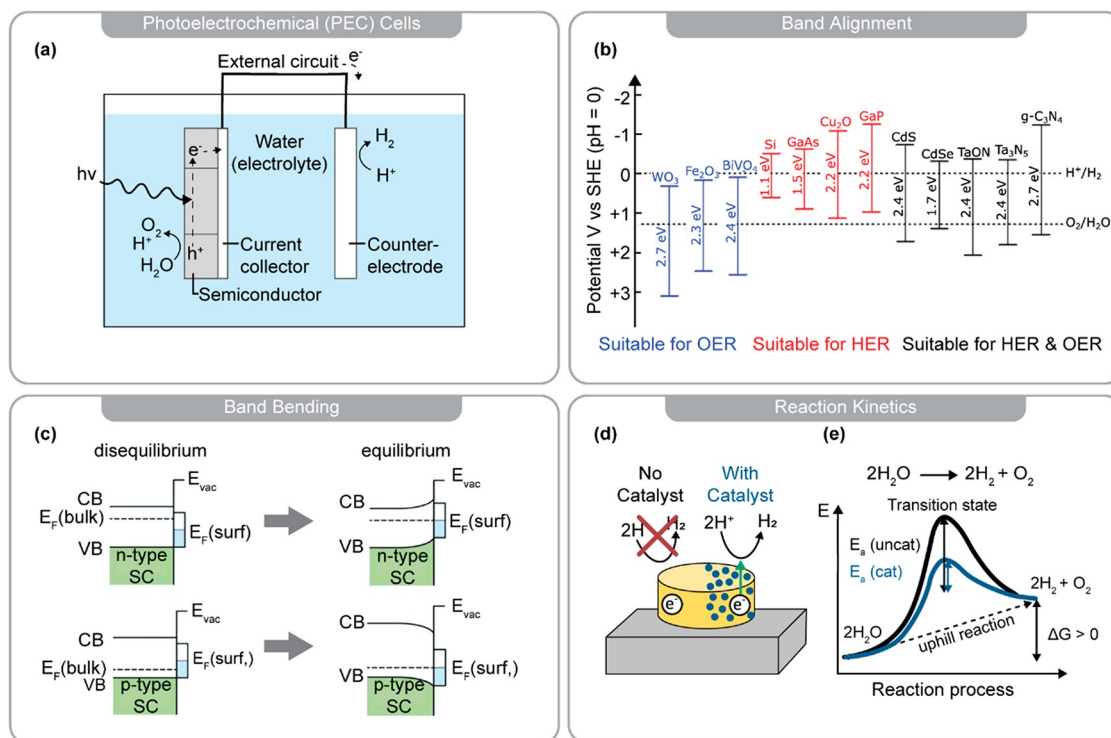
Figure 33. General requirements for photocatalysis. (a) Illustration of a photoelectrochemical (PEC) cell for solar water splitting. Process is shown for a *n*-doped semiconductor (photoanode). Illumination above the bandgap generates electron−hole pairs. Holes diffuse to the surface of the photoanode to drive the OER. Electrons are collected and transported to the CE to drive the HER. (b) Band edge positions of typical semiconductors for water splitting. (c) Schematic illustration of surface state induced band bending before contact (disequilibrium) and after contact (equilibrium) for a *n*-doped (top) and *p*-doped (bottom) semiconductor (SC). (d) Schematic illustration of a meta-atom with and without a catalyst. Without catalytic material reaction rates might be very low even though the reaction is thermodynamically feasible. (e) Schematic illustration of the role of catalyst reducing the required activation energy E_a for the chemical reaction. (a) Adapted with permission from ref 287. Copyright 2011 Springer Nature. (b) Adapted with permission from ref 840. Copyright 2018 American Chemical Society. (c) Adapted with permission from ref 655. Copyright 2016 The Royal Society of Chemistry. (e) Adapted with permission from ref 841. Copyright 2021 Springer Nature.

various metasurface designs for photodetectors that were presented in this review.

5.4. Metasurfaces for Photochemistry and Photocatalysis

In general, a major disadvantage of photovoltaic cells is the intermittency of solar energy, which varies with day-night cycles, seasons, and weather. Unfortunately, neither energy transport nor energy storage is currently efficient enough to satisfy global demands.[656] Nature circumvented this problem by converting the solar energy directly into chemical bonds, which can be stored and then used on demand. In this regard, the production of solar fuels via artificial photosynthesis, known broadly as photocatalysis, holds great promise to solve these current issues. Most research is done on solar water splitting, where a water molecule is photosplit into hydrogen and oxygen and the former can then be utilized as a clean, renewable energy source in fuel cells, where water is the only "waste" product:[833−835]

$$\text{Overall:} \quad 2H_2O + h\nu \rightarrow 2H_2 + O_2$$
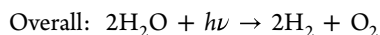
Besides solar water splitting, extensive research is also done on the photoreduction of CO_2 into products such as methane (CH_4), alkanes (C_nH_{2n+2}), alcohols, or others[836,837] and on the photoreduction of N_2 to generate NH_3, which is crucial for the production of fertilizers and other chemical products, currently synthesized via the energy intensive Haber-Bosch process.[838,839] In regard to metasurfaces, most research is done on solar water splitting, which will therefore be the focus of this review.

However, many of the discussed considerations apply for the other photocatalytic reactions as well.

The overall reaction for solar water splitting is shown above. The redox reaction is separated into the oxidation reaction, that is, the oxygen evolution reaction (OER) and the reduction reaction, that is, the hydrogen evolution reaction (HER). Under standard conditions, the free energy change is $\Delta G = 237.2$ kJ/mol, which corresponds to an energy of 1.23 V per transferred electron. Hence, photon energies of 1.23 eV must be absorbed by the material; however, higher potentials around 1.6−2.4 eV are typically required to account for electron-transfer losses:[833,840]

$$\text{Oxidation (OER):} \quad H_2O + 2h^+ \rightarrow \frac{1}{2}O_2 + 2H^+$$

$$E_{ox} = 1.23 \text{ V}$$
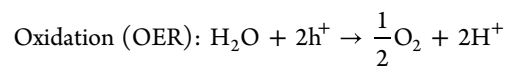
$$\text{Reduction (HER):} \quad 2H^+ + 2e^- \rightarrow H_2 \qquad E_{red} = 0 \text{ V}$$
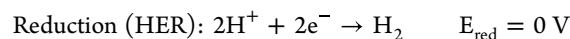
Photoelectrocatalysis is performed by either using particle systems or PEC cells.[287] In particle systems, the oxidation and reduction reactions occur on the same material, hence, both charge carriers have to be transported to the same surface. One the one hand, this increases the possibility of recombination and decreases the efficiency, while on the other hand particle systems are much more affordable. The other option, which is relevant for metasurfaces, are PEC cells, where reduction and oxidation occur on separate electrodes, the (photo)cathode and (photo)-anode, respectively. Generally, due to the requirements of large

band gap semiconductors (section 5.4.1) and the transfer of four holes to form one oxygen molecule (contrary to two electrons for one hydrogen molecule), the OER is much more challenging than the HER. While there are several different cell configurations possible,[655,833] we will focus on the most simple one, where both electrodes are immersed in the electrolyte and connected via an external circuit to a potentiostat allowing to measure currents and apply external potentials (Figure 33a).

5.4.1. Requirements for Photocatalysis. Many requirements for photocatalysis, such as absorption properties of semiconductors (section 2.1), theoretical photocurrent density (section 5.1.1), and charge carrier transport (section 5.1.2) are equal to photovoltaics and were already discussed in the previous sections. To improve charge carrier separation, $p-n$ junctions can be utilized for microstructures similarly to photovoltaics.[689] In general, doping will cause band bending at the semiconductor−liquid interface (Figure 33c). This band bending originates from the alignment of the semiconductors Fermi level (E_F) in regard to the surface potential ($E_F(surf)$) of the desired electrochemical reaction.[655,833] As such p-doping will create downward band bending, which will trap electrons close to the semiconductor-liquid interface, whereas n-doping creates upward band bending trapping holes.[655,694] Hence, p-doped semiconductors should be utilized for the reduction reaction and n-doped for oxidation reactions. Besides light absorption and charge carrier transport, photocatalytic devices have additional requirements since thermodynamic and kinetic requirements need to be fulfilled in order to drive chemical reactions on the surface of the material.

5.4.1.1. Band Alignment. From an energetic point of view, the valence and conduction bands of the semiconductors need to be properly aligned in regard to the oxidation and reduction potentials of the desired chemical reaction to make it thermodynamically feasible. This means that the conduction band needs to be energetically higher than the reduction potential, so that electrons can be injected from the material into the solution to drive the HER. Similarly, the valence band must be energetically lower than the oxidation potential, so that holes can be injected for the OER. This imposes an additional challenge to the material selection, besides having a small band gap to absorb most of the light. This band alignment is illustrated for solar water splitting in Figure 33b, where the semiconductors' band edge positions are plotted in regard to the standard hydrogen electrode (SHE). Unfortunately, small bandgap semiconductors (illustrated in red) that can achieve high photocurrents do not have suitable band positions for the OER. Contrary, large-band gap semiconductors are often suitable for the OER (illustrated in blue) and sometimes even for both reactions (illustrated in black); however, they only produce small photocurrents (Figure 30b) and often suffer from recombination due to their small charge carrier diffusion lengths L_d (section 5.1.2). Researchers overcome these requirements via semiconductor heterojunctions, known as Z-schemes, by having a small bandgap semiconductor for light absorption coated with a thin layer (smaller than or equal to L_d) of a large bandgap semiconductor to fulfill the band alignment conditions without suffering from recombination. The Z-scheme and detailed band energetics during cell operation will be explained in more detail in section 5.4.2. More extensive plots illustrating the band position of more semiconductors can be found in refs 655 and 842−846. In addition to these thermodynamic considerations, the utilized materials should be abundant and nontoxic to enable

affordable worldwide implementation and be stable in the aqueous environment.

Metasurfaces or nanostructured surfaces in general have the advantage that they offer high surface areas, thereby increasing the amount of active material exposed to the electrolyte in comparison to flat bulk materials. At the same time, light absorption is increased via photonic resonances or light trapping techniques, which results in high charge-carrier densities close to the surface of the material.

5.4.1.2. Kinetic Considerations. Unfortunately, semiconductors often show poor catalytic activity, and reactions are not occurring at high rates even if the energetic requirements are fulfilled (Figure 33d,e). While the semiconductors' task is to generate charge-carriers at the correct energy levels, catalytic materials must be implemented into the architecture to enhance the reaction rates (Figure 33d). The working principle of a catalyst is illustrated in Figure 33e.[841] Besides the energy difference of the chemical reaction (ΔG), an additional activation energy E_a needs to be reached before the chemical reaction occurs. For a noncatalytic material, E_a can be so large that the reaction is not efficient even if it is thermodynamically feasible and large overpotentials are required. The catalytic material lowers E_a significantly, thereby enhancing the reaction rate, that is, the reaction kinetics, while the catalyst itself is not changed during the reaction. The reduction of E_a originates from intermediate steps (transition states) during the electrochemical reaction. For example, in the HER, two H^+ have to be absorbed at the surface and diffuse to the reaction site. Next, charge carriers have to be injected and the chemical reaction must occur. Finally, the product, in this case H_2, must be desorbed from the surface. These intermediate steps or transition states can be energetically favorable on different materials and even on different crystallographic facets, which explains the enhanced reaction kinetics on catalytic materials. For more complex chemical reactions, where multiple products can be generated, the catalyst material can direct the selectivity of the chemical reaction, that is, the formation of specific products. For example, CO_2 reduction on copper single crystals, leads to around 30% methane (CH_4), 40% ethylene (C_2H_4) on (100)-crystals, while 46% CH_4 and 8% C_2H_4 is generated for (111)-crystals. The missing percentages are other products, such as CO, alcohols, aldehydes, etc.[836]

In general, the catalyst should provide sufficient catalytic activity, be affordable and show long-term stability in the acidic or alkaline aqueous environment. For solar water splitting, high performance catalysts are based on noble-metals, such as Pt, IrO_2/RuO_2.[841,847,848] Researchers are trying to replace this expensive noble-metals with other more affordable materials such as nickel-based[689,849−852] or cobalt-based[853−855] ones. More extensive literature on the different catalytic materials for solar water splitting can be found in refs 833 and 841. A higher mass loading is required for abundant, more affordable catalytic materials in comparison to the efficient noble metals and large amounts of catalytic material can be deposited on metasurfaces and nanostructured surfaces due to their large surface areas. However, too much catalyst can also lead to parasitic light absorption by the metal lowering light absorption in the semiconductor.[689,701] While most catalysts are deposited randomly on the surface via simple deposition techniques, such as sputtering,[212] a few examples of spatially controlled catalyst depositions are available.[298,299,689,851,856,857] In such an approach, Vijselaar et al. selectively deposited Ni−Mo catalysts onto silicon microwire arrays achieving efficiencies for the HER
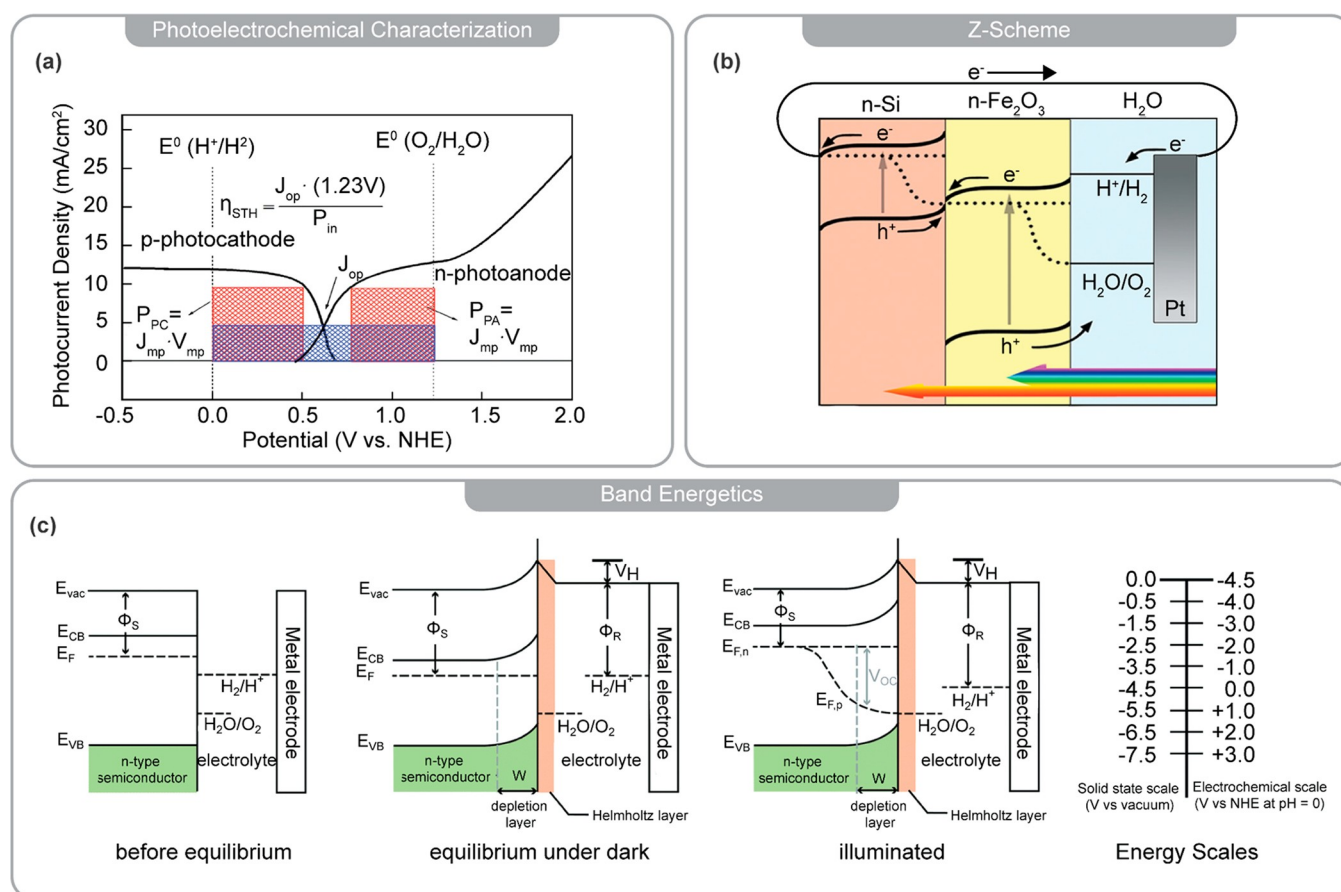
Figure 34. Performance and operation principles of photoelectrochemical (PEC) cells. (a) Overlaid current density plots from a *p*-doped photocathode and *n*-doped photoanode illustrating the maximum operating current density J_{op} and power (blue rectangle) and the maximum current densities and powers (red rectangles) of the individual photoelectrodes together with the overall solar-to-hydrogen efficiency η_{STH}. (b) Energy band schematics under illumination of a dual band gap device (Z-scheme). (c) Band energetics of a *n*-doped semiconductor-electrolyte interface illustrating the origin of band alignment (equilibrium under dark) and Fermi level splitting under illumination. (a) Adapted with permission from ref 833. Copyright 2010 American Chemical Society. (b) Adapted with permission from ref 862. Copyright 2012 American Chemical Society. (c) Adapted with permission from ref 655. Copyright 2017 The Royal Society of Chemistry.

ranging from 4.0% up to 10.8% for different catalyst coverages, highlighting the importance of optimizing both light absorption and catalytic activity simultaneously.[689]

5.4.2. Important Parameters in Photoelectrocatalysis (PEC). In electrochemistry, potentials are defined in respect to the reversible hydrogen electrode (RHE), where the reduction of water (HER) under standard conditions (25 °C, pH = 0) is defined to be 0 V. A comparison of the electrochemical potential scale to the solid-state potential scale can be found in Figure 34c. For an accurate measurement of the potential on both electrodes, a reference electrode (RE) with a stable, well-defined equilibrium potential is required.[858] Because of its simplicity, the silver/silver-chloride (Ag/AgCl) is the most used reference electrode, but the measured potential $E_{Ag/AgCl}$ is pH dependent and should be converted into the RHE scale to allow a comparison between the results in literature.[697] The potential shift depends on the pH of the electrolyte and on the potential shift of the Ag/AgCl reference electrode in respect to the SHE, $E_{Ag/AgCl \, vs \, SHE}$, which is set by the concentration in which the electrode is stored. For example, $E_{Ag/AgCl \, vs \, SHE}$ = 0.210 V for a reference electrode stored in 3.0 M KCl and the potential against RHE, E_{RHE}, can be calculated with the following equation:[697]

$$E_{RHE} = E_{Ag/AgCl} + 0.059 \times pH + E_{Ag/AgCl \, vs. \, SHE} \qquad (5.4)$$

Performing direct solar water splitting, where both photo-anode and photocathode operate simultaneously, is challenging since different semiconductors and catalysts for the HER and OER need to be integrated into the same nanoscale system.[857] Therefore, researchers usually focus on either the oxidation or reduction reaction, by having a photoanode or photocathode as working electrode (WE) and a counter-electrode (CE) (Figure 33a). The CE should have a large surface area and fast reaction kinetics,[697] so that there is no limitation on the reaction and typically platinum meshes are used. The WE needs to be electrically conducting, stable in the electrolyte and in the desired potential range. For metasurfaces, which are often fabricated on glass substrates, transparent conductive oxide (TCO) layers, such as ITO or fluorine-doped tin oxide (FTO) are utilized, since they will not affect the optical properties in the visible regime.[212,690,859,860] For a detailed discussion of the electrochemical stability for suitable substrate materials in different electrolytes and potential ranges see ref 859. In general, there should be ohmic contacts between the metasurface, the substrate and the external circuit to produce good charge transfer, while the edges of the substrate and inactive regions on the WE should be passivated.[212,299,697] The electrolyte should not react with the electrodes and have good ionic conductivity. Electrolytes can be either acidic (H_2SO_4, $HClO_4$), alkaline

(KOH, NaOH), neutral (Na_2SO_4, K_2SO_4, NaAc), or buffered (KH_2PO_4/K_2HPO_4) and concentrations are typically around 0.1−1 M.[697,859] Acidic electrolytes provide protons and are usually used for the HER, while alkaline electrolytes are utilized for the OER. Stability of the working electrode in the electrolyte under applied potential can be a concern and should be tested prior to any electrochemical characterization.

The standard characterization technique of PEC cells is cyclic voltammetry, where the current density J in mA/cm^2, that is, the measured current I normalized to the geometric surface area of the WE, is plotted against the applied potential E_{RHE} in V (Figure 34a). The measurements are done in dark and under illumination to compare the (electro)catalytic and photo-(electro)catalytic behavior. Besides the photocurrent, the potential at which the photocurrent initiates, that is, the onset potential V_{onset}, is an important parameter and defines the photovoltage generated by the cell or how much external energy is required to initiate the reaction. Besides cyclic voltammetry, amperometric measurements are usually done, where the photocurrent is measured at a fixed potential as a function of time to analyze long-term stability. To measure and quantify the gas yield, both electrodes need to be separated via a semipermeable membrane in an H-type reactor, so that the generated gases on each electrode are isolated and cannot react with each other. The amount of generated gases can then be analyzed using gas chromatography.[697,857] Similarly to photovoltaic cells, it is also possible to determine the filling factor ff via the short-circuit current density J_{sc} and open-circuit voltage V_{oc} and the current density and voltage at the maximum power point, J_{mp} and V_{mp}, respectively (section 5.1.3). The overall efficiency η of an individual photoelectrode (with external applied bias V_{app}) can be determined from the rate of hydrogen production[655,697] or indirectly calculated with[694]

$$\eta = \frac{P_{out}}{P_{in}} = \frac{J_{mp}(1.23V - V_{app})}{P_{in}}$$

(5.5)

To calculate the overall solar-to-hydrogen efficiency η_{STH} of a photocathode and photoanode working in combination, the individual current density−potential plots need to be overlapped to determine the maximum operating current density J_{op} (Figure 34a). η_{STH} is then calculated using the equation above for J_{mp}= J_{op} and V_{app} = 0 V. However, to determine η_{STH} accurately, measurements should be done in a two-electrode configuration and the faradaic efficiencies of the reactions have to be taken into account. More detailed considerations regarding the measurement and calculation of the overall solar-to-hydrogen efficiency η_{STH} can be found in refs 7, 655, 694, 697, and 701. Since photocathodes and photoanodes are usually fabricated and characterized separately and often lack the ability of performing unassisted water splitting (V_{app} = 0 V), efficiencies are often not calculated and their performance is rather evaluated by determining the external and internal quantum efficiencies, EQE (= IPCE) and IQE (= APCE), respectively, which were already discussed in section 5.1.3. In addition, we want to highlight ref 701 in which Fountaine et al. establish a framework for a theoretical efficiency evaluation for photoelectrochemical water splitting similar to the SQ model of photovoltaics. In addition, Ager et al. reviews the history of record water-splitting efficiencies until 2015.[861]

Jiang et al. gives a detailed overview over the band energetics and operation principle of PEC cells, which is summarized here and shown in Figure 34c for a n-doped semiconductor. A

more detailed explanation is given in refs.[655,656] When there is no contact between the photoelectrode and the electrolyte (Figure 34c, before equilibrium), the semiconductors bands (E_{CB}, E_{VB}) and Fermi level (E_F) are flat and the positions are defined in respect to the vacuum level (E_{vac}) by the semiconductors work function Φ_s. When the photoelectrode is brought into contact with the electrolyte (Figure 34c, equilibrium under dark), the semiconductors' Fermi level aligns in respect to the chemical potential of the reaction causing band bending in the semiconductors band and creating a depletion region W (Figures 33c and 34c). The position of the chemical reaction in regard to the vacuum level is defined via the Helmholtz layer potential drop (V_H) and the work function of the electrolyte (Φ_R). Under illumination (Figure 33c, Illuminated) the Fermi level splits into the quasi-Fermi levels ($E_{F,n}$, $E_{F,p}$), and their difference is the open-circuit voltage (V_{oc}) of the PEC cell. The generated electron−hole pairs are separated by the band bending at the semiconductor-electrolyte interface. Holes (for n-doped semiconductor) will be trapped at the interface and injected into the electrolyte to run the OER. The electrons diffuse through the material, are collected by the conductive substrate and transported to the counter-electrode, where they are injected into the electrolyte to drive the HER. Applying an additional external voltage will shift the semiconductors' band positions upward (negative bias) or downward (positive bias) and the extent of the band bending and thickness of the depletion region is modified or even eliminated, facilitating or impeding the reaction, depending on the type of photoelectrode. For example, if sufficient negative bias is applied to a n-doped semiconductor, the upward band bending can be completely eliminated.[655,656]

Because of the requirement of the band alignment (section 5.4.1), dual-band gap devices consisting of two different semiconductors are often utilized. The operation principle, shown in Figure 34b, is the same; however, Fermi level splitting occurs in both semiconductors, requiring a precise alignment of the band positions of both semiconductors (known as Z-scheme). In the illustrated scenario, the photogenerated holes in n-Fe_2O_3 are injected into the electrolyte to run the OER, while the photogenerated electrons have to recombine with the photogenerated holes of the n-Si at the interface of both semiconductors. The photogenerated electrons in n-Si are collected at the conductive substrate to drive the HER on the CE. In such a dual absorber device (Z-scheme), charge flow only occurs when both absorbers are excited simultaneously and the semiconductors bands are in correct position in respect to each other as otherwise charge accumulation occurs at the interface.[862]

5.4.3. Metasurfaces for Solar Water Splitting.
Metasurfaces provide an extensive platform to engineer photocatalytic materials, enhancing their solar light absorption capacity and the consequent hot-carrier generation. They also exhibit a high surface area, offering plenty of catalytic active sites for surface reactions to occur. In this section, we summarize the original design concepts that use metasurfaces for the solar water splitting reaction, for both anodic and cathodic sides. These ideas range from utilizing the collective photonic modes and using multicomponent programmable metasurfaces to implementing further complexity by building 3D metamaterials where the 2D metasurface forms the core basis of the architecture.

One approach in photonic engineering of metasurfaces for photocatalysis comes from the utilization of SLRs in both metal and dielectric materials. Such collective lattice excitations can
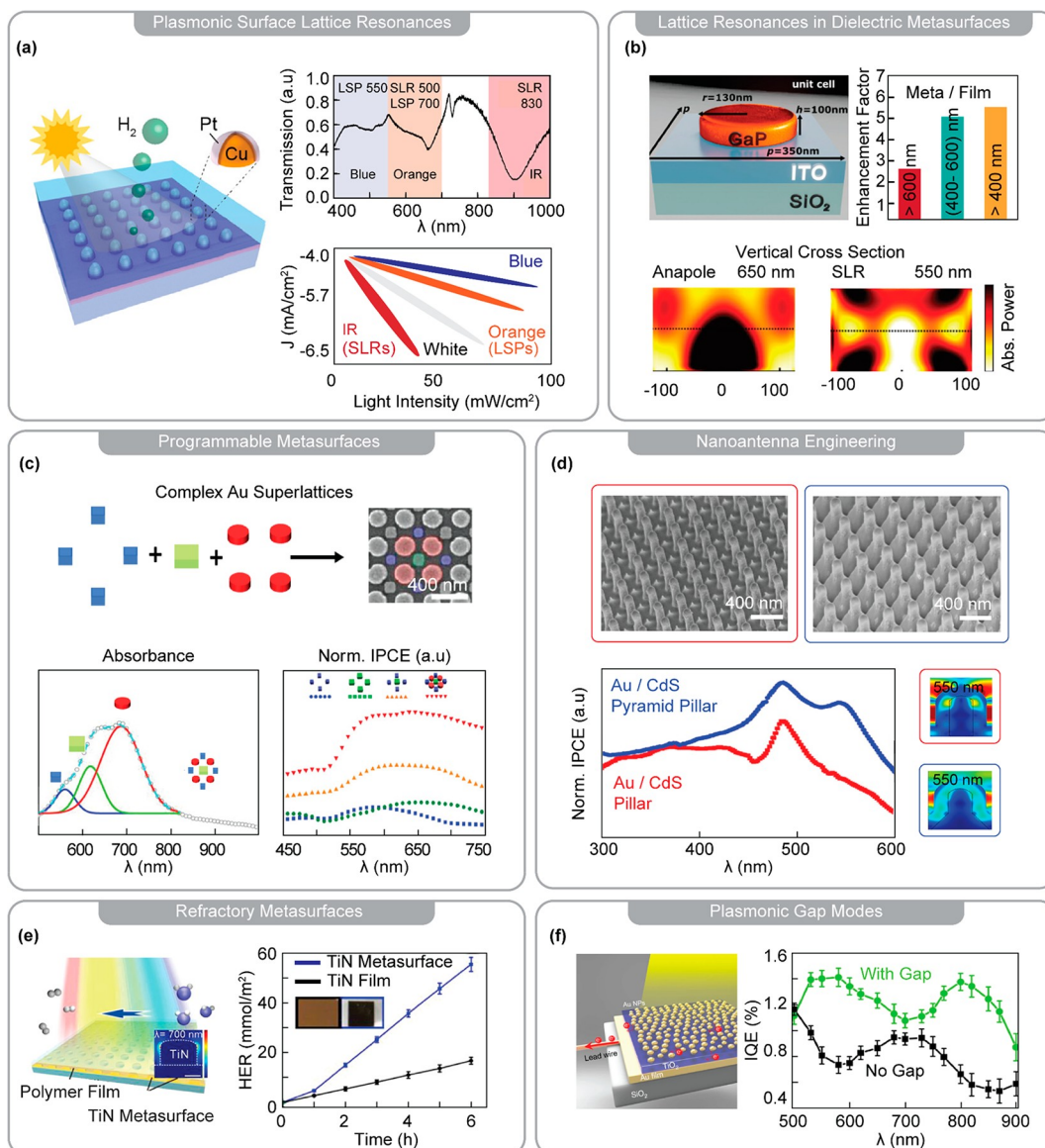
Figure 35. Metasurface design concepts for enhanced solar water splitting. (a) Core−shell Cu/Pt lattices with individual LSPRs and collective plasmonic SLRs. (b) Amorphous GaP metasurfaces with individual anapole modes and collective SLRs. (c) Multicomponent programmable Au superlattices. (d) Nanoantenna tip engineering in Au/CdS extended nanopillar structures. (e) Refractory TiN metasurfaces as broad-band solar light absorbers. (f) Nanoparticle on-a-mirror Au meta/TiO$_2$/Au mirror structure providing near-unity absorption and strong-coupling effects. (a) Adapted with permission from ref 285. Copyright 2021 American Chemical Society. (b) Adapted with permission from ref 212. Copyright 2021 Wiley-VCH GmbH. (c) Adapted with permission from ref 863. Copyright 2020 Wiley-VCH GmbH. (d) Adapted with permission from ref 864. Copyright 2017 American Chemical Society. (e) Adapted with permission from ref 865. Copyright 2021 American Chemical Society. (f) Adapted with permission from ref 866. Copyright 2018 Springer Nature.

produce stronger localized electromagnetic fields compared to single particle resonances (see section 2.2.2). Additionally, the SLR energy can be controlled to a great extent by modifying the symmetry and spacing of the array as well as the size and shape of individual single particle components. Hence, SLRs create a versatile platform to photonically engineer and enhance light-harvesting and photocatalytic properties of metasurfaces.[867] Two pioneering studies in this direction have demonstrated higher activities in HER when catalytic nanostructures are formed into metasurfaces that can sustain SLRs.

In one example, Deng et al. fabricated a 2D array of bimetallic Cu−Pt core−shell nanoparticle lattices via a combination of soft lithography techniques (Figure 35a).[285] Such bimetallic systems are expected to act as good photocatalysts for HER due to the combination of highly catalytically active Pt sites with strongly plasmonic effects of Cu. In addition to the interband transitions and the LSPR modes of single Cu particles, the lattices are engineered to exhibit a strong SLR mode in the near-IR region to extend the absorbed solar energy range of the material (Figure 35a). Excitation of either mode is expected to generate hot-carriers on plasmonic Cu, which can then be injected on the overlaying Pt shell.[868] Wavelength-dependent measurements exciting the spectrally separated interband, LSP and SLR modes revealed largest photocurrent densities under near-IR illumination (Figure 35a). SLRs have shown to be the main contributor to the observed photocurrent enhancement under white light illumination, surpassing LSPR excitations with 2-fold improvement in HER catalytic activity because of greater light

absorption and highly confined electromagnetic fields exhibited by the lattice modes.

Employing plasmonic metasurfaces on the anodic OER, Gao et al. have fabricated a metal–semiconductor hybrid structure in which an ultrathin layer of Fe_2O_3 is deposited on a Au nanopillar superlattice.[869] Up to 50% photocurrent enhancements were observed due to the broadband absorption of the hybrid structure, arising from the combination of LSPR and collective photonic modes of the superlattice. In a parallel study, Fe_2O_3 nanorods were grown on Au nanohole arrays.[870] This architecture can produce even larger photocurrent increases (∼10-fold) for the OER, as the nanowires act similar to an optical fiber when the collective modes are excited, further enhancing the absorption in Fe_2O_3. Both of these examples show that the problem regarding the short charge carrier diffusion length of Fe_2O_3 can be side-stepped by using careful photonic engineering of the plasmonic lattices and generating these charges close to the surface of catalytic material.

However, large dissipation losses in plasmonic materials can limit their application in photocatalysis. Additionally, even though earth-abundant alternatives are being developed (Mg, Al),[871,872] conventional plasmonic metals (Ag, Au) are rare and expensive. Dielectrics with moderate to high refractive index on the other hand can sustain Mie resonances with low energy losses (see section 2.2.1), while being low-cost and earth-abundant alternatives to plasmonic metals.[873,874] Anapole modes are particularly interesting for photocatalytic applications as they confine light within the dielectric material, minimizing far-field scattering effects and increasing the absorbed solar power (see section 2.2.1). Recent work has demonstrated that such excitations on TiO_{2-x} single nanoantennas can lead to enhanced photocarrier generation and higher catalytic rates on the surface under sub band gap excitation.[55]

Creating an extended metasurface from single particle dielectric nanoantennas will lead to the coupling of the anapole modes and the emergence of SLRs, similar to the plasmonic arrays described above. In a striking example, Hüttenhofer et al. have fabricated large-scale photoelectrodes (Figure 10d) from amorphous gallium phosphide (a-GaP) nanoantenna metasurfaces with individual anapole and collective SLR modes (Figure 35b).[105,212] The resonance wavelenghts are tuned within a wide range to achieve optimal broadband light absorption by altering single nanoantenna sizes and array spacings. When deposited with a thin Pt layer, such careful photonic engineering leads to a five times enhancement in the HER photon-electron conversion efficiency in comparison to thin films of a-GaP with the same amount of Pt (Figure 35b). Interestingly, the authors demonstrated that the SLR mode contributes (∼550 nm) more to the enhanced efficiency compared to single particle anapole mode (∼640 nm). FDTD calculated cross-sectional absorbed power profiles of single nanodiscs corresponding to each mode reveal that SLRs produce hotspots at the near-surface region (Figure 35b). In this way, a greater yield of photocarriers is generated closer to the surface–liquid interface when the metasurface is excited at the high energy range, contributing to the observed increase in the catalytic efficiency. From a broader perspective, concentrating photocarrier generation on the near-surface region opens up novel photonic strategies to utilize and nanopattern catalytically promising materials that have been traditionally suffering from low carrier diffusion lengths such as Fe_2O_3, $BiVO_4$, and Cu_2VO_7.

The structural complexity of metasurfaces can be further built up by incorporating arrays of nanoantennas of various shapes and sizes on a single photoelectrode (Figure 35c). In this way, each subset design can contribute to the overall broadband absorption at their particular resonant energy range. Importantly the resonance from each subset can be tuned independently or simultaneously, which leads to highly programmable multiple resonance designs. With this aim, Xu et al. have fabricated a library of centimeter scale 1, 2, and 3-subset Au/CdS nanoparticle superlattices by using multipore anodic aluminum oxide templates that have independent geometric controllability (Figure 35c).[863] Measurements on the photoelectrochemical performance revealed that indeed increasing the number of subsets on the photoelectrode resulted in higher photon-electron conversion efficiencies, with a 2.6-fold difference between 1 and 3-subset geometries (Figure 35c). It is also important to note that these programmable metasurfaces show minimal polarization angle dependence for their LSPR mode excitation, which can be a problem when trying to achieve broadband absorption by using anisotropic plasmonic systems such as nanorods.[875]

Direct engineering of metasurface lattice components and interparticle interactions can be used to design photonic modes for broadband solar absorption, high confinement of strong electromagnetic fields and near-surface photocarrier generation, all of which lead to significant enhancements in photocatalytic water splitting efficiencies. Alternatively, Xu et al. have demonstrated that detailed shape-tuning of individual nano-antennas on CdS covered Au nanopillar metasurfaces can also exhibit broadband function and boost photoelectrochemical activity.[864] Truncated pyramid CdS/Au pillars (TPP) with pointed tips were fabricated and compared with standard CdS/Au pillars (P) (Figure 35d). Spectrally resolved IPCE measurements reveal that TPP metasurfaces show substantially improved photocurrents compared to P structures, with an additional absorption peak at ∼550 nm (Figure 35d). FDTD simulations then show that LSPRs are only localized on the top part of the P structure, while TPP show distinct LSPRs both at the bottom pyramid and the top pointed pillar at 550 nm (Figure 35d). Utilizing these broadband resonances spread to larger volumes of the nanoantenna structure, CdS/Au TPP metasurfaces show an impressive ∼4-fold increase in photocurrents compared to planar control structures.

Other than the well-known and studied light absorbers and photocatalysts for the water splitting reaction, alternative material systems can also be utilized as metasurfaces. Refractory plasmonic materials have received great attention for various applications due to their low cost, high temperature resistance and easy processability.[439,876] One of such materials, titanium nitride (TiN), has been investigated in nanophotonic components for a number of optical and optoelectronic processes such as second harmonic generation,[877] lasing,[878] and light-emitting diodes.[879] While the high melting point (e.g., 3 times of Au) and tunability of plasmonic properties by growth conditions make TiN a highly promising candidate for such applications, it also suffers from large dissipation losses.[493,880] From the perspective of photocatalysis, these dissipation losses can be beneficial since they lead to nonradiative relaxation of the LSPR and the consequent generation of hot-carriers.[881] Additionally, broadband LSPRs can be achieved due to TiN's low Q factor in comparison to other traditional plasmonic metals.[865] Interestingly, it was demonstrated that due to this broadband absorption TiN nanoparticles can transfer twice as many hot-carriers across a semiconductor interface compared to Au nanoparticles.[489] In a very recent example, Yu et al. show that
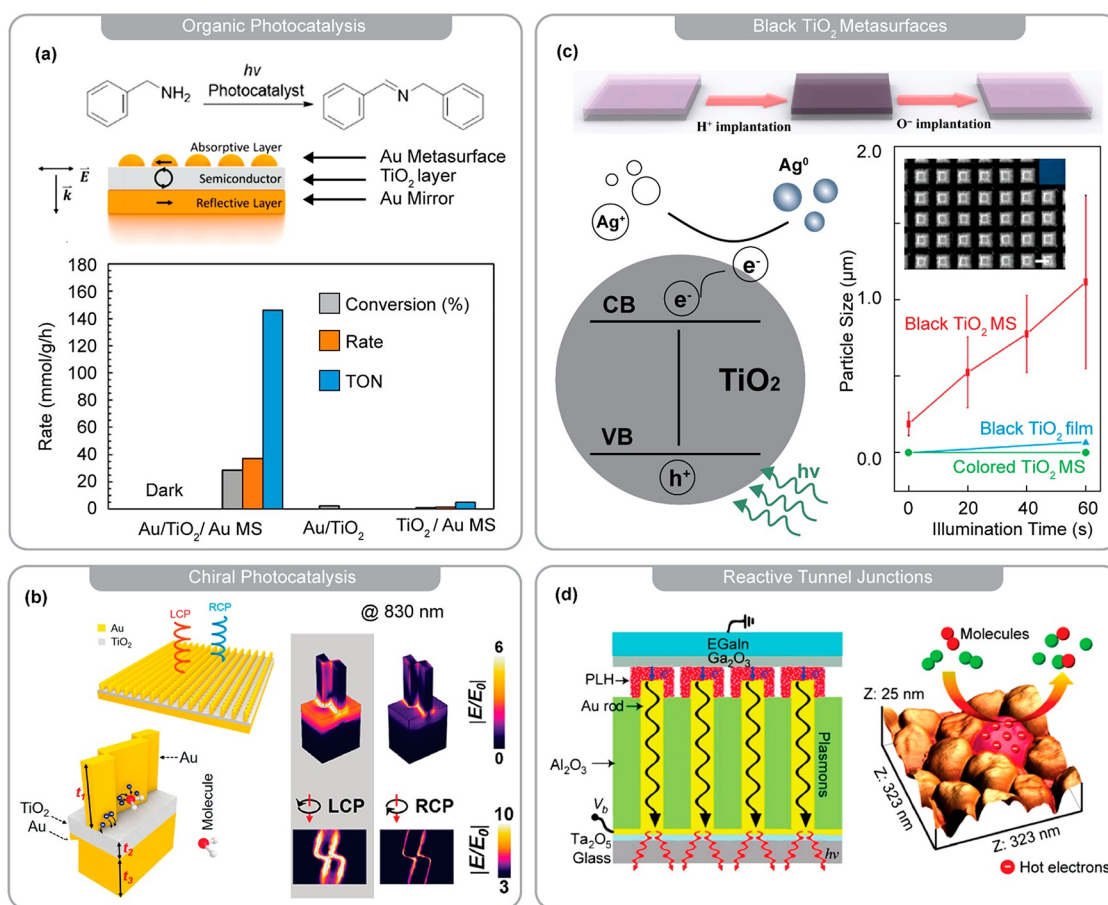
Figure 36. Miscellaneous reactions and future directions with metasurfaces and metamaterials. (a) Au meta/TiO$_2$/Au mirror NPoM super absorbers for hot-carrier organic catalysis. (b) Hot-carrier generation on chiral metamaterial NPoM super absorbers. (c) Broadband absorbing black TiO$_2$ metasurfaces demonstrating Ag reduction on the surface. (d) Hot-carrier chemistry with reactive tunnel junctions in plasmonic Au nanorod metamaterials. (a) Adapted with permission from ref 891. Copyright 2018 American Chemical Society. (b) Adapted with permission from ref 897. Copyright 2019 American Chemical Society. Copyright 2019 American Chemical Society. (c) Adapted with permission from ref 898. Copyright 2019 AAAS (d) Adapted with permission from ref 899. Copyright 2018 Springer Nature.

TiN nanodisc metasurfaces, fabricated by EBL, can be used to realize broad near-unity absorption (92% of incident light) compared to TiN thin film absorption (42% of incident light) (Figure 35e).[865] This drastic change between TiN metasurfaces and thin films was attributed to the emergence of a broad LSPR mode peaking at 700 nm upon nanostructuring. The LSPR mode complements the high-energy interband transitions of the material to cover the entire visible range. The hot-carriers generated on the TiN metasurface are then utilized by a polymer HER catalyst deposited on top of the structure, with a 3-fold enhancement in photocatalytic H$_2$ production efficiency compared to thin film control samples (Figure 35e).

A different photonic design strategy to drastically alter the absorption properties of catalytic materials is the use of plasmonic gap modes.[882] A single layer of plasmonic nano-antennas can have limited absorption and consequent low hot-carrier generation rates for photocatalytic applications. To overcome this limitation three-dimensional architectures can be devised for better solar light utilization. In this respect, nanoparticle on-a-mirror (NPoM) geometries (Figure 35f), consisting of a nanoantenna metasurface separated from a continuous metal film by a dielectric layer, have shown to absorb nearly all incident light in a broad spectral range.[883,884] Additionally, NPoMs behave similarly to a pair of coupled nanoantennas as they can sustain gap modes confined between

the two metal layers, resulting in significantly large field enhancements.[885,886] Placing a dielectric catalyst in this plasmonic gap holds the potential to boost photocatalytic efficiencies via increased absorption and photocarrier generation in the material.

Efforts so far employing NPoM structures for photocatalysis involved the use of TiO$_2$ as the dielectric catalyst sandwiched between two metallic layers.[866,883,884,887,888] In a typical setup where the photoelectrode consists of a Au meta/TiO$_2$/Au mirror (TiO$_2$ < 50 nm), the OER has shown to exhibit a 5-fold increase in photon-electron conversion efficiencies compared to conventional Au meta/TiO$_{-2}$ structures. This significant change was mainly attributed to the increase in the broadband absorption of the NPoM structure, sensitizing a wide band gap semiconductor like TiO$_2$ in the entire visible range.[884] In a highly intriguing work, Shi et al. went a step further and used the same architecture to study strong coupling between individual LSPR and gap modes and investigated its effect on the photocatalytic OER (Figure 35f[866]). The coupling between the two modes was controlled by varying the gap size. In principle, when the gap mode is on-resonance with the LSPR of Au nanoantennas, hybrid polariton modes with upper and lower states are formed that exhibit an energy splitting between them. Such strong coupling shows experimental signatures of dual band splitting in the absorption spectrum of NPoM structures,

as also demonstrated by the authors (Figure 35f). Photocatalytic action spectra performed on strongly coupled NPoMs for OER show that both upper and lower coupled states serve to enhance the absorption and contribute positively to the overall catalytic efficiency (Figure 35f). This observation is further supported by time-resolved photoemission electron microscopy and transient absorption spectroscopy measurements, in which LSPR dephasing times are significantly reduced when strong coupling with gap modes is present.[889] Such faster LSPR dephasing times are rationalized to occur due to the suppression of radiative relaxation pathways and the augmentation of nonradiative channels, such as hot-carrier injection to the middle TiO_2 layer, that results in improved photocarrier yields ready to be utilized for OER at the catalyst surface.[889] Other than TiO_2, an ultrathin Fe_2O_3 middle layer was also employed in an equivalent Au-based NPoM architecture for OER.[682] While a 2-fold photocurrent increase was observed above the band gap of Fe_2O_3 due to the plasmonic gap modes, a 6-fold photocurrent enhancement was detected below the band gap in the near-IR range, and was argued to occur due to hot-carrier injection from the top Au nanoantennas to the Fe_2O_3 layer. NPoMs provide a versatile platform for the photonic engineering of catalytic systems, either with simply near-unity absorption or exploiting the strong-coupling regime, but they also offer additional possibilities for chemical tuning. For example, the top metasurface layer in NPoMs can be fabricated out of multimetallic nanoantennas, such as Au/Pd alloys.[887] The resulting photoelectrodes can then be used for the full water splitting reaction where reductive HER can occur on Pd, while oxidative OER can happen on the TiO_2 layer. Finally, it should be crucially noted that due to the concentration of light in such small volumes, NPoM architectures can also be a great platform to investigate reaction mechanisms in catalysis and probe reaction intermediate at a single-particle level through energy-resolved spectroscopies, such as SERS.[890]

5.4.4. Further Reactions and Opportunities with Metasurfaces for Catalysis. Moving beyond water splitting, in this section we will summarize other types of reactions that were shown to benefit from nanophotonic engineering, discuss some of the advanced functionalities and concepts that can be utilized and outline future directions and opportunities for metasurfaces in photocatalytic applications.

Previously, we discussed intriguing cases where thin films of photocatalytically active semiconductors, such as Fe_2O_3 and TiO_2, were integrated into various metasurfaces to perform the solar water splitting reaction, with particular attention to NPoMs designs that make use of LSPR as well as gap-plasmon modes. Expanding on the type of reactions, Xiao et al. have investigated the potential of NPoMs, Au meta/TiO_2/Au mirror in this case, for solar driven organic synthesis (Figure 36a).[891] They chose the photocatalytic oxidation of benzylamine into the corresponding imines, which is an important process for the pharmaceutical industry that requires stoichiometric amounts of harmful and explosive reagents.[892,893] By studying the reaction kinetics, they show that the near-perfect NPoM absorber can produce ~29-fold increase in the rate compared to nonperfect absorber structure due to generation and transfer of hot-carriers into the catalytically active TiO_2 film (Figure 36a). In the near-future such studies are expected to be extended to other organic transformations, particularly for other C−C coupling reactions that form the backbone of many industrial chemical processes.

NPoM designs can be further enriched with novel functionalities, such as optical chirality, by tailoring the shape of individual nanoantennas on the top plasmonic metasurface layer. The concept of chirality has a crucial place in photochemistry to drive asymmetric reactions in relation to the optical response of the absorbing reagents to polarized light.[894] Recently, plasmonic nanocrystals have been shape-engineered to achieve chiral structures like helices and helicoids.[895] These complex nanocrystals can selectively concentrate EM hot-spots and hot-carrier generation on different regions of the particle when excited with either RCP or LCP light.[895,896] Among other applications, the chiral induced hot-carrier generation can have important implications for photochemical processes where polarization of the incident light can be an additional tuning knob to control reaction rates and outcomes.

In this respect, theoretical and experimental studies have identified three main reaction areas where chiral plasmonics can be of use: polarization-sensitive chemistry with nonchiral molecules, growth of anisotropic nanocrystals and separation of racemic colloidal mixtures.[897,900−903] Colloidal plasmonic nanocrystals have shown great potential in all these areas. However, their optical CD values and asymmetric g-factors for hot-carrier generation, both measures of the material response strength to LCP and RCP, have been below the potential upper limit. In a recent theoretical work, Wang et al. have demonstrated that NPoMs structures should also be considered for applications in chiral photocatalysis.[897] They show substantially increased CD values and giant g-factors (~1.52) when the top metasurface layer in an NPOM is designed from twisted and staggered Au walls (Figure 36b), potentially providing the strongest chiroptical response for hot-carrier generation in any plasmonic and metasurface design studied so far.[790,904] By exciting the structure either with LCP or RCP light, one can influence the rate of hot-carrier generation and their location on the structure, either on the Au wall or the TiO_2 spacer layer (Figure 36b). Such a difference makes it possible to direct the reaction into either a reduction or oxidation pathway by polarized light, one mediated by the spacer layer and the second at the metal-molecule interface on the Au walls. Overall, the use of NPoM metasurface designs opens up new avenues for developing novel approaches in polarization-sensitive photochemistry for plasmon-enhanced applications.

Alternative to NPoMs, catalytic materials themselves can be nanostructured to form metasurfaces with fine-tailored absorption properties. Two prominent examples in this direction have shown that nanopatterned TiO_2 arrays can drive photochemical processes on their surface with enhanced reaction rates compared to thin films.[898,905] Despite the highly catalytic surface, the large band gap of TiO_2 creates difficulties in implementing the material for solar-driven chemical reactions. In the past decades, a wide variety of strategies have been used to narrow down the band gap to visible-IR spectral range, one of which include the hydrogenation of the TiO_2 to create a broadband absorbing "black" material.[906] Inspired by this concept, Wu et al. fabricated transparent TiO_2 metasurfaces and hydrogenated the structure to achieve a black metasurface, which itself was shown to be a reversible process (Figure 36c). Compared to black TiO_2 films, the metasurfaces were shown to perform much better in photochemically reducing Ag ions to microcrystals (Figure 36c). The enhancement in the reaction rate was explained by the emergence of Mie resonances on the metasurface which served to improve the absorption of the material in the blue range, a feature that was lacking in the black control films. A similar TiO_2 metasurface structure was also

Table 5. Metasurfaces for Photochemistry and -Catalysis[a]

				photoelectrocatalytic water splitting			
year	design	light source	reaction conditions	current density (mA/cm^2)	IPCE$_{max}$ (%)	metasurface enhancement	ref
2021	dielectric nanodisc array (a-GaP/Pt)	1000 W Hg/Xe lamp ($\lambda > 400$ nm)	H$_2$ Evolution (1.0 M HClO$_4$)	-8.0 @ -0.7 V vs RHE	1.2% (400−800 nm)	5.7	212
2022	dielectric nanorod array (CrO$_x$/NiO$_x$)	300 W Xe lamp, 100 mW/cm^2 AM 1.5 G	H$_2$ Evolution (0.5 M Na$_2$SO$_4$/0.1 M PBS)	-0.2 @ -0.1 V vs RHE	1.0% (300−500 nm)	6	918
2021	plasmonic nanocrystal array (Cu/Pt)	white light, 220 mW/cm^2	H$_2$ Evolution (0.5 M Na$_2$SO$_4$)	-6.0 @ -0.2 V vs RHE			285
2021	NPoM Au/TiO$_2$/Au$_2$Pd$_2$ MS	300 W Xe lamp, 100 mW/cm^2 AM 1.5 G	H$_2$ Evolution (0.5 M KOH)	-0.006 @ -0.7 V vs RHE	0.07% (400−900 nm)		887
2013	plasmonic nanohole array (Au/Fe$_2$O$_3$ Nanorods)	300 W Xe lamp, 100 mW/cm^2 AM 1.5 G	O$_2$ Evolution (1.0 M NaOH)	1.0 @ 1.23 V vs RHE	22% (350−800 nm)	10	870
2012	plasmonic nanopillar array (Au/Fe$_2$O$_3$)	300 W Xe lamp, 100 mW/cm^2 AM 1.5 G	O$_2$ Evolution (1.0 M NaOH)	0.4 @ 1.5 V vs RHE	0.2% (350−700 nm)	2	869
2018	NPoM Au/TiO$_2$/Au MS	800 W Xe lamp (500 nm > λ > 900 nm)	O$_2$ Evolution (0.1 M KOH)		1.4% (500−900 nm)	11	866
2019	NPoM Au/Fe$_2$O$_3$/Au MS		O$_2$ Evolution (1.0 M NaOH)	0.3 @ 1.5 V vs RHE	9% (400−1100 nm)	7	682
			Photocatalytic Reactions				
year	design	light source	reaction conditions	product formation rate	QE (%)	metasurface enhancement	ref
2021	refractive plasmonic nanodisc array (TiN/polymer)	20 W LED ($\lambda > 420$ nm)	H$_2$ Evolution (MeOH/TEA$_{(aq)}$)	H$_2$, 10 mmol m^{-2} h^{-1}	0.26%*	4	865
2021	NPoM Au/Cu/ZnO MS	300 W Xe lamp, 200−600 mW/cm^2 AM 1.5 G	CO$_2$ Hydrogenation (H$_2$/CO$_2$ gas phase)	CH$_3$OH, 150 mmol g^{-1} h^{-1}		4	919

[a]Summary of the most important parameters of various metasurface designs for photoelectrocatalytic water splitting and photocatalytic reactions. The metasurface enhancement is calculated by comparison with a reference device (for example a planar film). *defined as QE = 2N(H$_2$)/N(hν).

investigated to demonstrate that environmentally relevant reactions, such as the degradation of NO in the atmosphere, can also be performed with such architectures.[905] Further efforts now are expected to be concentrated in implementing such metasurfaces to a wider range of chemical reactions, particularly to artificial photosynthesis processes.

Taking a more hybrid approach, the combination of metasurfaces with tunnel junctions can help create nanoscale reactors that can simultaneously act as highly confined catalytic spots as well as multimodal optical sensors, aiding the *in situ* monitoring of hot-carrier mediated chemical reactions.[907] In a seminal example, Wang et al. utilized Au nanorod metasurfaces in a metal−polymer−metal junction and fabricated a large-area device of 1 cm^2 (Figure 36d).[899] The metasurface plasmonic modes are excited when an external voltage is applied to the system through an inelastic tunneling process, which then radiatively relax and result in a measurable light emission. Additionally, the extremely efficient elastic tunneling triggers the formation of hot-carriers at the nanorods tips, creating highly reactive chemical spots. By using a model oxidation/reduction of a polymer, they demonstrate the capacity of the device for real-time tracking of the reaction either by the modulation of intensity in the light emission or by the changes in the tunneling currents (Figure 36d). This type of reactive tunnel junctions can be ideal as lab-on-a-chip devices where the precise monitoring of chemical reactions are of paramount importance. A number of chemical reactions in this direction include the oxidation of aromatic amines or the reduction of aromatic nitro compounds, and the gas-phase degradation of volatile organic compounds.[899,908,909] This concept also beautifully demonstrates that metasurfaces can be built into more complex platforms, combining the fields of electronics, chemistry and photonics at the nanoscale.

A final remark should be made regarding the potential of metasurfaces in the other important reaction of artificial photosynthesis, namely CO$_2$ reduction reaction (RR). While the literature on solar water splitting with metasurface designs have been growing at a fast pace in the past years, demonstrations on photocatalytic CO$_2$ RR have been largely lacking, most likely due to the multistep and complex nature of the reaction. It is well-established that Ag, Au, and Cu, while also being plasmonic metals, are outstanding catalysts for electrocatalytic CO$_2$ RR.[836,910] In particular, Cu is capable of producing various valuable hydrocarbon products including but not limited to methane, ethylene, and ethanol.[836] When colloidal nanocrystals of Cu are employed, the product selectivity and activity of the reaction can be influenced by tuning the shape, size, and composition of the particle.[911−913]

More recently, plasmon-induced photocatalytic CO$_2$ RR has also been investigated with colloidal plasmonic metals and showed promising results regarding their wide range of product distribution.[910] Hence, patterning these metals into metasurfaces can further enhance the absorption and affect hot-carrier generation. Metasurfaces of different shapes and sizes can be explored and the influence of hot-spots arising from the LSPRs and collective modes, on the reactivity and selectivity of CO$_2$ RR can be examined. Bimetallic metasurfaces can also be an alternative route to investigate, which can aid the issue relating to the ultrafast thermalization of the plasmon generated hot-carriers by providing charge separation at the metal−metal interface.[671,868,910,914] Lastly, novel hybrid materials can be tried out, with one example being 2D-metasurface architectures[910,915] (see section 2.2.3). In the presence of a secondary excitonic material, the coupling between the electronic transitions and the strong and sharp resonances created by metasurface modes can be further inspected for their influence on the reaction rates and

product selectivity, providing a potential avenue for polariton-based catalysis.[916,917]

A comparison of the various metasurface-designs for photo-electrocatalytic water splitting and other photocatalytic reactions highlighting the most important parameters such as current density, conversion efficiency and metasurface enhancement can be found in Table 5.

5.5. Section Summary

To summarize, the advantages of metasurfaces for photon—electron energy conversion are

1. In metasurfaces, light absorption is independent from the semiconductor thickness (LPD) allowing to reduce the required amount of material or to enhance light absorption in poor absorbing materials via photonically engineered resonances and light trapping techniques.

2. Metasurfaces decouple light absorption from charge carrier separation (L_d) since charge carriers only have to travel small distances to reach the interface or surface of the material. This enables the utilization of materials that could not have been considered as bulk material.

3. Metasurfaces can decrease fabrication costs by replacing currently utilized antireflective coatings.

4. Metasurfaces can bring advanced functionalities for photodetectors, such as improved response time emerging from their reduced dimensions, and enhanced photoresponse and sensitivity due to longer charge carrier lifetimes originating from their large surface-to-volume ratios.

5. Metasurfaces offer large surface areas in comparison to flat bulk material increasing the amount of active material at the interface, enabling higher catalyst loadings important for the shift toward less efficient but affordable catalyst materials.

6. Metasurfaces allow researchers to concentrate charge-carrier densities close to active reactions sites increasing photocatalytic efficiency.

7. Metasurfaces allow us to gain insight into the basic aspects governing photon—electron energy conversion processes by studying these processes at the nanoscale. This reveals fundamental aspects governing the physical principles useful to improve device performance and lowering production costs.

6. CONCLUSION AND OUTLOOK

In this review, we have attempted to outline how light harvesting facilitated via nanostructured surfaces can be utilized as the starting point for a number of energy conversion processes occurring on the nanoscale. The inherent compatibility of metasurfaces with "flat optics" further allows such structures to be combined with a wide variety of materials, from top-down deposited thin films, layer-by-layer assembled materials, to colloidal self-organized systems and 2D materials. This enables a plethora of possibilities to convert energy from the photon field to other forms of energy as outlined in this review. Many fascinating physical phenomena about the details of these processes remain to be discovered, due to the richness of light—matter interactions at this scale involving electromagnetic fields, heat and charge transfer processes in nanoconfined spaces.

From the application perspective, spectral operation bandwidth, efficiency of the energy conversion and subsequent collection as well as up-scaling are main challenges to be addressed. To give but one example, it is a reasonable question whether metasurfaces, or solar water splitting in general, will outperform the current silicon PV industry in the near future, which is decreasing costs for PV cells at a rate similar to Moore's law.[920] Nevertheless, studying photon—electron energy conversion at the nanoscale helps researchers to reveal the fundamental aspects governing the physical principles of generating energy or solar fuels from sunlight. This insight will lead to a new generation of devices with improved performance and lower production costs.

The same line of thought applies to the generation of phonons or frequency-shifted photons by employing 2D artificial materials, as the ones outlined here. As shown in this review, metasurfaces are already impacting a wide range of applications in these areas, such as perfect absorbers, polarizers, sensors, integrated fibers, light/heat transducers and lenses, among others. The fundamental knowledge gathered so far in these systems will definitively seed applications beyond proofs of concept, shaping the future of light management.

AUTHOR INFORMATION

Corresponding Authors

Emiliano Cortés − *Chair in Hybrid Nanosystems, Nano Institute Munich, Faculty of Physics, Ludwig-Maximilians-University Munich, 80539 Munich, Germany;* orcid.org/0000-0001-8248-4165; Email: Emiliano.Cortes@lmu.de

Stefan A. Maier − *School of Physics and Astronomy, Monash University, Clayton, Victoria 3800, Australia; Chair in Hybrid Nanosystems, Nano Institute Munich, Faculty of Physics, Ludwig-Maximilians-University Munich, 80539 Munich, Germany; Department of Phyiscs, Imperial College London, London SW7 2AZ, United Kingdom;* orcid.org/0000-0001-9704-7902; Email: stefan.maier@monash.edu

Authors

Fedja J. Wendisch − *Chair in Hybrid Nanosystems, Nano Institute Munich, Faculty of Physics, Ludwig-Maximilians-University Munich, 80539 Munich, Germany;* orcid.org/0000-0002-0110-4771

Luca Sortino − *Chair in Hybrid Nanosystems, Nano Institute Munich, Faculty of Physics, Ludwig-Maximilians-University Munich, 80539 Munich, Germany;* orcid.org/0000-0002-6284-6955

Andrea Mancini − *Chair in Hybrid Nanosystems, Nano Institute Munich, Faculty of Physics, Ludwig-Maximilians-University Munich, 80539 Munich, Germany;* orcid.org/0000-0001-5927-9032

Simone Ezendam − *Chair in Hybrid Nanosystems, Nano Institute Munich, Faculty of Physics, Ludwig-Maximilians-University Munich, 80539 Munich, Germany*

Seryio Saris − *Chair in Hybrid Nanosystems, Nano Institute Munich, Faculty of Physics, Ludwig-Maximilians-University Munich, 80539 Munich, Germany*

Leonardo de S. Menezes − *Chair in Hybrid Nanosystems, Nano Institute Munich, Faculty of Physics, Ludwig-Maximilians-University Munich, 80539 Munich, Germany; Departamento de Física, Universidade Federal de Pernambuco, 50670-901 Recife, Pernambuco, Brazil*

Andreas Tittl − *Chair in Hybrid Nanosystems, Nano Institute Munich, Faculty of Physics, Ludwig-Maximilians-University Munich, 80539 Munich, Germany;* orcid.org/0000-0003-3191-7164

Haoran Ren − *MQ Photonics Research Centre, Department of Physics and Astronomy, Macquarie University, Macquarie Park, New South Wales 2109, Australia*

Complete contact information is available at:
https://pubs.acs.org/10.1021/acs.chemrev.2c00078

Author Contributions

[#]E.C., F.J.W., and L.S. contributed equally.

Notes

The authors declare no competing financial interest.

Biographies

Emiliano Cortés is Professor in Energy Conversion and head of the Plasmonic and Photonic Chemistry group at the Faculty of Physics, Ludwig-Maximilians-University (LMU) Munich, Germany. He is also a visiting researcher at the Physics Department, Imperial College London, UK. Emiliano is coeditor of the first book in *Plasmonic Catalysis*, member of the excellence cluster e-conversion and cocoordinator of its graduate program, scientific board member in the Center for NanoScience, member of the Bavarian program Solar Technologies go Hybrid, and fellow of the Young Academy of Europe. In 2018, he was awarded with the 1.5M euros ERC Starting Grant from the European Commission for his project CATALIGHT. His group does research on nanoscale energy conversion, plasmonics and photonics (electro)catalysis, synthesis of functional nanomaterials, and single particle catalysis.

Fedja J. Wendisch received his Ph.D. at the department Chemistry and Physics of Materials at the Paris-Lodron-University Salzburg (PLUS), Austria, in 2020 and obtained the Young Investigators Award for Sustainability in the same year. He is currently a postdoctoral researcher at the chair of Hybrid Nanosystems at the Ludwig-Maximilians-University (LMU) Munich. His research interests focus mainly on dielectric and plasmonic metasurfaces for photocatalysis and for chiral nanophotonics.

Luca Sortino obtained a M.Sc. at the Material Science department at the University of Bicocca Milan, Italy, in 2016. He obtained his Ph.D. in early 2020 at the University of Sheffield, as part of the International Training Network "Spin-NANO" founded by Marie Skłodowska Curie Actions. After a postdoctoral experience at the hybrid plasmonic groups at Ludwig-Maximilians-University (LMU) Munich, he obtained a Humboldt Postdoctoral Research Fellowship in 2022 in the same group. His research interest lies between solid-state physics and nanophotonics, with a focus on 2D materials, and with expertise in experimental optics and time-resolved, ultrafast spectroscopy.

Andrea Mancini obtained his master's degree in physics from the University of Rome La Sapienza in 2017 and is currently a Ph.D. candidate under the supervision of Prof. Stefan Maier. His current research is focused on near-field optics of phonon polaritons in nanostructured materials.

Simone Ezendam obtained her master's degree in physics from Ludwig-Maximilians-Universität München (LMU) in 2018 and is currently a Ph.D. candidate under the supervision of Prof. Emiliano Cortés. Her current research interest is the operando mapping of reaction sites on nanocatalysts using super resolution techniques.

Seryio Saris received his M.Phil. in nanoscience from the University of Cambridge in 2015 and his Ph.D. in chemistry and chemical engineering from École Polytechnique Fédérale de Lausanne (EPFL) in 2020. He is currently a postdoctoral researcher at the chair of hybrid nanosystems at the Ludwig-Maximilians-University (LMU) Munich.

Currently, his research focus lies on the development of 2D materials and nanophotonic hybrids for their applications in photocatalysis.

Leonardo de S. Menezes studied Physics at Federal University of Rio de Janeiro (1994) and did his Physics Masters (1996) and Ph.D. (2001) at Universidade Federal de Pernambuco (UFPE), Recife, PE, Brazil. Postdoc, he stayed at Humboldt University of Berlin (2004) as an Alexander von Humboldt postdoc fellow, and UFPE (2005), when he became Adjunct Professor at the Physics Department/UFPE. In 2014, he spent a sabbatical year at the Max-Planck Institute for the Science of Light in Erlangen. Nowadays, he is Associate Professor at the Department of Physics/UFPE and subgroup leader at the Chair in Hybrid Nanosystems, Ludwig-Maximilians University Munich, working on optics in condensed matter, light−matter interaction, optical microresonators, nano optics, and nonlinear spectroscopy of individual nanoparticles. He was an Affiliate Member of the Brazilian Academy of Sciences (2009−2014) and Ambassador Scientist of the Alexander von Humboldt Foundation in Brazil (2014−2020).

Andreas Tittl holds a position as Emmy Noether Research Group Leader at LMU Munich, focusing on the design and experimental realization of novel metasurface concepts for enhanced light−matter coupling and ultrasensitive biodetection. After receiving his Ph.D. in Physics from the University of Stuttgart, he has worked as a postdoctoral researcher and Fellow at Ecole Polytechnique Fédérale de Lausanne (EPFL), where he pioneered the use of dielectric metasurfaces in biochemical spectroscopy. Dr. Tittl has received multiple awards for his work, including the "VDI Young Researcher Award Nanotechnology, the Young Investigator Award, Green Photonics" and the Jeffrey Hubbell and Melody Swartz Young Bioengineer Award.

Haoran Ren is an ARC DECRA Fellow. His nanophotonic research aims to develop structured light and nanophotonic materials for advanced light−matter interactions. Dr. Ren received a Ph.D. from Swinburne University of Technology in 2017. He was a postdoc at RMIT University from 2017 to 2018. In 2018, Dr. Ren won a Victoria Fellowship to visit the CNRS in France. In 2019, Dr. Ren was awarded a Humboldt Postdoctoral Research Fellowship at LMU Munich in Germany. In December 2020, he started a MQRF at Macquarie University. Dr. Ren won a 2022 ARC DECRA Fellowship. He is an Associate Investigator for the ARC Centre of Excellence for Transformative Meta-Optical Systems.

Stefan A. Maier obtained his Ph.D. degree in Applied Physics from the California Institute of Technology. He joined the Department of Physics at Imperial College London in 2007 and since 2016 holds the Lee-Lucas Chair in Experimental Physics. In 2017, he joined LMU Munich to set up the Chair in Hybrid Nanosystems. Since March 2022, he is the Head of the School of Physics and Astronomy at Monash University in Melbourne, Australia. His research focus spans many areas of nanophotonics, from fundamental investigations of nanocavities using photons and electron beams to applications in sensing, energy conversion, and optoelectronics. He is further Editor-in-Chief of the Journal *Nanophotonics*.

ABBREVIATIONS

1D	one-dimensional
2D	two-dimensional
3D	three-dimensional
β-BBO	β-barium borate
AC	alternating current
ACEO	alternating current electro-osmotic
AFM	atomic force microscope
APCE	absorbed photon-to-current conversion efficiency
AM 1.5 G	air mass coefficient 1.5 global
ARC	antireflective coating
BIC	bound states in the continuum
CB	conduction band
CBP	4,4′-bis(N-carbazolyl)-1,1′-biphenyl
CD	circular dichroism
CE	counter electrode
CIGS	CuInGaSe
CMOS	complementary metal−oxide semiconductor
CPL	circular polarized light
CVD	chemical vapor deposition
CW	continuous wave
DFG	difference frequency generation
EBL	electron-beam lithography
E_g	band gap
E_g^{PV}	photovoltaic band gap
EBL	electron beam lithography
E-field	electric field
EM	electromagnetic
EQE	external quantum efficiency
ETP	electro-thermoplasmonic
FDTD	finite-difference time domain
ff	filling factor
FIB	focused ion beam
FTO	fluorine-doped tin oxide
fwhm	full width at half-maximum
FWM	four-wave mixing
GST	$Ge_2Sb_2Te_5$
GSST	$Ge_2Sb_2Se_4Te$
hBN	hexagonal boron nitride
hcp	hexagonal close-packed
HER	hydrogen evolution reaction
HPhP	hyperbolic phonon polariton
HTC	heat transfer coefficient
IC	integrated circuit
IDT	interdigital transducer
IPCE	incident photon conversion efficiency
IQE	internal quantum efficiency
IR	infrared
ITO	indium tin oxide
LA	longitudinal acoustic
LB	lower band
LCP	left-circularly polarized
LO	longitudinal optical
LPD	light penetration depth
LPhP	localized phonon polariton
LSPP	localized surface plasmon polariton
LSPR	localized surface plasmon resonance
MB	middle band
MGM	metal−graphene−metal
MIM	metal−insulator−metal
MQW	multiquantum-wells
MS	metasurface
NA	numerical aperture
NEP	noise equivalent power
NFRHT	near-field radiative heat transfer
NIL	nano imprint lithography
NIR	near-infrared
NOM	nonlinear optical materials
NP	nanoparticle
NPG	nanoporous gold
NPoM	nanoparticle on-a-mirror
NRG	nanoring array
OER	oxygen evolution reaction
PCM	phase change materials
PEC	photoelectrochemical
PEDOT:PSS	poly(3,4-ethylene dioxythiophene):poly-(styrenesulfonate)
PDMS	polydimethylsiloxane
PMMA	polymethylmethacrylate
PS	polystyrene
PV	photovoltaic
QC	quantum cutting
QCL	quantum cascade laser
QE	electric quadrupole
Q factor	resonance quality factor
QM	magnetic quadrupole
QW	quantum well
RCP	right-circularly polarized
RE	reference electrode
RF	radiofrequency
RHE	reversible hydrogen electrode
RIE	reactive ion etching
RR	reduction reaction
SAM	self-assembled monolayer
SAW	surface acoustic wave
SEIRA	surface enhanced infrared absorption
SEM	scanning electron microscope
SERS	surface enhanced Raman spectroscopy
SFG	sum-frequency generation
SHE	standard hydrogen electrode
SHG	second harmonic generation
SLM	spatial light modulator
SLR	surface lattice resonance
SPDC	spontaneous parametric down-conversion
SPhP	surface phonon polariton
SPM	self-phase modulation
SPP	surface plasmon polariton
SPR	surface plasmon resonance
SQ	Shockley-Queisser
SRR	split-ring resonator
sSNOM	scattering scanning near-field optical microscopy
SSP	surface plasmon polariton
STPV	solar thermophotovoltaics
TA	transversal acoustic
TCO	transparent conductive oxide
TE	transverse electric

THG	third harmonic generation
TM	transverse magnetic
TMD	transition metal dichalcogenides
TO	transversal optical
TP	twin photons
TPA	two-photon absorption
TPP	truncated pyramid pillars
UC	upconversion
UV	ultraviolet
VB	valence band
vdW	van der Waals
VIS	visible
WE	working electrode
ZFLO	zone-folded longitudinal optical

REFERENCES

(1) Pendry, J. B.; Schurig, D.; Smith, D. R. Controlling Electromagnetic Fields. *Science* **2006**, *312*, 1780−1782.

(2) Shalaev, V. M. Optical Negative-Index Metamaterials. *Nat. Photonics* **2007**, *1*, 41−48.

(3) Jahani, S.; Jacob, Z. All-Dielectric Metamaterials. *Nat. Nanotechnol.* **2016**, *11*, 23−36.

(4) Soukoulis, C. M.; Wegener, M. Past Achievements and Future Challenges in the Development of Three-Dimensional Photonic Metamaterials. *Nat. Photonics* **2011**, *5*, 523−530.

(5) Ding, F.; Pors, A.; Bozhevolnyi, S. I. Gradient Metasurfaces: A Review of Fundamentals and Applications. *Rep. Prog. Phys.* **2018**, *81*, 026401.

(6) Genevet, P.; Capasso, F.; Aieta, F.; Khorasaninejad, M.; Devlin, R. Recent Advances in Planar Optics: From Plasmonic to Dielectric Metasurfaces. *Optica* **2017**, *4*, 139−152.

(7) Deng, J.; Su, Y.; Liu, D.; Yang, P.; Liu, B.; Liu, C. Nanowire Photoelectrochemistry. *Chem. Rev.* **2019**, *119*, 9221−9259.

(8) Barber, J. Photosynthetic Energy Conversion: Natural and Artificial. *Chem. Soc. Rev.* **2009**, *38*, 185−196.

(9) Jackson, J. D. *Classical Electrodynamics*, 3rd ed.; Wiley, 1999.

(10) Dressel, M.; Grüner, G. *Electrodynamics of Solids: Optical Properties of Electrons in Matter*; Cambridge University Press, 2002.

(11) Bohren, C. F.; Huffman, D. R. *Absorption and Scattering of Light by Small Particles*; Wiley-VCH, 2004.

(12) Zhou, H.; Li, D.; Hui, X.; Mu, X. Infrared Metamaterial for Surface-Enhanced Infrared Absorption Spectroscopy: Pushing the Frontier of Ultrasensitive On-Chip Sensing. *Int. J. Optomechatronics* **2021**, *15*, 97−119.

(13) Mayerhöfer, T. G.; Popp, J. Periodic Array-Based Substrates for Surface-Enhanced Infrared Spectroscopy. *Nanophotonics* **2018**, *7*, 39−79.

(14) Neubrech, F.; Huck, C.; Weber, K.; Pucci, A.; Giessen, H. Surface-Enhanced Infrared Spectroscopy Using Resonant Nanoantennas. *Chem. Rev.* **2017**, *117*, 5110−5145.

(15) Semenyshyn, R.; Hentschel, M.; Huck, C.; Vogt, J.; Weiher, F.; Giessen, H.; Neubrech, F. Resonant Plasmonic Nanoslits Enable in Vitro Observation of Single-Monolayer Collagen-Peptide Dynamics. *ACS Sens.* **2019**, *4*, 1966−1972.

(16) Brown, L. V.; Yang, X.; Zhao, K.; Zheng, B. Y.; Nordlander, P.; Halas, N. J. Fan-Shaped Gold Nanoantennas above Reflective Substrates for Surface-Enhanced Infrared Absorption (SEIRA). *Nano Lett.* **2015**, *15*, 1272−1280.

(17) Huck, C.; Vogt, J.; Sendner, M.; Hengstler, D.; Neubrech, F.; Pucci, A. Plasmonic Enhancement of Infrared Vibrational Signals: Nanoslits versus Nanorods. *ACS Photonics* **2015**, *2*, 1489−1497.

(18) Rodrigo, D.; Tittl, A.; Ait-Bouziad, N.; John-Herpin, A.; Limaj, O.; Kelly, C.; Yoo, D.; Wittenberg, N. J.; Oh, S.-H.; Lashuel, H. A.; et al. Resolving Molecule-Specific Information in Dynamic Lipid Membrane Processes with Multi-Resonant Infrared Metasurfaces. *Nat. Commun.* **2018**, *9*, 2160.

(19) Liu, N.; Mesch, M.; Weiss, T.; Hentschel, M.; Giessen, H. Infrared Perfect Absorber and Its Application As Plasmonic Sensor. *Nano Lett.* **2010**, *10*, 2342−2348.

(20) Landy, N. I.; Sajuyigbe, S.; Mock, J. J.; Smith, D. R.; Padilla, W. J. Perfect Metamaterial Absorber. *Phys. Rev. Lett.* **2008**, *100*, 207402.

(21) Tittl, A.; Harats, M. G.; Walter, R.; Yin, X.; Schäferling, M.; Liu, N.; Rapaport, R.; Giessen, H. Quantitative Angle-Resolved Small-Spot Reflectance Measurements on Plasmonic Perfect Absorbers: Impedance Matching and Disorder Effects. *ACS Nano* **2014**, *8*, 10885−10892.

(22) Tittl, A.; Mai, P.; Taubert, R.; Dregely, D.; Liu, N.; Giessen, H. Palladium-Based Plasmonic Perfect Absorber in the Visible Wavelength Range and Its Application to Hydrogen Sensing. *Nano Lett.* **2011**, *11*, 4366−4369.

(23) Hendrickson, J.; Guo, J.; Zhang, B.; Buchwald, W.; Soref, R. Wideband Perfect Light Absorber at Midwave Infrared Using Multiplexed Metal Structures. *Opt. Lett.* **2012**, *37*, 371−373.

(24) Grant, J.; McCrindle, I. J. H.; Li, C.; Cumming, D. R. S. Multispectral Metamaterial Absorber. *Opt. Lett.* **2014**, *39*, 1227−1230.

(25) Chen, K.; Adato, R.; Altug, H. Dual-Band Perfect Absorber for Multispectral Plasmon-Enhanced Infrared Spectroscopy. *ACS Nano* **2012**, *6*, 7998−8006.

(26) Huang, L.; Chen, X.; Mühlenbernd, H.; Zhang, H.; Chen, S.; Bai, B.; Tan, Q.; Jin, G.; Cheah, K.-W.; Qiu, C.-W.; et al. Three-Dimensional Optical Holography Using a Plasmonic Metasurface. *Nat. Commun.* **2013**, *4*, 2808.

(27) Li, J.; Chen, S.; Yang, H.; Li, J.; Yu, P.; Cheng, H.; Gu, C.; Chen, H.-T.; Tian, J. Simultaneous Control of Light Polarization and Phase Distributions Using Plasmonic Metasurfaces. *Adv. Funct. Mater.* **2015**, *25*, 704−710.

(28) Dolling, G.; Wegener, M.; Linden, S.; Hormann, C. Photorealistic Images of Objects in Effective Negative-Index Materials. *Opt. Express* **2006**, *14*, 1842−1849.

(29) Valentine, J.; Zhang, S.; Zentgraf, T.; Ulin-Avila, E.; Genov, D. A.; Bartal, G.; Zhang, X. Three-Dimensional Optical Metamaterial with a Negative Refractive Index. *Nature* **2008**, *455*, 376−379.

(30) Hartland, G. V. Optical Studies of Dynamics in Noble Metal Nanostructures. *Chem. Rev.* **2011**, *111*, 3858−3887.

(31) Dondapati, S. K.; Sau, T. K.; Hrelescu, C.; Klar, T. A.; Stefani, F. D.; Feldmann, J. Label-Free Biosensing Based on Single Gold Nanostars as Plasmonic Transducers. *ACS Nano* **2010**, *4*, 6318−6322.

(32) Hao, F.; Nehl, C. L.; Hafner, J. H.; Nordlander, P. Plasmon Resonances of a Gold Nanostar. *Nano Lett.* **2007**, *7*, 729−732.

(33) Liu, E.; Qi, L.; Bian, J.; Chen, Y.; Hu, X.; Fan, J.; Liu, H.; Zhu, C.; Wang, Q. A Facile Strategy to Fabricate Plasmonic Cu Modified TiO_2 Nano-Flower Films for Photocatalytic Reduction of CO_2 to Methanol. *Mater. Res. Bull.* **2015**, *68*, 203−209.

(34) Wang, H.; Sun, Z.; Yang, Y.; Su, D. The Growth and Enhanced Catalytic Performance of Au@Pd Core-Shell Nanodendrites. *Nanoscale* **2013**, *5*, 139−142.

(35) Maier, S. A. *Plasmonics: Fundamentals and Applications*; Springer, 2007.

(36) Mubeen, S.; Zhang, S.; Kim, N.; Lee, S.; Krämer, S.; Xu, H.; Moskovits, M. Plasmonic Properties of Gold Nanoparticles Separated from a Gold Mirror by an Ultrathin Oxide. *Nano Lett.* **2012**, *12*, 2088−2094.

(37) Hill, R. T.; Mock, J. J.; Hucknall, A.; Wolter, S. D.; Jokerst, N. M.; Smith, D. R.; Chilkoti, A. Plasmon Ruler with Angstrom Length Resolution. *ACS Nano* **2012**, *6*, 9237−9246.

(38) Cirací, C.; Hill, R. T.; Mock, J. J.; Urzhumov, Y.; Fernández-Domínguez, A. I.; Maier, S. A.; Pendry, J. B.; Chilkoti, A.; Smith, D. R. Probing the Ultimate Limits of Plasmonic Enhancement. *Science* **2012**, *337*, 1072−1074.

(39) Li, G.-C.; Lei, D.; Qiu, M.; Jin, W.; Lan, S.; Zayats, A. V. Light-Induced Symmetry Breaking for Enhancing Second-Harmonic Generation from an Ultrathin Plasmonic Nanocavity. *Nat. Commun.* **2021**, *12*, 4326.

(40) Monticone, F.; Alù, A. The Quest for Optical Magnetism: From Split-Ring Resonators to Plasmonic Nanoparticles and Nanoclusters. *J. Mater. Chem. C* **2014**, *2*, 9059−9072.

(41) Aydin, K.; Bulu, I.; Guven, K.; Kafesaki, M.; Soukoulis, C. M.; Ozbay, E. Investigation of Magnetic Resonances for Different Split-Ring Resonator Parameters and Designs. *New J. Phys.* **2005**, *7*, 168−168.

(42) Klein, M. W.; Enrich, C.; Wegener, M.; Soukoulis, C. M.; Linden, S. Single-Slit Split-Ring Resonators at Optical Frequencies: Limits of Size Scaling. *Opt. Lett.* **2006**, *31*, 1259−1261.

(43) Lovera, A.; Gallinet, B.; Nordlander, P.; Martin, O. J. F. Mechanisms of Fano Resonances in Coupled Plasmonic Systems. *ACS Nano* **2013**, *7*, 4527−4536.

(44) Luk'yanchuk, B.; Zheludev, N. I.; Maier, S. A.; Halas, N. J.; Nordlander, P.; Giessen, H.; Chong, C. T. The Fano Resonance in Plasmonic Nanostructures and Metamaterials. *Nat. Mater.* **2010**, *9*, 707−715.

(45) Gallinet, B.; Martin, O. J. F. Relation between Near-Field and Far-Field Properties of Plasmonic Fano Resonances. *Opt. Express* **2011**, *19*, 22167−22175.

(46) Verellen, N.; Sonnefraud, Y.; Sobhani, H.; Hao, F.; Moshchalkov, V. V.; Dorpe, P. V.; Nordlander, P.; Maier, S. A. Fano Resonances in Individual Coherent Plasmonic Nanocavities. *Nano Lett.* **2009**, *9*, 1663−1667.

(47) Liu, N.; Langguth, L.; Weiss, T.; Kästel, J.; Fleischhauer, M.; Pfau, T.; Giessen, H. Plasmonic Analogue of Electromagnetically Induced Transparency at the Drude Damping Limit. *Nat. Mater.* **2009**, *8*, 758−762.

(48) Hentschel, M.; Dregely, D.; Vogelgesang, R.; Giessen, H.; Liu, N. Plasmonic Oligomers: The Role of Individual Particles in Collective Behavior. *ACS Nano* **2011**, *5*, 2042−2050.

(49) Lassiter, J. B.; Sobhani, H.; Fan, J. A.; Kundu, J.; Capasso, F.; Nordlander, P.; Halas, N. J. Fano Resonances in Plasmonic Nano-clusters: Geometrical and Chemical Tunability. *Nano Lett.* **2010**, *10*, 3184−3189.

(50) Mousavi, S. H.; Kholmanov, I.; Alici, K. B.; Purtseladze, D.; Arju, N.; Tatar, K.; Fozdar, D. Y.; Suk, J. W.; Hao, Y.; Khanikaev, A. B.; et al. Inductive Tuning of Fano-Resonant Metasurfaces Using Plasmonic Response of Graphene in the Mid-Infrared. *Nano Lett.* **2013**, *13*, 1111−1117.

(51) Wu, C.; Khanikaev, A. B.; Adato, R.; Arju, N.; Yanik, A. A.; Altug, H.; Shvets, G. Fano-Resonant Asymmetric Metamaterials for Ultra-sensitive Spectroscopy and Identification of Molecular Monolayers. *Nat. Mater.* **2012**, *11*, 69−75.

(52) Simoncelli, S.; Li, Y.; Cortés, E.; Maier, S. A. Imaging Plasmon Hybridization of Fano Resonances via Hot-Electron-Mediated Absorption Mapping. *Nano Lett.* **2018**, *18*, 3400−3406.

(53) Kuznetsov, A. I.; Miroshnichenko, A. E.; Brongersma, M. L.; Kivshar, Y. S.; Luk'yanchuk, B. Optically Resonant Dielectric Nanostructures. *Science* **2016**, *354*, aag2472.

(54) Alaee, R.; Rockstuhl, C.; Fernandez-Corbaton, I. An Electro-magnetic Multipole Expansion beyond the Long-Wavelength Approx-imation. *Opt. Commun.* **2018**, *407*, 17−21.

(55) Hüttenhofer, L.; Eckmann, F.; Lauri, A.; Cambiasso, J.; Pensa, E.; Li, Y.; Cortés, E.; Sharp, I. D.; Maier, S. A. Anapole Excitations in Oxygen-Vacancy-Rich TiO$_{2-x}$ Nanoresonators: Tuning the Absorption for Photocatalysis in the Visible Spectrum. *ACS Nano* **2020**, *14*, 2456−2464.

(56) Hsu, C. W.; Zhen, B.; Stone, A. D.; Joannopoulos, J. D.; Soljačić, M. Bound States in the Continuum. *Nat. Rev. Mater.* **2016**, *1*, 16048.

(57) Azzam, S. I.; Kildishev, A. V. Photonic Bound States in the Continuum: From Basics to Applications. *Adv. Opt. Mater.* **2021**, *9*, 2001469.

(58) Koshelev, K.; Favraud, G.; Bogdanov, A.; Kivshar, Y.; Fratalocchi, A. Nonradiating Photonics with Resonant Dielectric Nanostructures. *Nanophotonics* **2019**, *8*, 725−745.

(59) Rybin, M. V.; Koshelev, K. L.; Sadrieva, Z. F.; Samusev, K. B.; Bogdanov, A. A.; Limonov, M. F.; Kivshar, Y. S. High-Q Supercavity

Modes in Subwavelength Dielectric Resonators. *Phys. Rev. Lett.* **2017**, *119*, 243901.

(60) Huang, L.; Xu, L.; Rahmani, M.; Neshev, D.; Miroshnichenko, A. E. Pushing the Limit of High-Q Mode of a Single Dielectric Nanocavity. *Adv. Photonics* **2021**, *3*, 016004.

(61) Koshelev, K.; Kruk, S.; Melik-Gaykazyan, E.; Choi, J.-H.; Bogdanov, A.; Park, H.-G.; Kivshar, Y. Subwavelength Dielectric Resonators for Nonlinear Nanophotonics. *Science* **2020**, *367*, 288−292.

(62) Yang, Y.; Peng, C.; Liang, Y.; Li, Z.; Noda, S. Analytical Perspective for Bound States in the Continuum in Photonic Crystal Slabs. *Phys. Rev. Lett.* **2014**, *113*, 037401.

(63) Melik-Gaykazyan, E.; Koshelev, K.; Choi, J.-H.; Kruk, S. S.; Bogdanov, A.; Park, H.-G.; Kivshar, Y. From Fano to Quasi-BIC Resonances in Individual Dielectric Nanoantennas. *Nano Lett.* **2021**, *21*, 1765−1771.

(64) Gorkunov, M. V.; Antonov, A. A.; Kivshar, Y. S. Metasurfaces with Maximum Chirality Empowered by Bound States in the Continuum. *Phys. Rev. Lett.* **2020**, *125*, 093903.

(65) Overvig, A.; Yu, N.; Alù, A. Chiral Quasi-Bound States in the Continuum. *Phys. Rev. Lett.* **2021**, *126*, 073001.

(66) Miroshnichenko, A. E.; Evlyukhin, A. B.; Yu, Y. F.; Bakker, R. M.; Chipouline, A.; Kuznetsov, A. I.; Luk'yanchuk, B.; Chichkov, B. N.; Kivshar, Y. S. Nonradiating Anapole Modes in Dielectric Nanoparticles. *Nat. Commun.* **2015**, *6*, 8069.

(67) Barrow, S. J.; Rossouw, D.; Funston, A. M.; Botton, G. A.; Mulvaney, P. Mapping Bright and Dark Modes in Gold Nanoparticle Chains Using Electron Energy Loss Spectroscopy. *Nano Lett.* **2014**, *14*, 3799−3808.

(68) Willingham, B.; Link, S. Energy Transport in Metal Nanoparticle Chains via Sub-Radiant Plasmon Modes. *Opt. Express* **2011**, *19*, 6450−6461.

(69) Brongersma, M. L.; Hartman, J. W.; Atwater, H. A. Electro-magnetic Energy Transfer and Switching in Nanoparticle Chain Arrays below the Diffraction Limit. *Phys. Rev. B* **2000**, *62*, R16356−R16359.

(70) Maier, S. A.; Kik, P. G.; Atwater, H. A. Observation of Coupled Plasmon-Polariton Modes in Au Nanoparticle Chain Waveguides of Different Lengths: Estimation of Waveguide Loss. *Appl. Phys. Lett.* **2002**, *81*, 1714−1716.

(71) Harris, N.; Arnold, M. D.; Blaber, M. G.; Ford, M. J. Plasmonic Resonances of Closely Coupled Gold Nanosphere Chains. *J. Phys. Chem. C* **2009**, *113*, 2784−2791.

(72) Fedotov, V. A.; Rose, M.; Prosvirnin, S. L.; Papasimakis, N.; Zheludev, N. I. Sharp Trapped-Mode Resonances in Planar Metamaterials with a Broken Structural Symmetry. *Phys. Rev. Lett.* **2007**, *99*, 147401.

(73) Liu, Z.; Ye, J. Highly Controllable Double Fano Resonances in Plasmonic Metasurfaces. *Nanoscale* **2016**, *8*, 17665−17674.

(74) Kravets, V. G.; Kabashin, A. V.; Barnes, W. L.; Grigorenko, A. N. Plasmonic Surface Lattice Resonances: A Review of Properties and Applications. *Chem. Rev.* **2018**, *118*, 5912−5951.

(75) Hamans, R. F.; Parente, M.; Castellanos, G. W.; Ramezani, M.; Gómez Rivas, J.; Baldi, A. Super-Resolution Mapping of Enhanced Emission by Collective Plasmonic Resonances. *ACS Nano* **2019**, *13*, 4514−4521.

(76) Ross, M. B.; Mirkin, C. A.; Schatz, G. C. Optical Properties of One-, Two-, and Three-Dimensional Arrays of Plasmonic Nanostruc-tures. *J. Phys. Chem. C* **2016**, *120*, 816−830.

(77) Chu, Y.; Schonbrun, E.; Yang, T.; Crozier, K. B. Experimental Observation of Narrow Surface Plasmon Resonances in Gold Nanoparticle Arrays. *Appl. Phys. Lett.* **2008**, *93*, 181108.

(78) Kravets, V. G.; Schedin, F.; Grigorenko, A. N. Extremely Narrow Plasmon Resonances Based on Diffraction Coupling of Localized Plasmons in Arrays of Metallic Nanoparticles. *Phys. Rev. Lett.* **2008**, *101*, 087403.

(79) Auguié, B.; Barnes, W. L. Collective Resonances in Gold Nanoparticle Arrays. *Phys. Rev. Lett.* **2008**, *101*, 143902.

(80) Cherqui, C.; Bourgeois, M. R.; Wang, D.; Schatz, G. C. Plasmonic Surface Lattice Resonances: Theory and Computation. *Acc. Chem. Res.* **2019**, *52*, 2548−2558.

(81) Bin-Alam, M. S.; Reshef, O.; Mamchur, Y.; Alam, M. Z.; Carlow, G.; Upham, J.; Sullivan, B. T.; Ménard, J.-M.; Huttunen, M. J.; Boyd, R. W.; et al. Ultra-High-Q Resonances in Plasmonic Metasurfaces. *Nat. Commun.* **2021**, *12*, 974.

(82) Zundel, L.; Manjavacas, A. Finite-Size Effects on Periodic Arrays of Nanostructures. *J. Phys. Photonics* **2019**, *1*, 015004.

(83) Rodriguez, S. R. K.; Schaafsma, M. C.; Berrier, A.; Gómez Rivas, J. Collective Resonances in Plasmonic Crystals: Size Matters. *Phys. B Condens. Matter* **2012**, *407*, 4081–4085.

(84) Zhou, W.; Odom, T. W. Tunable Subradiant Lattice Plasmons by Out-of-Plane Dipolar Interactions. *Nat. Nanotechnol.* **2011**, *6*, 423–427.

(85) Yang, A.; Hryn, A. J.; Bourgeois, M. R.; Lee, W.-K.; Hu, J.; Schatz, G. C.; Odom, T. W. Programmable and Reversible Plasmon Mode Engineering. *Proc. Natl. Acad. Sci. U. S. A.* **2016**, *113*, 14201–14206.

(86) Zundel, L.; May, A.; Manjavacas, A. Lattice Resonances Induced by Periodic Vacancies in Arrays of Nanoparticles. *ACS Photonics* **2021**, *8*, 360–368.

(87) Humphrey, A. D.; Meinzer, N.; Starkey, T. A.; Barnes, W. L. Surface Lattice Resonances in Plasmonic Arrays of Asymmetric Disc Dimers. *ACS Photonics* **2016**, *3*, 634–639.

(88) Cuartero-González, A.; Sanders, S.; Zundel, L.; Fernández-Domínguez, A. I.; Manjavacas, A. Super- and Subradiant Lattice Resonances in Bipartite Nanoparticle Arrays. *ACS Nano* **2020**, *14*, 11876–11887.

(89) Khlopin, D.; Laux, F.; Wardley, W. P.; Martin, J.; Wurtz, G. A.; Plain, J.; Bonod, N.; Zayats, A. V.; Dickson, W.; Gérard, D. Lattice Modes and Plasmonic Linewidth Engineering in Gold and Aluminum Nanoparticle Arrays. *J. Opt. Soc. Am. B* **2017**, *34*, 691–700.

(90) Zou, S.; Janel, N.; Schatz, G. C. Silver Nanoparticle Array Structures That Produce Remarkably Narrow Plasmon Lineshapes. *J. Chem. Phys.* **2004**, *120*, 10871–10875.

(91) Castellanos, G. W.; Bai, P.; Gómez Rivas, J. Lattice Resonances in Dielectric Metasurfaces. *J. Appl. Phys.* **2019**, *125*, 213105.

(92) Yang, Y.; Wang, W.; Moitra, P.; Kravchenko, I. I.; Briggs, D. P.; Valentine, J. Dielectric Meta-Reflectarray for Broadband Linear Polarization Conversion and Optical Vortex Generation. *Nano Lett.* **2014**, *14*, 1394–1399.

(93) Vaskin, A.; Bohn, J.; Chong, K. E.; Bucher, T.; Zilk, M.; Choi, D.-Y.; Neshev, D. N.; Kivshar, Y. S.; Pertsch, T.; Staude, I. Directional and Spectral Shaping of Light Emission with Mie-Resonant Silicon Nanoantenna Arrays. *ACS Photonics* **2018**, *5*, 1359–1364.

(94) Staude, I.; Miroshnichenko, A. E.; Decker, M.; Fofang, N. T.; Liu, S.; Gonzales, E.; Dominguez, J.; Luk, T. S.; Neshev, D. N.; Brener, I.; et al. Tailoring Directional Scattering through Magnetic and Electric Resonances in Subwavelength Silicon Nanodisks. *ACS Nano* **2013**, *7*, 7824–7832.

(95) Li, J.; Verellen, N.; Van Dorpe, P. Engineering Electric and Magnetic Dipole Coupling in Arrays of Dielectric Nanoparticles. *J. Appl. Phys.* **2018**, *123*, 083101.

(96) Babicheva, V. E.; Moloney, J. V. Lattice Effect Influence on the Electric and Magnetic Dipole Resonance Overlap in a Disk Array. *Nanophotonics* **2018**, *7*, 1663–1668.

(97) Conteduca, D.; Barth, I.; Pitruzzello, G.; Reardon, C. P.; Martins, E. R.; Krauss, T. F. Dielectric Nanohole Array Metasurface for High-Resolution Near-Field Sensing and Imaging. *Nat. Commun.* **2021**, *12*, 3293.

(98) Lepeshov, S.; Kivshar, Y. Near-Field Coupling Effects in Mie-Resonant Photonic Structures and All-Dielectric Metasurfaces. *ACS Photonics* **2018**, *5*, 2888–2894.

(99) Baryshnikova, K. V.; Petrov, M. I.; Babicheva, V. E.; Belov, P. A. Plasmonic and Silicon Spherical Nanoparticle Antireflective Coatings. *Sci. Rep.* **2016**, *6*, 22136.

(100) Murai, S.; Castellanos, G. W.; Raziman, T. V.; Curto, A. G.; Rivas, J. G. Enhanced Light Emission by Magnetic and Electric Resonances in Dielectric Metasurfaces. *Adv. Opt. Mater.* **2020**, *8*, 1902024.

(101) Wu, C.; Arju, N.; Kelp, G.; Fan, J. A.; Dominguez, J.; Gonzales, E.; Tutuc, E.; Brener, I.; Shvets, G. Spectrally Selective Chiral Silicon Metasurfaces Based on Infrared Fano Resonances. *Nat. Commun.* **2014**, *5*, 3892.

(102) Yang, Y.; Wang, W.; Boulesbaa, A.; Kravchenko, I. I.; Briggs, D. P.; Puretzky, A.; Geohegan, D.; Valentine, J. Nonlinear Fano-Resonant Dielectric Metasurfaces. *Nano Lett.* **2015**, *15*, 7388–7393.

(103) Zhao, W.; Leng, X.; Jiang, Y. Fano Resonance in All-Dielectric Binary Nanodisk Array Realizing Optical Filter with Efficient Linewidth Tuning. *Opt. Express* **2015**, *23*, 6858–6866.

(104) Campione, S.; Liu, S.; Basilio, L. I.; Warne, L. K.; Langston, W. L.; Luk, T. S.; Wendt, J. R.; Reno, J. L.; Keeler, G. A.; Brener, I.; et al. Broken Symmetry Dielectric Resonators for High Quality Factor Fano Metasurfaces. *ACS Photonics* **2016**, *3*, 2362–2367.

(105) Hüttenhofer, L.; Tittl, A.; Kühner, L.; Cortés, E.; Maier, S. A. Anapole-Assisted Absorption Engineering in Arrays of Coupled Amorphous Gallium Phosphide Nanodisks. *ACS Photonics* **2021**, *8*, 1469–1476.

(106) Ospanova, A. K.; Stenishchev, I. V.; Basharin, A. A. Anapole Mode Sustaining Silicon Metamaterials in Visible Spectral Range. *Laser Photonics Rev.* **2018**, *12*, 1800005.

(107) Tripathi, A.; Kim, H.-R.; Tonkaev, P.; Lee, S.-J.; Makarov, S. V.; Kruk, S. S.; Rybin, M. V.; Park, H.-G.; Kivshar, Y. Lasing Action from Anapole Metasurfaces. *Nano Lett.* **2021**, *21*, 6563–6568.

(108) Basharin, A. A.; Chuguevsky, V.; Volsky, N.; Kafesaki, M.; Economou, E. N. Extremely High Q-Factor Metamaterials Due to Anapole Excitation. *Phys. Rev. B* **2017**, *95*, 035104.

(109) Liu, S.-D.; Wang, Z.-X.; Wang, W.-J.; Chen, J.-D.; Chen, Z.-H. High Q-Factor with the Excitation of Anapole Modes in Dielectric Split Nanodisk Arrays. *Opt. Express* **2017**, *25*, 22375–22387.

(110) Koshelev, K.; Lepeshov, S.; Liu, M.; Bogdanov, A.; Kivshar, Y. Asymmetric Metasurfaces with High-Q Resonances Governed by Bound States in the Continuum. *Phys. Rev. Lett.* **2018**, *121*, 193903.

(111) Romano, S.; Mangini, M.; Penzo, E.; Cabrini, S.; De Luca, A. C.; Rendina, I.; Mocella, V.; Zito, G. Ultrasensitive Surface Refractive Index Imaging Based on Quasi-Bound States in the Continuum. *ACS Nano* **2020**, *14*, 15417–15427.

(112) Yesilkoy, F.; Arvelo, E. R.; Jahani, Y.; Liu, M.; Tittl, A.; Cevher, V.; Kivshar, Y.; Altug, H. Ultrasensitive Hyperspectral Imaging and Biodetection Enabled by Dielectric Metasurfaces. *Nat. Photonics* **2019**, *13*, 390–396.

(113) Tittl, A.; Leitis, A.; Liu, M.; Yesilkoy, F.; Choi, D.-Y.; Neshev, D. N.; Kivshar, Y. S.; Altug, H. Imaging-Based Molecular Barcoding with Pixelated Dielectric Metasurfaces. *Science* **2018**, *360*, 1105–1109.

(114) Liu, Z.; Wang, J.; Chen, B.; Wei, Y.; Liu, W.; Liu, J. Giant Enhancement of Continuous Wave Second Harmonic Generation from Few-Layer GaSe Coupled to High-Q Quasi Bound States in the Continuum. *Nano Lett.* **2021**, *21*, 7405–7410.

(115) Bernhardt, N.; Koshelev, K.; White, S. J. U.; Meng, K. W. C.; Fröch, J. E.; Kim, S.; Tran, T. T.; Choi, D.-Y.; Kivshar, Y.; Solntsev, A. S. Quasi-BIC Resonant Enhancement of Second-Harmonic Generation in WS$_2$ Monolayers. *Nano Lett.* **2020**, *20*, 5309–5314.

(116) Liu, Z.; Xu, Y.; Lin, Y.; Xiang, J.; Feng, T.; Cao, Q.; Li, J.; Lan, S.; Liu, J. High-Q Quasibound States in the Continuum for Nonlinear Metasurfaces. *Phys. Rev. Lett.* **2019**, *123*, 253901.

(117) Sekkat, Z.; Hayashi, S.; Nesterenko, D. V.; Rahmouni, A.; Refki, S.; Ishitobi, H.; Inouye, Y.; Kawata, S. Plasmonic Coupled Modes in Metal-Dielectric Multilayer Structures: Fano Resonance and Giant Field Enhancement. *Opt. Express* **2016**, *24*, 20080–20088.

(118) Shibanuma, T.; Grinblat, G.; Albella, P.; Maier, S. A. Efficient Third Harmonic Generation from Metal-Dielectric Hybrid Nanoantennas. *Nano Lett.* **2017**, *17*, 2647–2651.

(119) Aouani, H.; Rahmani, M.; Navarro-Cía, M.; Maier, S. A. Third-Harmonic-Upconversion Enhancement from a Single Semiconductor Nanoparticle Coupled to a Plasmonic Antenna. *Nat. Nanotechnol.* **2014**, *9*, 290–294.

(120) Yang, Y.; Miller, O. D.; Christensen, T.; Joannopoulos, J. D.; Soljačić, M. Low-Loss Plasmonic Dielectric Nanoresonators. *Nano Lett.* **2017**, *17*, 3238–3245.

(121) Jiang, R.; Li, B.; Fang, C.; Wang, J. Metal/Semiconductor Hybrid Nanostructures for Plasmon-Enhanced Applications. *Adv. Mater.* **2014**, *26*, 5274−5309.

(122) Kang, E. S. H.; Shiran Chaharsoughi, M.; Rossi, S.; Jonsson, M. P. Hybrid Plasmonic Metasurfaces. *J. Appl. Phys.* **2019**, *126*, 140901.

(123) Huang, Y.; Liu, L.; Pu, M.; Li, X.; Ma, X.; Luo, X. A Refractory Metamaterial Absorber for Ultra-Broadband, Omnidirectional and Polarization-Independent Absorption in the UV-NIR Spectrum. *Nanoscale* **2018**, *10*, 8298−8303.

(124) Rifat, A.; Rahmani, M.; Xu, L.; Miroshnichenko, A. Hybrid Metasurface Based Tunable Near-Perfect Absorber and Plasmonic Sensor. *Materials* **2018**, *11*, 1091.

(125) Guo, R.; Rusak, E.; Staude, I.; Dominguez, J.; Decker, M.; Rockstuhl, C.; Brener, I.; Neshev, D. N.; Kivshar, Y. S. Multipolar Coupling in Hybrid Metal-Dielectric Metasurfaces. *ACS Photonics* **2016**, *3*, 349−353.

(126) Miroshnichenko, A. E.; Luk'yanchuk, B.; Maier, S. A.; Kivshar, Y. S. Optically Induced Interaction of Magnetic Moments in Hybrid Metamaterials. *ACS Nano* **2012**, *6*, 837−842.

(127) Wang, H.; Wang, X.; Yan, C.; Zhao, H.; Zhang, J.; Santschi, C.; Martin, O. J. F. Full Color Generation Using Silver Tandem Nanodisks. *ACS Nano* **2017**, *11*, 4419−4427.

(128) Yalavarthi, R.; Mascaretti, L.; Kudyshev, Z. A.; Dutta, A.; Kalytchuk, S.; Zbořil, R.; Schmuki, P.; Shalaev, V. M.; Kment, Š.; Boltasseva, A.; et al. Enhancing Photoelectrochemical Energy Storage by Large-Area CdS-Coated Nickel Nanoantenna Arrays. *ACS Appl. Energy Mater.* **2021**, *4*, 11367−11376.

(129) Eames, C.; Frost, J. M.; Barnes, P. R. F.; O'Regan, B. C.; Walsh, A.; Islam, M. S. Ionic Transport in Hybrid Lead Iodide Perovskite Solar Cells. *Nat. Commun.* **2015**, *6*, 7497.

(130) Adamo, G.; Swaha Krishnamoorthy, H. N.; Cortecchia, D.; Chaudhary, B.; Nalla, V.; Zheludev, N. I.; Soci, C. Metamaterial Enhancement of Metal-Halide Perovskite Luminescence. *Nano Lett.* **2020**, *20*, 7906−7911.

(131) Jing, H.; Zhu, Y.; Peng, R.-W.; Li, C.-Y.; Xiong, B.; Wang, Z.; Liu, Y.; Wang, M. Hybrid Organic-Inorganic Perovskite Metamaterial for Light Trapping and Photon-to-Electron Conversion. *Nanophotonics* **2020**, *9*, 3323−3333.

(132) Zhang, W.; Eperon, G. E.; Snaith, H. J. Metal Halide Perovskites for Energy Applications. *Nat. Energy* **2016**, *1*, 16048.

(133) Shamsi, J.; Urban, A. S.; Imran, M.; De Trizio, L.; Manna, L. Metal Halide Perovskite Nanocrystals: Synthesis, Post-Synthesis Modifications, and Their Optical Properties. *Chem. Rev.* **2019**, *119*, 3296−3348.

(134) Ricciardulli, A. G.; Yang, S.; Smet, J. H.; Saliba, M. Emerging Perovskite Monolayers. *Nat. Mater.* **2021**, *20*, 1325−1336.

(135) Li, Z.; Smalley, J. S. T.; Haroldson, R.; Lin, D.; Hawkins, R.; Gharajeh, A.; Moon, J.; Hou, J.; Zhang, C.; Hu, W.; et al. Active Perovskite Hyperbolic Metasurface. *ACS Photonics* **2020**, *7*, 1754−1761.

(136) Tiguntseva, E.; Chebykin, A.; Ishteev, A.; Haroldson, R.; Balachandran, B.; Ushakova, E.; Komissarenko, F.; Wang, H.; Milichko, V.; Tsypkin, A.; et al. Resonant Silicon Nanoparticles for Enhancement of Light Absorption and Photoluminescence from Hybrid Perovskite Films and Metasurfaces. *Nanoscale* **2017**, *9*, 12486−12493.

(137) Fan, Y.; Tonkaev, P.; Wang, Y.; Song, Q.; Han, J.; Makarov, S. V.; Kivshar, Y.; Xiao, S. Enhanced Multiphoton Processes in Perovskite Metasurfaces. *Nano Lett.* **2021**, *21*, 7191−7197.

(138) Tiguntseva, E. Y.; Zograf, G. P.; Komissarenko, F. E.; Zuev, D. A.; Zakhidov, A. A.; Makarov, S. V.; Kivshar, Y. S. Light-Emitting Halide Perovskite Nanoantennas. *Nano Lett.* **2018**, *18*, 1185−1190.

(139) Tiguntseva, E.; Koshelev, K.; Furasova, A.; Tonkaev, P.; Mikhailovskii, V.; Ushakova, E. V.; Baranov, D. G.; Shegai, T.; Zakhidov, A. A.; Kivshar, Y.; et al. Room-Temperature Lasing from Mie-Resonant Nonplasmonic Nanoparticles. *ACS Nano* **2020**, *14*, 8149−8156.

(140) Gholipour, B.; Adamo, G.; Cortecchia, D.; Krishnamoorthy, H. N. S.; Birowosuto, M. D.; Zheludev, N. I.; Soci, C. Organometallic Perovskite Metasurfaces. *Adv. Mater.* **2017**, *29*, 1604268.

(141) Baryshnikova, K.; Gets, D.; Liashenko, T.; Pushkarev, A.; Mukhin, I.; Kivshar, Y.; Makarov, S. Broadband Antireflection with Halide Perovskite Metasurfaces. *Laser Photonics Rev.* **2020**, *14*, 2000338.

(142) Xu, M.; Liang, T.; Shi, M.; Chen, H. Graphene-Like Two-Dimensional Materials. *Chem. Rev.* **2013**, *113*, 3766−3798.

(143) Wang, F.; Zhang, Y.; Tian, C.; Girit, C.; Zettl, A.; Crommie, M.; Shen, Y. R. Gate-Variable Optical Transitions in Graphene. *Science* **2008**, *320*, 206−209.

(144) García de Abajo, F. J. Graphene Plasmonics: Challenges and Opportunities. *ACS Photonics* **2014**, *1*, 135−152.

(145) Yan, H.; Li, X.; Chandra, B.; Tulevski, G.; Wu, Y.; Freitag, M.; Zhu, W.; Avouris, P.; Xia, F. Tunable Infrared Plasmonic Devices Using Graphene/Insulator Stacks. *Nat. Nanotechnol.* **2012**, *7*, 330−334.

(146) Li, Z.; Yao, K.; Xia, F.; Shen, S.; Tian, J.; Liu, Y. Graphene Plasmonic Metasurfaces to Steer Infrared Light. *Sci. Rep.* **2015**, *5*, 12423.

(147) Han, S.; Kim, S.; Kim, S.; Low, T.; Brar, V. W.; Jang, M. S. Complete Complex Amplitude Modulation with Electronically Tunable Graphene Plasmonic Metamolecules. *ACS Nano* **2020**, *14*, 1166−1175.

(148) Lee, I.-H.; Yoo, D.; Avouris, P.; Low, T.; Oh, S.-H. Graphene Acoustic Plasmon Resonator for Ultrasensitive Infrared Spectroscopy. *Nat. Nanotechnol.* **2019**, *14*, 313−319.

(149) Zeng, B.; Huang, Z.; Singh, A.; Yao, Y.; Azad, A. K.; Mohite, A. D.; Taylor, A. J.; Smith, D. R.; Chen, H.-T. Hybrid Graphene Metasurfaces for High-Speed Mid-Infrared Light Modulation and Single-Pixel Imaging. *Light Sci. Appl.* **2018**, *7*, 51.

(150) Xu, X.; Yao, W.; Xiao, D.; Heinz, T. F. Spin and Pseudospins in Layered Transition Metal Dichalcogenides. *Nat. Phys.* **2014**, *10*, 343−350.

(151) San-Jose, P.; Parente, V.; Guinea, F.; Roldán, R.; Prada, E. Inverse Funnel Effect of Excitons in Strained Black Phosphorus. *Phys. Rev. X* **2016**, *6*, 031046.

(152) Sortino, L.; Brooks, M.; Zotev, P. G.; Genco, A.; Cambiasso, J.; Mignuzzi, S.; Maier, S. A.; Burkard, G.; Sapienza, R.; Tartakovskii, A. I. Dielectric Nanoantennas for Strain Engineering in Atomically Thin Two-Dimensional Semiconductors. *ACS Photonics* **2020**, *7*, 2413−2422.

(153) Feng, J.; Qian, X.; Huang, C.-W.; Li, J. Strain-Engineered Artificial Atom as a Broad-Spectrum Solar Energy Funnel. *Nat. Photonics* **2012**, *6*, 866−872.

(154) Wang, Z.; Dong, Z.; Gu, Y.; Chang, Y.-H.; Zhang, L.; Li, L.-J.; Zhao, W.; Eda, G.; Zhang, W.; Grinblat, G.; et al. Giant Photoluminescence Enhancement in Tungsten-Diselenide-Gold Plasmonic Hybrid Structures. *Nat. Commun.* **2016**, *7*, 11283.

(155) Sortino, L.; Zotev, P. G.; Mignuzzi, S.; Cambiasso, J.; Schmidt, D.; Genco, A.; Aßmann, M.; Bayer, M.; Maier, S. A.; Sapienza, R.; et al. Enhanced Light-Matter Interaction in an Atomically Thin Semiconductor Coupled with Dielectric Nano-Antennas. *Nat. Commun.* **2019**, *10*, 5119.

(156) Liu, W.; Lee, B.; Naylor, C. H.; Ee, H.-S.; Park, J.; Johnson, A. T. C.; Agarwal, R. Strong Exciton-Plasmon Coupling in MoS$_2$ Coupled with Plasmonic Lattice. *Nano Lett.* **2016**, *16*, 1262−1269.

(157) Wang, S.; Li, S.; Chervy, T.; Shalabney, A.; Azzini, S.; Orgiu, E.; Hutchison, J. A.; Genet, C.; Samorì, P.; Ebbesen, T. W. Coherent Coupling of WS$_2$ Monolayers with Metallic Photonic Nanostructures at Room Temperature. *Nano Lett.* **2016**, *16*, 4368−4374.

(158) Ding, Y.; Wei, C.; Su, H.; Sun, S.; Tang, Z.; Wang, Z.; Li, G.; Liu, D.; Gwo, S.; Dai, J.; et al. Second Harmonic Generation Covering the Entire Visible Range from a 2D Material-Plasmon Hybrid Metasurface. *Adv. Opt. Mater.* **2021**, *9*, 2100625.

(159) Bucher, T.; Vaskin, A.; Mupparapu, R.; Löchner, F. J. F.; George, A.; Chong, K. E.; Fasold, S.; Neumann, C.; Choi, D.-Y.; Eilenberger, F.; et al. Tailoring Photoluminescence from MoS$_2$ Monolayers by Mie-Resonant Metasurfaces. *ACS Photonics* **2019**, *6*, 1002−1009.

(160) Chen, Y.; Miao, S.; Wang, T.; Zhong, D.; Saxena, A.; Chow, C.; Whitehead, J.; Gerace, D.; Xu, X.; Shi, S.-F.; et al. Metasurface

Integrated Monolayer Exciton Polariton. *Nano Lett.* **2020**, *20*, 5292–5300.

(161) Rong, K.; Wang, B.; Reuven, A.; Maguid, E.; Cohn, B.; Kleiner, V.; Katznelson, S.; Koren, E.; Hasman, E. Photonic Rashba Effect from Quantum Emitters Mediated by a Berry-Phase Defective Photonic Crystal. *Nat. Nanotechnol.* **2020**, *15*, 927–933.

(162) Kravtsov, V.; Khestanova, E.; Benimetskiy, F. A.; Ivanova, T.; Samusev, A. K.; Sinev, I. S.; Pidgayko, D.; Mozharov, A. M.; Mukhin, I. S.; Lozhkin, M. S.; et al. Nonlinear Polaritons in a Monolayer Semiconductor Coupled to Optical Bound States in the Continuum. *Light Sci. Appl.* **2020**, *9*, 56.

(163) Dibos, A. M.; Zhou, Y.; Jauregui, L. A.; Scuri, G.; Wild, D. S.; High, A. A.; Taniguchi, T.; Watanabe, K.; Lukin, M. D.; Kim, P.; et al. Electrically Tunable Exciton-Plasmon Coupling in a WSe$_2$ Monolayer Embedded in a Plasmonic Crystal Cavity. *Nano Lett.* **2019**, *19*, 3543–3547.

(164) Dai, Z.; Hu, G.; Ou, Q.; Zhang, L.; Xia, F.; Garcia-Vidal, F. J.; Qiu, C.-W.; Bao, Q. Artificial Metaphotonics Born Naturally in Two Dimensions. *Chem. Rev.* **2020**, *120*, 6197–6246.

(165) Ermolaev, G. A.; Grudinin, D. V.; Stebunov, Y. V.; Voronin, K. V.; Kravets, V. G.; Duan, J.; Mazitov, A. B.; Tselikov, G. I.; Bylinkin, A.; Yakubovsky, D. I.; et al. Giant Optical Anisotropy in Transition Metal Dichalcogenides for Next-Generation Photonics. *Nat. Commun.* **2021**, *12*, 854.

(166) Verre, R.; Baranov, D. G.; Munkhbat, B.; Cuadra, J.; Käll, M.; Shegai, T. Transition Metal Dichalcogenide Nanodisks as High-Index Dielectric Mie Nanoresonators. *Nat. Nanotechnol.* **2019**, *14*, 679–683.

(167) Zotev, P. G.; Wang, Y.; Sortino, L.; Severs Millard, T.; Mullin, N.; Conteduca, D.; Shagar, M.; Genco, A.; Hobbs, J. K.; Krauss, T. F.; et al. Transition Metal Dichalcogenide Dimer Nanoantennas for Tailored Light-Matter Interactions. *ACS Nano* **2022**, *16*, 6493–6505.

(168) Munkhbat, B.; Yankovich, A. B.; Baranov, D. G.; Verre, R.; Olsson, E.; Shegai, T. O. Transition Metal Dichalcogenide Metamaterials with Atomic Precision. *Nat. Commun.* **2020**, *11*, 4604.

(169) Zhang, H.; Abhiraman, B.; Zhang, Q.; Miao, J.; Jo, K.; Roccasecca, S.; Knight, M. W.; Davoyan, A. R.; Jariwala, D. Hybrid Exciton-Plasmon-Polaritons in Van Der Waals Semiconductor Gratings. *Nat. Commun.* **2020**, *11*, 3552.

(170) Nauman, M.; Yan, J.; de Ceglia, D.; Rahmani, M.; Zangeneh Kamali, K.; De Angelis, C.; Miroshnichenko, A. E.; Lu, Y.; Neshev, D. N. Tunable Unidirectional Nonlinear Emission from Transition-Metal-Dichalcogenide Metasurfaces. *Nat. Commun.* **2021**, *12*, 5597.

(171) Liu, Y.; Weiss, N. O.; Duan, X.; Cheng, H.-C.; Huang, Y.; Duan, X. Van Der Waals Heterostructures and Devices. *Nat. Rev. Mater.* **2016**, *1*, 16042.

(172) Hu, G.; Krasnok, A.; Mazor, Y.; Qiu, C.-W.; Alù, A. Moiré Hyperbolic Metasurfaces. *Nano Lett.* **2020**, *20*, 3217–3224.

(173) Chia, X.; Pumera, M. Characteristics and Performance of Two-Dimensional Materials for Electrocatalysis. *Nat. Catal.* **2018**, *1*, 909–921.

(174) Chen, Y.-H.; Tamming, R. R.; Chen, K.; Zhang, Z.; Liu, F.; Zhang, Y.; Hodgkiss, J. M.; Blaikie, R. J.; Ding, B.; Qiu, M. Bandgap Control in Two-Dimensional Semiconductors via Coherent Doping of Plasmonic Hot Electrons. *Nat. Commun.* **2021**, *12*, 4332.

(175) Shaltout, A. M.; Shalaev, V. M.; Brongersma, M. L. Spatiotemporal Light Control with Active Metasurfaces. *Science* **2019**, *364*, No. eaat3100.

(176) Wang, Q.; Rogers, E. T. F.; Gholipour, B.; Wang, C.-M.; Yuan, G.; Teng, J.; Zheludev, N. I. Optically Reconfigurable Metasurfaces and Photonic Devices Based on Phase Change Materials. *Nat. Photonics* **2016**, *10*, 60–65.

(177) Abdollahramezani, S.; Hemmatyar, O.; Taghinejad, M.; Taghinejad, H.; Kiarashinejad, Y.; Zandehshahvar, M.; Fan, T.; Deshmukh, S.; Eftekhar, A. A.; Cai, W.; et al. Dynamic Hybrid Metasurfaces. *Nano Lett.* **2021**, *21*, 1238–1245.

(178) Sámson, Z. L.; MacDonald, K. F.; De Angelis, F.; Gholipour, B.; Knight, K.; Huang, C. C.; Di Fabrizio, E.; Hewak, D. W.; Zheludev, N. I. Metamaterial Electro-Optic Switch of Nanoscale Thickness. *Appl. Phys. Lett.* **2010**, *96*, 143105.

(179) Kamali, S. M.; Arbabi, E.; Arbabi, A.; Horie, Y.; Faraon, A. Highly Tunable Elastic Dielectric Metasurface Lenses. *Laser Photonics Rev.* **2016**, *10*, 1002–1008.

(180) Zhang, Y.; Fowler, C.; Liang, J.; Azhar, B.; Shalaginov, M. Y.; Deckoff-Jones, S.; An, S.; Chou, J. B.; Roberts, C. M.; Liberman, V.; et al. Electrically Reconfigurable Non-Volatile Metasurface Using Low-Loss Optical Phase-Change Material. *Nat. Nanotechnol.* **2021**, *16*, 661–666.

(181) Cao, T.; Zhang, X.; Dong, W.; Lu, L.; Zhou, X.; Zhuang, X.; Deng, J.; Cheng, X.; Li, G.; Simpson, R. E. Tuneable Thermal Emission Using Chalcogenide Metasurface. *Adv. Opt. Mater.* **2018**, *6*, 1800169.

(182) Tittl, A.; Michel, A.-K. U.; Schäferling, M.; Yin, X.; Gholipour, B.; Cui, L.; Wuttig, M.; Taubner, T.; Neubrech, F.; Giessen, H. A Switchable Mid-Infrared Plasmonic Perfect Absorber with Multi-spectral Thermal Imaging Capability. *Adv. Mater.* **2015**, *27*, 4597–4603.

(183) Yin, X.; Steinle, T.; Huang, L.; Taubner, T.; Wuttig, M.; Zentgraf, T.; Giessen, H. Beam Switching and Bifocal Zoom Lensing Using Active Plasmonic Metasurfaces. *Light Sci. Appl.* **2017**, *6*, No. e17016.

(184) Shao, Z.; Cao, X.; Luo, H.; Jin, P. Recent Progress in the Phase-Transition Mechanism and Modulation of Vanadium Dioxide Materials. *NPG Asia Mater.* **2018**, *10*, 581–605.

(185) Muskens, O. L.; Bergamini, L.; Wang, Y.; Gaskell, J. M.; Zabala, N.; de Groot, C.; Sheel, D. W.; Aizpurua, J. Antenna-Assisted Picosecond Control of Nanoscale Phase Transition in Vanadium Dioxide. *Light Sci. Appl.* **2016**, *5*, No. e16173.

(186) Earl, S. K.; James, T. D.; Gómez, D. E.; Marvel, R. E.; Haglund, R. F.; Roberts, A. Switchable Polarization Rotation of Visible Light Using a Plasmonic Metasurface. *APL Photonics* **2017**, *2*, 016103.

(187) Cueff, S.; John, J.; Zhang, Z.; Parra, J.; Sun, J.; Orobtchouk, R.; Ramanathan, S.; Sanchis, P. VO$_2$ Nanophotonics. *APL Photonics* **2020**, *5*, 110901.

(188) Tripathi, A.; John, J.; Kruk, S.; Zhang, Z.; Nguyen, H. S.; Berguiga, L.; Romeo, P. R.; Orobtchouk, R.; Ramanathan, S.; Kivshar, Y.; Cueff, S. Tunable Mie-Resonant Dielectric Metasurfaces Based on VO$_2$ Phase-Transition Materials. *ACS Photonics* **2021**, *8*, 1206–1213.

(189) Howes, A.; Zhu, Z.; Curie, D.; Avila, J. R.; Wheeler, V. D.; Haglund, R. F.; Valentine, J. G. Optical Limiting Based on Huygens' Metasurfaces. *Nano Lett.* **2020**, *20*, 4638–4644.

(190) Liu, X.; Padilla, W. J. Reconfigurable Room Temperature Metamaterial Infrared Emitter. *Optica* **2017**, *4*, 430–433.

(191) Yao, Y.; Shankar, R.; Kats, M. A.; Song, Y.; Kong, J.; Loncar, M.; Capasso, F. Electrically Tunable Metasurface Perfect Absorbers for Ultrathin Mid-Infrared Optical Modulators. *Nano Lett.* **2014**, *14*, 6526–6532.

(192) Emani, N. K.; Chung, T.-F.; Kildishev, A. V.; Shalaev, V. M.; Chen, Y. P.; Boltasseva, A. Electrical Modulation of Fano Resonance in Plasmonic Nanostructures Using Graphene. *Nano Lett.* **2014**, *14*, 78–82.

(193) Zhang, C.; Xiao, S.; Wang, Y.; Gao, Y.; Fan, Y.; Huang, C.; Zhang, N.; Yang, W.; Song, Q. Lead Halide Perovskite-Based Dynamic Metasurfaces. *Laser Photonics Rev.* **2019**, *13*, 1900079.

(194) Yulaev, A.; Zhu, W.; Zhang, C.; Westly, D. A.; Lezec, H. J.; Agrawal, A.; Aksyuk, V. Metasurface-Integrated Photonic Platform for Versatile Free-Space Beam Projection with Polarization Control. *ACS Photonics* **2019**, *6*, 2902–2909.

(195) Meng, Y.; Chen, Y.; Lu, L.; Ding, Y.; Cusano, A.; Fan, J. A.; Hu, Q.; Wang, K.; Xie, Z.; Liu, Z.; et al. Optical Meta-Waveguides for Integrated Photonics and Beyond. *Light Sci. Appl.* **2021**, *10*, 235.

(196) Aćimović, S. S.; Ortega, M. A.; Sanz, V.; Berthelot, J.; Garcia-Cordero, J. L.; Renger, J.; Maerkl, S. J.; Kreuzer, M. P.; Quidant, R. LSPR Chip for Parallel, Rapid, and Sensitive Detection of Cancer Markers in Serum. *Nano Lett.* **2014**, *14*, 2636–2641.

(197) Yavas, O.; Svedendahl, M.; Dobosz, P.; Sanz, V.; Quidant, R. On-A-Chip Biosensing Based on All-Dielectric Nanoresonators. *Nano Lett.* **2017**, *17*, 4421–4426.

(198) Liu, D.; Yang, D.; Gao, Y.; Ma, J.; Long, R.; Wang, C.; Xiong, Y. Flexible Near-Infrared Photovoltaic Devices Based on Plasmonic Hot-

Electron Injection into Silicon Nanowire Arrays. *Angew. Chem.* **2016**, *128*, 4653−4657.

(199) Jiao, F.; Li, F.; Shen, J.; Guan, C.; Khan, S. A.; Wang, J.; Yang, Z.; Zhu, J. Wafer-Scale Flexible Plasmonic Metasurface with Passivated Aluminum Nanopillars for High-Sensitivity Immunosensors. *Sens. Actuators B Chem.* **2021**, *344*, 130170.

(200) Walia, S.; Shah, C. M.; Gutruf, P.; Nili, H.; Chowdhury, D. R.; Withayachumnankul, W.; Bhaskaran, M.; Sriram, S. Flexible Metasurfaces and Metamaterials: A Review of Materials and Fabrication Processes at Micro- and Nano-Scales. *Appl. Phys. Rev.* **2015**, *2*, 011303.

(201) Hu, T.; Landy, N. I.; Fan, K.; Strikwerda, A. C.; Padilla, W. J.; Averitt, R. D.; Xin, Z. Flexible Terahertz Metamaterials: Towards a Terahertz Metamaterial Invisible Cloak. In *2008 IEEE International Electron Devices Meeting*; IEEE: San Francisco, CA, USA, 2008; pp 1−4.

(202) Kim, H.; Lee, D.; Lim, S. A Fluidically Tunable Metasurface Absorber for Flexible Large-Scale Wireless Ethanol Sensor Applications. *Sensors* **2016**, *16*, 1246.

(203) Wang, J.; Mbah, C. F.; Przybilla, T.; Apeleo Zubiri, B.; Spiecker, E.; Engel, M.; Vogel, N. Magic Number Colloidal Clusters as Minimum Free Energy Structures. *Nat. Commun.* **2018**, *9*, 5259.

(204) Song, C.; Blaber, M. G.; Zhao, G.; Zhang, P.; Fry, H. C.; Schatz, G. C.; Rosi, N. L. Tailorable Plasmonic Circular Dichroism Properties of Helical Nanoparticle Superstructures. *Nano Lett.* **2013**, *13*, 3256−3261.

(205) Ai, B.; Zhao, Y. Glancing Angle Deposition Meets Colloidal Lithography: A New Evolution in the Design of Nanostructures. *Nanophotonics* **2018**, *8*, 1−26.

(206) Wang, Y.; Zhang, M.; Lai, Y.; Chi, L. Advanced Colloidal Lithography: From Patterning to Applications. *Nano Today* **2018**, *22*, 36−61.

(207) Senefelder, A. *Senefelder on Lithography: The Classic 1819 Treatise*; Dover Publications, 2005.

(208) Pimpin, A.; Srituravanich, W. Review on Micro- and Nanolithography Techniques and Their Applications. *Eng. J.* **2012**, *16*, 37−56.

(209) Gates, B. D.; Xu, Q.; Stewart, M.; Ryan, D.; Willson, C. G.; Whitesides, G. M. New Approaches to Nanofabrication: Molding, Printing, and Other Techniques. *Chem. Rev.* **2005**, *105*, 1171−1196.

(210) Liu, N.; Tang, M. L.; Hentschel, M.; Giessen, H.; Alivisatos, A. P. Nanoantenna-Enhanced Gas Sensing in a Single Tailored Nanofocus. *Nat. Mater.* **2011**, *10*, 631−636.

(211) Pala, N.; Karabiyik, M. Electron Beam Lithography (EBL). In *Encyclopedia of Nanotechnology*; Bhushan, B., Ed.; Springer Netherlands: Dordrecht, 2016; pp 1033−1057.

(212) Hüttenhofer, L.; Golibrzuch, M.; Bienek, O.; Wendisch, F. J.; Lin, R.; Becerer, M.; Sharp, I. D.; Maier, S. A.; Cortés, E. Metasurface Photoelectrodes for Enhanced Solar Fuel Generation. *Adv. Energy Mater.* **2021**, *11*, 2102877.

(213) Kim, S.; Jin, J.; Kim, Y.-J.; Park, I.-Y.; Kim, Y.; Kim, S.-W. High-Harmonic Generation by Resonant Plasmon Field Enhancement. *Nature* **2008**, *453*, 757−760.

(214) Li, J.; Hill, E. H.; Lin, L.; Zheng, Y. Optical Nanoprinting of Colloidal Particles and Functional Structures. *ACS Nano* **2019**, *13*, 3783−3795.

(215) Violi, I. L.; Martinez, L. P.; Barella, M.; Zaza, C.; Chvátal, L.; Zemánek, P.; Gutiérrez, M. V.; Paredes, M. Y.; Scarpettini, A.; et al. Challenges on Optical Printing of Colloidal Nanoparticles. *J. Chem. Phys.* **2022**, *156*, 034201.

(216) Gargiulo, J.; Violi, I. L.; Cerrota, S.; Chvátal, L.; Cortés, E.; Perassi, E. M.; Diaz, F.; Zemánek, P.; Stefani, F. D. Accuracy and Mechanistic Details of Optical Printing of Single Au and Ag Nanoparticles. *ACS Nano* **2017**, *11*, 9678−9688.

(217) Ahn, S. H.; Guo, L. J. Large-Area Roll-to-Roll and Roll-to-Plate Nanoimprint Lithography: A Step toward High-Throughput Application of Continuous Nanoimprinting. *ACS Nano* **2009**, *3*, 2304−2310.

(218) Wagner, C.; Harned, N. Lithography Gets Extreme. *Nat. Photonics* **2010**, *4*, 24−26.

(219) Oh, D. K.; Lee, T.; Ko, B.; Badloe, T.; Ok, J. G.; Rho, J. Nanoimprint Lithography for High-Throughput Fabrication of Metasurfaces. *Front. Optoelectron.* **2021**, *14*, 229−251.

(220) Chou, S. Y.; Krauss, P. R.; Renstrom, P. J. Imprint Lithography with 25-Nanometer Resolution. *Science* **1996**, *272*, 85−87.

(221) Kessel, A.; Frydendahl, C.; Indukuri, S. R. K. C.; Mazurski, N.; Arora, P.; Levy, U. Soft Lithography for Manufacturing Scalable Perovskite Metasurfaces with Enhanced Emission and Absorption. *Adv. Opt. Mater.* **2020**, *8*, 2001627.

(222) Xia, Y.; Whitesides, G. M. Soft Lithography. *Annu. Rev. Mater. Sci.* **1998**, *28*, 153−184.

(223) Zhang, J.; Li, Y.; Zhang, X.; Yang, B. Colloidal Self-Assembly Meets Nanofabrication: From Two-Dimensional Colloidal Crystals to Nanostructure Arrays. *Adv. Mater.* **2010**, *22*, 4249−4269.

(224) Vogel, N.; Goerres, S.; Landfester, K.; Weiss, C. K. A Convenient Method to Produce Close- and Non-Close-Packed Monolayers Using Direct Assembly at the Air-Water Interface and Subsequent Plasma-Induced Size Reduction. *Macromol. Chem. Phys.* **2011**, *212*, 1719−1734.

(225) Wendisch, F. J.; Rey, M.; Vogel, N.; Bourret, G. R. Large-Scale Synthesis of Highly Uniform Silicon Nanowire Arrays Using Metal-Assisted Chemical Etching. *Chem. Mater.* **2020**, *32*, 9425−9434.

(226) Rey, M.; Law, A. D.; Buzza, D. M. A.; Vogel, N. Anisotropic Self-Assembly from Isotropic Colloidal Building Blocks. *J. Am. Chem. Soc.* **2017**, *139*, 17464−17473.

(227) Tang, J. S. J.; Bader, R. S.; Goerlitzer, E. S. A.; Wendisch, J. F.; Bourret, G. R.; Rey, M.; Vogel, N. Surface Patterning with SiO$_2$@PNiPAm Core-Shell Particles. *ACS Omega* **2018**, *3*, 12089−12098.

(228) Rycenga, M.; Cobley, C. M.; Zeng, J.; Li, W.; Moran, C. H.; Zhang, Q.; Qin, D.; Xia, Y. Controlling the Synthesis and Assembly of Silver Nanostructures for Plasmonic Applications. *Chem. Rev.* **2011**, *111*, 3669−3712.

(229) Wendisch, F. J.; Oberreiter, R.; Salihovic, M.; Elsaesser, M. S.; Bourret, G. R. Confined Etching within 2D and 3D Colloidal Crystals for Tunable Nanostructured Templates: Local Environment Matters. *ACS Appl. Mater. Interfaces* **2017**, *9*, 3931−3939.

(230) Rey, M.; Wendisch, F. J.; Aaron Goerlitzer, E. S.; Julia Tang, J. S.; Bader, R. S.; Bourret, G. R.; Vogel, N. Anisotropic Silicon Nanowire Arrays Fabricated by Colloidal Lithography. *Nanoscale Adv.* **2021**, *3*, 3634−3642.

(231) Bley, K.; Semmler, J.; Rey, M.; Zhao, C.; Martic, N.; Klupp Taylor, R. N.; Stingl, M.; Vogel, N. Hierarchical Design of Metal Micro/Nanohole Array Films Optimizes Transparency and Haze Factor. *Adv. Funct. Mater.* **2018**, *28*, 1706965.

(232) Goerlitzer, E. S. A.; Mohammadi, R.; Nechayev, S.; Banzer, P.; Vogel, N. Large-Area 3D Plasmonic Crescents with Tunable Chirality. *Adv. Opt. Mater.* **2019**, *7*, 1801770.

(233) Nemiroski, A.; Gonidec, M.; Fox, J. M.; Jean-Remy, P.; Turnage, E.; Whitesides, G. M. Engineering Shadows to Fabricate Optical Metasurfaces. *ACS Nano* **2014**, *8*, 11061−11070.

(234) Lotito, V.; Zambelli, T. Playing with Sizes and Shapes of Colloidal Particles via Dry Etching Methods. *Adv. Colloid Interface Sci.* **2022**, *299*, 102538.

(235) Fuhrmann, B.; Leipner, H. S.; Höche, H.-R.; Schubert, L.; Werner, P.; Gösele, U. Ordered Arrays of Silicon Nanowires Produced by Nanosphere Lithography and Molecular Beam Epitaxy. *Nano Lett.* **2005**, *5*, 2524−2527.

(236) Molet, P.; Passarelli, N.; Pérez, L. A.; Scarabelli, L.; Mihi, A. Engineering Plasmonic Colloidal Meta-Molecules for Tunable Photonic Supercrystals. *Adv. Opt. Mater.* **2021**, *9*, 2100761.

(237) Hanske, C.; González-Rubio, G.; Hamon, C.; Formentín, P.; Modin, E.; Chuvilin, A.; Guerrero-Martínez, A.; Marsal, L. F.; Liz-Marzán, L. M. Large-Scale Plasmonic Pyramidal Supercrystals via Templated Self-Assembly of Monodisperse Gold Nanospheres. *J. Phys. Chem. C* **2017**, *121*, 10899−10906.

(238) Tao, A.; Sinsermsuksakul, P.; Yang, P. Tunable Plasmonic Lattices of Silver Nanocrystals. *Nat. Nanotechnol.* **2007**, *2*, 435−440.

(239) Mayer, M.; Schnepf, M. J.; König, T. A. F.; Fery, A. Colloidal Self-Assembly Concepts for Plasmonic Metasurfaces. *Adv. Opt. Mater.* **2019**, 7, 1800564.

(240) Yang, G.; Hallinan, D. T. Gold Nanoparticle Monolayers from Sequential Interfacial Ligand Exchange and Migration in a Three-Phase System. *Sci. Rep.* **2016**, 6, 35339.

(241) Rozin, M. J.; Rosen, D. A.; Dill, T. J.; Tao, A. R. Colloidal Metasurfaces Displaying Near-Ideal and Tunable Light Absorbance in the Infrared. *Nat. Commun.* **2015**, 6, 7325.

(242) Lee, J. B.; Walker, H.; Li, Y.; Nam, T. W.; Rakovich, A.; Sapienza, R.; Jung, Y. S.; Nam, Y. S.; Maier, S. A.; Cortés, E. Template Dissolution Interfacial Patterning of Single Colloids for Nano-electrochemistry and Nanosensing. *ACS Nano* **2020**, 14, 17693–17703.

(243) Scarabelli, L.; Vila-Liarte, D.; Mihi, A.; Liz-Marzán, L. M. Templated Colloidal Self-Assembly for Lattice Plasmon Engineering. *Acc. Mater. Res.* **2021**, 2, 816–827.

(244) Vila-Liarte, D.; Feil, M. W.; Manzi, A.; Garcia-Pomar, J. L.; Huang, H.; Döblinger, M.; Liz-Marzán, L. M.; Feldmann, J.; Polavarapu, L.; Mihi, A. Templated-Assembly of CsPbBr$_3$ Perovskite Nanocrystals into 2D Photonic Supercrystals with Amplified Spontaneous Emission. *Angew. Chem., Int. Ed.* **2020**, 59, 17750–17756.

(245) Fu, Y. Q.; Colli, A.; Fasoli, A.; Luo, J. K.; Flewitt, A. J.; Ferrari, A. C.; Milne, W. I. Deep Reactive Ion Etching as a Tool for Nanostructure Fabrication. *J. Vac. Sci. Technol. B Microelectron. Nanometer Struct.* **2009**, 27, 1520–1526.

(246) Hung, Y.-J.; Lee, S.-L.; Thibeault, B. J.; Coldren, L. A. Fabrication of Highly Ordered Silicon Nanowire Arrays With Controllable Sidewall Profiles for Achieving Low-Surface Reflection. *IEEE J. Sel. Top. Quantum Electron.* **2011**, 17, 869–877.

(247) Ko, M.; Baek, S.-H.; Song, B.; Kang, J.-W.; Kim, S.-A.; Cho, C.-H. Periodically Diameter-Modulated Semiconductor Nanowires for Enhanced Optical Absorption. *Adv. Mater.* **2016**, 28, 2504–2510.

(248) Huang, Z.; Fang, H.; Zhu, J. Fabrication of Silicon Nanowire Arrays with Controlled Diameter, Length, and Density. *Adv. Mater.* **2007**, 19, 744–748.

(249) Bartschmid, T.; Wendisch, F. J.; Farhadi, A.; Bourret, G. R. Recent Advances in Structuring and Patterning Silicon Nanowire Arrays for Engineering Light Absorption in Three Dimensions. *ACS Appl. Energy Mater.* **2022**, 5, 5307.

(250) Huang, Z.; Geyer, N.; Werner, P.; de Boor, J.; Gösele, U. Metal-Assisted Chemical Etching of Silicon: A Review: In Memory of Prof. Ulrich Gösele. *Adv. Mater.* **2011**, 23, 285–308.

(251) Schmidt, V.; Wittemann, J. V.; Senz, S.; Gösele, U. Silicon Nanowires: A Review on Aspects of Their Growth and Their Electrical Properties. *Adv. Mater.* **2009**, 21, 2681–2702.

(252) Wu, Y.; Yan, H.; Huang, M.; Messer, B.; Song, J. H.; Yang, P. Inorganic Semiconductor Nanowires: Rational Growth, Assembly, and Novel Properties. *Chem. - Eur. J.* **2002**, 8, 1260–1268.

(253) Liu, N.; Guo, H.; Fu, L.; Kaiser, S.; Schweizer, H.; Giessen, H. Three-Dimensional Photonic Metamaterials at Optical Frequencies. *Nat. Mater.* **2008**, 7, 31–37.

(254) Liu, N.; Liu, H.; Zhu, S.; Giessen, H. Stereometamaterials. *Nat. Photonics* **2009**, 3, 157–162.

(255) Decker, M.; Zhao, R.; Soukoulis, C. M.; Linden, S.; Wegener, M. Twisted Split-Ring-Resonator Photonic Metamaterial with Huge Optical Activity. *Opt. Lett.* **2010**, 35, 1593–1595.

(256) Tanaka, K.; Arslan, D.; Fasold, S.; Steinert, M.; Sautter, J.; Falkner, M.; Pertsch, T.; Decker, M.; Staude, I. Chiral Bilayer All-Dielectric Metasurfaces. *ACS Nano* **2020**, 14, 15926–15935.

(257) Esposito, M.; Tasco, V.; Cuscunà, M.; Todisco, F.; Benedetti, A.; Tarantini, I.; Giorgi, M. D.; Sanvitto, D.; Passaseo, A. Nanoscale 3D Chiral Plasmonic Helices with Circular Dichroism at Visible Frequencies. *ACS Photonics* **2015**, 2, 105–114.

(258) Huang, M. H.; Thoka, S. Formation of Supercrystals through Self-Assembly of Polyhedral Nanocrystals. *Nano Today* **2015**, 10, 81–92.

(259) Lauri, A.; Velleman, L.; Xiao, X.; Cortés, E.; Edel, J. B.; Giannini, V.; Rakovich, A.; Maier, S. A. 3D Confocal Raman Tomography to Probe Field Enhancements inside Supercluster Metamaterials. *ACS Photonics* **2017**, 4, 2070–2077.

(260) Matricardi, C.; Hanske, C.; Garcia-Pomar, J. L.; Langer, J.; Mihi, A.; Liz-Marzán, L. M. Gold Nanoparticle Plasmonic Superlattices as Surface-Enhanced Raman Spectroscopy Substrates. *ACS Nano* **2018**, 12, 8531–8539.

(261) Dey, J.; Lee, S.-J.; Kim, J.; Lim, S.-H.; Ha, J.-M.; Lee, M.-J.; Choi, S.-M. Spontaneous Formation of Highly Stable Nanoparticle Super-crystals Driven by a Covalent Bonding Interaction. *Nano Lett.* **2021**, 21, 258–264.

(262) Mueller, N. S.; Okamura, Y.; Vieira, B. G. M.; Juergensen, S.; Lange, H.; Barros, E. B.; Schulz, F.; Reich, S. Deep Strong Light-Matter Coupling in Plasmonic Nanoparticle Crystals. *Nature* **2020**, 583, 780–784.

(263) Hamon, C.; Novikov, S. M.; Scarabelli, L.; Solís, D. M.; Altantzis, T.; Bals, S.; Taboada, J. M.; Obelleiro, F.; Liz-Marzán, L. M. Collective Plasmonic Properties in Few-Layer Gold Nanorod Super-crystals. *ACS Photonics* **2015**, 2, 1482–1488.

(264) Mueller, N. S.; Vieira, B. G. M.; Schulz, F.; Kusch, P.; Oddone, V.; Barros, E. B.; Lange, H.; Reich, S. Dark Interlayer Plasmons in Colloidal Gold Nanoparticle Bi- and Few-Layers. *ACS Photonics* **2018**, 5, 3962–3969.

(265) Fischer, A. C.; Mäntysalo, M.; Niklaus, F. Inkjet Printing, Laser-Based Micromachining and Micro 3D Printing Technologies for MEMS. In *Handbook of Silicon Based MEMS Materials and Technologies*; Elsevier, 2015; pp 550–564.

(266) Li, L.; Fourkas, J. T. Multiphoton Polymerization. *Mater. Today* **2007**, 10, 30–37.

(267) Thiel, M.; Rill, M. S.; von Freymann, G.; Wegener, M. Three-Dimensional Bi-Chiral Photonic Crystals. *Adv. Mater.* **2009**, 21, 4680–4682.

(268) Liu, Y.; Wang, H.; Ho, J.; Ng, R. C.; Ng, R. J. H.; Hall-Chen, V. H.; Koay, E. H. H.; Dong, Z.; Liu, H.; Qiu, C.-W.; et al. Structural Color Three-Dimensional Printing by Shrinking Photonic Crystals. *Nat. Commun.* **2019**, 10, 4340.

(269) Alcântara, C. C. J.; Landers, F. C.; Kim, S.; De Marco, C.; Ahmed, D.; Nelson, B. J.; Pané, S. Mechanically Interlocked 3D Multi-Material Micromachines. *Nat. Commun.* **2020**, 11, 5957.

(270) Seniutinas, G.; Weber, A.; Padeste, C.; Sakellari, I.; Farsari, M.; David, C. Beyond 100 Nm Resolution in 3D Laser Lithography — Post Processing Solutions. *Microelectron. Eng.* **2018**, 191, 25–31.

(271) Gansel, J. K.; Thiel, M.; Rill, M. S.; Decker, M.; Bade, K.; Saile, V.; von Freymann, G.; Linden, S.; Wegener, M. Gold Helix Photonic Metamaterial as Broadband Circular Polarizer. *Science* **2009**, 325, 1513–1515.

(272) Kuzyk, A.; Jungmann, R.; Acuna, G. P.; Liu, N. DNA Origami Route for Nanophotonics. *ACS Photonics* **2018**, 5, 1151–1163.

(273) Liu, N.; Liedl, T. DNA-Assembled Advanced Plasmonic Architectures. *Chem. Rev.* **2018**, 118, 3032–3053.

(274) Xu, A.; Harb, J. N.; Kostiainen, M. A.; Hughes, W. L.; Woolley, A. T.; Liu, H.; Gopinath, A. DNA Origami: The Bridge From Bottom to Top. *MRS Bull.* **2017**, 42, 943–950.

(275) Kershner, R. J.; Bozano, L. D.; Micheel, C. M.; Hung, A. M.; Fornof, A. R.; Cha, J. N.; Rettner, C. T.; Bersani, M.; Frommer, J.; Rothemund, P. W. K.; et al. Placement and Orientation of Individual DNA Shapes on Lithographically Patterned Surfaces. *Nat. Nanotechnol.* **2009**, 4, 557–561.

(276) Gopinath, A.; Rothemund, P. W. K. Optimized Assembly and Covalent Coupling of Single-Molecule DNA Origami Nanoarrays. *ACS Nano* **2014**, 8, 12030–12040.

(277) Hung, A. M.; Micheel, C. M.; Bozano, L. D.; Osterbur, L. W.; Wallraff, G. M.; Cha, J. N. Large-Area Spatially Ordered Arrays of Gold Nanoparticles Directed by Lithographically Confined DNA Origami. *Nat. Nanotechnol.* **2010**, 5, 121–126.

(278) Shen, X. S.; Wang, G. Z.; Hong, X.; Zhu, W. Simple-Cubic Microcubes Assembled by Palladium Nanocubes. *CrystEngComm* **2009**, 11, 753–755.

(279) Jun, Y. C.; Huang, K. C. Y.; Brongersma, M. L. Plasmonic Beaming and Active Control over Fluorescent Emission. *Nat. Commun.* **2011**, *2*, 283.

(280) Ganesh, N.; Zhang, W.; Mathias, P. C.; Chow, E.; Soares, J. A. N. T.; Malyarchuk, V.; Smith, A. D.; Cunningham, B. T. Enhanced Fluorescence Emission from Quantum Dots on a Photonic Crystal Surface. *Nat. Nanotechnol.* **2007**, *2*, 515−520.

(281) Wang, H.; Wang, H.-Y.; Gao, B.-R.; Jiang, Y.; Yang, Z.-Y.; Hao, Y.-W.; Chen, Q.-D.; Du, X.-B.; Sun, H.-B. Surface Plasmon Enhanced Absorption Dynamics of Regioregular Poly(3-Hexylthiophene). *Appl. Phys. Lett.* **2011**, *98*, 251501.

(282) Meinzer, N.; Hendry, E.; Barnes, W. L. Probing the Chiral Nature of Electromagnetic Fields Surrounding Plasmonic Nanostructures. *Phys. Rev. B* **2013**, *88*, 041407.

(283) Dai, W.; Wang, Y.; Li, R.; Fan, Y.; Qu, G.; Wu, Y.; Song, Q.; Han, J.; Xiao, S. Achieving Circularly Polarized Surface Emitting Perovskite Microlasers with All-Dielectric Metasurfaces. *ACS Nano* **2020**, *14*, 17063−17070.

(284) Zhang, S.; Liang, Y.; Jing, Q.; Lu, Z.; Lu, Y.; Xu, T. Broadband Enhancement of Photoluminance From Colloidal Metal Halide Perovskite Nanocrystals on Plasmonic Nanostructured Surfaces. *Sci. Rep.* **2017**, *7*, 14695.

(285) Deng, S.; Zhang, B.; Choo, P.; Smeets, P. J. M.; Odom, T. W. Plasmonic Photoelectrocatalysis in Copper-Platinum Core-Shell Nanoparticle Lattices. *Nano Lett.* **2021**, *21*, 1523−1529.

(286) Ghobadi, A.; Ulusoy Ghobadi, T. G.; Karadas, F.; Ozbay, E. Semiconductor Thin Film Based Metasurfaces and Metamaterials for Photovoltaic and Photoelectrochemical Water Splitting Applications. *Adv. Opt. Mater.* **2019**, *7*, 1900028.

(287) Linic, S.; Christopher, P.; Ingram, D. B. Plasmonic-Metal Nanostructures for Efficient Conversion of Solar to Chemical Energy. *Nat. Mater.* **2011**, *10*, 911−921.

(288) Zheng, Z.; Xie, W.; Huang, B.; Dai, Y. Plasmon-Enhanced Solar Water Splitting on Metal-Semiconductor Photocatalysts. *Chem. - Eur. J.* **2018**, *24*, 18322−18333.

(289) Frisenda, R.; Navarro-Moratalla, E.; Gant, P.; Pérez De Lara, D.; Jarillo-Herrero, P.; Gorbachev, R. V.; Castellanos-Gomez, A. Recent Progress in the Assembly of Nanodevices and van Der Waals Heterostructures by Deterministic Placement of 2D Materials. *Chem. Soc. Rev.* **2018**, *47*, 53−68.

(290) Dinda, S.; Suresh, V.; Thoniyot, P.; Balčytis, A.; Juodkazis, S.; Krishnamoorthy, S. Engineering 3D Nanoplasmonic Assemblies for High Performance Spectroscopic Sensing. *ACS Appl. Mater. Interfaces* **2015**, *7*, 27661−27666.

(291) Kanipe, K. N.; Chidester, P. P. F.; Stucky, G. D.; Meinhart, C. D.; Moskovits, M. Properly Structured, Any Metal Can Produce Intense Surface Enhanced Raman Spectra. *J. Phys. Chem. C* **2017**, *121*, 14269−14273.

(292) Cambiasso, J.; König, M.; Cortés, E.; Schlücker, S.; Maier, S. A. Surface-Enhanced Spectroscopies of a Molecular Monolayer in an All-Dielectric Nanoantenna. *ACS Photonics* **2018**, *5*, 1546−1557.

(293) Lin, D.; Wu, Z.; Li, S.; Zhao, W.; Ma, C.; Wang, J.; Jiang, Z.; Zhong, Z.; Zheng, Y.; Yang, X. Large-Area Au-Nanoparticle-Functionalized Si Nanorod Arrays for Spatially Uniform Surface-Enhanced Raman Spectroscopy. *ACS Nano* **2017**, *11*, 1478−1487.

(294) Ozel, T.; Zhang, B. A.; Gao, R.; Day, R. W.; Lieber, C. M.; Nocera, D. G. Electrochemical Deposition of Conformal and Functional Layers on High Aspect Ratio Silicon Micro/Nanowires. *Nano Lett.* **2017**, *17*, 4502−4507.

(295) Forcherio, G. T.; Baker, D. R.; Boltersdorf, J.; Leff, A. C.; McClure, J. P.; Grew, K. N.; Lundgren, C. A. Targeted Deposition of Platinum onto Gold Nanorods by Plasmonic Hot Electrons. *J. Phys. Chem. C* **2018**, *122*, 28901−28909.

(296) Qiu, J.; Wu, Y.-C.; Wang, Y.-C.; Engelhard, M. H.; McElwee-White, L.; Wei, W. D. Surface Plasmon Mediated Chemical Solution Deposition of Gold Nanoparticles on a Nanostructured Silver Surface at Room Temperature. *J. Am. Chem. Soc.* **2013**, *135*, 38−41.

(297) Xia, K.; Chiang, W.-Y.; Lockhart de la Rosa, C. J.; Fujita, Y.; Toyouchi, S.; Yuan, H.; Su, J.; Masuhara, H.; De Gendt, S.; De Feyter, S.; et al. Photo-Induced Electrodeposition of Metallic Nanostructures on Graphene. *Nanoscale* **2020**, *12*, 11063−11069.

(298) Wendisch, F. J.; Saller, M. S.; Eadie, A.; Reyer, A.; Musso, M.; Rey, M.; Vogel, N.; Diwald, O.; Bourret, G. R. Three-Dimensional Electrochemical Axial Lithography on Si Micro- and Nanowire Arrays. *Nano Lett.* **2018**, *18*, 7343−7349.

(299) Wendisch, F. J.; Abazari, M.; Werner, V.; Barb, H.; Rey, M.; Goerlitzer, E. S. A.; Vogel, N.; Mahdavi, H.; Bourret, G. R. Spatioselective Deposition of Passivating and Electrocatalytic Layers on Silicon Nanowire Arrays. *ACS Appl. Mater. Interfaces* **2020**, *12*, 52581−52587.

(300) Cortés, E.; Xie, W.; Cambiasso, J.; Jermyn, A. S.; Sundararaman, R.; Narang, P.; Schlücker, S.; Maier, S. A. Plasmonic Hot Electron Transport Drives Nano-Localized Chemistry. *Nat. Commun.* **2017**, *8*, 14880.

(301) Lin, R.; Zhai, Y.; Xiong, C.; Li, X. Inverse Design of Plasmonic Metasurfaces by Convolutional Neural Network. *Opt. Lett.* **2020**, *45*, 1362.

(302) Tanriover, I.; Hadibrata, W.; Aydin, K. Physics-Based Approach for a Neural Networks Enabled Design of All-Dielectric Metasurfaces. *ACS Photonics* **2020**, *7*, 1957−1964.

(303) Liu, C.; Maier, S. A.; Li, G. Genetic-Algorithm-Aided Meta-Atom Multiplication for Improved Absorption and Coloration in Nanophotonics. *ACS Photonics* **2020**, *7*, 1716−1722.

(304) Wiecha, P. R.; Muskens, O. L. Deep Learning Meets Nanophotonics: A Generalized Accurate Predictor for Near Fields and Far Fields of Arbitrary 3D Nanostructures. *Nano Lett.* **2020**, *20*, 329−338.

(305) Kudyshev, Z. A.; Kildishev, A. V.; Shalaev, V. M.; Boltasseva, A. Machine-Learning-Assisted Metasurface Design for High-Efficiency Thermal Emitter Optimization. *Appl. Phys. Rev.* **2020**, *7*, 021407.

(306) Ma, W.; Liu, Z.; Kudyshev, Z. A.; Boltasseva, A.; Cai, W.; Liu, Y. Deep Learning for the Design of Photonic Structures. *Nat. Photonics* **2021**, *15*, 77−90.

(307) Wang, Q.; Makarenko, M.; Burguete Lopez, A.; Getman, F.; Fratalocchi, A. Advancing Statistical Learning and Artificial Intelligence in Nanophotonics Inverse Design. *Nanophotonics* **2021**, *11*, 2483.

(308) Yao, K.; Unni, R.; Zheng, Y. Intelligent Nanophotonics: Merging Photonics and Artificial Intelligence at the Nanoscale. *Nanophotonics* **2019**, *8*, 339−366.

(309) Molesky, S.; Lin, Z.; Piggott, A. Y.; Jin, W.; Vucković, J.; Rodriguez, A. W. Inverse Design in Nanophotonics. *Nat. Photonics* **2018**, *12*, 659−670.

(310) Kühne, J.; Wang, J.; Weber, T.; Kühner, L.; Maier, S. A.; Tittl, A. Fabrication Robustness in BIC Metasurfaces. *Nanophotonics* **2021**, *10*, 4305−4312.

(311) Steinmeyer, G.; Sutter, D. H.; Gallmann, L.; Matuschek, N.; Keller, U. Frontiers in Ultrashort Pulse Generation: Pushing the Limits in Linear and Nonlinear Optics. *Science* **1999**, *286*, 1507−1512.

(312) Shcherbakov, M. R.; Vabishchevich, P. P.; Shorokhov, A. S.; Chong, K. E.; Choi, D.-Y.; Staude, I.; Miroshnichenko, A. E.; Neshev, D. N.; Fedyanin, A. A.; Kivshar, Y. S. Ultrafast All-Optical Switching with Magnetic Resonances in Nonlinear Dielectric Nanostructures. *Nano Lett.* **2015**, *15*, 6985−6990.

(313) Grinblat, G.; Zhang, H.; Nielsen, M. P.; Krivitsky, L.; Berté, R.; Li, Y.; Tilmann, B.; Cortés, E.; Oulton, R. F.; Kuznetsov, A. I.; et al. Efficient Ultrafast All-Optical Modulation in a Nonlinear Crystalline Gallium Phosphide Nanodisk at the Anapole Excitation. *Sci. Adv.* **2020**, *6*, No. eabb3123.

(314) Ye, W.; Zeuner, F.; Li, X.; Reineke, B.; He, S.; Qiu, C.-W.; Liu, J.; Wang, Y.; Zhang, S.; Zentgraf, T. Spin and Wavelength Multiplexed Nonlinear Metasurface Holography. *Nat. Commun.* **2016**, *7*, 11930.

(315) Frischwasser, K.; Cohen, K.; Kher-Alden, J.; Dolev, S.; Tsesses, S.; Bartal, G. Real-Time Sub-Wavelength Imaging of Surface Waves with Nonlinear Near-Field Optical Microscopy. *Nat. Photonics* **2021**, *15*, 442−448.

(316) Kravtsov, V.; Ulbricht, R.; Atkin, J. M.; Raschke, M. B. Plasmonic Nanofocused Four-Wave Mixing for Femtosecond Near-Field Imaging. *Nat. Nanotechnol.* **2016**, *11*, 459−464.

(317) Seyler, K. L.; Schaibley, J. R.; Gong, P.; Rivera, P.; Jones, A. M.; Wu, S.; Yan, J.; Mandrus, D. G.; Yao, W.; Xu, X. Electrical Control of Second-Harmonic Generation in a WSe$_2$ Monolayer Transistor. *Nat. Nanotechnol.* **2015**, *10*, 407−411.

(318) *Nonlinear Optics*; Elsevier, 2020.

(319) Smekal, A. Zur Quantentheorie der Dispersion. *Naturwissenschaften* **1923**, *11*, 873−875.

(320) Raman, C. V.; Krishnan, K. S. A New Type of Secondary Radiation. *Nature* **1928**, *121*, 501−502.

(321) Jones, R. R.; Hooper, D. C.; Zhang, L.; Wolverson, D.; Valev, V. K. Raman Techniques: Fundamentals and Frontiers. *Nanoscale Res. Lett.* **2019**, *14*, 231.

(322) Das, R. S.; Agrawal, Y. K. Raman Spectroscopy: Recent Advancements, Techniques and Applications. *Vib. Spectrosc.* **2011**, *57*, 163−176.

(323) Boyd, R. W. Stimulated Raman Scattering and Stimulated Rayleigh-Wing Scattering. In *Nonlinear Opt.*; Elsevier, 2008; pp 473−509.

(324) Fiore, A.; Berger, V.; Rosencher, E.; Bravetti, P.; Nagle, J. Phase Matching Using an Isotropic Nonlinear Optical Material. *Nature* **1998**, *391*, 463−466.

(325) Myers, L. E.; Eckardt, R. C.; Fejer, M. M.; Byer, R. L.; Bosenberg, W. R.; Pierce, J. W. Quasi-Phase-Matched Optical Parametric Oscillators in Bulk Periodically Poled LiNbO$_3$. *J. Opt. Soc. Am. B* **1995**, *12*, 2102−2116.

(326) Dimitropoulos, D.; Raghunathan, V.; Claps, R.; Jalali, B. Phase-Matching and Nonlinear Optical Processes in Silicon Waveguides. *Opt. Express* **2004**, *12*, 149−160.

(327) Li, G.; Zhang, S.; Zentgraf, T. Nonlinear Photonic Metasurfaces. *Nat. Rev. Mater.* **2017**, *2*, 17010.

(328) Lee, J.; Tymchenko, M.; Argyropoulos, C.; Chen, P.-Y.; Lu, F.; Demmerle, F.; Boehm, G.; Amann, M.-C.; Alù, A.; Belkin, M. A. Giant Nonlinear Response from Plasmonic Metasurfaces Coupled to Intersubband Transitions. *Nature* **2014**, *511*, 65−69.

(329) Kauranen, M.; Zayats, A. V. Nonlinear Plasmonics. *Nat. Photonics* **2012**, *6*, 737−748.

(330) Krasnok, A.; Tymchenko, M.; Alù, A. Nonlinear Metasurfaces: A Paradigm Shift in Nonlinear Optics. *Mater. Today* **2018**, *21*, 8−21.

(331) Butet, J.; Martin, O. J. F. Evaluation of the Nonlinear Response of Plasmonic Metasurfaces: Miller's Rule, Nonlinear Effective Susceptibility Method, and Full-Wave Computation. *J. Opt. Soc. Am. B* **2016**, *33*, A8−A15.

(332) Klein, M. W.; Enkrich, C.; Wegener, M.; Linden, S. Second-Harmonic Generation from Magnetic Metamaterials. *Science* **2006**, *313*, 502−504.

(333) Kujala, S.; Canfield, B. K.; Kauranen, M.; Svirko, Y.; Turunen, J. Multipole Interference in the Second-Harmonic Optical Radiation from Gold Nanoparticles. *Phys. Rev. Lett.* **2007**, *98*, 167403.

(334) Valev, V. K.; Silhanek, A. V.; Verellen, N.; Gillijns, W.; Van Dorpe, P.; Aktsipetrov, O. A.; Vandenbosch, G. A. E.; Moshchalkov, V. V.; Verbiest, T. Asymmetric Optical Second-Harmonic Generation from Chiral G-Shaped Gold Nanostructures. *Phys. Rev. Lett.* **2010**, *104*, 127401.

(335) Gennaro, S. D.; Rahmani, M.; Giannini, V.; Aouani, H.; Sidiropoulos, T. P. H.; Navarro-Cía, M.; Maier, S. A.; Oulton, R. F. The Interplay of Symmetry and Scattering Phase in Second Harmonic Generation from Gold Nanoantennas. *Nano Lett.* **2016**, *16*, 5278−5285.

(336) Grinblat, G. Nonlinear Dielectric Nanoantennas and Metasurfaces: Frequency Conversion and Wavefront Control. *ACS Photonics* **2021**, *8*, 3406−3432.

(337) Shcherbakov, M. R.; Neshev, D. N.; Hopkins, B.; Shorokhov, A. S.; Staude, I.; Melik-Gaykazyan, E. V.; Decker, M.; Ezhov, A. A.; Miroshnichenko, A. E.; Brener, I.; et al. Enhanced Third-Harmonic Generation in Silicon Nanoparticles Driven by Magnetic Response. *Nano Lett.* **2014**, *14*, 6488−6492.

(338) Grinblat, G.; Li, Y.; Nielsen, M. P.; Oulton, R. F.; Maier, S. A. Enhanced Third Harmonic Generation in Single Germanium Nanodisks Excited at the Anapole Mode. *Nano Lett.* **2016**, *16*, 4635−4640.

(339) Ahmed, S.; Jiang, X.; Wang, C.; Kalsoom, U. E.; Wang, B.; Khan, J.; Muhammad, Y.; Duan, Y.; Zhu, H.; Ren, X.; et al. An Insightful Picture of Nonlinear Photonics in 2D Materials and Their Applications: Recent Advances and Future Prospects. *Adv. Opt. Mater.* **2021**, *9*, 2001671.

(340) Hu, G.; Hong, X.; Wang, K.; Wu, J.; Xu, H.-X.; Zhao, W.; Liu, W.; Zhang, S.; Garcia-Vidal, F.; Wang, B.; et al. Coherent Steering of Nonlinear Chiral Valley Photons with a Synthetic Au-WS$_2$ Metasurface. *Nat. Photonics* **2019**, *13*, 467−472.

(341) Moskovits, M. Surface-Enhanced Spectroscopy. *Rev. Mod. Phys.* **1985**, *57*, 783−826.

(342) Hayashi, S.; Koh, R.; Ichiyama, Y.; Yamamoto, K. Evidence for Surface-Enhanced Raman Scattering on Nonmetallic Surfaces: Copper Phthalocyanine Molecules on GaP Small Particles. *Phys. Rev. Lett.* **1988**, *60*, 1085−1088.

(343) Baranov, D. G.; Verre, R.; Karpinski, P.; Käll, M. Anapole-Enhanced Intrinsic Raman Scattering from Silicon Nanodisks. *ACS Photonics* **2018**, *5*, 2730−2736.

(344) Mannino, G.; Alberti, A.; Ruggeri, R.; Libertino, S.; Pennisi, A. R.; Faraci, G. Octahedral Faceted Si Nanoparticles as Optical Traps with Enormous Yield Amplification. *Sci. Rep.* **2015**, *5*, 8354.

(345) Liu, F. M.; Ren, B.; Wu, J. H.; Yan, J. W.; Xue, X. F.; Mao, B. W.; Tian, Z. Q. Enhanced-Raman Scattering from Silicon Nanoparticle Substrates. *Chem. Phys. Lett.* **2003**, *382*, 502−507.

(346) Dmitriev, P. A.; Baranov, D. G.; Milichko, V. A.; Makarov, S. V.; Mukhin, I. S.; Samusev, A. K.; Krasnok, A. E.; Belov, P. A.; Kivshar, Y. S. Resonant Raman Scattering from Silicon Nanoparticles Enhanced by Magnetic Response. *Nanoscale* **2016**, *8*, 9721−9726.

(347) Alessandri, I.; Lombardi, J. R. Enhanced Raman Scattering with Dielectrics. *Chem. Rev.* **2016**, *116*, 14921−14981.

(348) Raza, S.; Kristensen, A. Raman Scattering in High-Refractive-Index Nanostructures. *Nanophotonics* **2021**, *10*, 1197−1209.

(349) Pittman, T. B.; Jacobs, B. C.; Franson, J. D. Single Photons on Pseudodemand from Stored Parametric Down-Conversion. *Phys. Rev. A* **2002**, *66*, 042303.

(350) Lamas-Linares, A.; Howell, J. C.; Bouwmeester, D. Stimulated Emission of Polarization-Entangled Photons. *Nature* **2001**, *412*, 887−890.

(351) Braunstein, S. L.; van Loock, P. Quantum Information with Continuous Variables. *Rev. Mod. Phys.* **2005**, *77*, 513−577.

(352) dos Santos, R. G.; Maia, L. J. Q.; de Araujo, C. B.; de S. Menezes, L. Nonlinear Optical Characterization of Single *β*-Barium-Borate Nanocrystals Using Second-Harmonic Confocal Microscopy. *Chin. Opt. Lett.* **2018**, *16*, 041902.

(353) Solntsev, A. S.; Agarwal, G. S.; Kivshar, Y. S. Metasurfaces for Quantum Photonics. *Nat. Photonics* **2021**, *15*, 327−336.

(354) Lee, J.; Nookala, N.; Gomez-Diaz, J. S.; Tymchenko, M.; Demmerle, F.; Boehm, G.; Amann, M.; Alù, A.; Belkin, M. A. Ultrathin Second-Harmonic Metasurfaces with Record-High Nonlinear Optical Response. *Adv. Opt. Mater.* **2016**, *4*, 664−670.

(355) Sarma, R.; Xu, J.; de Ceglia, D.; Carletti, L.; Campione, S.; Klem, J.; Sinclair, M. B.; Belkin, M. A.; Brener, I. An All-Dielectric Polaritonic Metasurface with a Giant Nonlinear Optical Response. *Nano Lett.* **2022**, *22*, 896−903.

(356) Ghirardini, L.; Carletti, L.; Gili, V.; Pellegrini, G.; Duò, L.; Finazzi, M.; Rocco, D.; Locatelli, A.; De Angelis, C.; Favero, I.; et al. Polarization Properties of Second-Harmonic Generation in AlGaAs Optical Nanoantennas. *Opt. Lett.* **2017**, *42*, 559.

(357) Gili, V. F.; Carletti, L.; Locatelli, A.; Rocco, D.; Finazzi, M.; Ghirardini, L.; Favero, I.; Gomez, C.; Lemaître, A.; Celebrano, M.; et al. Monolithic AlGaAs Second-Harmonic Nanoantennas. *Opt. Express* **2016**, *24*, 15965.

(358) Liu, S.; Sinclair, M. B.; Saravi, S.; Keeler, G. A.; Yang, Y.; Reno, J.; Peake, G. M.; Setzpfandt, F.; Staude, I.; Pertsch, T.; et al. Resonantly Enhanced Second-Harmonic Generation Using III-V Semiconductor All-Dielectric Metasurfaces. *Nano Lett.* **2016**, *16*, 5426−5432.

(359) Fedotova, A.; Younesi, M.; Sautter, J.; Vaskin, A.; Löchner, F. J. F.; Steinert, M.; Geiss, R.; Pertsch, T.; Staude, I.; Setzpfandt, F. Second-

Harmonic Generation in Resonant Nonlinear Metasurfaces Based on Lithium Niobate. *Nano Lett.* **2020**, *20*, 8608−8614.

(360) Li, J.; Hu, G.; Shi, L.; He, N.; Li, D.; Shang, Q.; Zhang, Q.; Fu, H.; Zhou, L.; Xiong, W.; et al. Full-Color Enhanced Second Harmonic Generation Using Rainbow Trapping in Ultrathin Hyperbolic Metamaterials. *Nat. Commun.* **2021**, *12*, 6425.

(361) Shorokhov, A. S.; Melik-Gaykazyan, E. V.; Smirnova, D. A.; Hopkins, B.; Chong, K. E.; Choi, D.-Y.; Shcherbakov, M. R.; Miroshnichenko, A. E.; Neshev, D. N.; Fedyanin, A. A.; et al. Multifold Enhancement of Third-Harmonic Generation in Dielectric Nanoparticles Driven by Magnetic Fano Resonances. *Nano Lett.* **2016**, *16*, 4857−4861.

(362) Koshelev, K.; Tang, Y.; Li, K.; Choi, D.-Y.; Li, G.; Kivshar, Y. Nonlinear Metasurfaces Governed by Bound States in the Continuum. *ACS Photonics* **2019**, *6*, 1639−1644.

(363) Ginsberg, J. S.; Overvig, A. C.; Jadidi, M. M.; Malek, S. C.; Patwardhan, G. N.; Swenson, N.; Yu, N.; Gaeta, A. L. Enhanced Harmonic Generation in Gases Using an All-Dielectric Metasurface. *Nanophotonics* **2020**, *10*, 733−740.

(364) Kim, K.-H.; Kim, I.-P. Quasi-Bound States in the Continuum with High Q-Factors in Metasurfaces of Lower-Index Dielectrics Supported by Metallic Substrates. *RSC Adv.* **2022**, *12*, 1961−1967.

(365) de Araújo, C. B.; Maciel, G. S.; Menezes, L. de S.; Rakov, N.; Falcão-Filho, E. L.; Jerez, V. A.; Messaddeq, Y. Frequency Upconversion in Rare-Earth Doped Fluoroindate Glasses. *Comptes Rendus Chim.* **2002**, *5*, 885−898.

(366) Menezes, L. de S.; Maciel, G. S.; Araújo, C. B. de; Messaddeq, Y. Thermally Enhanced Frequency Upconversion in Nd^{3+}-Doped Fluoroindate Glass. *J. Appl. Phys.* **2001**, *90*, 4498−4501.

(367) Mi, C.; Zhou, J.; Wang, F.; Lin, G.; Jin, D. Ultrasensitive Ratiometric Nanothermometer with Large Dynamic Range and Photostability. *Chem. Mater.* **2019**, *31*, 9480−9487.

(368) Menezes, L. de S.; Araújo, C. B. de. Optically Detected Thermal Effects in Rare-Earth Doped Materials for Host Characterization, Thermometric Devices, Nanothermometry and Biothermometry. *J. Braz. Chem. Soc.* **2015**, *26*, 2405−2417.

(369) Chen, C.; Wang, F.; Wen, S.; Su, Q. P.; Wu, M. C. L.; Liu, Y.; Wang, B.; Li, D.; Shan, X.; Kianinia, M.; et al. Multi-Photon Near-Infrared Emission Saturation Nanoscopy Using Upconversion Nanoparticles. *Nat. Commun.* **2018**, *9*, 3290.

(370) Kushida, T.; Geusic, J. E. Optical Refrigeration in Nd-Doped Yttrium Aluminum Garnet. *Phys. Rev. Lett.* **1968**, *21*, 1172−1175.

(371) Yang, Y.; Shao, Q.; Deng, R.; Wang, C.; Teng, X.; Cheng, K.; Cheng, Z.; Huang, L.; Liu, Z.; Liu, X.; et al. In Vitro and In Vivo Uncaging and Bioluminescence Imaging by Using Photocaged Upconversion Nanoparticles. *Angew. Chem.* **2012**, *124*, 3179−3183.

(372) Zhou, B.; Shi, B.; Jin, D.; Liu, X. Controlling Upconversion Nanocrystals for Emerging Applications. *Nat. Nanotechnol.* **2015**, *10*, 924−936.

(373) Rakov, N.; Maciel, G. S.; Sundheimer, M. L.; de S. Menezes, L.; Gomes, A. S. L.; Messaddeq, Y.; Cassanjes, F. C.; Poirier, G.; Ribeiro, S. J. L. Blue Upconversion Enhancement by a Factor of 200 in Tm^{3+}-Doped Tellurite Glass by Codoping with Nd^{3+} Ions. *J. Appl. Phys.* **2002**, *92*, 6337−6339.

(374) Gómez, L. A.; Menezes, L. de S.; de Araújo, C. B.; Gonçalves, R. R.; Ribeiro, S. J. L.; Messaddeq, Y. Upconversion Luminescence in Er^{3+} Doped and Er^{3+}/Yb^{3+} Codoped Zirconia and Hafnia Nanocrystals Excited at 980 Nm. *J. Appl. Phys.* **2010**, *107*, 113508.

(375) D'Aléo, A.; Pompidor, G.; Elena, B.; Vicat, J.; Baldeck, P. L.; Toupet, L.; Kahn, R.; Andraud, C.; Maury, O. Two-Photon Microscopy and Spectroscopy of Lanthanide Bioprobes. *ChemPhysChem* **2007**, *8*, 2125−2132.

(376) Maciel, G. S.; Menezes, L. de S.; Gomes, A. S. L.; De Araujo, C. B.; Messaddeq, Y.; Florez, A.; Aegerter, A. Temperature Sensor Based on Frequency Upconversion in Er^{3+}-Doped Fluoroindate Glass. *IEEE Photonics Technol. Lett.* **1995**, *7*, 1474−1476.

(377) Lin, J. H.; Liou, H. Y.; Wang, C.-D.; Tseng, C.-Y.; Lee, C.-T.; Ting, C.-C.; Kan, H.-C.; Hsu, C. C. Giant Enhancement of Upconversion Fluorescence of $NaYF_4:Yb^{3+},Tm^{3+}$ Nanocrystals with

Resonant Waveguide Grating Substrate. *ACS Photonics* **2015**, *2*, 530−536.

(378) Wang, H.; Yin, Z.; Xu, W.; Zhou, D.; Cui, S.; Chen, X.; Cui, H.; Song, H. Remarkable Enhancement of Upconversion Luminescence on 2-D Anodic Aluminum Oxide Photonic Crystals. *Nanoscale* **2016**, *8*, 10004−10009.

(379) Khardikov, V. V.; Iarko, E. O.; Prosvirnin, S. L. A Giant Red Shift and Enhancement of the Light Confinement in a Planar Array of Dielectric Bars. *J. Opt.* **2012**, *14*, 035103.

(380) Tuz, V. R.; Khardikov, V. V.; Kivshar, Y. S. All-Dielectric Resonant Metasurfaces with a Strong Toroidal Response. *ACS Photonics* **2018**, *5*, 1871−1876.

(381) Basharin, A. A.; Kafesaki, M.; Economou, E. N.; Soukoulis, C. M.; Fedotov, V. A.; Savinov, V.; Zheludev, N. I. Dielectric Metamaterials with Toroidal Dipolar Response. *Phys. Rev. X* **2015**, *5*, 011036.

(382) Yang, Y.; Zenin, V. A.; Bozhevolnyi, S. I. Anapole-Assisted Strong Field Enhancement in Individual All-Dielectric Nanostructures. *ACS Photonics* **2018**, *5*, 1960−1966.

(383) Gong, C.; Liu, W.; He, N.; Dong, H.; Jin, Y.; He, S. Upconversion Enhancement by a Dual-Resonance All-Dielectric Metasurface. *Nanoscale* **2019**, *11*, 1856−1862.

(384) Würth, C.; Manley, P.; Voigt, R.; Ahiboz, D.; Becker, C.; Resch-Genger, U. Metasurface Enhanced Sensitized Photon Upconversion: Toward Highly Efficient Low Power Upconversion Applications and Nanoscale E-Field Sensors. *Nano Lett.* **2020**, *20*, 6682−6689.

(385) Yin, A.; Zhang, Y.; Sun, L.; Yan, C. Colloidal Synthesis and Blue Based Multicolor Upconversion Emissions of Size and Composition Controlled Monodisperse Hexagonal $NaYF_4:Yb,Tm$ Nanocrystals. *Nanoscale* **2010**, *2*, 953−959.

(386) Xu, F.; Sun, Y.; Gao, H.; Jin, S.; Zhang, Z.; Zhang, H.; Pan, G.; Kang, M.; Ma, X.; Mao, Y. High-Performance Perovskite Solar Cells Based on $NaCsWO_3@NaYF_4@NaYF_4:Yb,Er$ Upconversion Nanoparticles. *ACS Appl. Mater. Interfaces* **2021**, *13*, 2674−2684.

(387) Gonçalves, I. M.; Pessoa, A. R.; Hazra, C.; Correales, Y. S.; Ribeiro, S. J. L.; de S. Menezes, L. Phonon-Assisted NIR-to-Visible Upconversion in Single β-$NaYF_4$ Microcrystals Codoped with Er^{3+} and Yb^{3+} for Microthermometry Applications: Experiment and Theory. *J. Lumin.* **2021**, *231*, 117801.

(388) Ahiboz, D.; Andresen, E.; Manley, P.; Resch-Genger, U.; Würth, C.; Becker, C. Metasurface-Enhanced Photon Upconversion upon 1550 Nm Excitation. *Adv. Opt. Mater.* **2021**, *9*, 2101285.

(389) Manley, P.; Segantini, M.; Ahiboz, D.; Hammerschmidt, M.; Arnaoutakis, G.; MacQueen, R. W.; Burger, S.; Becker, C. Double-Layer Metasurface for Enhanced Photon Up-Conversion. *APL Photonics* **2021**, *6*, 036103.

(390) Trupke, T.; Green, M. A.; Würfel, P. Improving Solar Cell Efficiencies by Down-Conversion of High-Energy Photons. *J. Appl. Phys.* **2002**, *92*, 1668−1674.

(391) Wegh, R. T.; Donker, H.; Oskam, K. D.; Meijerink, A. Visible Quantum Cutting in $LiGdF_4:Eu^{3+}$ Through Downconversion. *Science* **1999**, *283*, 663−666.

(392) Matsuzaki, K.; Liu, H.-W.; Götzinger, S.; Sandoghdar, V. On Quantum Efficiency Measurements and Plasmonic Antennas. *ACS Photonics* **2021**, *8*, 1508−1521.

(393) Milstein, T. J.; Kroupa, D. M.; Gamelin, D. R. Picosecond Quantum Cutting Generates Photoluminescence Quantum Yields Over 100% in Ytterbium-Doped $CsPbCl_3$ Nanocrystals. *Nano Lett.* **2018**, *18*, 3792−3799.

(394) Wang, Q.; Qiu, J.; Song, Z.; Yang, Z.; Yin, Z.; Zhou, D.; Wang, S. Enhancement of Tb-Yb Quantum Cutting Emission by Inverse Opal Photonic Crystals. *Opt. Mater.* **2016**, *54*, 229−233.

(395) Shamsi, J.; Urban, A. S.; Imran, M.; De Trizio, L.; Manna, L. Metal Halide Perovskite Nanocrystals: Synthesis, Post-Synthesis Modifications, and Their Optical Properties. *Chem. Rev.* **2019**, *119*, 3296−3348.

(396) Dey, A.; Ye, J.; De, A.; Debroye, E.; Ha, S. K.; Bladt, E.; Kshirsagar, A. S.; Wang, Z.; Yin, J.; Wang, Y.; et al. State of the Art and

Prospects for Halide Perovskite Nanocrystals. *ACS Nano* **2021**, *15*, 10775−10981.

(397) Milstein, T. J.; Kluherz, K. T.; Kroupa, D. M.; Erickson, C. S.; De Yoreo, J. J.; Gamelin, D. R. Anion Exchange and the Quantum-Cutting Energy Threshold in Ytterbium-Doped $CsPb(Cl_{1-x}Br_x)_3$ Perovskite Nanocrystals. *Nano Lett.* **2019**, *19*, 1931−1937.

(398) Zeng, S.; Pian, S.; Su, M.; Wang, Z.; Wu, M.; Liu, X.; Chen, M.; Xiang, Y.; Wu, J.; Zhang, M.; et al. Hierarchical-Morphology Metafabric for Scalable Passive Daytime Radiative Cooling. *Science* **2021**, *373*, 692−696.

(399) Ashcroft, N. W.; Mermin, N. D. *Solid State Physics*; Holt, Rinehart and Winston, 1976.

(400) Wolff, C.; Smith, M. J. A.; Stiller, B.; Poulton, C. G. Brillouin Scattering—Theory and Experiment: Tutorial. *J. Opt. Soc. Am. B* **2021**, *38*, 1243−1269.

(401) Dil, J. G. Brillouin Scattering in Condensed Matter. *Rep. Prog. Phys.* **1982**, *45*, 285−334.

(402) Langer, J.; Jimenez de Aberasturi, D.; Aizpurua, J.; Alvarez-Puebla, R. A.; Auguié, B.; Baumberg, J. J.; Bazan, G. C.; Bell, S. E. J.; Boisen, A.; Brolo, A. G.; et al. Present and Future of Surface-Enhanced Raman Scattering. *ACS Nano* **2020**, *14*, 28−117.

(403) Pieczonka, N. P. W.; Aroca, R. F. Single Molecule Analysis by Surfaced-Enhanced Raman Scattering. *Chem. Soc. Rev.* **2008**, *37*, 946−954.

(404) Stedman, R.; Almqvist, L.; Nilsson, G. Phonon-Frequency Distributions and Heat Capacities of Aluminum and Lead. *Phys. Rev.* **1967**, *162*, 549−557.

(405) Dal Corso, A.; Pasquarello, A.; Baldereschi, A. Density-Functional Perturbation Theory for Lattice Dynamics with Ultrasoft Pseudopotentials. *Phys. Rev. B* **1997**, *56*, R11369−R11372.

(406) Gonze, X.; Rignanese, G.-M.; Caracas, R. First-Principle Studies of the Lattice Dynamics of Crystals, and Related Properties. *Z. Für Krist. - Cryst. Mater.* **2005**, *220*, 458−472.

(407) Sparavigna, A. Role of Nonpairwise Interactions on Phonon Thermal Transport. *Phys. Rev. B* **2003**, *67*, 144305.

(408) Foteinopoulou, S.; Devarapu, G. C. R.; Subramania, G. S.; Krishna, S.; Wasserman, D. Phonon-Polaritonics: Enabling Powerful Capabilities for Infrared Photonics. *Nanophotonics* **2019**, *8*, 2129−2175.

(409) Caldwell, J. D.; Lindsay, L.; Giannini, V.; Vurgaftman, I.; Reinecke, T. L.; Maier, S. A.; Glembocki, O. J. Low-Loss, Infrared and Terahertz Nanophotonics Using Surface Phonon Polaritons. *Nanophotonics* **2015**, *4*, 44−68.

(410) Luxmoore, I. J.; Gan, C. H.; Liu, P. Q.; Valmorra, F.; Li, P.; Faist, J.; Nash, G. R. Strong Coupling in the Far-Infrared between Graphene Plasmons and the Surface Optical Phonons of Silicon Dioxide. *ACS Photonics* **2014**, *1*, 1151−1155.

(411) Huber, A. J.; Deutsch, B.; Novotny, L.; Hillenbrand, R. Focusing of Surface Phonon Polaritons. *Appl. Phys. Lett.* **2008**, *92*, 203104.

(412) Dai, S.; Fei, Z.; Ma, Q.; Rodin, A. S.; Wagner, M.; McLeod, A. S.; Liu, M. K.; Gannett, W.; Regan, W.; Watanabe, K.; et al. Tunable Phonon Polaritons in Atomically Thin van Der Waals Crystals of Boron Nitride. *Science* **2014**, *343*, 1125−1129.

(413) Mancini, A.; Gubbin, C. R.; Berté, R.; Martini, F.; Politi, A.; Cortés, E.; Li, Y.; De Liberato, S.; Maier, S. A. Near-Field Spectroscopy of Cylindrical Phonon-Polariton Antennas. *ACS Nano* **2020**, *14*, 8508−8517.

(414) Caldwell, J. D.; Kretinin, A. V.; Chen, Y.; Giannini, V.; Fogler, M. M.; Francescato, Y.; Ellis, C. T.; Tischler, J. G.; Woods, C. R.; Giles, A. J.; et al. Sub-Diffractional Volume-Confined Polaritons in the Natural Hyperbolic Material Hexagonal Boron Nitride. *Nat. Commun.* **2014**, *5*, 5221.

(415) Caldwell, J. D.; Glembocki, O. J.; Francescato, Y.; Sharac, N.; Giannini, V.; Bezares, F. J.; Long, J. P.; Owrutsky, J. C.; Vurgaftman, I.; Tischler, J. G.; et al. Low-Loss, Extreme Subdiffraction Photon Confinement via Silicon Carbide Localized Surface Phonon Polariton Resonators. *Nano Lett.* **2013**, *13*, 3690−3697.

(416) Tamayo-Arriola, J.; Castellano, E. M.; Bajo, M. M.; Huerta-Barberà, A.; Muñoz, E.; Muñoz-Sanjosé, V.; Hierro, A. Controllable and Highly Propagative Hybrid Surface Plasmon-Phonon Polariton in a CdZnO-Based Two-Interface System. *ACS Photonics* **2019**, *6*, 2816−2822.

(417) Pufahl, K.; Passler, N. C.; Grosse, N. B.; Wolf, M.; Woggon, U.; Paarmann, A. Controlling Nanoscale Air-Gaps for Critically Coupled Surface Polaritons by Means of Non-Invasive White-Light Interferometry. *Appl. Phys. Lett.* **2018**, *113*, 161103.

(418) Lee, S. C.; Ng, S. S.; Ooi, P. K.; Abu Hassan, H.; Hassan, Z.; Al-Hardan, N. H.; Abdullah, M. J.; Yakovlev, V. A.; Novikova, N. N. Surface and Interface Phonon Polariton Characteristics of Wurtzite ZnO/GaN Heterostructure. *Appl. Phys. Lett.* **2011**, *98*, 241909.

(419) Fali, A.; White, S. T.; Folland, T. G.; He, M.; Aghamiri, N. A.; Liu, S.; Edgar, J. H.; Caldwell, J. D.; Haglund, R. F.; Abate, Y. Refractive Index-Based Control of Hyperbolic Phonon-Polariton Propagation. *Nano Lett.* **2019**, *19*, 7725−7734.

(420) Chaudhary, K.; Tamagnone, M.; Yin, X.; Spägele, C. M.; Oscurato, S. L.; Li, J.; Persch, C.; Li, R.; Rubin, N. A.; Jauregui, L. A.; et al. Polariton Nanophotonics Using Phase-Change Materials. *Nat. Commun.* **2019**, *10*, 4487.

(421) Ambrosio, A.; Tamagnone, M.; Chaudhary, K.; Jauregui, L. A.; Kim, P.; Wilson, W. L.; Capasso, F. Selective Excitation and Imaging of Ultraslow Phonon Polaritons in Thin Hexagonal Boron Nitride Crystals. *Light Sci. Appl.* **2018**, *7*, 27.

(422) Ambrosio, A.; Jauregui, L. A.; Dai, S.; Chaudhary, K.; Tamagnone, M.; Fogler, M. M.; Basov, D. N.; Capasso, F.; Kim, P.; Wilson, W. L. Mechanical Detection and Imaging of Hyperbolic Phonon Polaritons in Hexagonal Boron Nitride. *ACS Nano* **2017**, *11*, 8741−8746.

(423) Folland, T. G.; Fali, A.; White, S. T.; Matson, J. R.; Liu, S.; Aghamiri, N. A.; Edgar, J. H.; Haglund, R. F.; Abate, Y.; Caldwell, J. D. Reconfigurable Infrared Hyperbolic Metasurfaces Using Phase Change Materials. *Nat. Commun.* **2018**, *9*, 4371.

(424) Hillenbrand, R.; Taubner, T.; Keilmann, F. Phonon-Enhanced Light-Matter Interaction at the Nanometre Scale. *Nature* **2002**, *418*, 159−162.

(425) Zhang, Q.; Hu, G.; Ma, W.; Li, P.; Krasnok, A.; Hillenbrand, R.; Alù, A.; Qiu, C.-W. Interface Nano-Optics with Van Der Waals Polaritons. *Nature* **2021**, *597*, 187−195.

(426) Narimanov, E. E.; Kildishev, A. V. Naturally Hyperbolic. *Nat. Photonics* **2015**, *9*, 214−216.

(427) Pavlidis, G.; Schwartz, J. J.; Matson, J.; Folland, T.; Liu, S.; Edgar, J. H.; Caldwell, J. D.; Centrone, A. Experimental Confirmation of Long Hyperbolic Polariton Lifetimes in Monoisotopic (^{10}B) Hexagonal Boron Nitride at Room Temperature. *APL Mater.* **2021**, *9*, 091109.

(428) Ni, G.; McLeod, A. S.; Sun, Z.; Matson, J. R.; Lo, C. F. B.; Rhodes, D. A.; Ruta, F. L.; Moore, S. L.; Vitalone, R. A.; Cusco, R.; et al. Long-Lived Phonon Polaritons in Hyperbolic Materials. *Nano Lett.* **2021**, *21*, 5767−5773.

(429) Giles, A. J.; Dai, S.; Vurgaftman, I.; Hoffman, T.; Liu, S.; Lindsay, L.; Ellis, C. T.; Assefa, N.; Chatzakis, I.; Reinecke, T. L.; et al. Ultralow-Loss Polaritons in Isotopically Pure Boron Nitride. *Nat. Mater.* **2018**, *17*, 134−139.

(430) Li, P.; Lewin, M.; Kretinin, A. V.; Caldwell, J. D.; Novoselov, K. S.; Taniguchi, T.; Watanabe, K.; Gaussmann, F.; Taubner, T. Hyperbolic Phonon-Polaritons in Boron Nitride for Near-Field Optical Imaging and Focusing. *Nat. Commun.* **2015**, *6*, 7507.

(431) Duan, J.; Capote-Robayna, N.; Taboada-Gutiérrez, J.; Álvarez-Pérez, G.; Prieto, I.; Martín-Sánchez, J.; Nikitin, A. Y.; Alonso-González, P. Twisted Nano-Optics: Manipulating Light at the Nanoscale with Twisted Phonon Polaritonic Slabs. *Nano Lett.* **2020**, *20*, 5323−5329.

(432) Zheng, Z.; Xu, N.; Oscurato, S. L.; Tamagnone, M.; Sun, F.; Jiang, Y.; Ke, Y.; Chen, J.; Huang, W.; Wilson, W. L.; et al. A Mid-Infrared Biaxial Hyperbolic van Der Waals Crystal. *Sci. Adv.* **2019**, *5*, No. eaav8690.

(433) Schwartz, J. J.; Le, S. T.; Krylyuk, S.; Richter, C. A.; Davydov, A. V.; Centrone, A. Substrate-Mediated Hyperbolic Phonon Polaritons in MoO_3. *Nanophotonics* **2021**, *10*, 1517−1527.

(434) Ma, W.; Hu, G.; Hu, D.; Chen, R.; Sun, T.; Zhang, X.; Dai, Q.; Zeng, Y.; Alù, A.; Qiu, C.-W.; et al. Ghost Hyperbolic Surface Polaritons in Bulk Anisotropic Crystals. *Nature* **2021**, *596*, 362−366.

(435) Baffou, G.; Quidant, R. Thermo-Plasmonics: Using Metallic Nanostructures as Nano-Sources of Heat. *Laser Photonics Rev.* **2013**, *7*, 171−187.

(436) Khurgin, J. B. Expanding the Photonic Palette: Exploring High Index Materials. *ACS Photonics* **2022**, *9*, 743−751.

(437) Barreda, A. I.; Saiz, J. M.; González, F.; Moreno, F.; Albella, P. Recent Advances in High Refractive Index Dielectric Nanoantennas: Basics and Applications. *AIP Adv.* **2019**, *9*, 040701.

(438) Zograf, G. P.; Petrov, M. I.; Makarov, S. V.; Kivshar, Y. S. All-Dielectric Thermonanophotonics. *Adv. Opt. Photonics* **2021**, *13*, 643.

(439) West, P. R.; Ishii, S.; Naik, G. V.; Emani, N. K.; Shalaev, V. M.; Boltasseva, A. Searching for Better Plasmonic Materials. *Laser Photonics Rev.* **2010**, *4*, 795−808.

(440) Khurgin, J. B. How to Deal with the Loss in Plasmonics and Metamaterials. *Nat. Nanotechnol.* **2015**, *10*, 2−6.

(441) Boltasseva, A.; Atwater, H. A. Low-Loss Plasmonic Metamaterials. *Science* **2011**, *331*, 290−291.

(442) Zograf, G. P.; Petrov, M. I.; Zuev, D. A.; Dmitriev, P. A.; Milichko, V. A.; Makarov, S. V.; Belov, P. A. Resonant Nonplasmonic Nanoparticles for Efficient Temperature-Feedback Optical Heating. *Nano Lett.* **2017**, *17*, 2945−2952.

(443) Baffou, G.; Berto, P.; Bermúdez Ureña, E.; Quidant, R.; Monneret, S.; Polleux, J.; Rigneault, H. Photoinduced Heating of Nanoparticle Arrays. *ACS Nano* **2013**, *7*, 6478−6488.

(444) Baffou, G.; Ureña, E. B.; Berto, P.; Monneret, S.; Quidant, R.; Rigneault, H. Deterministic Temperature Shaping Using Plasmonic Nanoparticle Assemblies. *Nanoscale* **2014**, *6*, 8984−8989.

(445) Girard, C.; Wiecha, P. R.; Cuche, A.; Dujardin, E. Designing Thermoplasmonic Properties of Metallic Metasurfaces. *J. Opt.* **2018**, *20*, 075004.

(446) Liu, C.; Tessier, G.; Flores Esparza, S. I.; Guillon, M.; Berto, P. Reconfigurable Temperature Control at the Microscale by Light Shaping. *ACS Photonics* **2019**, *6*, 422−428.

(447) Coppola, G. Advance in Thermo-Optical Switches: Principles, Materials, Design, and Device Structure. *Opt. Eng.* **2011**, *50*, 071112.

(448) Baffou, G.; Bon, P.; Savatier, J.; Polleux, J.; Zhu, M.; Merlin, M.; Rigneault, H.; Monneret, S. Thermal Imaging of Nanostructures by Quantitative Optical Phase Analysis. *ACS Nano* **2012**, *6*, 2452−2458.

(449) Donner, J. S.; Morales-Dalmau, J.; Alda, I.; Marty, R.; Quidant, R. Fast and Transparent Adaptive Lens Based on Plasmonic Heating. *ACS Photonics* **2015**, *2*, 355−360.

(450) Afridi, A.; Canet-Ferrer, J.; Philippet, L.; Osmond, J.; Berto, P.; Quidant, R. Electrically Driven Varifocal Silicon Metalens. *ACS Photonics* **2018**, *5*, 4497−4503.

(451) Berto, P.; Philippet, L.; Osmond, J.; Liu, C. F.; Afridi, A.; Montagut Marques, M.; Molero Agudo, B.; Tessier, G.; Quidant, R. Tunable and Free-Form Planar Optics. *Nat. Photonics* **2019**, *13*, 649−656.

(452) Robert, H. M. L.; Holanová, K.; Bujak, Ł.; Vala, M.; Henrichs, V.; Lánský, Z.; Piliarik, M. Fast Photothermal Spatial Light Modulation for Quantitative Phase Imaging at the Nanoscale. *Nat. Commun.* **2021**, *12*, 2921.

(453) Carletti, L.; Gandolfi, M.; Rocco, D.; Tognazzi, A.; de Ceglia, D.; Vincenti, M. A.; De Angelis, C. Reconfigurable Nonlinear Response of Dielectric and Semiconductor Metasurfaces. *Nanophotonics* **2021**, *10*, 4209−4221.

(454) Makarov, S. V.; Zalogina, A. S.; Tajik, M.; Zuev, D. A.; Rybin, M. V.; Kuchmizhak, A. A.; Juodkazis, S.; Kivshar, Y. Light-Induced Tuning and Reconfiguration of Nanophotonic Structures: Light-Induced Tuning and Reconfiguration of Nanophotonic Structures. *Laser Photonics Rev.* **2017**, *11*, 1700108.

(455) Zangeneh Kamali, K.; Xu, L.; Ward, J.; Wang, K.; Li, G.; Miroshnichenko, A. E.; Neshev, D.; Rahmani, M. Reversible Image Contrast Manipulation with Thermally Tunable Dielectric Metasurfaces. *Small* **2019**, *15*, 1805142.

(456) Tsoulos, T. V.; Tagliabue, G. Self-Induced Thermo-Optical Effects in Silicon and Germanium Dielectric Nanoresonators. *Nanophotonics* **2020**, *9*, 3849−3861.

(457) Lewi, T.; Butakov, N. A.; Schuller, J. A. Thermal Tuning Capabilities of Semiconductor Metasurface Resonators. *Nanophotonics* **2018**, *8*, 331−338.

(458) Rahmani, M.; Xu, L.; Miroshnichenko, A. E.; Komar, A.; Camacho-Morales, R.; Chen, H.; Zárate, Y.; Kruk, S.; Zhang, G.; Neshev, D. N.; et al. Reversible Thermal Tuning of All-Dielectric Metasurfaces. *Adv. Funct. Mater.* **2017**, *27*, 1700580.

(459) Rocco, D.; Gandolfi, M.; Tognazzi, A.; Pashina, O.; Zograf, G.; Frizyuk, K.; Gigli, C.; Leo, G.; Makarov, S.; Petrov, M.; et al. Opto-Thermally Controlled Beam Steering in Nonlinear All-Dielectric Metastructures. *Opt. Express* **2021**, *29*, 37128.

(460) Celebrano, M.; Rocco, D.; Gandolfi, M.; Zilli, A.; Rusconi, F.; Tognazzi, A.; Mazzanti, A.; Ghirardini, L.; Pogna, E. A. A.; Carletti, L.; et al. Optical Tuning of Dielectric Nanoantennas for Thermo-Optically Reconfigurable Nonlinear Metasurfaces. *Opt. Lett.* **2021**, *46*, 2453.

(461) Zhu, X.; Yan, W.; Levy, U.; Mortensen, N. A.; Kristensen, A. Resonant Laser Printing of Structural Colors on High-Index Dielectric Metasurfaces. *Sci. Adv.* **2017**, *3*, No. e1602487.

(462) Aouassa, M.; Mitsai, E.; Syubaev, S.; Pavlov, D.; Zhizhchenko, A.; Jadli, I.; Hassayoun, L.; Zograf, G.; Makarov, S.; Kuchmizhak, A. Temperature-Feedback Direct Laser Reshaping of Silicon Nanostructures. *Appl. Phys. Lett.* **2017**, *111*, 243103.

(463) Chen, Z.; Li, J.; Zheng, Y. Heat-Mediated Optical Manipulation. *Chem. Rev.* **2022**, *122*, 3122−3179.

(464) Piazza, R. Thermophoresis: Moving Particles with Thermal Gradients. *Soft Matter* **2008**, *4*, 1740−1744.

(465) Würger, A. Transport in Charged Colloids Driven by Thermoelectricity. *Phys. Rev. Lett.* **2008**, *101*, 108302.

(466) Gong, Z.; Pan, Y.-L.; Videen, G.; Wang, C. Optical Trapping and Manipulation of Single Particles in Air: Principles, Technical Details, and Applications. *J. Quant. Spectrosc. Radiat. Transfer* **2018**, *214*, 94−119.

(467) Donner, J. S.; Baffou, G.; McCloskey, D.; Quidant, R. Plasmon-Assisted Optofluidics. *ACS Nano* **2011**, *5*, 5457−5462.

(468) Wu, Z.; Kelp, G.; Yogeesh, M. N.; Li, W.; McNicholas, K. M.; Briggs, A.; Rajeeva, B. B.; Akinwande, D.; Bank, S. R.; Shvets, G.; et al. Dual-Band Moiré Metasurface Patches for Multifunctional Biomedical Applications. *Nanoscale* **2016**, *8*, 18461−18468.

(469) Ndukaife, J. C.; Kildishev, A. V.; Nnanna, A. G. A.; Shalaev, V. M.; Wereley, S. T.; Boltasseva, A. Long-Range and Rapid Transport of Individual Nano-Objects by a Hybrid Electrothermoplasmonic Nanotweezer. *Nat. Nanotechnol.* **2016**, *11*, 53−59.

(470) Garcia-Guirado, J.; Rica, R. A.; Ortega, J.; Medina, J.; Sanz, V.; Ruiz-Reina, E.; Quidant, R. Overcoming Diffusion-Limited Biosensing by Electrothermoplasmonics. *ACS Photonics* **2018**, *5*, 3673−3679.

(471) Ndukaife, J. C.; Mishra, A.; Guler, U.; Nnanna, A. G. A.; Wereley, S. T.; Boltasseva, A. Photothermal Heating Enabled by Plasmonic Nanostructures for Electrokinetic Manipulation and Sorting of Particles. *ACS Nano* **2014**, *8*, 9035−9043.

(472) Ndukaife, J. C.; Xuan, Y.; Nnanna, A. G. A.; Kildishev, A. V.; Shalaev, V. M.; Wereley, S. T.; Boltasseva, A. High-Resolution Large-Ensemble Nanoparticle Trapping with Multifunctional Thermoplasmonic Nanohole Metasurface. *ACS Nano* **2018**, *12*, 5376−5384.

(473) Hong, C.; Yang, S.; Ndukaife, J. C. Stand-Off Trapping and Manipulation of Sub-10 Nm Objects and Biomolecules Using Opto-Thermo-Electrohydrodynamic Tweezers. *Nat. Nanotechnol.* **2020**, *15*, 908−913.

(474) Blázquez-Castro, A. Optical Tweezers: Phototoxicity and Thermal Stress in Cells and Biomolecules. *Micromachines* **2019**, *10*, 507.

(475) Ma, C.; Yu, P.; Wang, W.; Zhu, Y.; Lin, F.; Wang, J.; Jing, Z.; Kong, X.-T.; Li, P.; Govorov, A. O.; et al. Chiral Optofluidics with a Plasmonic Metasurface Using the Photothermal Effect. *ACS Nano* **2021**, *15*, 16357−16367.

(476) Mancini, A.; Giliberti, V.; Alabastri, A.; Calandrini, E.; De Angelis, F.; Garoli, D.; Ortolani, M. Nanoscale Thermal Gradients

Activated by Antenna-Enhanced Molecular Absorption in the Mid-Infrared. *Appl. Phys. Lett.* **2019**, *114*, 023105.

(477) Mancini, A.; Giliberti, V.; Alabastri, A.; Calandrini, E.; De Angelis, F.; Garoli, D.; Ortolani, M. Thermoplasmonic Effect of Surface-Enhanced Infrared Absorption in Vertical Nanoantenna Arrays. *J. Phys. Chem. C* **2018**, *122*, 13072−13081.

(478) Hasan, D.; Ho, C. P.; Pitchappa, P.; Yang, B.; Yang, C.; Lee, C. Thermoplasmonic Study of a Triple Band Optical Nanoantenna Strongly Coupled to Mid IR Molecular Mode. *Sci. Rep.* **2016**, *6*, 22227.

(479) Zhou, L.; Tan, Y.; Wang, J.; Xu, W.; Yuan, Y.; Cai, W.; Zhu, S.; Zhu, J. 3D Self-Assembly of Aluminium Nanoparticles for Plasmon-Enhanced Solar Desalination. *Nat. Photonics* **2016**, *10*, 393−398.

(480) Walker, C.; Mitridis, E.; Kreiner, T.; Eghlidi, H.; Schutzius, T. M.; Poulikakos, D. Transparent Metasurfaces Counteracting Fogging by Harnessing Sunlight. *Nano Lett.* **2019**, *19*, 1595−1604.

(481) Mitridis, E.; Schutzius, T. M.; Sicher, A.; Hail, C. U.; Eghlidi, H.; Poulikakos, D. Metasurfaces Leveraging Solar Energy for Icephobicity. *ACS Nano* **2018**, *12*, 7009−7017.

(482) Mitridis, E.; Lambley, H.; Tröber, S.; Schutzius, T. M.; Poulikakos, D. Transparent Photothermal Metasurfaces Amplifying Superhydrophobicity by Absorbing Sunlight. *ACS Nano* **2020**, *14*, 11712−11721.

(483) González-Rubio, G.; Guerrero-Martínez, A.; Liz-Marzán, L. M. Reshaping, Fragmentation, and Assembly of Gold Nanoparticles Assisted by Pulse Lasers. *Acc. Chem. Res.* **2016**, *49*, 678−686.

(484) Inasawa, S.; Sugiyama, M.; Yamaguchi, Y. Laser-Induced Shape Transformation of Gold Nanoparticles below the Melting Point: The Effect of Surface Melting. *J. Phys. Chem. B* **2005**, *109*, 3104−3111.

(485) Lee, J.; Tanaka, T.; Lee, J.; Mori, H. Effect of Substrates on the Melting Temperature of Gold Nanoparticles. *Calphad* **2007**, *31*, 105−111.

(486) Lalisse, A.; Tessier, G.; Plain, J.; Baffou, G. Quantifying the Efficiency of Plasmonic Materials for Near-Field Enhancement and Photothermal Conversion. *J. Phys. Chem. C* **2015**, *119*, 25518−25528.

(487) Setoura, K.; Ito, S. Quantifying the Durability of Transition Metal Nitrides in Thermoplasmonics at the Single-Nanoparticle Level. *AIP Adv.* **2021**, *11*, 115027.

(488) Patsalas, P. Zirconium Nitride: A Viable Candidate for Photonics and Plasmonics? *Thin Solid Films* **2019**, *688*, 137438.

(489) Naldoni, A.; Guler, U.; Wang, Z.; Marelli, M.; Malara, F.; Meng, X.; Besteiro, L. V.; Govorov, A. O.; Kildishev, A. V.; Boltasseva, A.; et al. Broadband Hot-Electron Collection for Solar Water Splitting with Plasmonic Titanium Nitride. *Adv. Opt. Mater.* **2017**, *5*, 1601031.

(490) Guler, U.; Ndukaife, J. C.; Naik, G. V.; Nnanna, A. G. A.; Kildishev, A. V.; Shalaev, V. M.; Boltasseva, A. Local Heating with Lithographically Fabricated Plasmonic Titanium Nitride Nanoparticles. *Nano Lett.* **2013**, *13*, 6078−6083.

(491) Guler, U.; Naik, G. V.; Boltasseva, A.; Shalaev, V. M.; Kildishev, A. V. Performance Analysis of Nitride Alternative Plasmonic Materials for Localized Surface Plasmon Applications. *Appl. Phys. B: Laser Opt.* **2012**, *107*, 285−291.

(492) Kharintsev, S. S.; Chernykh, E. A.; Shelaev, A. V.; Kazarian, S. G. Nanoscale Sensing Vitrification of 3D Confined Glassy Polymers Through Refractory Thermoplasmonics. *ACS Photonics* **2021**, *8*, 1477−1488.

(493) Li, W.; Guler, U.; Kinsey, N.; Naik, G. V.; Boltasseva, A.; Guan, J.; Shalaev, V. M.; Kildishev, A. V. Refractory Plasmonics with Titanium Nitride: Broadband Metamaterial Absorber. *Adv. Mater.* **2014**, *26*, 7959−7965.

(494) Dongare, P. D.; Zhao, Y.; Renard, D.; Yang, J.; Neumann, O.; Metz, J.; Yuan, L.; Alabastri, A.; Nordlander, P.; Halas, N. J. A 3D Plasmonic Antenna-Reactor for Nanoscale Thermal Hotspots and Gradients. *ACS Nano* **2021**, *15*, 8761−8769.

(495) Baffou, G.; Quidant, R. Nanoplasmonics for Chemistry. *Chem. Soc. Rev.* **2014**, *43*, 3898−3907.

(496) Zhou, L.; Swearer, D. F.; Zhang, C.; Robatjazi, H.; Zhao, H.; Henderson, L.; Dong, L.; Christopher, P.; Carter, E. A.; Nordlander, P.; et al. Quantifying Hot Carrier and Thermal Contributions in Plasmonic Photocatalysis. *Science* **2018**, *362*, 69−72.

(497) Cortés, E.; Besteiro, L. V.; Alabastri, A.; Baldi, A.; Tagliabue, G.; Demetriadou, A.; Narang, P. Challenges in Plasmonic Catalysis. *ACS Nano* **2020**, *14*, 16202−16219.

(498) Modest, M. F.; Mazumder, S. *Radiative Heat Transfer*; Elsevier Science, 2021.

(499) Cuevas, J. C.; García-Vidal, F. J. Radiative Heat Transfer. *ACS Photonics* **2018**, *5*, 3896−3915.

(500) Baranov, D. G.; Xiao, Y.; Nechepurenko, I. A.; Krasnok, A.; Alù, A.; Kats, M. A. Nanophotonic Engineering of Far-Field Thermal Emitters. *Nat. Mater.* **2019**, *18*, 920−930.

(501) Li, W.; Fan, S. Nanophotonic Control of Thermal Radiation for Energy Applications. *Opt. Express* **2018**, *26*, 15995−16021.

(502) Brucoli, G.; Bouchon, P.; Haïdar, R.; Besbes, M.; Benisty, H.; Greffet, J.-J. High Efficiency Quasi-Monochromatic Infrared Emitter. *Appl. Phys. Lett.* **2014**, *104*, 081101.

(503) Gmachl, C.; Capasso, F.; Sivco, D. L.; Cho, A. Y. Recent Progress in Quantum Cascade Lasers and Applications. *Rep. Prog. Phys.* **2001**, *64*, 1533−1601.

(504) Werle, P.; Slemr, F.; Maurer, K.; Kormann, R.; Mücke, R.; Jänker, B. Near- and Mid-Infrared Laser-Optical Sensors for Gas Analysis. *Opt. Lasers Eng.* **2002**, *37*, 101−114.

(505) Li, J.; Yu, B.; Shen, S. Scale Law of Far-Field Thermal Radiation from Plasmonic Metasurfaces. *Phys. Rev. Lett.* **2020**, *124*, 137401.

(506) Toyoda, H.; Kimino, K.; Kawano, A.; Takahara, J. Incandescent Light Bulbs Based on a Refractory Metasurface. *Photonics* **2019**, *6*, 105.

(507) Yokoyama, T.; Dao, T. D.; Chen, K.; Ishii, S.; Sugavaneshwar, R. P.; Kitajima, M.; Nagao, T. Spectrally Selective Mid-Infrared Thermal Emission from Molybdenum Plasmonic Metamaterial Operated up to 1000 °C. *Adv. Opt. Mater.* **2016**, *4*, 1987−1992.

(508) Molesky, S.; Dewalt, C. J.; Jacob, Z. High Temperature Epsilon-Near-Zero and Epsilon-Near-Pole Metamaterial Emitters for Thermo-photovoltaics. *Opt. Express* **2013**, *21*, A96−A110.

(509) Liu, B.; Gong, W.; Yu, B.; Li, P.; Shen, S. Perfect Thermal Emission by Nanoscale Transmission Line Resonators. *Nano Lett.* **2017**, *17*, 666−672.

(510) Liu, X.; Tyler, T.; Starr, T.; Starr, A. F.; Jokerst, N. M.; Padilla, W. J. Taming the Blackbody with Infrared Metamaterials as Selective Thermal Emitters. *Phys. Rev. Lett.* **2011**, *107*, 045901.

(511) Ikeda, K.; Miyazaki, H. T.; Kasaya, T.; Yamamoto, K.; Inoue, Y.; Fujimura, K.; Kanakugi, T.; Okada, M.; Hatade, K.; Kitagawa, S. Controlled Thermal Emission of Polarized Infrared Waves from Arrayed Plasmon Nanocavities. *Appl. Phys. Lett.* **2008**, *92*, 021117.

(512) Puscasu, I.; Pralle, M.; McNeal, M.; Daly, J.; Greenwald, A.; Johnson, E.; Biswas, R.; Ding, C. G. Extraordinary Emission from Two-Dimensional Plasmonic-Photonic Crystals. *J. Appl. Phys.* **2005**, *98*, 013531.

(513) Inoue, T.; De Zoysa, M.; Asano, T.; Noda, S. Realization of Narrowband Thermal Emission with Optical Nanostructures. *Optica* **2015**, *2*, 27−35.

(514) Dyakov, S. A.; Semenenko, V. A.; Gippius, N. A.; Tikhodeev, S. G. Magnetic Field Free Circularly Polarized Thermal Emission from a Chiral Metasurface. *Phys. Rev. B* **2018**, *98*, 235416.

(515) Wang, B. X.; Liu, M. Q.; Huang, T. C.; Zhao, C. Y. Micro/Nanostructures for Far-Field Thermal Emission Control: An Overview. *ES Energy Environ.* **2019**, *6*, 18−38.

(516) Xie, X.; Li, X.; Pu, M.; Ma, X.; Liu, K.; Guo, Y.; Luo, X. Plasmonic Metasurfaces for Simultaneous Thermal Infrared Invisibility and Holographic Illusion. *Adv. Funct. Mater.* **2018**, *28*, 1706673.

(517) Zhang, X.; Zhang, Z.; Wang, Q.; Zhu, S.; Liu, H. Controlling Thermal Emission by Parity-Symmetric Fano Resonance of Optical Absorbers in Metasurfaces. *ACS Photonics* **2019**, *6*, 2671−2676.

(518) Costantini, D.; Lefebvre, A.; Coutrot, A.-L.; Moldovan-Doyen, I.; Hugonin, J.-P.; Boutami, S.; Marquier, F.; Benisty, H.; Greffet, J.-J. Plasmonic Metasurface for Directional and Frequency-Selective Thermal Emission. *Phys. Rev. Appl.* **2015**, *4*, 014023.

(519) De Zoysa, M.; Asano, T.; Mochizuki, K.; Oskooi, A.; Inoue, T.; Noda, S. Conversion of Broadband to Narrowband Thermal Emission Through Energy Recycling. *Nat. Photonics* **2012**, *6*, 535−539.

(520) Blanchard, C.; Wojszvzyk, L.; Jamois, C.; Leclercq, J.-L.; Chevalier, C.; Ferrier, L.; Viktorovitch, P.; Moldovan-Doyen, I.; Marquier, F.; Greffet, J.-J.; et al. Metallo-Dielectric Metasurfaces for Thermal Emission with Controlled Spectral Bandwidth and Angular Aperture. *Opt. Mater. Express* **2022**, *12*, 1−12.

(521) Zhou, M.; Khoram, E.; Liu, D.; Liu, B.; Fan, S.; Povinelli, M. L.; Yu, Z. Self-Focused Thermal Emission and Holography Realized by Mesoscopic Thermal Emitters. *ACS Photonics* **2021**, *8*, 497−504.

(522) Wojszvzyk, L.; Nguyen, A.; Coutrot, A.-L.; Zhang, C.; Vest, B.; Greffet, J.-J. An Incandescent Metasurface for Quasimonochromatic Polarized Mid-Wave Infrared Emission Modulated Beyond 10 MHz. *Nat. Commun.* **2021**, *12*, 1492.

(523) Miyazaki, H. T.; Kasaya, T.; Oosato, H.; Sugimoto, Y.; Choi, B.; Iwanaga, M.; Sakoda, K. Ultraviolet-Nanoimprinted Packaged Metasurface Thermal Emitters for Infrared CO_2 Sensing. *Sci. Technol. Adv. Mater.* **2015**, *16*, 035005.

(524) Inoue, T.; Zoysa, M. D.; Asano, T.; Noda, S. Realization of Dynamic Thermal Emission Control. *Nat. Mater.* **2014**, *13*, 928−931.

(525) Park, J.; Kang, J.-H.; Liu, X.; Maddox, S. J.; Tang, K.; McIntyre, P. C.; Bank, S. R.; Brongersma, M. L. Dynamic Thermal Emission Control with InAs-Based Plasmonic Metasurfaces. *Sci. Adv.* **2018**, *4*, No. eaat3163.

(526) Sokolov, P. S.; Mukhanov, V. A.; Chauveau, T.; Solozhenko, V. L. On Melting of Silicon Carbide under Pressure. *J. Superhard Mater.* **2012**, *34*, 339−341.

(527) Greffet, J.-J.; Carminati, R.; Joulain, K.; Mulet, J.-P.; Mainguy, S.; Chen, Y. Coherent Emission of Light by Thermal Sources. *Nature* **2002**, *416*, 61−64.

(528) Chalabi, H.; Alù, A.; Brongersma, M. L. Focused Thermal Emission from a Nanostructured SiC Surface. *Phys. Rev. B* **2016**, *94*, 094307.

(529) Inampudi, S.; Cheng, J.; Salary, M. M.; Mosallaei, H. Unidirectional Thermal Radiation from a SiC Metasurface. *J. Opt. Soc. Am. B* **2018**, *35*, 39−46.

(530) Ito, K.; Matsui, T.; Iizuka, H. Thermal Emission Control by Evanescent Wave Coupling Between Guided Mode of Resonant Grating and Surface Phonon Polariton on Silicon Carbide Plate. *Appl. Phys. Lett.* **2014**, *104*, 051127.

(531) Arnold, C.; Marquier, F.; Garin, M.; Pardo, F.; Collin, S.; Bardou, N.; Pelouard, J.-L.; Greffet, J.-J. Coherent Thermal Infrared Emission by Two-Dimensional Silicon Carbide Gratings. *Phys. Rev. B* **2012**, *86*, 035316.

(532) Wang, T.; Li, P.; Chigrin, D. N.; Giles, A. J.; Bezares, F. J.; Glembocki, O. J.; Caldwell, J. D.; Taubner, T. Phonon-Polaritonic Bowtie Nanoantennas: Controlling Infrared Thermal Radiation at the Nanoscale. *ACS Photonics* **2017**, *4*, 1753−1760.

(533) Shitrit, N.; Yulevich, I.; Maguid, E.; Ozeri, D.; Veksler, D.; Kleiner, V.; Hasman, E. Spin-Optical Metamaterial Route to Spin-Controlled Photonics. *Science* **2013**, *340*, 724−726.

(534) Frischwasser, K.; Yulevich, I.; Kleiner, V.; Hasman, E. Rashba-Like Spin Degeneracy Breaking in Coupled Thermal Antenna Lattices. *Opt. Express* **2011**, *19*, 23475−23482.

(535) Dahan, N.; Gorodetski, Y.; Frischwasser, K.; Kleiner, V.; Hasman, E. Geometric Doppler Effect: Spin-Split Dispersion of Thermal Radiation. *Phys. Rev. Lett.* **2010**, *105*, 136402.

(536) Gubbin, C. R.; Berte, R.; Meeker, M. A.; Giles, A. J.; Ellis, C. T.; Tischler, J. G.; Wheeler, V. D.; Maier, S. A.; Caldwell, J. D.; De Liberato, S. Hybrid Longitudinal-Transverse Phonon Polaritons. *Nat. Commun.* **2019**, *10*, 1682.

(537) Lu, G.; Gubbin, C. R.; Nolen, J. R.; Folland, T.; Tadjer, M. J.; De Liberato, S.; Caldwell, J. D. Engineering the Spectral and Spatial Dispersion of Thermal Emission via Polariton-Phonon Strong Coupling. *Nano Lett.* **2021**, *21*, 1831−1838.

(538) Lu, G.; Nolen, J. R.; Folland, T. G.; Tadjer, M. J.; Walker, D. G.; Caldwell, J. D. Narrowband Polaritonic Thermal Emitters Driven by Waste Heat. *ACS Omega* **2020**, *5*, 10900−10908.

(539) Hossain, M. M.; Jia, B.; Gu, M. A Metamaterial Emitter for Highly Efficient Radiative Cooling. *Adv. Opt. Mater.* **2015**, *3*, 1047−1051.

(540) Zou, C.; Ren, G.; Hossain, M. M.; Nirantar, S.; Withayachumnankul, W.; Ahmed, T.; Bhaskaran, M.; Sriram, S.; Gu, M.; Fumeaux, C. Metal-Loaded Dielectric Resonator Metasurfaces for Radiative Cooling. *Adv. Opt. Mater.* **2017**, *5*, 1700460.

(541) Wang, W.; Zhao, Z.; Zou, Q.; Hong, B.; Zhang, W.; Wang, G. P. Self-Adaptive Radiative Cooling and Solar Heating Based on a Compound Metasurface. *J. Mater. Chem. C* **2020**, *8*, 3192−3199.

(542) Hao, Q.; Li, W.; Xu, H.; Wang, J.; Yin, Y.; Wang, H.; Ma, L.; Ma, F.; Jiang, X.; Schmidt, O. G.; et al. VO_2/TiN Plasmonic Thermochromic Smart Coatings for Room-Temperature Applications. *Adv. Mater.* **2018**, *30*, 1705421.

(543) Zhu, L.; Raman, A. P.; Fan, S. Radiative Cooling of Solar Absorbers Using a Visibly Transparent Photonic Crystal Thermal Blackbody. *Proc. Natl. Acad. Sci. U. S. A.* **2015**, *112*, 12282−12287.

(544) Vollmer, M.; Möllmann, K.-P. *Infrared Thermal Imaging: Fundamentals, Research and Applications*; Wiley-VCH, 2018.

(545) Huang, S.; Fan, Q.; Xu, C.; Wang, B.; Wang, J.; Yang, B.; Tian, C.; Meng, Z. A Visible-Light-Transparent Camouflage-Compatible Flexible Metasurface for Infrared-Radar Stealth Applications. *J. Phys. Appl. Phys.* **2021**, *54*, 015001.

(546) Liu, Y.; Song, J.; Zhao, W.; Ren, X.; Cheng, Q.; Luo, X.; Fang, N. X.; Hu, R. Dynamic Thermal Camouflage via a Liquid-Crystal-Based Radiative Metasurface. *Nanophotonics* **2020**, *9*, 855−863.

(547) Coppens, Z. J.; Valentine, J. G. Spatial and Temporal Modulation of Thermal Emission. *Adv. Mater.* **2017**, *29*, 1701275.

(548) Liu, X.; Wang, L.; Zhang, Z. M. Near-Field Thermal Radiation: Recent Progress and Outlook. *Nanoscale Microscale Thermophys. Eng.* **2015**, *19*, 98−126.

(549) Rousseau, E.; Siria, A.; Jourdan, G.; Volz, S.; Comin, F.; Chevrier, J.; Greffet, J.-J. Radiative Heat Transfer at the Nanoscale. *Nat. Photonics* **2009**, *3*, 514−517.

(550) Joulain, K.; Mulet, J.-P.; Marquier, F.; Carminati, R.; Greffet, J.-J. Surface Electromagnetic Waves Thermally Excited: Radiative Heat Transfer, Coherence Properties and Casimir Forces Revisited in the Near Field. *Surf. Sci. Rep.* **2005**, *57*, 59−112.

(551) Mulet, J.-P.; Joulain, K.; Carminati, R.; Greffet, J.-J. Enhanced Radiative Heat Transfer at Nanometric Distances. *Microscale Thermophys. Eng.* **2002**, *6*, 209−222.

(552) Shchegrov, A. V.; Joulain, K.; Carminati, R.; Greffet, J.-J. Near-Field Spectral Effects Due to Electromagnetic Surface Excitations. *Phys. Rev. Lett.* **2000**, *85*, 1548−1551.

(553) Carminati, R.; Greffet, J.-J. Near-Field Effects in Spatial Coherence of Thermal Sources. *Phys. Rev. Lett.* **1999**, *82*, 1660−1663.

(554) Babuty, A.; Joulain, K.; Chapuis, P.-O.; Greffet, J.-J.; De Wilde, Y. Blackbody Spectrum Revisited in the Near Field. *Phys. Rev. Lett.* **2013**, *110*, 146103.

(555) Kim, K.; Song, B.; Fernández-Hurtado, V.; Lee, W.; Jeong, W.; Cui, L.; Thompson, D.; Feist, J.; Reid, M. T. H.; García-Vidal, F. J.; et al. Radiative Heat Transfer in the Extreme Near Field. *Nature* **2015**, *528*, 387−391.

(556) Kloppstech, K.; Könne, N.; Biehs, S.-A.; Rodriguez, A. W.; Worbes, L.; Hellmann, D.; Kittel, A. Giant Heat Transfer in the Crossover Regime Between Conduction and Radiation. *Nat. Commun.* **2017**, *8*, 14475.

(557) Song, B.; Ganjeh, Y.; Sadat, S.; Thompson, D.; Fiorino, A.; Fernández-Hurtado, V.; Feist, J.; Garcia-Vidal, F. J.; Cuevas, J. C.; Reddy, P.; et al. Enhancement of Near-Field Radiative Heat Transfer Using Polar Dielectric Thin Films. *Nat. Nanotechnol.* **2015**, *10*, 253−258.

(558) Fiorino, A.; Thompson, D.; Zhu, L.; Song, B.; Reddy, P.; Meyhofer, E. Giant Enhancement in Radiative Heat Transfer in Sub-30 Nm Gaps of Plane Parallel Surfaces. *Nano Lett.* **2018**, *18*, 3711−3715.

(559) Song, B.; Thompson, D.; Fiorino, A.; Ganjeh, Y.; Reddy, P.; Meyhofer, E. Radiative Heat Conductances Between Dielectric and Metallic Parallel Plates with Nanoscale Gaps. *Nat. Nanotechnol.* **2016**, *11*, 509−514.

(560) Fernández-Hurtado, V.; García-Vidal, F. J.; Fan, S.; Cuevas, J. C. Enhancing Near-Field Radiative Heat Transfer with Si-Based Metasurfaces. *Phys. Rev. Lett.* **2017**, *118*, 203901.

(561) Elshaari, A. W.; Pernice, W.; Srinivasan, K.; Benson, O.; Zwiller, V. Hybrid Integrated Quantum Photonic Circuits. *Nat. Photonics* **2020**, *14*, 285−298.

(562) Volz, S.; Ordonez-Miranda, J.; Shchepetov, A.; Prunnila, M.; Ahopelto, J.; Pezeril, T.; Vaudel, G.; Gusev, V.; Ruello, P.; Weig, E. M.; et al. Nanophononics: State of the Art and Perspectives. *Eur. Phys. J. B* **2016**, *89*, 15.

(563) Wigger, D.; Gawarecki, K.; Machnikowski, P. Remote Phonon Control of Quantum Dots and Other Artificial Atoms. *Adv. Quantum Technol.* **2021**, *4*, 2000128.

(564) Matsuda, O.; Larciprete, M. C.; Li Voti, R.; Wright, O. B. Fundamentals of Picosecond Laser Ultrasonics. *Ultrasonics* **2015**, *56*, 3−20.

(565) Berte, R.; Della Picca, F.; Poblet, M.; Li, Y.; Cortés, E.; Craster, R. V.; Maier, S. A.; Bragas, A. V. Acoustic Far-Field Hypersonic Surface Wave Detection with Single Plasmonic Nanoantennas. *Phys. Rev. Lett.* **2018**, *121*, 253902.

(566) Imade, Y.; Gusev, V. E.; Matsuda, O.; Tomoda, M.; Otsuka, P. H.; Wright, O. B. Gigahertz Optomechanical Photon-Phonon Transduction between Nanostructure Lines. *Nano Lett.* **2021**, *21*, 6261−6267.

(567) Ahmadi, T. S.; Logunov, S. L.; El-Sayed, M. A. Picosecond Dynamics of Colloidal Gold Nanoparticles. *J. Phys. Chem.* **1996**, *100*, 8053−8056.

(568) Perner, M.; Gresillon, S.; März, J.; von Plessen, G.; Feldmann, J.; Porstendorfer, J.; Berg, K.-J.; Berg, G. Observation of Hot-Electron Pressure in the Vibration Dynamics of Metal Nanoparticles. *Phys. Rev. Lett.* **2000**, *85*, 792−795.

(569) Voisin, C.; Del Fatti, N.; Christofilos, D.; Vallée, F. Ultrafast Electron Dynamics and Optical Nonlinearities in Metal Nanoparticles. *J. Phys. Chem. B* **2001**, *105*, 2264−2280.

(570) Ahmed, A.; Pelton, M.; Guest, J. R. Understanding How Acoustic Vibrations Modulate the Optical Response of Plasmonic Metal Nanoparticles. *ACS Nano* **2017**, *11*, 9360−9369.

(571) Della Picca, F.; Berte, R.; Rahmani, M.; Albella, P.; Bujjamer, J. M.; Poblet, M.; Cortés, E.; Maier, S. A.; Bragas, A. V. Tailored Hypersound Generation in Single Plasmonic Nanoantennas. *Nano Lett.* **2016**, *16*, 1428−1434.

(572) Poblet, M.; Berté, R.; Boggiano, H. D.; Li, Y.; Cortés, E.; Grinblat, G.; Maier, S. A.; Bragas, A. V. Acoustic Coupling between Plasmonic Nanoantennas: Detection and Directionality of Surface Acoustic Waves. *ACS Photonics* **2021**, *8*, 2846−2852.

(573) Profunser, D. M.; Muramoto, E.; Matsuda, O.; Wright, O. B.; Lang, U. Dynamic Visualization of Surface Acoustic Waves on a Two-Dimensional Phononic Crystal. *Phys. Rev. B* **2009**, *80*, 014301.

(574) Maznev, A. A.; Wright, O. B. Optical Generation of Long-Lived Surface Vibrations in a Periodic Microstructure. *J. Appl. Phys.* **2009**, *105*, 123530.

(575) Maznev, A. A.; Wright, O. B.; Matsuda, O. Mapping the Band Structure of a Surface Phononic Crystal. *New J. Phys.* **2011**, *13*, 013037.

(576) Matsuda, O.; Tsutsui, K.; Vaudel, G.; Pezeril, T.; Fujita, K.; Gusev, V. Optical Generation and Detection of Gigahertz Shear Acoustic Waves in Solids Assisted by a Metallic Diffraction Grating. *Phys. Rev. B* **2020**, *101*, 224307.

(577) Imade, Y.; Ulbricht, R.; Tomoda, M.; Matsuda, O.; Seniutinas, G.; Juodkazis, S.; Wright, O. B. Gigahertz Optomechanical Modulation by Split-Ring-Resonator Nanophotonic Meta-Atom Arrays. *Nano Lett.* **2017**, *17*, 6684−6689.

(578) Markoš, P.; Soukoulis, C. M. Transmission Studies of Left-Handed Materials. *Phys. Rev. B* **2001**, *65*, 033401.

(579) Ebbesen, T. W.; Lezec, H. J.; Ghaemi, H. F.; Thio, T.; Wolff, P. A. Extraordinary Optical Transmission Through Sub-Wavelength Hole Arrays. *Nature* **1998**, *391*, 667−669.

(580) Devaux, T.; Tozawa, H.; Otsuka, P. H.; Mezil, S.; Tomoda, M.; Matsuda, O.; Bok, E.; Lee, S. H.; Wright, O. B. Giant Extraordinary Transmission of Acoustic Waves Through a Nanowire. *Sci. Adv.* **2020**, *6*, No. eaay8507.

(581) Chen, Y.; Francescato, Y.; Caldwell, J. D.; Giannini, V.; Maß, T. W. W.; Glembocki, O. J.; Bezares, F. J.; Taubner, T.; Kasica, R.; Hong, M.; et al. Spectral Tuning of Localized Surface Phonon Polariton Resonators for Low-Loss Mid-IR Applications. *ACS Photonics* **2014**, *1*, 718−724.

(582) Berte, R.; Gubbin, C. R.; Wheeler, V. D.; Giles, A. J.; Giannini, V.; Maier, S. A.; De Liberato, S.; Caldwell, J. D. Sub-Nanometer Thin Oxide Film Sensing with Localized Surface Phonon Polaritons. *ACS Photonics* **2018**, *5*, 2807−2815.

(583) Gubbin, C. R.; Maier, S. A.; De Liberato, S. Theoretical Investigation of Phonon Polaritons in SiC Micropillar Resonators. *Phys. Rev. B* **2017**, *95*, 035313.

(584) Gubbin, C. R.; Martini, F.; Politi, A.; Maier, S. A.; De Liberato, S. Strong and Coherent Coupling between Localized and Propagating Phonon Polaritons. *Phys. Rev. Lett.* **2016**, *116*, 246402.

(585) Razdolski, I.; Passler, N. C.; Gubbin, C. R.; Winta, C. J.; Cernansky, R.; Martini, F.; Politi, A.; Maier, S. A.; Wolf, M.; Paarmann, A.; et al. Second Harmonic Generation from Strongly Coupled Localized and Propagating Phonon-Polariton Modes. *Phys. Rev. B* **2018**, *98*, 125425.

(586) Razdolski, I.; Chen, Y.; Giles, A. J.; Gewinner, S.; Schöllkopf, W.; Hong, M.; Wolf, M.; Giannini, V.; Caldwell, J. D.; Maier, S. A.; et al. Resonant Enhancement of Second-Harmonic Generation in the Mid-Infrared Using Localized Surface Phonon Polaritons in Subdiffractional Nanostructures. *Nano Lett.* **2016**, *16*, 6954−6959.

(587) Spann, B. T.; Compton, R.; Ratchford, D.; Long, J. P.; Dunkelberger, A. D.; Klein, P. B.; Giles, A. J.; Caldwell, J. D.; Owrutsky, J. C. Photoinduced Tunability of the Reststrahlen Band in 4H-SiC. *Phys. Rev. B* **2016**, *93*, 085205.

(588) Dunkelberger, A. D.; Ellis, C. T.; Ratchford, D. C.; Giles, A. J.; Kim, M.; Kim, C. S.; Spann, B. T.; Vurgaftman, I.; Tischler, J. G.; Long, J. P.; et al. Active Tuning of Surface Phonon Polariton Resonances via Carrier Photoinjection. *Nat. Photonics* **2018**, *12*, 50−56.

(589) Giles, A. J.; Dai, S.; Glembocki, O. J.; Kretinin, A. V.; Sun, Z.; Ellis, C. T.; Tischler, J. G.; Taniguchi, T.; Watanabe, K.; Fogler, M. M.; et al. Imaging of Anomalous Internal Reflections of Hyperbolic Phonon-Polaritons in Hexagonal Boron Nitride. *Nano Lett.* **2016**, *16*, 3858−3865.

(590) Brown, L. V.; Davanco, M.; Sun, Z.; Kretinin, A.; Chen, Y.; Matson, J. R.; Vurgaftman, I.; Sharac, N.; Giles, A. J.; Fogler, M. M.; et al. Nanoscale Mapping and Spectroscopy of Nonradiative Hyperbolic Modes in Hexagonal Boron Nitride Nanostructures. *Nano Lett.* **2018**, *18*, 1628−1636.

(591) Ramer, G.; Tuteja, M.; Matson, J. R.; Davanco, M.; Folland, T. G.; Kretinin, A.; Taniguchi, T.; Watanabe, K.; Novoselov, K. S.; Caldwell, J. D.; et al. High-Q Dark Hyperbolic Phonon-Polaritons in Hexagonal Boron Nitride Nanostructures. *Nanophotonics* **2020**, *9*, 1457−1467.

(592) Alfaro-Mozaz, F. J.; Rodrigo, S. G.; Alonso-González, P.; Vélez, S.; Dolado, I.; Casanova, F.; Hueso, L. E.; Martín-Moreno, L.; Hillenbrand, R.; Nikitin, A. Y. Deeply Subwavelength Phonon-Polaritonic Crystal Made of a Van Der Waals Material. *Nat. Commun.* **2019**, *10*, 42.

(593) Yang, J.; Krix, Z. E.; Kim, S.; Tang, J.; Mayyas, M.; Wang, Y.; Watanabe, K.; Taniguchi, T.; Li, L. H.; Hamilton, A. R.; et al. Near-Field Excited Archimedean-like Tiling Patterns in Phonon-Polaritonic Crystals. *ACS Nano* **2021**, *15*, 9134−9142.

(594) Alfaro-Mozaz, F. J.; Rodrigo, S. G.; Vélez, S.; Dolado, I.; Govyadinov, A.; Alonso-González, P.; Casanova, F.; Hueso, L. E.; Martín-Moreno, L.; Hillenbrand, R.; et al. Hyperspectral Nanoimaging of van Der Waals Polaritonic Crystals. *Nano Lett.* **2021**, *21*, 7109−7115.

(595) Lee, I.-H.; He, M.; Zhang, X.; Luo, Y.; Liu, S.; Edgar, J. H.; Wang, K.; Avouris, P.; Low, T.; Caldwell, J. D.; et al. Image Polaritons in Boron Nitride for Extreme Polariton Confinement with Low Losses. *Nat. Commun.* **2020**, *11*, 3649.

(596) Li, P.; Hu, G.; Dolado, I.; Tymchenko, M.; Qiu, C.-W.; Alfaro-Mozaz, F. J.; Casanova, F.; Hueso, L. E.; Liu, S.; Edgar, J. H.; et al. Collective Near-Field Coupling and Nonlocal Phenomena in Infrared-Phononic Metasurfaces for Nano-Light Canalization. *Nat. Commun.* **2020**, *11*, 3663.

(597) Li, P.; Dolado, I.; Alfaro-Mozaz, F. J.; Casanova, F.; Hueso, L. E.; Liu, S.; Edgar, J. H.; Nikitin, A. Y.; Vélez, S.; Hillenbrand, R. Infrared Hyperbolic Metasurface Based on Nanostructured Van Der Waals Materials. *Science* **2018**, *359*, 892−896.

(598) Guddala, S.; Komissarenko, F.; Kiriushechkina, S.; Vakulenko, A.; Li, M.; Menon, V. M.; Alù, A.; Khanikaev, A. B. Topological Phonon-Polariton Funneling in Midinfrared Metasurfaces. *Science* **2021**, *374*, 225−227.

(599) Xiong, H.; Lu, Y.; Wu, Q.; Li, Z.; Qi, J.; Xu, X.; Ma, R.; Xu, J. Topological Valley Transport of Terahertz Phonon-Polaritons in a LiNbO₃ Chip. *ACS Photonics* **2021**, *8*, 2737−2745.

(600) Ozawa, T.; Price, H. M.; Amo, A.; Goldman, N.; Hafezi, M.; Lu, L.; Rechtsman, M. C.; Schuster, D.; Simon, J.; Zilberberg, O.; et al. Topological Photonics. *Rev. Mod. Phys.* **2019**, *91*, 015006.

(601) Barik, S.; Karasahin, A.; Flower, C.; Cai, T.; Miyake, H.; DeGottardi, W.; Hafezi, M.; Waks, E. A Topological Quantum Optics Interface. *Science* **2018**, *359*, 666−668.

(602) Parappurath, N.; Alpeggiani, F.; Kuipers, L.; Verhagen, E. Direct Observation of Topological Edge States in Silicon Photonic Crystals: Spin, Dispersion, and Chiral Routing. *Sci. Adv.* **2020**, *6*, No. eaaw4137.

(603) Huang, C.; Lan, Y. Thermophysical Study of Surface Phonon Polaritons in Multilayer Systems for Heat Dissipation. *Int. J. Therm. Sci.* **2021**, *159*, 106548.

(604) Tranchant, L.; Hamamura, S.; Ordonez-Miranda, J.; Yabuki, T.; Vega-Flick, A.; Cervantes-Alvarez, F.; Alvarado-Gil, J. J.; Volz, S.; Miyazaki, K. Two-Dimensional Phonon Polariton Heat Transport. *Nano Lett.* **2019**, *19*, 6924−6930.

(605) Feng, K.; Streyer, W.; Islam, S. M.; Verma, J.; Jena, D.; Wasserman, D.; Hoffman, A. J. Localized Surface Phonon Polariton Resonances in Polar Gallium Nitride. *Appl. Phys. Lett.* **2015**, *107*, 081108.

(606) Breslin, V. M.; Ratchford, D. C.; Giles, A. J.; Dunkelberger, A. D.; Owrutsky, J. C. Hyperbolic Phonon Polariton Resonances in Calcite Nanopillars. *Opt. Express* **2021**, *29*, 11760−11772.

(607) Haas, J.; Mizaikoff, B. Advances in Mid-Infrared Spectroscopy for Chemical Analysis. *Annu. Rev. Anal. Chem.* **2016**, *9*, 45−68.

(608) Das, R. S.; Agrawal, Y. K. Raman Spectroscopy: Recent Advancements, Techniques and Applications. *Vib. Spectrosc.* **2011**, *57*, 163−176.

(609) Biagioni, P.; Huang, J.-S.; Hecht, B. Nanoantennas for Visible and Infrared Radiation. *Rep. Prog. Phys.* **2012**, *75*, 024402.

(610) Le Ru, E. C.; Etchegoin, P. G. *Principles of Surface-Enhanced Raman Spectroscopy*; Elsevier, 2009.

(611) Neubrech, F.; Pucci, A.; Cornelius, T. W.; Karim, S.; García-Etxarri, A.; Aizpurua, J. Resonant Plasmonic and Vibrational Coupling in a Tailored Nanoantenna for Infrared Detection. *Phys. Rev. Lett.* **2008**, *101*, 157403.

(612) Adato, R.; Yanik, A. A.; Amsden, J. J.; Kaplan, D. L.; Omenetto, F. G.; Hong, M. K.; Erramilli, S.; Altug, H. Ultra-Sensitive Vibrational Spectroscopy of Protein Monolayers with Plasmonic Nanoantenna Arrays. *Proc. Natl. Acad. Sci. U. S. A.* **2009**, *106*, 19227−19232.

(613) Chae, J.; Lahiri, B.; Centrone, A. Engineering Near-Field SEIRA Enhancements in Plasmonic Resonators. *ACS Photonics* **2016**, *3*, 87−95.

(614) Bagheri, S.; Weber, K.; Gissibl, T.; Weiss, T.; Neubrech, F.; Giessen, H. Fabrication of Square-Centimeter Plasmonic Nanoantenna Arrays by Femtosecond Direct Laser Writing Lithography: Effects of Collective Excitations on SEIRA Enhancement. *ACS Photonics* **2015**, *2*, 779−786.

(615) Chen, X.; Ciracì, C.; Smith, D. R.; Oh, S.-H. Nanogap-Enhanced Infrared Spectroscopy with Template-Stripped Wafer-Scale Arrays of Buried Plasmonic Cavities. *Nano Lett.* **2015**, *15*, 107−113.

(616) Garoli, D.; Calandrini, E.; Bozzola, A.; Ortolani, M.; Cattarin, S.; Barison, S.; Toma, A.; De Angelis, F. Boosting Infrared Energy Transfer in 3D Nanoporous Gold Antennas. *Nanoscale* **2017**, *9*, 915−922.

(617) Yoo, D.; Mohr, D. A.; Vidal-Codina, F.; John-Herpin, A.; Jo, M.; Kim, S.; Matson, J.; Caldwell, J. D.; Jeon, H.; Nguyen, N.-C.; et al. High-Contrast Infrared Absorption Spectroscopy via Mass-Produced Coaxial Zero-Mode Resonators with Sub-10 Nm Gaps. *Nano Lett.* **2018**, *18*, 1930−1936.

(618) Dregely, D.; Neubrech, F.; Duan, H.; Vogelgesang, R.; Giessen, H. Vibrational Near-Field Mapping of Planar and Buried Three-Dimensional Plasmonic Nanostructures. *Nat. Commun.* **2013**, *4*, 2237.

(619) Wang, H.-L.; You, E.-M.; Panneerselvam, R.; Ding, S.-Y.; Tian, Z.-Q. Advances of Surface-Enhanced Raman and IR Spectroscopies: From Nano/Microstructures to Macro-Optical Design. *Light Sci. Appl.* **2021**, *10*, 161.

(620) De Angelis, F.; Malerba, M.; Patrini, M.; Miele, E.; Das, G.; Toma, A.; Zaccaria, R. P.; Di Fabrizio, E. 3D Hollow Nanostructures as Building Blocks for Multifunctional Plasmonics. *Nano Lett.* **2013**, *13*, 3553−3558.

(621) Malerba, M.; Alabastri, A.; Miele, E.; Zilio, P.; Patrini, M.; Bajoni, D.; Messina, G. C.; Dipalo, M.; Toma, A.; Proietti Zaccaria, R.; et al. 3D Vertical Nanostructures for Enhanced Infrared Plasmonics. *Sci. Rep.* **2015**, *5*, 16436.

(622) Neuman, T.; Huck, C.; Vogt, J.; Neubrech, F.; Hillenbrand, R.; Aizpurua, J.; Pucci, A. Importance of Plasmonic Scattering for an Optimal Enhancement of Vibrational Absorption in SEIRA with Linear Metallic Antennas. *J. Phys. Chem. C* **2015**, *119*, 26652−26662.

(623) Naik, G. V.; Shalaev, V. M.; Boltasseva, A. Alternative Plasmonic Materials: Beyond Gold and Silver. *Adv. Mater.* **2013**, *25*, 3264−3294.

(624) Biagioni, P.; Frigerio, J.; Samarelli, A.; Gallacher, K.; Baldassarre, L.; Sakat, E.; Calandrini, E.; Millar, R. W.; Giliberti, V.; Isella, G.; et al. Group-IV Midinfrared Plasmonics. *J. Nanophotonics* **2015**, *9*, 093789.

(625) Baldassarre, L.; Sakat, E.; Frigerio, J.; Samarelli, A.; Gallacher, K.; Calandrini, E.; Isella, G.; Paul, D. J.; Ortolani, M.; Biagioni, P. Midinfrared Plasmon-Enhanced Spectroscopy with Germanium Antennas on Silicon Substrates. *Nano Lett.* **2015**, *15*, 7225−7231.

(626) Law, S.; Yu, L.; Rosenberg, A.; Wasserman, D. All-Semiconductor Plasmonic Nanoantennas for Infrared Sensing. *Nano Lett.* **2013**, *13*, 4569−4574.

(627) Rodrigo, D.; Limaj, O.; Janner, D.; Etezadi, D.; García de Abajo, F. J.; Pruneri, V.; Altug, H. Mid-Infrared Plasmonic Biosensing with Graphene. *Science* **2015**, *349*, 165−168.

(628) Autore, M.; Li, P.; Dolado, I.; Alfaro-Mozaz, F. J.; Esteban, R.; Atxabal, A.; Casanova, F.; Hueso, L. E.; Alonso-González, P.; Aizpurua, J.; et al. Boron Nitride Nanoresonators for Phonon-Enhanced Molecular Vibrational Spectroscopy at the Strong Coupling Limit. *Light Sci. Appl.* **2018**, *7*, 17172−17172.

(629) Folland, T. G.; Lu, G.; Bruncz, A.; Nolen, J. R.; Tadjer, M.; Caldwell, J. D. Vibrational Coupling to Epsilon-Near-Zero Waveguide Modes. *ACS Photonics* **2020**, *7*, 614−621.

(630) Barho, F. B.; Gonzalez-Posada, F.; Bomers, M.; Mezy, A.; Cerutti, L.; Taliercio, T. Surface-Enhanced Thermal Emission Spectroscopy with Perfect Absorber Metasurfaces. *ACS Photonics* **2019**, *6*, 1506−1514.

(631) Autore, M.; Dolado, I.; Li, P.; Esteban, R.; Alfaro-Mozaz, F. J.; Atxabal, A.; Liu, S.; Edgar, J. H.; Vélez, S.; Casanova, F.; et al. Enhanced Light-Matter Interaction in ¹⁰B Monoisotopic Boron Nitride Infrared Nanoresonators. *Adv. Opt. Mater.* **2021**, *9*, 2001958.

(632) Leitis, A.; Tittl, A.; Liu, M.; Lee, B. H.; Gu, M. B.; Kivshar, Y. S.; Altug, H. Angle-Multiplexed All-Dielectric Metasurfaces for Broadband Molecular Fingerprint Retrieval. *Sci. Adv.* **2019**, *5*, No. eaaw2871.

(633) Tseng, M. L.; Jahani, Y.; Leitis, A.; Altug, H. Dielectric Metasurfaces Enabling Advanced Optical Biosensors. *ACS Photonics* **2021**, *8*, 47−60.

(634) Leitis, A.; Tseng, M. L.; John-Herpin, A.; Kivshar, Y. S.; Altug, H. Wafer-Scale Functional Metasurfaces for Mid-Infrared Photonics and Biosensing. *Adv. Mater.* **2021**, *33*, 2102232.

(635) Bell, S. E. J.; Charron, G.; Cortés, E.; Kneipp, J.; Chapelle, M. L.; Langer, J.; Procházka, M.; Tran, V.; Schlücker, S. Towards Reliable and Quantitative Surface-Enhanced Raman Scattering (SERS): From Key Parameters to Good Analytical Practice. *Angew. Chem., Int. Ed.* **2020**, *59*, 5454−5462.

(636) Le Ru, E. C.; Etchegoin, P. G. Rigorous Justification of the |E|⁴ Enhancement Factor in Surface Enhanced Raman Spectroscopy. *Chem. Phys. Lett.* **2006**, *423*, 63−66.

(637) Wang, Y.; Zhao, C.; Wang, J.; Luo, X.; Xie, L.; Zhan, S.; Kim, J.; Wang, X.; Liu, X.; Ying, Y. Wearable Plasmonic-Metasurface Sensor for Noninvasive and Universal Molecular Fingerprint Detection on Biointerfaces. *Sci. Adv.* **2021**, *7*, No. eabe4553.

(638) Liu, X.; Wang, J.; Tang, L.; Xie, L.; Ying, Y. Flexible Plasmonic Metasurfaces with User-Designed Patterns for Molecular Sensing and Cryptography. *Adv. Funct. Mater.* **2016**, *26*, 5515−5523.

(639) García-Lojo, D.; Núñez-Sánchez, S.; Gómez-Graña, S.; Grzelczak, M.; Pastoriza-Santos, I.; Pérez-Juste, J.; Liz-Marzán, L. M. Plasmonic Supercrystals. *Acc. Chem. Res.* **2019**, *52*, 1855−1864.

(640) Mueller, N. S.; Pfitzner, E.; Okamura, Y.; Gordeev, G.; Kusch, P.; Lange, H.; Heberle, J.; Schulz, F.; Reich, S. Surface-Enhanced Raman Scattering and Surface-Enhanced Infrared Absorption by Plasmon Polaritons in Three-Dimensional Nanoparticle Supercrystals. *ACS Nano* **2021**, *15*, 5523−5533.

(641) Chu, Y.; Banaee, M. G.; Crozier, K. B. Double-Resonance Plasmon Substrates for Surface-Enhanced Raman Scattering with Enhancement at Excitation and Stokes Frequencies. *ACS Nano* **2010**, *4*, 2804−2810.

(642) Kumar, S.; Cherukulappurath, S.; Johnson, T. W.; Oh, S.-H. Millimeter-Sized Suspended Plasmonic Nanohole Arrays for Surface-Tension-Driven Flow-Through SERS. *Chem. Mater.* **2014**, *26*, 6523−6530.

(643) Sabathi, G.; Reyer, A.; Cefarin, N.; Sepperer, T.; Eckardt, J.; Neubauer, J.; Jan Wendisch, F.; D'Amico, F.; Vaccari, L.; Tondi, G.; et al. Tannin-Furanic Foams Used as Biomaterial Substrates for SERS Sensing in Possible Wastewater Filter Applications. *Mater. Res. Express* **2021**, *8*, 115404.

(644) Reyer, A.; Prinz, A.; Giancristofaro, S.; Schneider, J.; Bertoldo Menezes, D.; Zickler, G.; Bourret, G. R.; Musso, M. E. Investigation of Mass-Produced Substrates for Reproducible Surface-Enhanced Raman Scattering Measurements over Large Areas. *ACS Appl. Mater. Interfaces* **2017**, *9*, 25445−25454.

(645) Im, H.; Bantz, K. C.; Lee, S. H.; Johnson, T. W.; Haynes, C. L.; Oh, S.-H. Self-Assembled Plasmonic Nanoring Cavity Arrays for SERS and LSPR Biosensing. *Adv. Mater.* **2013**, *25*, 2678−2685.

(646) Jeong, J. W.; Arnob, M. M. P.; Baek, K.-M.; Lee, S. Y.; Shih, W.-C.; Jung, Y. S. 3D Cross-Point Plasmonic Nanoarchitectures Containing Dense and Regular Hot Spots for Surface-Enhanced Raman Spectroscopy Analysis. *Adv. Mater.* **2016**, *28*, 8695−8704.

(647) Wei, W.; Wang, Y.; Ji, J.; Zuo, S.; Li, W.; Bai, F.; Fan, H. Fabrication of Large-Area Arrays of Vertically Aligned Gold Nanorods. *Nano Lett.* **2018**, *18*, 4467−4472.

(648) Luo, S.; Mancini, A.; Berté, R.; Hoff, B. H.; Maier, S. A.; de Mello, J. C. Massively Parallel Arrays of Size-Controlled Metallic Nanogaps with Gap-Widths Down to the Sub-3-nm Level. *Adv. Mater.* **2021**, *33*, 2100491.

(649) Ayas, S.; Güner, H.; Türker, B.; Ekiz, O. Ö.; Dirisaglik, F.; Okyay, A. K.; Dâna, A. Raman Enhancement on a Broadband Meta-Surface. *ACS Nano* **2012**, *6*, 6852−6861.

(650) Zhang, N.; Liu, K.; Liu, Z.; Song, H.; Zeng, X.; Ji, D.; Cheney, A.; Jiang, S.; Gan, Q. Ultrabroadband Metasurface for Efficient Light Trapping and Localization: A Universal Surface-Enhanced Raman Spectroscopy Substrate for "All" Excitation Wavelengths. *Adv. Mater. Interfaces* **2015**, *2*, 1500142.

(651) Mao, P.; Liu, C.; Chen, Q.; Han, M.; Maier, S. A.; Zhang, S. Broadband SERS Detection with Disordered Plasmonic Hybrid Aggregates. *Nanoscale* **2020**, *12*, 93−102.

(652) Caldarola, M.; Albella, P.; Cortés, E.; Rahmani, M.; Roschuk, T.; Grinblat, G.; Oulton, R. F.; Bragas, A. V.; Maier, S. A. Non-Plasmonic Nanoantennas for Surface Enhanced Spectroscopies with Ultra-Low Heat Conversion. *Nat. Commun.* **2015**, *6*, 7915.

(653) Romano, S.; Zito, G.; Managò, S.; Calafiore, G.; Penzo, E.; Cabrini, S.; De Luca, A. C.; Mocella, V. Surface-Enhanced Raman and Fluorescence Spectroscopy with an All-Dielectric Metasurface. *J. Phys. Chem. C* **2018**, *122*, 19738−19745.

(654) Kenworthy, C. F.; Pjotr Stoevelaar, L.; Alexander, A. J.; Gerini, G. Using the Near Field Optical Trapping Effect of a Dielectric Metasurface to Improve SERS Enhancement for Virus Detection. *Sci. Rep.* **2021**, *11*, 6873.

(655) Jiang, C.; Moniz, S. J. A.; Wang, A.; Zhang, T.; Tang, J. Photoelectrochemical Devices for Solar Water Splitting - Materials and Challenges. *Chem. Soc. Rev.* **2017**, *46*, 4645−4660.

(656) van de Krol, R.; Grätzel, M. *Photoelectrochemical Hydrogen Production*; Springer US, 2012.

(657) Dale, M.; Benson, S. M. Energy Balance of the Global Photovoltaic (PV) Industry - Is the PV Industry a Net Electricity Producer? *Environ. Sci. Technol.* **2013**, *47*, 3482−3489.

(658) Delannoy, Y. Purification of Silicon for Photovoltaic Applications. *J. Cryst. Growth* **2012**, *360*, 61−67.

(659) Liu, C.; Dasgupta, N. P.; Yang, P. Semiconductor Nanowires for Artificial Photosynthesis. *Chem. Mater.* **2014**, *26*, 415−422.

(660) Rau, U.; Kirchartz, T. Charge Carrier Collection and Contact Selectivity in Solar Cells. *Adv. Mater. Interfaces* **2019**, *6*, 1900252.

(661) McEvoy, A. J.; Markvart, T.; Castañer, L. *Practical Handbook of Photovoltaics: Fundamentals and Applications*; Academic Press, 2012.

(662) deGraaf, G.; Wolffenbuttel, R. F. Illumination Source Identification Using a CMOS Optical Microsystem. *IEEE Trans. Instrum. Meas.* **2004**, *53*, 238−242.

(663) Nayak, P. K.; Mahesh, S.; Snaith, H. J.; Cahen, D. Photovoltaic Solar Cell Technologies: Analysing the State of the Art. *Nat. Rev. Mater.* **2019**, *4*, 269−285.

(664) Zhang, G.; Finefrock, S.; Liang, D.; Yadav, G. G.; Yang, H.; Fang, H.; Wu, Y. Semiconductor Nanostructure-Based Photovoltaic Solar Cells. *Nanoscale* **2011**, *3*, 2430−2443.

(665) Lin, Y.; Yuan, G.; Liu, R.; Zhou, S.; Sheehan, S. W.; Wang, D. Semiconductor Nanostructure-Based Photoelectrochemical Water Splitting: A Brief Review. *Chem. Phys. Lett.* **2011**, *507*, 209−215.

(666) Kamat, P. V.; Tvrdy, K.; Baker, D. R.; Radich, E. J. Beyond Photovoltaics: Semiconductor Nanoarchitectures for Liquid-Junction Solar Cells. *Chem. Rev.* **2010**, *110*, 6664−6688.

(667) Warren, S. C.; Voïtchovsky, K.; Dotan, H.; Leroy, C. M.; Cornuz, M.; Stellacci, F.; Hébert, C.; Rothschild, A.; Grätzel, M. Identifying Champion Nanostructures for Solar Water-Splitting. *Nat. Mater.* **2013**, *12*, 842−849.

(668) Sivula, K.; Le Formal, F.; Grätzel, M. Solar Water Splitting: Progress Using Hematite (α-Fe2O3) Photoelectrodes. *ChemSusChem* **2011**, *4*, 432−449.

(669) Bohren, C. F. How Can a Particle Absorb More Than the Light Incident on It? *Am. J. Phys.* **1983**, *51*, 323−327.

(670) Zhang, Y.; He, S.; Guo, W.; Hu, Y.; Huang, J.; Mulcahy, J. R.; Wei, W. D. Surface-Plasmon-Driven Hot Electron Photochemistry. *Chem. Rev.* **2018**, *118*, 2927−2954.

(671) Brongersma, M. L.; Halas, N. J.; Nordlander, P. Plasmon-Induced Hot Carrier Science and Technology. *Nat. Nanotechnol.* **2015**, *10*, 25−34.

(672) Camargo, P. H. C.; Cortés, E. *Plasmonic Catalysis: From Fundamentals to Applications*; Wiley-VCH, 2021.

(673) O'Regan, B.; Grätzel, M. A Low-Cost, High-Efficiency Solar Cell Based on Dye-Sensitized Colloidal TiO2 Films. *Nature* **1991**, *353*, 737−740.

(674) Gong, J.; Sumathy, K.; Qiao, Q.; Zhou, Z. Review on Dye-Sensitized Solar Cells (DSSCs): Advanced Techniques and Research Trends. *Renew. Sustain. Energy Rev.* **2017**, *68*, 234−246.

(675) Garnett, E.; Yang, P. Light Trapping in Silicon Nanowire Solar Cells. *Nano Lett.* **2010**, *10*, 1082−1087.

(676) Wendisch, F. J.; Abazari, M.; Mahdavi, H.; Rey, M.; Vogel, N.; Musso, M.; Diwald, O.; Bourret, G. R. Morphology-Graded Silicon Nanowire Arrays via Chemical Etching: Engineering Optical Properties at the Nanoscale and Macroscale. *ACS Appl. Mater. Interfaces* **2020**, *12*, 13140−13147.

(677) Wang, W.; Qi, L. Light Management with Patterned Micro- and Nanostructure Arrays for Photocatalysis, Photovoltaics, and Optoelectronic and Optical Devices. *Adv. Funct. Mater.* **2019**, *29*, 1807275.

(678) Oh, J.; Yuan, H.-C.; Branz, H. M. An 18.2%-Efficient Black-Silicon Solar Cell Achieved Through Control of Carrier Recombination in Nanostructures. *Nat. Nanotechnol.* **2012**, *7*, 743−748.

(679) Savin, H.; Repo, P.; von Gastrow, G.; Ortega, P.; Calle, E.; Garín, M.; Alcubilla, R. Black Silicon Solar Cells with Interdigitated Back-Contacts Achieve 22.1% Efficiency. *Nat. Nanotechnol.* **2015**, *10*, 624−628.

(680) He, J.; Zhou, Y.; Li, C.-Y.; Xiong, B.; Jing, H.; Peng, R.; Wang, M. Metasurface-Assisted Broadband Optical Absorption in Ultrathin Perovskite Films. *Opt. Express* **2021**, *29*, 19170−19182.

(681) Hodes, G.; Kamat, P. V. Understanding the Implication of Carrier Diffusion Length in Photovoltaic Cells. *J. Phys. Chem. Lett.* **2015**, *6*, 4090−4092.

(682) Dutta, A.; Naldoni, A.; Malara, F.; Govorov, A. O.; Shalaev, V. M.; Boltasseva, A. Gap-Plasmon Enhanced Water Splitting with Ultrathin Hematite Films: The Role of Plasmonic-Based Light Trapping and Hot Electrons. *Faraday Discuss.* **2019**, *214*, 283−295.

(683) Mayer, M. T.; Lin, Y.; Yuan, G.; Wang, D. Forming Heterojunctions at the Nanoscale for Improved Photoelectrochemical Water Splitting by Semiconductor Materials: Case Studies on Hematite. *Acc. Chem. Res.* **2013**, *46*, 1558−1566.

(684) Würfel, P.; Trupke, T.; Puzzer, T.; Schäffer, E.; Warta, W.; Glunz, S. W. Diffusion Lengths of Silicon Solar Cells from Luminescence Images. *J. Appl. Phys.* **2007**, *101*, 123110.

(685) Fuyuki, T.; Kondo, H.; Yamazaki, T.; Takahashi, Y.; Uraoka, Y. Photographic Surveying of Minority Carrier Diffusion Length in Polycrystalline Silicon Solar Cells by Electroluminescence. *Appl. Phys. Lett.* **2005**, *86*, 262108.

(686) Kirchartz, T.; Bisquert, J.; Mora-Sero, I.; Garcia-Belmonte, G. Classification of Solar Cells According to Mechanisms of Charge Separation and Charge Collection. *Phys. Chem. Chem. Phys.* **2015**, *17*, 4007−4014.

(687) Lipovšek, B.; Smole, F.; Topič, M.; Humar, I.; Sinigoj, A. R. Driving Forces and Charge-Carrier Separation in p-n Junction Solar Cells. *AIP Adv.* **2019**, *9*, 055026.

(688) Hara, K. O.; Usami, N. Theory of Open-Circuit Voltage and the Driving Force of Charge Separation in Pn-Junction Solar Cells. *J. Appl. Phys.* **2013**, *114*, 153101.

(689) Vijselaar, W.; Westerik, P.; Veerbeek, J.; Tiggelaar, R. M.; Berenschot, E.; Tas, N. R.; Gardeniers, H.; Huskens, J. Spatial Decoupling of Light Absorption and Catalytic Activity of Ni-Mo-Loaded High-Aspect-Ratio Silicon Microwire Photocathodes. *Nat. Energy* **2018**, *3*, 185−192.

(690) Kim, S. J.; Thomann, I.; Park, J.; Kang, J.-H.; Vasudev, A. P.; Brongersma, M. L. Light Trapping for Solar Fuel Generation with Mie Resonances. *Nano Lett.* **2014**, *14*, 1446−1452.

(691) Kim, T. W.; Choi, K.-S. Nanoporous BiVO$_4$ Photoanodes with Dual-Layer Oxygen Evolution Catalysts for Solar Water Splitting. *Science* **2014**, *343*, 990−994.

(692) He, J.; Yang, Z.; Liu, P.; Wu, S.; Gao, P.; Wang, M.; Zhou, S.; Li, X.; Cao, H.; Ye, J. Enhanced Electro-Optical Properties of Nanocone/Nanopillar Dual-Structured Arrays for Ultrathin Silicon/Organic Hybrid Solar Cell Applications. *Adv. Energy Mater.* **2016**, *6*, 1501793.

(693) Zhang, G.; Lan, C.; Bian, H.; Gao, R.; Zhou, J. Flexible, All-Dielectric Metasurface Fabricated via Nanosphere Lithography and Its Applications in Sensing. *Opt. Express* **2017**, *25*, 22038−22045.

(694) Walter, M. G.; Warren, E. L.; McKone, J. R.; Boettcher, S. W.; Mi, Q.; Santori, E. A.; Lewis, N. S. Solar Water Splitting Cells. *Chem. Rev.* **2010**, *110*, 6446−6473.

(695) Kerschaver, E. V.; Beaucarne, G. Back-Contact Solar Cells: A Review. *Prog. Photovolt. Res. Appl.* **2006**, *14*, 107−123.

(696) Ehrler, B.; Alarcón-Lladó, E.; Tabernig, S. W.; Veeken, T.; Garnett, E. C.; Polman, A. Photovoltaics Reaching for the Shockley-Queisser Limit. *ACS Energy Lett.* **2020**, *5*, 3029−3033.

(697) Shi, X.; Cai, L.; Ma, M.; Zheng, X.; Park, J. H. General Characterization Methods for Photoelectrochemical Cells for Solar Water Splitting. *ChemSusChem* **2015**, *8*, 3192−3203.

(698) Shockley, W.; Queisser, H. J. Detailed Balance Limit of Efficiency of P-n Junction Solar Cells. *J. Appl. Phys.* **1961**, *32*, 510−519.

(699) Nelson, C. A.; Monahan, N. R.; Zhu, X.-Y. Exceeding the Shockley-Queisser Limit in Solar Energy Conversion. *Energy Environ. Sci.* **2013**, *6*, 3508−3519.

(700) Rühle, S. Tabulated Values of the Shockley-Queisser Limit for Single Junction Solar Cells. *Sol. Energy* **2016**, *130*, 139−147.

(701) Fountaine, K. T.; Lewerenz, H. J.; Atwater, H. A. Efficiency Limits for Photoelectrochemical Water-Splitting. *Nat. Commun.* **2016**, *7*, 13706.

(702) Krogstrup, P.; Jørgensen, H. I.; Heiss, M.; Demichel, O.; Holm, J. V.; Aagesen, M.; Nygard, J.; Fontcuberta i Morral, A. Single-Nanowire Solar Cells Beyond the Shockley-Queisser Limit. *Nat. Photonics* **2013**, *7*, 306−310.

(703) Xu, Y.; Gong, T.; Munday, J. N. The Generalized Shockley-Queisser Limit for Nanostructured Solar Cells. *Sci. Rep.* **2015**, *5*, 13536.

(704) Rephaeli, E.; Fan, S. Absorber and Emitter for Solar Thermo-Photovoltaic Systems to Achieve Efficiency Exceeding the Shockley-Queisser Limit. *Opt. Express* **2009**, *17*, 15145.

(705) Brédas, J.-L.; Norton, J. E.; Cornil, J.; Coropceanu, V. Molecular Understanding of Organic Solar Cells: The Challenges. *Acc. Chem. Res.* **2009**, *42*, 1691−1699.

(706) Deibel, C.; Strobel, T.; Dyakonov, V. Role of the Charge Transfer State in Organic Donor-Acceptor Solar Cells. *Adv. Mater.* **2010**, *22*, 4097−4111.

(707) Steim, R.; Kogler, F. R.; Brabec, C. J. Interface Materials for Organic Solar Cells. *J. Mater. Chem.* **2010**, *20*, 2499−2512.

(708) Elshorbagy, M. H.; Sánchez, P. A.; Cuadrado, A.; Alda, J.; Esteban, Ó. Resonant Nano-Dimer Metasurface for Ultra-Thin a-Si:H Solar Cells. *Sci. Rep.* **2021**, *11*, 7179.

(709) Pala, R. A.; Butun, S.; Aydin, K.; Atwater, H. A. Omnidirectional and Broadband Absorption Enhancement from Trapezoidal Mie Resonators in Semiconductor Metasurfaces. *Sci. Rep.* **2016**, *6*, 31451.

(710) Odebo Länk, N.; Verre, R.; Johansson, P.; Käll, M. Large-Scale Silicon Nanophotonic Metasurfaces with Polarization Independent Near-Perfect Absorption. *Nano Lett.* **2017**, *17*, 3054−3060.

(711) Teperik, T. V.; García de Abajo, F. J.; Borisov, A. G.; Abdelsalam, M.; Bartlett, P. N.; Sugawara, Y.; Baumberg, J. J. Omnidirectional Absorption in Nanostructured Metal Surfaces. *Nat. Photonics* **2008**, *2*, 299−301.

(712) Pillai, S.; Catchpole, K. R.; Trupke, T.; Green, M. A. Surface Plasmon Enhanced Silicon Solar Cells. *J. Appl. Phys.* **2007**, *101*, 093105.

(713) Atwater, H. A.; Polman, A. Plasmonics for Improved Photovoltaic Devices. In *Materials for Sustainable Energy*; Co-Published with Macmillan Publishers Ltd, UK, 2010; pp 1−11.

(714) Ferry, V. E.; Sweatlock, L. A.; Pacifici, D.; Atwater, H. A. Plasmonic Nanostructure Design for Efficient Light Coupling into Solar Cells. *Nano Lett.* **2008**, *8*, 4391−4397.

(715) Aydin, K.; Ferry, V. E.; Briggs, R. M.; Atwater, H. A. Broadband Polarization-Independent Resonant Light Absorption Using Ultrathin Plasmonic Super Absorbers. *Nat. Commun.* **2011**, *2*, 517.

(716) Pala, R. A.; White, J.; Barnard, E.; Liu, J.; Brongersma, M. L. Design of Plasmonic Thin-Film Solar Cells with Broadband Absorption Enhancements. *Adv. Mater.* **2009**, *21*, 3504−3509.

(717) Wang, Y.; Sun, T.; Paudel, T.; Zhang, Y.; Ren, Z.; Kempa, K. Metamaterial-Plasmonic Absorber Structure for High Efficiency Amorphous Silicon Solar Cells. *Nano Lett.* **2012**, *12*, 440−445.

(718) Sinev, I. S.; Voroshilov, P. M.; Mukhin, I. S.; Denisyuk, A. I.; Guzhva, M. E.; Samusev, A. K.; Belov, P. A.; Simovski, C. R. Demonstration of Unusual Nanoantenna Array Modes Through Direct Reconstruction of the Near-Field Signal. *Nanoscale* **2015**, *7*, 765−770.

(719) Martin-Cano, D.; Nesterov, M. L.; Fernandez-Dominguez, A. I.; Garcia-Vidal, F. J.; Martin-Moreno, L.; Moreno, E. Domino Plasmons for Subwavelength Terahertz Circuitry. *Opt. Express* **2010**, *18*, 754−764.

(720) Simovski, C.; Morits, D.; Voroshilov, P.; Guzhva, M.; Belov, P.; Kivshar, Y. Enhanced Efficiency of Light-Trapping Nanoantenna Arrays for Thin-Film Solar Cells. *Opt. Express* **2013**, *21*, A714−A725.

(721) Voroshilov, P. M.; Ovchinnikov, V.; Papadimitratos, A.; Zakhidov, A. A.; Simovski, C. R. Light Trapping Enhancement by

Silver Nanoantennas in Organic Solar Cells. *ACS Photonics* **2018**, *5*, 1767−1772.

(722) Ou, Q.-D.; Xie, H.-J.; Chen, J.-D.; Zhou, L.; Li, Y.-Q.; Tang, J.-X. Enhanced Light Harvesting in Flexible Polymer Solar Cells: Synergistic Simulation of a Plasmonic Meta-Mirror and a Transparent Silver Mesowire Electrode. *J. Mater. Chem. A* **2016**, *4*, 18952−18962.

(723) Petoukhoff, C. E.; O'Carroll, D. M. Absorption-Induced Scattering and Surface Plasmon Out-Coupling from Absorber-Coated Plasmonic Metasurfaces. *Nat. Commun.* **2015**, *6*, 7899.

(724) Esfandyarpour, M.; Garnett, E. C.; Cui, Y.; McGehee, M. D.; Brongersma, M. L. Metamaterial Mirrors in Optoelectronic Devices. *Nat. Nanotechnol.* **2014**, *9*, 542−547.

(725) Pecora, E. F.; Cordaro, A.; Kik, P. G.; Brongersma, M. L. Broadband Antireflection Coatings Employing Multiresonant Dielectric Metasurfaces. *ACS Photonics* **2018**, *5*, 4456−4462.

(726) Shameli, M. A.; Yousefi, L. Absorption Enhancement in Thin-Film Solar Cells Using an Integrated Metasurface Lens. *J. Opt. Soc. Am. B* **2018**, *35*, 223−230.

(727) Chang, C.-C.; Kort-Kamp, W. J. M.; Nogan, J.; Luk, T. S.; Azad, A. K.; Taylor, A. J.; Dalvit, D. A. R.; Sykora, M.; Chen, H.-T. High-Temperature Refractory Metasurfaces for Solar Thermophotovoltaic Energy Harvesting. *Nano Lett.* **2018**, *18*, 7665−7673.

(728) Brongersma, M. L.; Cui, Y.; Fan, S. Light Management for Photovoltaics Using High-Index Nanostructures. *Nat. Mater.* **2014**, *13*, 451−460.

(729) Cai, J.; Qi, L. Recent Advances in Antireflective Surfaces Based on Nanostructure Arrays. *Mater. Horiz.* **2015**, *2*, 37−53.

(730) Dong, C.; Lu, H.; Yu, K.; Shen, K.-S.; Zhang, J.; Xia, S.-Q.; Xiong, Z.-G.; Liu, X.-Y.; Zhang, B.; Wang, Z.-J.; et al. Low Emissivity Double Sides Antireflection Coatings for Silicon Wafer at Infrared Region. *J. Alloys Compd.* **2018**, *742*, 729−735.

(731) Zhao, J.; Wang, A.; Altermatt, P.; Green, M. A. Twenty-Four Percent Efficient Silicon Solar Cells with Double Layer Antireflection Coatings and Reduced Resistance Loss. *Appl. Phys. Lett.* **1995**, *66*, 3636−3638.

(732) Park, J. Y.; Lee, I.; Ham, J.; Gim, S.; Lee, J.-L. Simple and Scalable Growth of AgCl Nanorods by Plasma-Assisted Strain Relaxation on Flexible Polymer Substrates. *Nat. Commun.* **2017**, *8*, 15650.

(733) Zhang, C.; Li, W.; Yu, D.; Wang, Y.; Yin, M.; Wang, H.; Song, Y.; Zhu, X.; Chang, P.; Chen, X.; et al. Wafer-Scale Highly Ordered Anodic Aluminum Oxide by Soft Nanoimprinting Lithography for Optoelectronics Light Management. *Adv. Mater. Interfaces* **2017**, *4*, 1601116.

(734) Benito, N.; Recio-Sánchez, G.; Escobar-Galindo, R.; Palacio, C. Formation of Antireflection Zn/ZnO Core-Shell Nano-Pyramidal Arrays by O_2^+ Ion Bombardment of Zn Surfaces. *Nanoscale* **2017**, *9*, 14201−14207.

(735) Huang, Y.-F.; Chattopadhyay, S.; Jen, Y.-J.; Peng, C.-Y.; Liu, T.-A.; Hsu, Y.-K.; Pan, C.-L.; Lo, H.-C.; Hsu, C.-H.; Chang, Y.-H.; et al. Improved Broadband and Quasi-Omnidirectional Anti-Reflection Properties with Biomimetic Silicon Nanostructures. *Nat. Nanotechnol.* **2007**, *2*, 770−774.

(736) van de Groep, J.; Spinelli, P.; Polman, A. Single-Step Soft-Imprinted Large-Area Nanopatterned Antireflection Coating. *Nano Lett.* **2015**, *15*, 4223−4228.

(737) Spinelli, P.; Verschuuren, M. A.; Polman, A. Broadband Omnidirectional Antireflection Coating Based on Subwavelength Surface Mie Resonators. *Nat. Commun.* **2012**, *3*, 692.

(738) Cordaro, A.; van de Groep, J.; Raza, S.; Pecora, E. F.; Priolo, F.; Brongersma, M. L. Antireflection High-Index Metasurfaces Combining Mie and Fabry-Pérot Resonances. *ACS Photonics* **2019**, *6*, 453−459.

(739) Khaidarov, E.; Hao, H.; Paniagua-Domínguez, R.; Yu, Y. F.; Fu, Y. H.; Valuckas, V.; Yap, S. L. K.; Toh, Y. T.; Ng, J. S. K.; Kuznetsov, A. I. Asymmetric Nanoantennas for Ultrahigh Angle Broadband Visible Light Bending. *Nano Lett.* **2017**, *17*, 6267−6272.

(740) Ra'di, Y.; Sounas, D. L.; Alù, A. Metagratings: Beyond the Limits of Graded Metasurfaces for Wave Front Control. *Phys. Rev. Lett.* **2017**, *119*, 067404.

(741) Røyset, A.; Kolås, T.; Jelle, B. P. Coloured Building Integrated Photovoltaics: Influence on Energy Efficiency. *Energy Build.* **2020**, *208*, 109623.

(742) Neder, V.; Luxembourg, S. L.; Polman, A. Efficient Colored Silicon Solar Modules Using Integrated Resonant Dielectric Nano-scatterers. *Appl. Phys. Lett.* **2017**, *111*, 073902.

(743) Uleman, F.; Neder, V.; Cordaro, A.; Alù, A.; Polman, A. Resonant Metagratings for Spectral and Angular Control of Light for Colored Rooftop Photovoltaics. *ACS Appl. Energy Mater.* **2020**, *3*, 3150−3156.

(744) Shameli, M. A.; Salami, P.; Yousefi, L. Light Trapping in Thin Film Solar Cells Using a Polarization Independent Phase Gradient Metasurface. *J. Opt.* **2018**, *20*, 125004.

(745) Andreev, V. M.; Grilikhes, V. A.; Khvostikov, V. P.; Khvostikova, O. A.; Rumyantsev, V. D.; Sadchikov, N. A.; Shvarts, M. Z. Concentrator PV Modules and Solar Cells for TPV Systems. *Sol. Energy Mater. Sol. Cells* **2004**, *84*, 3−17.

(746) Aieta, F.; Genevet, P.; Kats, M. A.; Yu, N.; Blanchard, R.; Gaburro, Z.; Capasso, F. Aberration-Free Ultrathin Flat Lenses and Axicons at Telecom Wavelengths Based on Plasmonic Metasurfaces. *Nano Lett.* **2012**, *12*, 4932−4936.

(747) Paniagua-Domínguez, R.; Yu, Y. F.; Khaidarov, E.; Choi, S.; Leong, V.; Bakker, R. M.; Liang, X.; Fu, Y. H.; Valuckas, V.; Krivitsky, L. A.; et al. A Metalens with a Near-Unity Numerical Aperture. *Nano Lett.* **2018**, *18*, 2124−2132.

(748) Yu, N.; Genevet, P.; Kats, M. A.; Aieta, F.; Tetienne, J.-P.; Capasso, F.; Gaburro, Z. Light Propagation with Phase Discontinuities: Generalized Laws of Reflection and Refraction. *Science* **2011**, *334*, 333−337.

(749) Lalanne, P.; Chavel, P. Metalenses at Visible Wavelengths: Past, Present, Perspectives. *Laser Photonics Rev.* **2017**, *11*, 1600295.

(750) Arinze, E. S.; Qiu, B.; Nyirjesy, G.; Thon, S. M. Plasmonic Nanoparticle Enhancement of Solution-Processed Solar Cells: Practical Limits and Opportunities. *ACS Photonics* **2016**, *3*, 158−173.

(751) Hossain, M. I.; Yumnam, N.; Qarony, W.; Salleo, A.; Wagner, V.; Knipp, D.; Tsang, Y. H. Non-Resonant Metal-Oxide Metasurfaces for Efficient Perovskite Solar Cells. *Sol. Energy* **2020**, *198*, 570−577.

(752) Wang, C.; Zhang, Z. Broadband Optical Absorption Enhancement in Hybrid Organic-Inorganic Perovskite Metasurfaces. *AIP Adv.* **2021**, *11*, 025107.

(753) Wang, Y.; Liu, H.; Zhu, J. Solar Thermophotovoltaics: Progress, Challenges, and Opportunities. *APL Mater.* **2019**, *7*, 080906.

(754) Lenert, A.; Bierman, D. M.; Nam, Y.; Chan, W. R.; Celanović, I.; Soljačić, M.; Wang, E. N. A Nanophotonic Solar Thermophotovoltaic Device. *Nat. Nanotechnol.* **2014**, *9*, 126−130.

(755) Bierman, D. M.; Lenert, A.; Chan, W. R.; Bhatia, B.; Celanović, I.; Soljačić, M.; Wang, E. N. Enhanced Photovoltaic Energy Conversion Using Thermally Based Spectral Shaping. *Nat. Energy* **2016**, *1*, 16068.

(756) Li, X.-F.; Chen, Y.-R.; Miao, J.; Zhou, P.; Zheng, Y.-X.; Chen, L.-Y.; Lee, Y.-P. High Solar Absorption of a Multilayered Thin Film Structure. *Opt. Express* **2007**, *15*, 1907−1912.

(757) Søndergaard, T.; Novikov, S. M.; Holmgaard, T.; Eriksen, R. L.; Beermann, J.; Han, Z.; Pedersen, K.; Bozhevolnyi, S. I. Plasmonic Black Gold by Adiabatic Nanofocusing and Absorption of Light in Ultra-Sharp Convex Grooves. *Nat. Commun.* **2012**, *3*, 969.

(758) Woolf, D. N.; Kadlec, E. A.; Bethke, D.; Grine, A. D.; Nogan, J. J.; Cederberg, J. G.; Bruce Burckel, D.; Luk, T. S.; Shaner, E. A.; Hensley, J. M. High-Efficiency Thermophotovoltaic Energy Conversion Enabled by a Metamaterial Selective Emitter. *Optica* **2018**, *5*, 213−218.

(759) Li, J.; Liu, B.; Shen, S. Tunable Narrow-Band Near-Field Thermal Emitters Based on Resonant Metamaterials. *Phys. Rev. B* **2017**, *96*, 075413.

(760) Shameli, M. A.; Fallah, A.; Yousefi, L. Developing an Optimized Metasurface for Light Trapping in Thin-Film Solar Cells Using a Deep Neural Network and a Genetic Algorithm. *J. Opt. Soc. Am. B* **2021**, *38*, 2728−2735.

(761) Nadell, C. C.; Huang, B.; Malof, J. M.; Padilla, W. J. Deep Learning for Accelerated All-Dielectric Metasurface Design. *Opt. Express* **2019**, *27*, 27523−27535.

(762) Yeung, C.; Tsai, J.-M.; King, B.; Kawagoe, Y.; Ho, D.; Knight, M. W.; Raman, A. P. Elucidating the Behavior of Nanophotonic Structures through Explainable Machine Learning Algorithms. *ACS Photonics* **2020**, *7*, 2309−2318.

(763) Chen, H.; Liu, H.; Zhang, Z.; Hu, K.; Fang, X. Nanostructured Photodetectors: From Ultraviolet to Terahertz. *Adv. Mater.* **2016**, *28*, 403−433.

(764) Konstantatos, G.; Howard, I.; Fischer, A.; Hoogland, S.; Clifford, J.; Klem, E.; Levina, L.; Sargent, E. H. Ultrasensitive Solution-Cast Quantum Dot Photodetectors. *Nature* **2006**, *442*, 180−183.

(765) García de Arquer, F. P.; Armin, A.; Meredith, P.; Sargent, E. H. Solution-Processed Semiconductors for Next-Generation Photodetectors. *Nat. Rev. Mater.* **2017**, *2*, 16100.

(766) Armin, A.; Hambsch, M.; Kim, I. K.; Burn, P. L.; Meredith, P.; Namdas, E. B. Thick Junction Broadband Organic Photodiodes: Thick Junction Broadband Organic Photodiodes with Extremely Low Dark Current. *Laser Photonics Rev.* **2014**, *8*, 924−932.

(767) Armin, A.; Jansen-van Vuuren, R. D.; Kopidakis, N.; Burn, P. L.; Meredith, P. Narrowband Light Detection via Internal Quantum Efficiency Manipulation of Organic Photodiodes. *Nat. Commun.* **2015**, *6*, 6343.

(768) Fang, Y.; Armin, A.; Meredith, P.; Huang, J. Accurate Characterization of Next-Generation Thin-Film Photodetectors. *Nat. Photonics* **2019**, *13*, 1−4.

(769) Quimby, R. S. *Photonics and Lasers: An Introduction*; John Wiley & Sons, Inc., 2006.

(770) Tian, W.; Liu, D.; Cao, F.; Li, L. Hybrid Nanostructures for Photodetectors. *Adv. Opt. Mater.* **2017**, *5*, 1600468.

(771) Andriotis, A. N.; Menon, M. Band Gap Engineering via Doping: A Predictive Approach. *J. Appl. Phys.* **2015**, *117*, 125708.

(772) Samsudin, E. M.; Abd Hamid, S. B. Effect of Band Gap Engineering in Anionic-Doped TiO$_2$ Photocatalyst. *Appl. Surf. Sci.* **2017**, *391*, 326−336.

(773) Moiz, M. A.; Mumtaz, A.; Salman, M.; Husain, S. W.; Baluch, A. H.; Ramzan, M. Band Gap Engineering of ZnO via Transition Metal Doping: An Ab Initio Study. *Chem. Phys. Lett.* **2021**, *781*, 138979.

(774) Woo, G.; Lee, D. H.; Heo, Y.; Kim, E.; On, S.; Kim, T.; Yoo, H. Energy-Band Engineering by Remote Doping of Self-Assembled Monolayers Leads to High-Performance IGZO/P-Si Heterostructure Photodetectors. *Adv. Mater.* **2022**, *34*, 2107364.

(775) Alidoust, N.; Toroker, M. C.; Keith, J. A.; Carter, E. A. Significant Reduction in NiO Band Gap Upon Formation of Li$_x$Ni$_{1-x}$O Alloys: Applications To Solar Energy Conversion. *ChemSusChem* **2014**, *7*, 195−201.

(776) Mares, J. W.; Boutwell, R. C.; Wei, M.; Scheurer, A.; Schoenfeld, W. V. Deep-Ultraviolet Photodetectors from Epitaxially Grown Ni$_x$Mg$_{1-x}$O. *Appl. Phys. Lett.* **2010**, *97*, 161113.

(777) Cicek, E.; McClintock, R.; Cho, C. Y.; Rahnema, B.; Razeghi, M. Al$_x$Ga$_{1-x}$ N-Based Back-Illuminated Solar-Blind Photodetectors with External Quantum Efficiency of 89%. *Appl. Phys. Lett.* **2013**, *103*, 191108.

(778) Zhou, W.; Umezawa, N. Band Gap Engineering of Bulk and Nanosheet SnO: An Insight into the Interlayer Sn-Sn Lone Pair Interactions. *Phys. Chem. Chem. Phys.* **2015**, *17*, 17816−17820.

(779) Tripathi, A.; Dixit, T.; Agrawal, J.; Singh, V. Bandgap Engineering in CuO Nanostructures: Dual-Band, Broadband, and UV-C Photodetectors. *Appl. Phys. Lett.* **2020**, *116*, 111102.

(780) Das Mahapatra, A.; Basak, D. Investigation on Sub-Band Gap Defects Aided UV to NIR Broad-Band Low-Intensity Photodetection by SnO$_2$ Thin Film. *Sens. Actuators Phys.* **2020**, *312*, 112168.

(781) Kim, S. H.; lee, J.; Cho, E.; Lee, J.; Yun, D.-J.; Lee, D.; Kim, Y.; Ro, T.; Heo, C.-J.; Lee, G. H.; et al. The Role of Defects in Organic Image Sensors for Green Photodiode. *Sci. Rep.* **2019**, *9*, 1745.

(782) Liu, Y.; Qiao, S.; Sun, H.; Liu, J.; Guo, L.; Yang, Z.; Fu, G.; Wang, S. Large-Area Heterojunction Photodetectors Based on Nanometer-Thick CH$_3$NH$_3$PbI$_3$ Films Modified with Poly(Methyl Methacrylate) Nanofilms. *ACS Appl. Nano Mater.* **2021**, *4*, 1682−1691.

(783) Li, C.; Wang, H.; Wang, F.; Li, T.; Xu, M.; Wang, H.; Wang, Z.; Zhan, X.; Hu, W.; Shen, L. Ultrafast and Broadband Photodetectors Based on a Perovskite/Organic Bulk Heterojunction for Large-Dynamic-Range Imaging. *Light Sci. Appl.* **2020**, *9*, 31.

(784) Flöry, N.; Ma, P.; Salamin, Y.; Emboras, A.; Taniguchi, T.; Watanabe, K.; Leuthold, J.; Novotny, L. Waveguide-Integrated van Der Waals Heterostructure Photodetector at Telecom Wavelengths with High Speed and High Responsivity. *Nat. Nanotechnol.* **2020**, *15*, 118−124.

(785) Dong, R.; Bi, C.; Dong, Q.; Guo, F.; Yuan, Y.; Fang, Y.; Xiao, Z.; Huang, J. An Ultraviolet-to-NIR Broad Spectral Nanocomposite Photodetector with Gain. *Adv. Opt. Mater.* **2014**, *2*, 549−554.

(786) Wang, J.-J.; Hu, J.-S.; Guo, Y.-G.; Wan, L.-J. Eco-Friendly Visible-Wavelength Photodetectors Based on Bandgap Engineerable Nanomaterials. *J. Mater. Chem.* **2011**, *21*, 17582−17589.

(787) Sharma, N.; Bar-David, J.; Mazurski, N.; Levy, U. Metasurfaces for Enhancing Light Absorption in Thermoelectric Photodetectors. *ACS Photonics* **2020**, *7*, 2468−2473.

(788) Kubo, W.; Kondo, M.; Miwa, K. Quantitative Analysis of the Plasmonic Photo-Thermoelectric Phenomenon. *J. Phys. Chem. C* **2019**, *123*, 21670−21675.

(789) Miwa, K.; Ebihara, H.; Fang, X.; Kubo, W. Photo-Thermo-electric Conversion of Plasmonic Nanohole Array. *Appl. Sci.* **2020**, *10*, 2681.

(790) Li, W.; Coppens, Z. J.; Besteiro, L. V.; Wang, W.; Govorov, A. O.; Valentine, J. Circularly Polarized Light Detection with Hot Electrons in Chiral Plasmonic Metamaterials. *Nat. Commun.* **2015**, *6*, 8379.

(791) Chai, M.; Wang, Y.; Chen, C.; Zhao, Z.; Jin, M.; He, T. Metamaterials-Based Photoelectric Conversion: From Microwave to Optical Range. *Laser Photonics Rev.* **2022**, *16*, 2100458.

(792) Liang, F.-X.; Wang, J.-Z.; Li, Z.-P.; Luo, L.-B. Near-Infrared-Light Photodetectors Based on One-Dimensional Inorganic Semi-conductor Nanostructures. *Adv. Opt. Mater.* **2017**, *5*, 1700081.

(793) Stiff-Roberts, A. D. Quantum-Dot Infrared Photodetectors. In *Comprehensive Semiconductor Science and Technology*; Elsevier, 2011; pp 452−485.

(794) Li, J.; Li, J.; Zhou, S.; Yi, F. Metasurface Photodetectors. *Micromachines* **2021**, *12*, 1584.

(795) Dhanabalan, S. C.; Ponraj, J. S.; Zhang, H.; Bao, Q. Present Perspectives of Broadband Photodetectors Based on Nanobelts, Nanoribbons, Nanosheets and the Emerging 2D Materials. *Nanoscale* **2016**, *8*, 6410−6434.

(796) Yao, J.; Yang, G. 2D Material Broadband Photodetectors. *Nanoscale* **2020**, *12*, 454−476.

(797) Dutta, A. K.; Islam, M. S. *Novel Broadband Photodetector for Optical Communication*; Dutta, A. K., Ohishi, Y., Dutta, N. K., Moerk, J., Eds.; Boston, MA, 2005; p 60140C.

(798) Koppens, F. H. L.; Mueller, T.; Avouris, Ph.; Ferrari, A. C.; Vitiello, M. S.; Polini, M. Photodetectors Based on Graphene, Other Two-Dimensional Materials and Hybrid Systems. *Nat. Nanotechnol.* **2014**, *9*, 780−793.

(799) Brenneis, A.; Gaudreau, L.; Seifert, M.; Karl, H.; Brandt, M. S.; Huebl, H.; Garrido, J. A.; Koppens, F. H. L.; Holleitner, A. W. Ultrafast Electronic Readout of Diamond Nitrogen-Vacancy Centres Coupled to Graphene. *Nat. Nanotechnol.* **2015**, *10*, 135−139.

(800) Shiue, R.-J.; Gao, Y.; Wang, Y.; Peng, C.; Robertson, A. D.; Efetov, D. K.; Assefa, S.; Koppens, F. H. L.; Hone, J.; Englund, D. High-Responsivity Graphene-Boron Nitride Photodetector and Autocorrelator in a Silicon Photonic Integrated Circuit. *Nano Lett.* **2015**, *15*, 7288−7293.

(801) Tielrooij, K. J.; Massicotte, M.; Piatkowski, L.; Woessner, A.; Ma, Q.; Jarillo-Herrero, P.; van Hulst, N. F.; Koppens, F. H. L. Hot-Carrier Photocurrent Effects at Graphene-Metal Interfaces. *J. Phys.: Condens. Matter* **2015**, *27*, 164207.

(802) Liu, Y.; Cheng, R.; Liao, L.; Zhou, H.; Bai, J.; Liu, G.; Liu, L.; Huang, Y.; Duan, X. Plasmon Resonance Enhanced Multicolour Photodetection by Graphene. *Nat. Commun.* **2011**, *2*, 579.

(803) Echtermeyer, T. J.; Britnell, L.; Jasnos, P. K.; Lombardo, A.; Gorbachev, R. V.; Grigorenko, A. N.; Geim, A. K.; Ferrari, A. C.; Novoselov, K. S. Strong Plasmonic Enhancement of Photovoltage in Graphene. *Nat. Commun.* **2011**, *2*, 458.

(804) Yao, Y.; Shankar, R.; Rauter, P.; Song, Y.; Kong, J.; Loncar, M.; Capasso, F. High-Responsivity Mid-Infrared Graphene Detectors with Antenna-Enhanced Photocarrier Generation and Collection. *Nano Lett.* **2014**, *14*, 3749−3754.

(805) Gottheim, S.; Zhang, H.; Govorov, A. O.; Halas, N. J. Fractal Nanoparticle Plasmonics: The Cayley Tree. *ACS Nano* **2015**, *9*, 3284−3292.

(806) Afshinmanesh, F.; Curto, A. G.; Milaninia, K. M.; van Hulst, N. F.; Brongersma, M. L. Transparent Metallic Fractal Electrodes for Semiconductor Devices. *Nano Lett.* **2014**, *14*, 5068−5074.

(807) Fang, J.; Wang, D.; DeVault, C. T.; Chung, T.-F.; Chen, Y. P.; Boltasseva, A.; Shalaev, V. M.; Kildishev, A. V. Enhanced Graphene Photodetector with Fractal Metasurface. *Nano Lett.* **2017**, *17*, 57−62.

(808) De Nicola, F.; Puthiya Purayil, N. S.; Miseikis, V.; Spirito, D.; Tomadin, A.; Coletti, C.; Polini, M.; Krahne, R.; Pellegrini, V. Graphene Plasmonic Fractal Metamaterials for Broadband Photodetectors. *Sci. Rep.* **2020**, *10*, 6882.

(809) Sobhani, A.; Knight, M. W.; Wang, Y.; Zheng, B.; King, N. S.; Brown, L. V.; Fang, Z.; Nordlander, P.; Halas, N. J. Narrowband Photodetection in the Near-Infrared with a Plasmon-Induced Hot Electron Device. *Nat. Commun.* **2013**, *4*, 1643.

(810) Li, L.; Wang, J.; Kang, L.; Liu, W.; Yu, L.; Zheng, B.; Brongersma, M. L.; Werner, D. H.; Lan, S.; Shi, Y.; et al. Monolithic Full-Stokes Near-Infrared Polarimetry with Chiral Plasmonic Metasurface Integrated Graphene-Silicon Photodetector. *ACS Nano* **2020**, *14*, 16634−16642.

(811) Goykhman, I.; Sassi, U.; Desiatov, B.; Mazurski, N.; Milana, S.; de Fazio, D.; Eiden, A.; Khurgin, J.; Shappir, J.; Levy, U.; et al. On-Chip Integrated, Silicon-Graphene Plasmonic Schottky Photodetector with High Responsivity and Avalanche Photogain. *Nano Lett.* **2016**, *16*, 3005−3013.

(812) Knight, M. W.; Sobhani, H.; Nordlander, P.; Halas, N. J. Photodetection with Active Optical Antennas. *Science* **2011**, *332*, 702−704.

(813) Knight, M. W.; Wang, Y.; Urban, A. S.; Sobhani, A.; Zheng, B. Y.; Nordlander, P.; Halas, N. J. Embedding Plasmonic Nanostructure Diodes Enhances Hot Electron Emission. *Nano Lett.* **2013**, *13*, 1687−1692.

(814) Chalabi, H.; Schoen, D.; Brongersma, M. L. Hot-Electron Photodetection with a Plasmonic Nanostripe Antenna. *Nano Lett.* **2014**, *14*, 1374−1380.

(815) Li, W.; Valentine, J. Metamaterial Perfect Absorber Based Hot Electron Photodetection. *Nano Lett.* **2014**, *14*, 3510−3514.

(816) Wang, W.; Besteiro, L. V.; Yu, P.; Lin, F.; Govorov, A. O.; Xu, H.; Wang, Z. Plasmonic Hot-Electron Photodetection with Quasi-Bound States in the Continuum and Guided Resonances. *Nanophotonics* **2021**, *10*, 1911−1921.

(817) Togan, E.; Chu, Y.; Trifonov, A. S.; Jiang, L.; Maze, J.; Childress, L.; Dutt, M. V. G.; Sørensen, A. S.; Hemmer, P. R.; Zibrov, A. S.; et al. Quantum Entanglement Between an Optical Photon and a Solid-State Spin Qubit. *Nature* **2010**, *466*, 730−734.

(818) Farshchi, R.; Ramsteiner, M.; Herfort, J.; Tahraoui, A.; Grahn, H. T. Optical Communication of Spin Information Between Light Emitting Diodes. *Appl. Phys. Lett.* **2011**, *98*, 162508.

(819) Stanciu, C. D.; Hansteen, F.; Kimel, A. V.; Kirilyuk, A.; Tsukamoto, A.; Itoh, A.; Rasing, Th. All-Optical Magnetic Recording with Circularly Polarized Light. *Phys. Rev. Lett.* **2007**, *99*, 047601.

(820) Chen, C.; Gao, L.; Gao, W.; Ge, C.; Du, X.; Li, Z.; Yang, Y.; Niu, G.; Tang, J. Circularly Polarized Light Detection Using Chiral Hybrid Perovskite. *Nat. Commun.* **2019**, *10*, 1927.

(821) Wang, L.; Xue, Y.; Cui, M.; Huang, Y.; Xu, H.; Qin, C.; Yang, J.; Dai, H.; Yuan, M. A Chiral Reduced-Dimension Perovskite for an Efficient Flexible Circularly Polarized Light Photodetector. *Angew. Chem., Int. Ed.* **2020**, *59*, 6442−6450.

(822) Afshinmanesh, F.; White, J. S.; Cai, W.; Brongersma, M. L. Measurement of the Polarization State of Light Using an Integrated Plasmonic Polarimeter. *Nanophotonics* **2012**, *1*, 125−129.

(823) Zhao, Y.; Belkin, M. A.; Alù, A. Twisted Optical Metamaterials for Planarized Ultrathin Broadband Circular Polarizers. *Nat. Commun.* **2012**, *3*, 870.

(824) Ding, F.; Pors, A.; Chen, Y.; Zenin, V. A.; Bozhevolnyi, S. I. Beam-Size-Invariant Spectropolarimeters Using Gap-Plasmon Metasurfaces. *ACS Photonics* **2017**, *4*, 943−949.

(825) Shi, X.; Xiao, W.; Fan, Q.; Zhou, T.; Song, W.; Zhang, C.; Zeng, Y.; Peng, W. Circularly Polarized Light Photodetector Based on X-Shaped Chiral Metamaterial. *IEEE Sens. J.* **2018**, *18*, 9203−9206.

(826) Cotton, D. V.; Bailey, J.; Howarth, I. D.; Bott, K.; Kedziora-Chudczer, L.; Lucas, P. W.; Hough, J. H. Polarization Due to Rotational Distortion in the Bright Star Regulus. *Nat. Astron.* **2017**, *1*, 690−696.

(827) Tyo, J. S.; Goldstein, D. L.; Chenault, D. B.; Shaw, J. A. Review of Passive Imaging Polarimetry for Remote Sensing Applications. *Appl. Opt.* **2006**, *45*, 5453−5469.

(828) Tata, A.; Gribble, A.; Ventura, M.; Ganguly, M.; Bluemke, E.; Ginsberg, H. J.; Jaffray, D. A.; Ifa, D. R.; Vitkin, A.; Zarrine-Afsar, A. Wide-Field Tissue Polarimetry Allows Efficient Localized Mass Spectrometry Imaging of Biological Tissues. *Chem. Sci.* **2016**, *7*, 2162−2169.

(829) Chen, Z.; Weng, Y.; Liu, J.; Guo, N.; Yu, Y.; Xiao, L. Dual-Band Perfect Absorber for a Mid-Infrared Photodetector Based on a Dielectric Metal Metasurface. *Photonics Res.* **2021**, *9*, 27−33.

(830) Mitrofanov, O.; Hale, L. L.; Vabishchevich, P. P.; Luk, T. S.; Addamane, S. J.; Reno, J. L.; Brener, I. Perfectly Absorbing Dielectric Metasurfaces for Photodetection. *APL Photonics* **2020**, *5*, 101304.

(831) Wei, S.; Yang, Z.; Zhao, M. Design of Ultracompact Polarimeters Based on Dielectric Metasurfaces. *Opt. Lett.* **2017**, *42*, 1580−1583.

(832) Liu, T.; Xu, R.; Yu, P.; Wang, Z.; Takahara, J. Multipole and Multimode Engineering in Mie Resonance-Based Metastructures. *Nanophotonics* **2020**, *9*, 1115−1137.

(833) Walter, M. G.; Warren, E. L.; McKone, J. R.; Boettcher, S. W.; Mi, Q.; Santori, E. A.; Lewis, N. S. Solar Water Splitting Cells. *Chem. Rev.* **2010**, *110*, 6446−6473.

(834) Serpone, N.; Emeline, A. V.; Ryabchuk, V. K.; Kuznetsov, V. N.; Artem'ev, Y. M.; Horikoshi, S. Why Do Hydrogen and Oxygen Yields from Semiconductor-Based Photocatalyzed Water Splitting Remain Disappointingly Low? Intrinsic and Extrinsic Factors Impacting Surface Redox Reactions. *ACS Energy Lett.* **2016**, *1*, 931−948.

(835) Kudo, A.; Miseki, Y. Heterogeneous Photocatalyst Materials for Water Splitting. *Chem. Soc. Rev.* **2009**, *38*, 253−278.

(836) Nitopi, S.; Bertheussen, E.; Scott, S. B.; Liu, X.; Engstfeld, A. K.; Horch, S.; Seger, B.; Stephens, I. E. L.; Chan, K.; Hahn, C.; et al. Progress and Perspectives of Electrochemical CO_2 Reduction on Copper in Aqueous Electrolyte. *Chem. Rev.* **2019**, *119*, 7610−7672.

(837) Ulmer, U.; Dingle, T.; Duchesne, P. N.; Morris, R. H.; Tavasoli, A.; Wood, T.; Ozin, G. A. Fundamentals and Applications of Photocatalytic CO_2 Methanation. *Nat. Commun.* **2019**, *10*, 3169.

(838) Hirakawa, H.; Hashimoto, M.; Shiraishi, Y.; Hirai, T. Photocatalytic Conversion of Nitrogen to Ammonia with Water on Surface Oxygen Vacancies of Titanium Dioxide. *J. Am. Chem. Soc.* **2017**, *139*, 10929−10936.

(839) Chen, X.; Li, N.; Kong, Z.; Ong, W.-J.; Zhao, X. Photocatalytic Fixation of Nitrogen to Ammonia: State-of-the-Art Advancements and Future Prospects. *Mater. Horiz.* **2018**, *5*, 9−27.

(840) Wang, Y.; Suzuki, H.; Xie, J.; Tomita, O.; Martin, D. J.; Higashi, M.; Kong, D.; Abe, R.; Tang, J. Mimicking Natural Photosynthesis: Solar to Renewable H_2 Fuel Synthesis by Z-Scheme Water Splitting Systems. *Chem. Rev.* **2018**, *118*, 5201−5241.

(841) Wang, S.; Lu, A.; Zhong, C.-J. Hydrogen Production from Water Electrolysis: Role of Catalysts. *Nano Converg.* **2021**, *8*, 4.

(842) Zhao, Z.; Wang, Z.; Bao, J. Nanomaterials for Hydrogen Generation from Solar Water Splitting. In *Nanomaterials for Sustainable*

Energy; Li, Q., Ed.; NanoScience and Technology; Springer International Publishing: Cham, 2016; pp 445−470.

(843) Li, X.; Yu, J.; Low, J.; Fang, Y.; Xiao, J.; Chen, X. Engineering Heterogeneous Semiconductors for Solar Water Splitting. *J. Mater. Chem. A* **2015**, *3*, 2485−2534.

(844) Tamirat, A. G.; Rick, J.; Dubale, A. A.; Su, W.-N.; Hwang, B.-J. Using Hematite for Photoelectrochemical Water Splitting: A Review of Current Progress and Challenges. *Nanoscale Horiz.* **2016**, *1*, 243−267.

(845) Lu, Q.; Yu, Y.; Ma, Q.; Chen, B.; Zhang, H. 2D Transition-Metal-Dichalcogenide-Nanosheet-Based Composites for Photocatalytic and Electrocatalytic Hydrogen Evolution Reactions. *Adv. Mater.* **2016**, *28*, 1917−1933.

(846) Wang, G.; Ling, Y.; Wang, H.; Xihong, L.; Li, Y. Chemically Modified Nanostructures for Photoelectrochemical Water Splitting. *J. Photochem. Photobiol. C Photochem. Rev.* **2014**, *19*, 35−51.

(847) Licht, S.; Wang, B.; Mukerji, S.; Soga, T.; Umeno, M.; Tributsch, H. Efficient Solar Water Splitting, Exemplified by RuO$_2$ -Catalyzed AlGaAs/Si Photoelectrolysis. *J. Phys. Chem. B* **2000**, *104*, 8920−8924.

(848) May, M. M.; Lewerenz, H.-J.; Lackner, D.; Dimroth, F.; Hannappel, T. Efficient Direct Solar-to-Hydrogen Conversion by In Situ Interface Transformation of a Tandem Structure. *Nat. Commun.* **2015**, *6*, 8286.

(849) Raj, I. A. Nickel-Based, Binary-Composite Electrocatalysts for the Cathodes in the Energy-Efficient Industrial Production of Hydrogen from Alkaline-Water Electrolytic Cells. *J. Mater. Sci.* **1993**, *28*, 4375−4382.

(850) Hou, J.; Sun, Y.; Li, Z.; Zhang, B.; Cao, S.; Wu, Y.; Gao, Z.; Sun, L. Electrical Behavior and Electron Transfer Modulation of Nickel-Copper Nanoalloys Confined in Nickel-Copper Nitrides Nanowires Array Encapsulated in Nitrogen-Doped Carbon Framework as Robust Bifunctional Electrocatalyst for Overall Water Splitting. *Adv. Funct. Mater.* **2018**, *28*, 1803278.

(851) Vijselaar, W.; Tiggelaar, R. M.; Gardeniers, H.; Huskens, J. Efficient and Stable Silicon Microwire Photocathodes with a Nickel Silicide Interlayer for Operation in Strongly Alkaline Solutions. *ACS Energy Lett.* **2018**, *3*, 1086−1092.

(852) Zhang, F.-Q.; Hu, Y.; Meng, X.-M.; Peng, K.-Q. Fabrication and Photoelectrochemical Properties of Silicon/Nickel Oxide Core/Shell Nanowire Arrays. *RSC Adv.* **2015**, *5*, 88209−88213.

(853) Gerken, J. B.; McAlpin, J. G.; Chen, J. Y. C.; Rigsby, M. L.; Casey, W. H.; Britt, R. D.; Stahl, S. S. Electrochemical Water Oxidation with Cobalt-Based Electrocatalysts from PH 0−14: The Thermodynamic Basis for Catalyst Structure, Stability, and Activity. *J. Am. Chem. Soc.* **2011**, *133*, 14431−14442.

(854) Dogutan, D. K.; McGuire, R.; Nocera, D. G. Electocatalytic Water Oxidation by Cobalt(III) Hangman β-Octafluoro Corroles. *J. Am. Chem. Soc.* **2011**, *133*, 9178−9180.

(855) Han, L.; Abdi, F. F.; van de Krol, R.; Liu, R.; Huang, Z.; Lewerenz, H.-J.; Dam, B.; Zeman, M.; Smets, A. H. M. Efficient Water-Splitting Device Based on a Bismuth Vanadate Photoanode and Thin-Film Silicon Solar Cells. *ChemSusChem* **2014**, *7*, 2832−2838.

(856) Milbrat, A.; Elbersen, R.; Kas, R.; Tiggelaar, R. M.; Gardeniers, H.; Mul, G.; Huskens, J. Spatioselective Electrochemical and Photoelectrochemical Functionalization of Silicon Microwires with Axial p/n Junctions. *Adv. Mater.* **2016**, *28*, 1400−1405.

(857) Liu, C.; Tang, J.; Chen, H. M.; Liu, B.; Yang, P. A Fully Integrated Nanosystem of Semiconductor Nanowires for Direct Solar Water Splitting. *Nano Lett.* **2013**, *13*, 2989−2992.

(858) Alnoush, W.; Black, R.; Higgins, D. Judicious Selection, Validation, and Use of Reference Electrodes for In Situ and Operando Electrocatalysis Studies. *Chem. Catal.* **2021**, *1*, 997−1013.

(859) Benck, J. D.; Pinaud, B. A.; Gorlin, Y.; Jaramillo, T. F. Substrate Selection for Fundamental Studies of Electrocatalysts and Photoelectrodes: Inert Potential Windows in Acidic, Neutral, and Basic Electrolyte. *PLoS One* **2014**, *9*, No. e107942.

(860) Rao, P. M.; Cai, L.; Liu, C.; Cho, I. S.; Lee, C. H.; Weisse, J. M.; Yang, P.; Zheng, X. Simultaneously Efficient Light Absorption and Charge Separation in WO$_3$/BiVO$_4$ Core/Shell Nanowire Photoanode

for Photoelectrochemical Water Oxidation. *Nano Lett.* **2014**, *14*, 1099−1105.

(861) Ager, J. W.; Shaner, M. R.; Walczak, K. A.; Sharp, I. D.; Ardo, S. Experimental Demonstrations of Spontaneous, Solar-Driven Photoelectrochemical Water Splitting. *Energy Environ. Sci.* **2015**, *8*, 2811−2824.

(862) Mayer, M. T.; Du, C.; Wang, D. Hematite/Si Nanowire Dual-Absorber System for Photoelectrochemical Water Splitting at Low Applied Potentials. *J. Am. Chem. Soc.* **2012**, *134*, 12406−12409.

(863) Xu, R.; Wen, L.; Wang, Z.; Zhao, H.; Mu, G.; Zeng, Z.; Zhou, M.; Bohm, S.; Zhang, H.; Wu, Y.; et al. Programmable Multiple Plasmonic Resonances of Nanoparticle Superlattice for Enhancing Photoelectrochemical Activity. *Adv. Funct. Mater.* **2020**, *30*, 2005170.

(864) Xu, R.; Wen, L.; Wang, Z.; Zhao, H.; Xu, S.; Mi, Y.; Xu, Y.; Sommerfeld, M.; Fang, Y.; Lei, Y. Three-Dimensional Plasmonic Nanostructure Design for Boosting Photoelectrochemical Activity. *ACS Nano* **2017**, *11*, 7382−7389.

(865) Yu, M.-J.; Chang, C.-L.; Lan, H.-Y.; Chiao, Z.-Y.; Chen, Y.-C.; Howard Lee, H. W.; Chang, Y.-C.; Chang, S.-W.; Tanaka, T.; Tung, V.; et al. Plasmon-Enhanced Solar-Driven Hydrogen Evolution Using Titanium Nitride Metasurface Broadband Absorbers. *ACS Photonics* **2021**, *8*, 3125−3132.

(866) Shi, X.; Ueno, K.; Oshikiri, T.; Sun, Q.; Sasaki, K.; Misawa, H. Enhanced Water Splitting Under Modal Strong Coupling Conditions. *Nat. Nanotechnol.* **2018**, *13*, 953−958.

(867) Bosomtwi, D.; Osiński, M.; Babicheva, V. E. Lattice Effect for Enhanced Hot-Electron Generation in Nanoelectrodes. *Opt. Mater. Express* **2021**, *11*, 3232−3244.

(868) Aslam, U.; Chavez, S.; Linic, S. Controlling Energy Flow in Multimetallic Nanostructures for Plasmonic Catalysis. *Nat. Nanotechnol.* **2017**, *12*, 1000−1005.

(869) Gao, H.; Liu, C.; Jeong, H. E.; Yang, P. Plasmon-Enhanced Photocatalytic Activity of Iron Oxide on Gold Nanopillars. *ACS Nano* **2012**, *6*, 234−240.

(870) Li, J.; Cushing, S. K.; Zheng, P.; Meng, F.; Chu, D.; Wu, N. Plasmon-Induced Photonic and Energy-Transfer Enhancement of Solar Water Splitting by a Hematite Nanorod Array. *Nat. Commun.* **2013**, *4*, 2651.

(871) Knight, M. W.; King, N. S.; Liu, L.; Everitt, H. O.; Nordlander, P.; Halas, N. J. Aluminum for Plasmonics. *ACS Nano* **2014**, *8*, 834−840.

(872) Biggins, J. S.; Yazdi, S.; Ringe, E. Magnesium Nanoparticle Plasmonics. *Nano Lett.* **2018**, *18*, 3752−3758.

(873) Yang, Z.-J.; Jiang, R.; Zhuo, X.; Xie, Y.-M.; Wang, J.; Lin, H.-Q. Dielectric Nanoresonators for Light Manipulation. *Phys. Rep.* **2017**, *701*, 1−50.

(874) Baranov, D. G.; Zuev, D. A.; Lepeshov, S. I.; Kotov, O. V.; Krasnok, A. E.; Evlyukhin, A. B.; Chichkov, B. N. All-Dielectric Nanophotonics: The Quest for Better Materials and Fabrication Techniques. *Optica* **2017**, *4*, 814−825.

(875) Ng, K. C.; Udagedara, I. B.; Rukhlenko, I. D.; Chen, Y.; Tang, Y.; Premaratne, M.; Cheng, W. Free-Standing Plasmonic-Nanorod Superlattice Sheets. *ACS Nano* **2012**, *6*, 925−934.

(876) Guler, U.; Boltasseva, A.; Shalaev, V. M. Refractory Plasmonics. *Science* **2014**, *344*, 263−264.

(877) Gui, L.; Bagheri, S.; Strohfeldt, N.; Hentschel, M.; Zgrabik, C. M.; Metzger, B.; Linnenbank, H.; Hu, E. L.; Giessen, H. Nonlinear Refractory Plasmonics with Titanium Nitride Nanoantennas. *Nano Lett.* **2016**, *16*, 5708−5713.

(878) Lu, Y.-J.; Shen, T. L.; Peng, K.-N.; Cheng, P.-J.; Chang, S.-W.; Lu, M.-Y.; Chu, C. W.; Guo, T.-F.; Atwater, H. A. Upconversion Plasmonic Lasing from an Organolead Trihalide Perovskite Nanocrystal with Low Threshold. *ACS Photonics* **2021**, *8*, 335−342.

(879) Lu, Y.-J.; Sokhoyan, R.; Cheng, W.-H.; Kafaie Shirmanesh, G.; Davoyan, A. R.; Pala, R. A.; Thyagarajan, K.; Atwater, H. A. Dynamically Controlled Purcell Enhancement of Visible Spontaneous Emission in a Gated Plasmonic Heterostructure. *Nat. Commun.* **2017**, *8*, 1631.

(880) Patsalas, P.; Kalfagiannis, N.; Kassavetis, S. Optical Properties and Plasmonic Performance of Titanium Nitride. *Materials* 2015, 8, 3128−3154.

(881) Ishii, S.; Shinde, S. L.; Jevasuwan, W.; Fukata, N.; Nagao, T. Hot Electron Excitation from Titanium Nitride Using Visible Light. *ACS Photonics* 2016, 3, 1552−1557.

(882) Gargiulo, J.; Berté, R.; Li, Y.; Maier, S. A.; Cortés, E. From Optical to Chemical Hot Spots in Plasmonics. *Acc. Chem. Res.* 2019, 52, 2525−2535.

(883) Ng, C.; Cadusch, J. J.; Dligatch, S.; Roberts, A.; Davis, T. J.; Mulvaney, P.; Gómez, D. E. Hot Carrier Extraction with Plasmonic Broadband Absorbers. *ACS Nano* 2016, 10, 4704−4711.

(884) Lu, Y.; Dong, W.; Chen, Z.; Pors, A.; Wang, Z.; Bozhevolnyi, S. I. Gap-Plasmon Based Broadband Absorbers for Enhanced Hot-Electron and Photocurrent Generation. *Sci. Rep.* 2016, 6, 30650.

(885) Baumberg, J. J.; Aizpurua, J.; Mikkelsen, M. H.; Smith, D. R. Extreme Nanophotonics from Ultrathin Metallic Gaps. *Nat. Mater.* 2019, 18, 668−678.

(886) Lee, S.; Hwang, H.; Lee, W.; Schebarchov, D.; Wy, Y.; Grand, J.; Auguié, B.; Wi, D. H.; Cortés, E.; Han, S. W. Core-Shell Bimetallic Nanoparticle Trimers for Efficient Light-to-Chemical Energy Conversion. *ACS Energy Lett.* 2020, 5, 3881−3890.

(887) Xiao, Q.; Kinnear, C.; Connell, T. U.; Kashif, M. K.; Easton, C. D.; Seeber, A.; Bourgeois, L.; Bonin, G. O.; Duffy, N. W.; Chesman, A. S. R.; et al. Dual Photolytic Pathways in an Alloyed Plasmonic Near-Perfect Absorber: Implications for Photoelectrocatalysis. *ACS Appl. Nano Mater.* 2021, 4, 2702−2712.

(888) Liu, Z.; Liu, X.; Huang, S.; Pan, P.; Chen, J.; Liu, G.; Gu, G. Automatically Acquired Broadband Plasmonic-Metamaterial Black Absorber during the Metallic Film-Formation. *ACS Appl. Mater. Interfaces* 2015, 7, 4962−4968.

(889) Zeng, P.; Cadusch, J.; Chakraborty, D.; Smith, T. A.; Roberts, A.; Sader, J. E.; Davis, T. J.; Gómez, D. E. Photoinduced Electron Transfer in the Strong Coupling Regime: Waveguide-Plasmon Polaritons. *Nano Lett.* 2016, 16, 2651−2656.

(890) Oksenberg, E.; Shlesinger, I.; Xomalis, A.; Baldi, A.; Baumberg, J. J.; Koenderink, A. F.; Garnett, E. C. Energy-Resolved Plasmonic Chemistry in Individual Nanoreactors. *Nat. Nanotechnol.* 2021, 16, 1378−1385.

(891) Xiao, Q.; Connell, T. U.; Cadusch, J. J.; Roberts, A.; Chesman, A. S. R.; Gómez, D. E. Hot-Carrier Organic Synthesis via the Near-Perfect Absorption of Light. *ACS Catal.* 2018, 8, 10331−10339.

(892) Reeves, J. T.; Visco, M. D.; Marsini, M. A.; Grinberg, N.; Busacca, C. A.; Mattson, A. E.; Senanayake, C. H. A General Method for Imine Formation Using B(OCH₂CF₃)₃. *Org. Lett.* 2015, 17, 2442−2445.

(893) Kobayashi, S.; Mori, Y.; Fossey, J. S.; Salter, M. M. Catalytic Enantioselective Formation of C-C Bonds by Addition to Imines and Hydrazones: A Ten-Year Update. *Chem. Rev.* 2011, 111, 2626−2704.

(894) Direct Asymmetric Photochemistry with Circularly Polarized Light. In *Chiral Photochemistry*; Inoue, Y., Ramamurthy, V., Eds.; CRC Press, 2004; pp 13−56.

(895) Wu, W.; Pauly, M. Chiral Plasmonic Nanostructures: Recent Advances in Their Synthesis and Applications. *Mater. Adv.* 2022, 3, 186−215.

(896) Fang, Y.; Verre, R.; Shao, L.; Nordlander, P.; Käll, M. Hot Electron Generation and Cathodoluminescence Nanoscopy of Chiral Split Ring Resonators. *Nano Lett.* 2016, 16, 5183−5190.

(897) Wang, W.; Besteiro, L. V.; Liu, T.; Wu, C.; Sun, J.; Yu, P.; Chang, L.; Wang, Z.; Govorov, A. O. Generation of Hot Electrons with Chiral Metamaterial Perfect Absorbers: Giant Optical Chirality for Polarization-Sensitive Photochemistry. *ACS Photonics* 2019, 6, 3241−3252.

(898) Wu, Y.; Yang, W.; Fan, Y.; Song, Q.; Xiao, S. TiO₂ Metasurfaces: From Visible Planar Photonics to Photochemistry. *Sci. Adv.* 2019, 5, No. eaax0939.

(899) Wang, P.; Krasavin, A. V.; Nasir, M. E.; Dickson, W.; Zayats, A. V. Reactive Tunnel Junctions in Electrically Driven Plasmonic Nanorod Metamaterials. *Nat. Nanotechnol.* 2018, 13, 159−164.

(900) Khorashad, L. K.; Besteiro, L. V.; Correa-Duarte, M. A.; Burger, S.; Wang, Z. M.; Govorov, A. O. Hot Electrons Generated in Chiral Plasmonic Nanocrystals as a Mechanism for Surface Photochemistry and Chiral Growth. *J. Am. Chem. Soc.* 2020, 142, 4193−4205.

(901) Liu, T.; Besteiro, L. V.; Liedl, T.; Correa-Duarte, M. A.; Wang, Z.; Govorov, A. O. Chiral Plasmonic Nanocrystals for Generation of Hot Electrons: Toward Polarization-Sensitive Photochemistry. *Nano Lett.* 2019, 19, 1395−1407.

(902) Besteiro, L. V.; Movsesyan, A.; Ávalos-Ovando, O.; Lee, S.; Cortés, E.; Correa-Duarte, M. A.; Wang, Z. M.; Govorov, A. O. Local Growth Mediated by Plasmonic Hot Carriers: Chirality from Achiral Nanocrystals Using Circularly Polarized Light. *Nano Lett.* 2021, 21, 10315−10324.

(903) Hao, C.; Xu, L.; Ma, W.; Wu, X.; Wang, L.; Kuang, H.; Xu, C. Unusual Circularly Polarized Photocatalytic Activity in Nanogapped Gold-Silver Chiroplasmonic Nanostructures. *Adv. Funct. Mater.* 2015, 25, 5816−5822.

(904) Wang, Z.; Jia, H.; Yao, K.; Cai, W.; Chen, H.; Liu, Y. Circular Dichroism Metamirrors with Near-Perfect Extinction. *ACS Photonics* 2016, 3, 2096−2101.

(905) Capitolis, J.; Hamandi, M.; Hochedel, M.; El-Jallal, S.; Drouard, E.; Chevalier, C.; Leclercq, J.; Penuelas, J.; Dursap, T.; Brottet, S.; et al. Two-Dimensional Photonic Metasurfaces for Slow Light-Controlled Photocatalysis. *Nano Sel.* 2022, 3, 108−117.

(906) Chen, X.; Liu, L.; Yu, P. Y.; Mao, S. S. Increasing Solar Absorption for Photocatalysis with Black Hydrogenated Titanium Dioxide Nanocrystals. *Science* 2011, 331, 746−750.

(907) Wang, P.; Nasir, M. E.; Krasavin, A. V.; Dickson, W.; Jiang, Y.; Zayats, A. V. Plasmonic Metamaterials for Nanochemistry and Sensing. *Acc. Chem. Res.* 2019, 52, 3018−3028.

(908) Zhao, L.-B.; Zhang, M.; Huang, Y.-F.; Williams, C. T.; Wu, D.-Y.; Ren, B.; Tian, Z.-Q. Theoretical Study of Plasmon-Enhanced Surface Catalytic Coupling Reactions of Aromatic Amines and Nitro Compounds. *J. Phys. Chem. Lett.* 2014, 5, 1259−1266.

(909) Christopher, P.; Xin, H.; Linic, S. Visible-Light-Enhanced Catalytic Oxidation Reactions on Plasmonic Silver Nanostructures. *Nat. Chem.* 2011, 3, 467−472.

(910) Ezendam, S.; Herran, M.; Nan, L.; Gruber, C.; Kang, Y.; Gröbmeyer, F.; Lin, R.; Gargiulo, J.; Sousa-Castillo, A.; Cortés, E. Hybrid Plasmonic Nanomaterials for Hydrogen Generation and Carbon Dioxide Reduction. *ACS Energy Lett.* 2022, 7, 778−815.

(911) Varandili, S. B.; Huang, J.; Oveisi, E.; De Gregorio, G. L.; Mensi, M.; Strach, M.; Vavra, J.; Gadiyar, C.; Bhowmik, A.; Buonsanti, R. Synthesis of Cu/CeO₂₋ₓ Nanocrystalline Heterodimers with Interfacial Active Sites To Promote CO₂ Electroreduction. *ACS Catal.* 2019, 9, 5035−5046.

(912) Loiudice, A.; Lobaccaro, P.; Kamali, E. A.; Thao, T.; Huang, B. H.; Ager, J. W.; Buonsanti, R. Tailoring Copper Nanocrystals towards C₂ Products in Electrochemical CO₂ Reduction. *Angew. Chem., Int. Ed.* 2016, 55, 5789−5792.

(913) Iyengar, P.; Kolb, M. J.; Pankhurst, J. R.; Calle-Vallejo, F.; Buonsanti, R. Elucidating the Facet-Dependent Selectivity for CO₂ Electroreduction to Ethanol of Cu-Ag Tandem Catalysts. *ACS Catal.* 2021, 11, 4456−4463.

(914) Chavez, S.; Aslam, U.; Linic, S. Design Principles for Directing Energy and Energetic Charge Flow in Multicomponent Plasmonic Nanostructures. *ACS Energy Lett.* 2018, 3, 1590−1596.

(915) Voiry, D.; Shin, H. S.; Loh, K. P.; Chhowalla, M. Low-Dimensional Catalysts for Hydrogen Evolution and CO₂ Reduction. *Nat. Rev. Chem.* 2018, 2, 0105.

(916) Hutchison, J. A.; Schwartz, T.; Genet, C.; Devaux, E.; Ebbesen, T. W. Modifying Chemical Landscapes by Coupling to Vacuum Fields. *Angew. Chem., Int. Ed.* 2012, 51, 1592−1596.

(917) Hertzog, M.; Wang, M.; Mony, J.; Börjesson, K. Strong Light-Matter Interactions: A New Direction within Chemistry. *Chem. Soc. Rev.* 2019, 48, 937−961.

(918) Ulusoy Ghobadi, T. G.; Ghobadi, A.; Odabasi, O.; Karadas, F.; Ozbay, E. Subwavelength Densely Packed Disordered Semiconductor

Metasurface Units for Photoelectrochemical Hydrogen Generation. *ACS Appl. Energy Mater.* **2022**, *5*, 2826−2837.

(919) Loh, J. Y. Y.; Safari, M.; Mao, C.; Viasus, C. J.; Eleftheriades, G. V.; Ozin, G. A.; Kherani, N. P. Near-Perfect Absorbing Copper Metamaterial for Solar Fuel Generation. *Nano Lett.* **2021**, *21*, 9124−9130.

(920) Hutchby, J. A. A "Moore's Law"-like Approach to Roadmapping Photovoltaic Technologies. *Renew. Sustain. Energy Rev.* **2014**, *29*, 883−890.